

**Phase Behavior, Rheology, and Characterization of Lysozyme – Single-Walled Carbon  
Nanotube Dispersions**

by

Daniel Wallace Horn

A dissertation submitted to the Graduate Faculty of  
Auburn University  
in partial fulfillment of the  
requirements for the Degree of  
Doctor of Philosophy

Auburn, Alabama  
December 8, 2012

Copyright 2012 by Daniel Wallace Horn

Approved by

Virginia A. Davis, Chair, Mary and John H. Sanders Associate Professor of Chemical  
Engineering  
Mark E. Byrne, Daniel F. and Josephine Breeden Associate Professor of Chemical Engineering  
Steve R. Duke, Alumni Associate Professor of Chemical Engineering  
Chris J. Easley, Assistant Professor of Chemistry and Biochemistry

## ABSTRACT

Single-walled carbon nanotubes (SWNT) are one of the most promising materials in nanoscale science and technology with potential applications ranging from polymer nanocomposites to biocompatible smart materials. However, translating the extraordinary mechanical, thermal, optical and electrical properties of individual SWNT into macroscopic assemblies such as films and fibers is challenged by the aggregation of pristine SWNT. In order to achieve individual SWNT, their mutual attractive forces must be overcome. At that point, there must be a force of repulsion to stabilize the SWNT, thereby not allowing them to reaggregate. The research presented here concentrated on the application of lysozyme (LSZ) as a dispersing agent for SWNT. The structural nature of LSZ make it a well-suited dispersant for SWNT. Not only does LSZ enable the mechanical, electrical, thermal, and optical properties of SWNT to be exploited, but it also enhances the system by making it antibacterial. During this research, it was found that LSZ interacts with SWNT through  $\pi$ -bonding of the aromatic SWNT sidewall with the tryptophan residue within the LSZ hydrophobic core allowing for SWNT to be soluble in aqueous solutions. Furthermore, this research showed that dispersions of LSZ-SWNT exhibit phase transitions from isotropic liquid to gel as the concentration of both LSZ and SWNT are increased via evaporation. It was then determined that the phase transitions were caused by depletion interactions between LSZ and SWNT due to the loss in free energy of mixing of the system at increased LSZ and SWNT concentrations. In order to increase the concentration of SWNT at which depletion aggregation occurred, the cationic surfactant

tetradecyltrimethylammonium bromide (TTAB) was added to stabilize the system. Through stabilization of the LSZ-SWNT dispersions and the addition of synthetic or natural polymers, it was possible to assemble and process of concentrated dispersions into films and fibers which showed unique tailorability for use in novel applications.

## ACKNOWLEDGMENTS

I would like to thank my committee members for providing both their time and knowledge in the preparation and review of this manuscript. I would like to thank Dr. Virginia Davis for allowing me to formulate and tests my hypotheses while following my interest in this research. Thank you to Dr. Chris Easley for his hours of critical discussion and testing on the links between biology, chemistry, and engineering. Thank you to Dr. Mark Byrne and Dr. Steve Duke for providing inspirational advice, sometimes unrelated to research, and for showing that having a family in graduate school is not only possible but rewarding. Thank you to Brian Schwieker for the many hours of hard work in making all of my ideas of processing equipment become a reality and teaching me about everything outside of chemical engineering. Thank you to Georgetta Dennis and Karen Cochran for all the many miscellaneous things you did for me and my family during my stay here. Acknowledgement and thanks are also extended to Dr. Matthew Kayatin, Dr. Geyou Ao, Dr. Phillipe Poulin, Teng Xu, Joyanta Goswami, Zan Haywood, Phillip Higginbotham, Gloria Nyankima, Suzie Murdock, and Shannon McGee for teaching me numerous things and making research fun. Thank you to all my parents – mom, Dick, and Mr. and Mrs. Ehrhart – for your continued support throughout this process. Finally, no amount of thanks is enough to be given to my wife, Katie, and two sons, Caleb and Carter, for the time, effort, support, and love they have given to allow me to pursue my dreams, and always showing me that the troubles of this world are easily washed away with help and love from family.

## Table of Contents

Abstract .....	ii
Acknowledgments .....	iv
List of Tables .....	ix
List of Figures .....	x
1. Introduction.....	1
2. Background.....	4
2.1. Carbon Nanotubes.....	4
2.1.1. Carbon Nanotube Molecular Structure .....	5
2.1.2. Carbon Nanotube Mechanical, Electrical, and Thermal Properties.....	9
2.2. Lysozyme.....	10
2.2.1. Lysozyme Protein Structure.....	11
2.2.2. Lysozyme Enzymatic Activity.....	14
2.2.3. Lysozyme Phase Behavior .....	16
2.3. Lysozyme Dispersions of Carbon Nanotubes.....	17
2.3.1. Aqueous Lysozyme – Carbon Nanotube Dispersions .....	18
2.3.2. Liquid Crystalline Lysozyme – Carbon Nanotube Dispersions .....	20
2.3.3. Gel Lysozyme – Carbon Nanotube Dispersions.....	24
2.4. Colloid Theory.....	25
2.4.1. van der Waals Forces .....	25

2.4.2. D.L.V.O. Theory .....	28
2.4.3. Binding Energy of Carbon Nanotubes .....	30
2.5. Thermodynamics of Carbon Nanotube Solutions .....	32
2.5.1. Cylindrical Particle Theory .....	33
2.5.1.1. Cylindrical Particle Entropy of Mixing .....	36
2.5.1.2. Cylindrical Particle Enthalpy of Mixing .....	37
2.5.1.3. Cylindrical Particle Free Energy of Mixing .....	40
2.5.2. Cylindrical – Sphere Particle Theory .....	42
2.5.2.1. Cylindrical – Sphere Excluded Volume Interaction .....	42
2.5.2.2. Cylindrical – Sphere Free Energy .....	45
2.5.2.3. Cylindrical –Sphere Phase Behavior .....	48
2.6. Rheology Theory .....	51
2.6.1. Cone and Plate Rheology .....	52
2.6.2. Parallel Plate Rheology .....	54
2.6.3. Linear Viscoelasticity .....	57
2.6.4. Oscillatory Flow .....	59
2.6.5. Shear Flow .....	64
2.6.6. Rheology of Particulate Suspensions .....	68
2.6.7. Rheology of Non-Spherical Particulate Suspensions .....	69
3. Experimental Details .....	74
3.1. Raw Materials .....	74
3.2. Methods of Preparation .....	75
3.2.1. Sonication .....	75

3.2.2. Centrifugation .....	75
3.3. Methods of Characterization.....	76
3.3.1. Microscopy .....	76
3.3.1.1. Atomic Force Microscopy .....	77
3.3.1.2. Optical Microscopy.....	78
3.3.1.3. Scanning Electron Microscopy .....	79
3.3.1.4. Transmission Electron Microscopy .....	80
3.3.2. Rheology.....	81
3.3.2.1. Amplitude Sweep Test.....	82
3.3.2.2. Frequency Sweep Test .....	83
3.3.2.3. Transient Test.....	84
3.3.2.4. Flow Curve Test.....	85
3.3.3. Spectroscopy.....	86
3.3.3.1. Ultraviolet-Visible Spectroscopy.....	86
3.3.3.2. Circular Dichroic Spectroscopy .....	87
3.3.3.3. Fourier Transform Infrared Spectroscopy .....	88
3.3.3.4. Raman Spectroscopy.....	89
3.3.3.5. Fluorescence Spectroscopy .....	91
3.3.3.6. Energy Dispersive X-Ray Spectroscopy.....	93
3.3.4. Thermogravimetric Analysis .....	94
3.3.5. Turbidimetric Analysis .....	95
3.3.6. Ultimate Tensile Strength Analysis .....	96
3.3.7. Electrical Resistivity Analysis .....	97

3.4. Methods of Macroscopic Assembly.....	98
3.4.1. Fiber Spinning.....	98
3.4.2. Film Drying.....	101
3.5. Mathematical Conversions.....	102
3.6. Preparation of Carbon Nanotube – Lysozyme Dispersions.....	104
4. Results and Discussion .....	110
4.1. Lysozyme Solution Characterization.....	110
4.1.1. Ultraviolet-Visible Spectroscopy.....	110
4.1.2. Circular Dichroic Spectroscopy .....	114
4.1.3. Enzymatic Activity Analysis .....	116
4.1.4. Thermogravimetric Analysis .....	118
4.1.5. Rheological Behavior.....	122
4.2. Lysozyme – Carbon Nanotube Interaction .....	129
4.3. Lysozyme – Carbon Nanotube Phase Behavior.....	147
4.4. Lysozyme – Carbon Nanotube Phase Behavior Alteration .....	164
4.5. Lysozyme – Carbon Nanotube Macroscopic Assemblies .....	179
4.5.1. Fibers.....	179
4.5.2. Films .....	192
4.6 Lysozyme – Carbon Nanotube Antibacterial Activity.....	197
5. Conclusions.....	203
References .....	206

## List of Tables

Table 1. Raman spectroscopy data for LSZ, SWNT, and LSZ-SWNT dispersions.....	136
Table 2. UV-vis calibration curve data for SWNT.....	146
Table 3. UV-vis calibration curve data for LSZ.....	147
Table 4. Phase transition data for LSZ-SWNT dispersions.....	153
Table 5. Phase transition data for LSZ-SWNT and LSZ-TTAB-SWNT dispersions.....	167
Table 6. Mechanical property data of LSZ-SWNT and LSZ-TTAB-SWNT fibers.....	182
Table 7. Raman spectroscopy data for LSZ-TTAB-SWNT fibers.....	187
Table 8. Electrical property data of LSZ-SWNT and LSZ-TTAB-SWNT fibers.....	188
Table 9. Raman spectroscopy data for LSZ-SWNT in PVA fibers.....	191
Table 10. Mechanical property data of LSZ-SWNT in PVA films.....	196

## List of Figures

Figure 1. Geometrical construct of $C_h$ on a graphene sheet .....	6
Figure 2. Vectors specified by $(n,m)$ for general CNT .....	7
Figure 3. Schematic theoretical models for SWNT .....	8
Figure 4. Corey-Pauling-Koltun model of LSZ.....	10
Figure 5. Ribbon diagram of LSZ.....	11
Figure 6. General structure of alpha helix .....	12
Figure 7. General structure of anti-parallel and parallel beta sheets.....	12
Figure 8. Ball-and-stick representation of LSZ structure .....	13
Figure 9. Schematic mechanism of LSZ hydrolyses .....	15
Figure 10. SEM of turbidity measurements for aqueous LSZ-SWNT dispersions .....	20
Figure 11. Schematic of a general liquid crystal showing order and orientation .....	21
Figure 12. Images of LSZ crystals in a liquid crystalline phase.....	21
Figure 13. Schematic representation of D.L.V.O theory .....	28
Figure 14. TEM of SWNT bundle .....	30
Figure 15. Rigid rod in the Flory lattice .....	35
Figure 16. Rigid rod divided into $y_i$ submolecules in the Flory lattice.....	35
Figure 17. Schematic illustration of excluded volume effects.....	43
Figure 18. Volume excluded to the center of mass of a rod and sphere .....	44
Figure 19. Phase behavior simulation results for addition of small spheres.....	49

Figure 20. Diagrams of three phases of rod-sphere mixtures .....	50
Figure 21. Coordinate system and geometric parameters for cone and plate geometry .....	52
Figure 22. Coordinate system and geometric parameters for parallel plate geometry .....	55
Figure 23. Illustration of the shear strain of a fluid between two parallel sliding plates .....	57
Figure 24. Illustration of a stress relaxation experiment.....	58
Figure 25. Schematic of the imposed strain wave and resulting steady-state stress wave .....	60
Figure 26. Schematic of the trigonometric deconvolution of the steady-state stress wave .....	61
Figure 27. Prototypical linear viscoelastic responses of a solid and fluid .....	62
Figure 28. Sliding plate model and relative coordinate system for simple shear .....	64
Figure 29. Schematic diagram showing the notation for normal stresses in a shear field.....	66
Figure 30. Concentration regimes used to describe rod-like particles.....	71
Figure 31. Schematic mechanism by which sonication leads to dispersion of LSZ-SWNT ....	106
Figure 32. Absorbance spectrum of LSZ solutions .....	111
Figure 33. Absorbance spectrum of various concentrations of LSZ solutions.....	112
Figure 34. Calibration curve for LSZ showing deviation from Beer-Lambert law .....	113
Figure 35. Calibration curve for LSZ .....	113
Figure 36. Far-UV CD spectrum of LSZ solution .....	115
Figure 37. Near-UV CD spectrum of LSZ solution.....	115
Figure 38. Turbidimetric analysis of LSZ solutions .....	117
Figure 39. Turbidimetric analysis of <i>M. lysodeikticus</i> .....	118
Figure 40. Weight loss curve versus temperature for LSZ in argon and air .....	120
Figure 41. Weight loss derivative curve versus temperature for LSZ in argon and air .....	121
Figure 42. Amplitude sweep data for LSZ solutions .....	123

Figure 43. Frequency sweep data for LSZ solutions .....	124
Figure 44. Frequency sweep data versus concentration for LSZ solutions .....	125
Figure 45. Steady shear viscosity data for LSZ solutions.....	126
Figure 46. Steady shear viscosity data versus concentration for LSZ solutions.....	128
Figure 47. TEM image of LSZ-SWNT dispersion .....	131
Figure 48. SEM image of LSZ-SWNT dispersion.....	132
Figure 49. ATR-FTIR spectrum of SWNT, LSZ, and LSZ-SWNT dispersion.....	133
Figure 50. Raman spectra of SWNT and LSZ-SWNT dispersions .....	135
Figure 51. UV-vis spectrum of LSZ-SWNT dispersion .....	138
Figure 52. UV-vis difference spectra of LSZ solution and LSZ-SWNT dispersion .....	140
Figure 53. CD spectrum of LSZ solution and LSZ-SWNT dispersion .....	142
Figure 54. Fluorescence spectra of LSZ solution and LSZ-SWNT dispersion .....	144
Figure 55. Calibration curve for SWNT in LSZ-SWNT dispersions .....	145
Figure 56. Calibration curve for LSZ in LSZ-SWNT dispersions.....	146
Figure 57. Phase transition diagram for LSZ-SWNT .....	151
Figure 58. Amplitude sweep data for LSZ-SWNT dispersions .....	154
Figure 59. Frequency sweep data for LSZ-SWNT dispersions .....	155
Figure 60. Frequency sweep data showing crossover for LSZ-SWNT dispersions .....	156
Figure 61. Graphical analysis of $\tan(\delta)$ versus angular frequency and concentration.....	157
Figure 62. Steady shear viscosity data for LSZ-SWNT dispersions .....	158
Figure 63. Graphical representation of the Cox-Merz rule for LSZ-SWNT dispersions .....	160
Figure 64. Inherent viscosity of LSZ-SWNT dispersions as a function of concentration.....	163
Figure 65. SEM image of LSZ-TTAB-SWNT dispersion.....	168

Figure 66. UV-vis spectra of LSZ and LSZ-TTAB-SWNT .....	169
Figure 67. Amplitude sweep data for LSZ-TTAB-SWNT dispersions .....	171
Figure 68. Frequency sweep data for LSZ-TTAB-SWNT dispersions .....	172
Figure 69. Stead shear viscosity data for LSZ-TTAB-SWNT dispersions.....	173
Figure 70. Amplitude sweep data for LSZ-SWNT and LSZ-TTAB-SWNT in PVA .....	175
Figure 71. Frequency sweep data for LSZ-SWNT and LSZ-TTAB-SWNT in PVA.....	176
Figure 72. Steady shear viscosity data for LSZ-SWNT and LSZ-TTAB SWNT in PVA .....	177
Figure 73. Inherent viscosity of all LSZ-SWNT dispersions as a function of concentration...	178
Figure 74. SEM image of LSZ-TTAB-SWNT in PVA fiber.....	184
Figure 75. Raman spectra of SWNT and LSZ-TTAB-SWNT in PVA fibers .....	186
Figure 76. Optical micrographs of LSZ-TTAB-SWNT fibers before drawing .....	189
Figure 77. Optical micrographs of LSZ-TTAB-SWNT fibers after drawing.....	190
Figure 78. Raman spectra of LSZ-SWNT in PVA fibers before and after drawing.....	191
Figure 79. SEM images of LSZ-SWNT in PVA film .....	193
Figure 80. Optical micrographs of post-process drawn LSZ-SWNT in PVA film .....	194
Figure 81. ATR-FTIR spectrum of LSZ-SWNT in PVA films .....	195
Figure 82. Far-UV CD spectrum of LSZ solution and LSZ-SWNT dispersion .....	198
Figure 83. Turbidity of constituents in LSZ-SWNT dispersions or macroscopic assemblies..	199
Figure 84. Lytic activity of LSZ-SWNT dispersions and macroscopic assemblies .....	201

## 1. INTRODUCTION

Single-walled carbon nanotubes (SWNT) are strong, rolled layers of graphene having a diameter of approximately one nanometer, and a length ranging from a 100 nm to a few micrometers. Lysozyme (LSZ) is a small, globular polyampholytic enzyme with natural antibacterial activity. The intellectual contribution to science and engineering of this research was the understanding of phase behavior and rheology of LSZ-SWNT dispersion mixtures and supernatants, development of the initial methods of macroscopic assembly of LSZ-SWNT dispersions, and elucidation of the specific interaction between LSZ and SWNT. A key motivation for this research is the need for robust, antibacterial fibers, films, composites, or coatings for use in applications ranging from preventing bacterial growth to reducing the spread of communicable illnesses. In order to achieve these results, LSZ and SWNT were processed together. The goal of this research was to exploit the antibacterial properties of LSZ and the mechanical, electrical, thermal, and optical properties of SWNT to create dispersions, capable of macroscopic assembly for tailorable applications. In order to fully realize this goal to create solid macroscopic assemblies, the phase behavior and interaction between LSZ and SWNT had to first be understood. The following hypotheses were tested: dispersion mixtures of LSZ-SWNT transition from isotropic liquid to physically networked gels, supernatant dispersions of LSZ-SWNT show no phase transition, and manipulation of the phase behavior for supernatants and mixtures enable processing into robust, solid macroscopic assemblies.

Carbon nanotubes (CNT) have been recognized as very promising nanoscale materials with remarkable mechanical, electrical, optical and thermal properties. Their potential applications have been widely studied ever since the discovery of multi-walled carbon nanotubes (MWNT) by Iijima in 1989.<sup>1</sup> The major obstacle in translating the unique properties of

individual CNT into macroscopic assemblies of films and fibers is dispersion of CNT as individuals or small bundles. Due to the smooth and highly polarizable side-walls, CNT exist as crystalline ropes or bundles with a characteristic van der Waals interaction energy of approximately  $0.5 \text{ eV nm}^{-1}$  of parallel contact.<sup>2</sup> Considering the length of CNT is on the order of hundreds to thousands of nanometers, separation of individual CNT require significant energy. However, liquid dispersion processing techniques using solvents, polymers, and biopolymers have been shown to disperse CNT as individuals or small bundles at low volume fractions. More highly ordered liquid phases of CNT, such as gels or liquid crystalline phases, could be favorable starting materials for translating nanoscale properties into macroscopic assemblies composed of nanotubes.<sup>3-8</sup> Non-covalent nanotube functionalization with natural biomolecules, such as LSZ or DNA, is an effective approach for obtaining novel materials with synergistic properties of both CNT and the biomolecule.<sup>3, 9</sup> In addition, use of aqueous solutions of biomolecules, as opposed to solvents or polymers, has the capability to be more environmentally friendly and green.

Previous work on LSZ-SWNT has shown the ability of LSZ to disperse SWNT as individuals or small bundles in the supernatant dispersion, determined the maintenance of LSZ activity in the presence of SWNT, and shown the capability of being processed into macroscopic assemblies through dilute layer-by-layer assembly.<sup>8, 10</sup> To date, depending on the processing technique, either gel or isotropic phases have resulted from dispersions of purified SWNT in LSZ. In this research, the phase behavior of LSZ-SWNT dispersions were analyzed by rheological characterization coupled with cross-polarized optical microscopy. Evaporation of LSZ-SWNT dispersions without centrifugation resulted in a gel phase formation. However, evaporation of LSZ-SWNT supernatant after centrifugation resulted in maintenance of an isotropic liquid phase. The LSZ-SWNT supernatants contained more individually dispersed

SWNT compared to the non-centrifuged dispersion. In order to produce LSZ-SWNT dispersions with less aggregation at increased SWNT concentrations the synthetic surfactant trimethyltetradecylammonium bromide (TTAB) was added. After determination of phase behavior at large volume fractions of SWNT, various approaches of macroscopic assembly and post-assembly processing of LSZ-stabilized SWNT dispersions was explored. Rheology plays a central role in elucidating the structure-processing-property interrelationships for macroscopic assemblies produced from nanotube dispersions. Furthermore, understanding the molecular interaction between LSZ and SWNT allowed for understanding of changes when manipulation of the dispersion state occurred to alter the phase behavior.

This dissertation outlines the phase behavior, rheology, characterization, and macroscopic assembly of LSZ-SWNT aqueous dispersions. Chapter 2 provides background information on materials used including LSZ and SWNT, general colloid theory, thermodynamics and phase behavior of rods and rod-sphere systems, and general theory of rheology. Chapter 3 provides information on the materials used in this research, instrumentation used for characterization, and experimental techniques. Chapter 4 presents the results and discussion on the characterization of LSZ solution, the LSZ-SWNT molecular interaction, phase behavior and alteration of LSZ-SWNT dispersions, and the resulting macroscopic assemblies. Lastly, Chapter 5 provides the conclusions of this research and presents possible directions for future work in the field of LSZ-SWNT dispersions.

## **2. BACKGROUND**

The observation of MWNT by Iijima in 1989 and the subsequent identification of SWNT along with Bethune et al. two years later launched the current explosion of interests in carbon nanotubes (CNT).<sup>1, 11-12</sup> The extraordinary properties of CNT have resulted in their great potential in various applications including strong antimicrobial coatings, artificial muscles, chemical sensors and hydrogen storage.<sup>8, 13-16</sup> After their discovery, the large scale production of carbon nanomaterials was the next step in stimulating the growth of research on small diameter nanoscale materials. CNT production methods include laser vaporization, electric arc, chemical vapor deposition (CVD), and high-pressure carbon monoxide processing.<sup>2, 17-19</sup> Synthesized nanotubes have polydisperse length and diameter distributions, and contain impurities such as metal catalyst particles, amorphous carbons, and fullerenes. These factors often complicate the translation of nanoscale properties into macroscopic objects. Thus, purification after synthesis is often performed, but this can lead to more defects in the nanotubes. By obtaining improved properties through optimized synthetic processing of CNT, the experimental and theoretical efforts in exploring the intrinsic characteristics of CNT during synthesis and their further application in novel materials have been made possible.

### **2.1. CARBON NANOTUBES**

SWNT have been described as ladder polymers of pure carbon, where more than one bond needs to be broken in order to cleave the backbone.<sup>20</sup> However, SWNT are much more robust than typical ladder polymers due to the highly ordered carbon-carbon bonds that must be cleaved in order for tube scission to occur. Since the  $sp^2$  hybridized carbon-carbon bond is among the strongest known, individualized, pristine SWNT are likely one of the most mechanically robust materials that will ever be discovered.<sup>21</sup> However, the major obstacle for

current studies is difficulty in dispersing SWNT as individuals or small bundles. The barrier is due to the van der Waals forces between SWNT. To overcome this problem, chemical functionalization of SWNT by both covalent and non-covalent bonding has become a major focus. The end goal is to translate SWNT unique properties into macroscopic applications. In recent studies, covalent and non-covalent modification of SWNT with biological molecules has attracted significant attention to allow a pathway to translate SWNT properties into macroscopic assemblies.

### **2.1.1. CARBON NANOTUBE MOLECULAR STRUCTURE**

SWNT are hollow cylinders of rolled graphene sheets having a diameter on the order of one nanometer and lengths of up to one micron or greater. Double-walled carbon nanotubes (DWNT) and MWNT are comprised of coaxially arranged, nested cylinders of graphene with diameters ranging from 2 to >50 nm with a concentric layer spacing of 0.34 nm.<sup>22-23</sup> With variations in diameter and length even for each type, they have aspect ratios ranging from approximately 100 to 1000.<sup>23</sup> However, the length, diameter, and, hence, aspect ratio, vary within and between samples, batches, laboratories, and manufacturers.<sup>22</sup> In the absence of defects, the carbon atoms that make up the graphene sheet are covalently joined by an  $sp^2$  hybridized bonds. However, the strain associated with bending of the graphene surface increases with decreasing tube radius and increases the  $sp^3$  hybrid character of the surface.<sup>24-26</sup> Therefore, small diameter CNT are the most reactive. For this reason, MWNT and large diameter SWNT show weak  $sp^3$  hybridization unless the surface is chemically altered or functionalized.<sup>26</sup>

All known SWNT synthesis methods give mixtures of diameters, lengths, and chiralities.<sup>21</sup> The chirality of a CNT refers to the number of ways a graphene sheet can be rolled into a CNT. More specifically, tube chirality is identified with a pair of integers  $(n,m)$  which

define the circumferential chiral vector,  $\mathbf{C}_h$ , which the graphene is rolled upon. Figure 1 displays the geometrical construct of  $\mathbf{C}_h$  on a graphene sheet, and Equation 2.1 defines the chiral vector,  $\mathbf{C}_h$ . The length of  $\mathbf{C}_h$  is represented by the vector  $\mathbf{OA}$ , the nanotube circumference. Orthogonal to  $\mathbf{C}_h$  lays the translation vector  $\mathbf{T}$  which defines the unit cell. The chiral indices  $(n,m)$  describe the number of steps along the hexagonal unit vectors  $\mathbf{a}_1$  and  $\mathbf{a}_2$  as shown in Figure 2.

$$\vec{C}_h = n\vec{a}_1 + m\vec{a}_2 \quad (2.1)$$

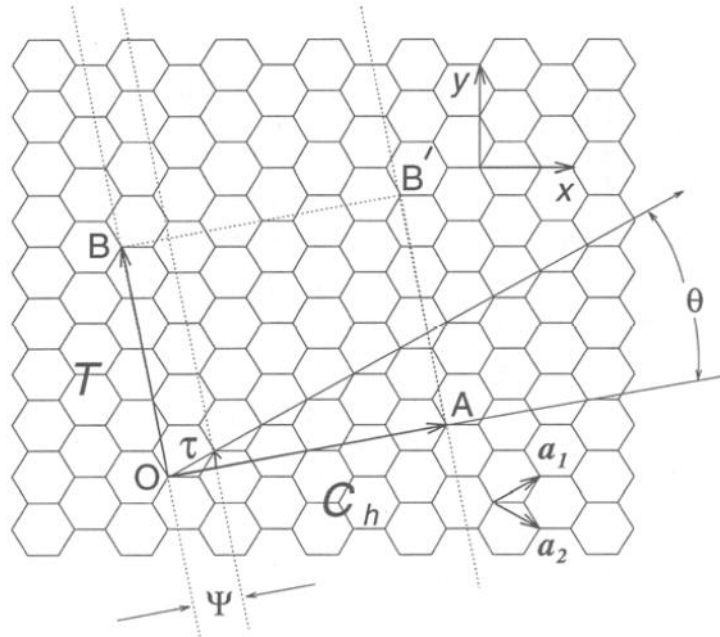


**Figure 1.**  $\mathbf{C}_h$  is defined on the graphene lattice by unit vectors  $\mathbf{a}_1$  and  $\mathbf{a}_2$  and the chiral angle  $\theta$  with respect to the zigzag axis ( $\theta = 0^\circ$ ). The lattice vector of the one-dimensional unit cell is defined by  $\mathbf{T}$ . The rotation angle  $\psi$  and the translation  $\tau$  constitute the basic symmetry operation  $R = (\psi|\tau)$  for the carbon nanotube. The diagram is constructed for  $(n,m) = (4,2)$ . Reproduced from Dresselhaus et al.<sup>23</sup>

The magnitude of the unit vector  $\mathbf{a}_i$  can be easily determined using geometry. The distance between adjacent vertices on a single hexagon is given by the carbon-carbon bond length,  $L_{C-C}$ ,

which is approximately 1.42 nm for graphene.<sup>23</sup> From geometry, a hexagon is composed of six equilateral triangles, and each unit vector will bisect two equilateral triangles along a length of distance  $\sqrt{3} L_{C-C}$ , defining the lattice constant as 0.246 nm. Therefore, the length of vector  $C_h$  given by Equation 2.1 can be derived using the lattice constant. Equation 2.2 displays the relationship between tube diameter, tube intergers, and the magnitude of  $C_h$ .

$$d = \frac{\sqrt{3}L_{C-C}(m^2+mn+n^2)^{\frac{1}{2}}}{\pi} = \frac{|C_h|}{\pi} \quad (2.2)$$

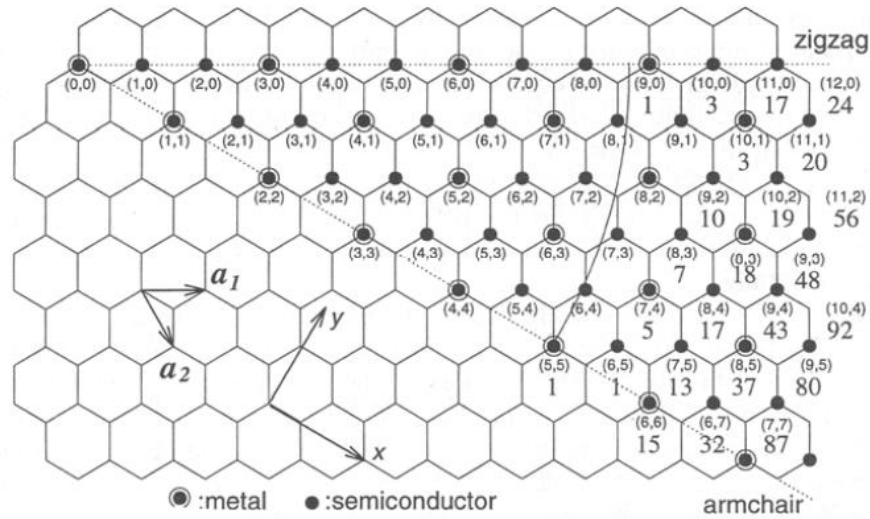


**Figure 2.** Possible vectors specified by  $(n,m)$  for general CNT, including zigzag, armchair, and chiral tubes. Below each integer pair is listed the number of distinct caps that can be joined continuously to the CNT denoted by  $(n,m)$ . Encircled dots denote metallic structure and small dots are for semiconducting tubes. Reproduced from Dresselhaus et al.<sup>23</sup>

The division by  $\pi$  is necessary to relate the tube circumference to the diameter. As shown in Figure 2, the indicies  $(n,m)$  and therefore  $C_h$  determine the tubes electronic structure. Despite the structural similarity to a single sheet of graphite, which is a semiconductor with zero band gap, SWNT may be either metallic or semiconducting.<sup>27</sup> More specifically, if the difference  $n - m$  is

equal to zero the nanotube is a metallic, ballistic conductor with a band gap of zero. If the difference is nonzero and divisible by three, the nanotube is considered semimetallic with a band gap on the order of meV. In all other cases when the difference is nonzero and not divisible by three the nanotube is semiconducting with a band gap ranging from approximately 0.5 to 1.0 eV.<sup>21</sup> Structurally, the vectors  $(n,0)$  and  $(0,m)$  denote zigzag tubes, and the vectors having indicies of  $n = m$  denote armchair tubes; so named by examining a ring of carbon atoms around the circumference. Both armchair and zigzag tubes are achiral whereas all other vectors  $n \neq m$  or zero are chiral as shown in Figure 3.

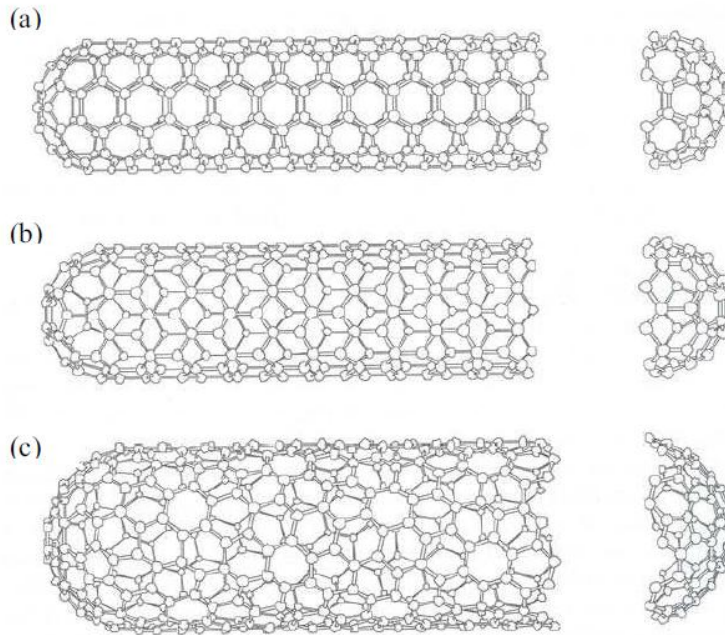


**Figure 3.** Schematic theoretical model for a SWNT with the tube axis normal to: (a) the  $\theta = 30^\circ$  direction with  $(n,m) = (5,5)$  (an “armchair” tube), (b) the  $\theta = 0^\circ$  direction with  $(n,m) = (9,0)$  (a “zigzag” tube), and (c) a general direction  $0^\circ < \theta < 90^\circ$  with  $(n,m) = (10,5)$  (a “chiral” tube). Reproduced from Dresselhaus et al.<sup>23</sup>

## 2.1.2. CARBON NANOTUBE MECHANICAL, ELECTRICAL, AND THERMAL PROPERTIES

The mechanical properties of CNT have been determined by both theory and experiment. The Young's modulus, a mechanical measure of stiffness from the stress and strain exerted on a material, has been determined theoretically as 0.64 TPa for individual SWNT.<sup>28</sup> In addition, the average experimental values as determined by atomic force microscopy for individual SWNT is 1.25 TPa.<sup>29</sup> This is consistent with experimental values for SWNT bundles ranging from 0.32 to 1.47 TPa.<sup>30</sup> Small diameter SWNT ropes have been experimentally extended elastically to 5.8%, therefore, the SWNT tensile strength can be calculated as approximately 37 GPa.<sup>31</sup> For typical SWNT, the density normalized Young's modulus is approximately 19 times that of steel and 2.4 times that of silicon carbide nanorods. Similarly, the density normalized tensile strength is approximately 56 times that of steel wire and approximately 1.7 times greater than silicon carbide.<sup>27</sup> It is because of these mechanical properties that assembly of macroscopic materials composed of CNT is of such importance.

The electronic properties of MWNT and SWNT are quite similar in perfectly structured CNT.<sup>27</sup> Due to their nearly one-dimensional structure, electronic transport occurs ballistically in the axial direction for metallic CNT.<sup>32</sup> Therefore, high currents can be carried with resistivity on the order of 0.1 to 200  $\mu\Omega\text{-cm}$ .<sup>2, 33</sup> The thermal conductivity of an individual MWNT has been reported in excess of 3,000  $\text{W m}^{-1}\text{K}^{-1}$ .<sup>34</sup> Correspondingly, the thermal conductivity for SWNT has been shown as 2,700  $\text{W m}^{-1}\text{K}^{-1}$  which exceeds that of diamond at 2,500  $\text{W m}^{-1}\text{K}^{-1}$ , which is the current benchmark.<sup>35</sup> In addition, superconductivity, an electrical resistance of approximately zero, has been experimentally observed in SWNT at extremely low temperatures.<sup>36-37</sup> Thermal stability has been reported at temperatures as high as 2,800°C in inerts and 750°C in air.<sup>38</sup>

## 2.2. LYSOZYME

LSZ was the second protein to have its crystal structure determined via X-ray diffraction, and has been studied extensively.<sup>39</sup> LSZ is a polyampholyte, containing multiple hydrophobic and hydrophilic domains. This polyampholytic nature makes it a good dispersant for either hydrophobic or hydrophilic molecules. In the native, non-denatured conformation, the exposed LSZ surface is primarily hydrophilic. The surface hydrophilicity allows for stabilization and solubility in water. The stability and weak interactions are determined by colloid theory of the protein in solution, as discussed later. LSZ is a relatively small, globular protein, as shown in Figure 4. It has a diameter of approximately 3 nm and a molecular weight of approximately 14,000 g mol<sup>-1</sup> and is comprised of a single polypeptide chain of 129 amino acid residues.<sup>10, 40</sup> Of the 129 residues, approximately 6 are lysine and 11 are arginine. These residues contain primary amines making the LSZ molecule strongly cationic with solubility in water of 10 mg mL<sup>-1</sup>.<sup>10</sup>

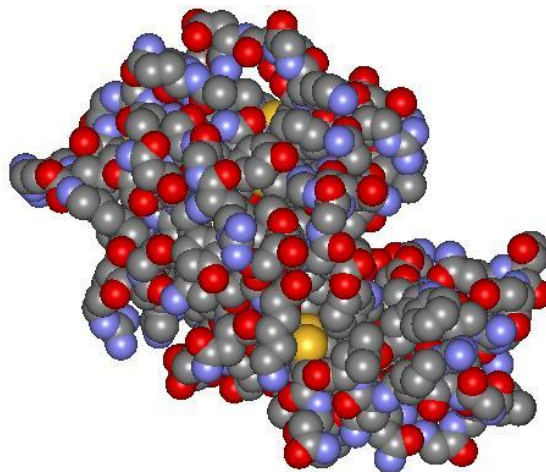


**Figure 4.** Corey-Pauling-Koltun model of LSZ showing the globular nature of the tertiary structure. Carbon, nitrogen, oxygen and sulfur atoms are colored grey, blue, red and yellow, respectively. Adapted from Szymanska et al.<sup>41</sup>

### 2.2.1. LYSOZYME PROTEIN STRUCTURE

LSZ contains two domains within its folded polypeptide chain, an  $\alpha$  and a  $\beta$  domain as shown in Figure 5. The  $\alpha$ -domain contains four  $\alpha$ -helices and one  $3_{10}$  helix. The  $\beta$ -domain has one three-stranded, anti-parallel  $\beta$ -sheet, one  $3_{10}$  helix, and one amorphous loop.<sup>40</sup>

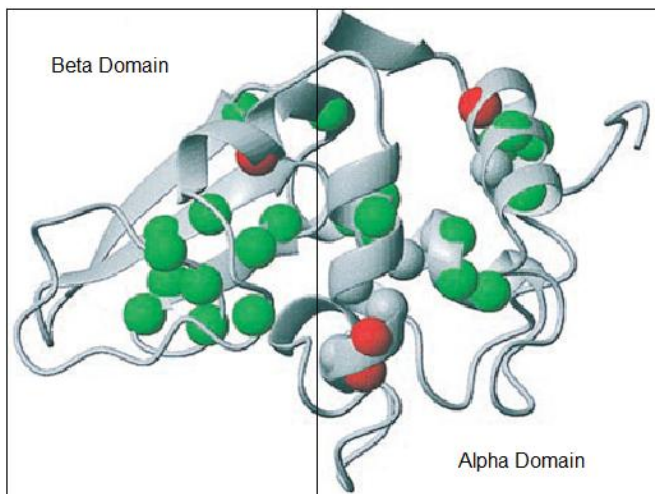


**Figure 5.** Ribbon diagram of LSZ showing the two primary domains,  $\alpha$  and  $\beta$ . The  $\alpha$ -domain consisting of the primary  $\alpha$ -helices, and the  $\beta$ -domain consisting of the primary anti-parallel, pleated  $\beta$ -sheet. Adapted from Knubovets et al.<sup>42</sup>

The  $\alpha$ -helices are a common secondary structure of proteins that can vary in size from eight to hundreds of amino acid residues. The  $\alpha$ -helix is a right-handed coiled or spiral conformation, in which every backbone amino group hydrogen bonds to the backbone carbonyl group of the amino acid four residues earlier as shown in Figure 6. A  $3_{10}$  helix, comprised of only ten amino acid residues, is a right-handed coil in which every backbone amino group hydrogen bonds to the backbone carbonyl group of the amino acid three residues earlier.  $3_{10}$  helices are less common secondary structures of proteins.

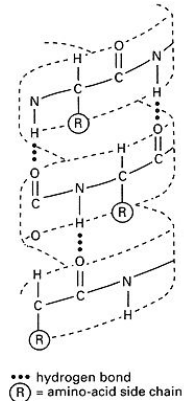


**Figure 6.** Structure of alpha helix showing hydrogen bonding between amine and carbonyl groups of every fourth amino acid residue. Adapted from White.<sup>43</sup>

$\beta$ -sheets are regular secondary structures in proteins.  $\beta$ -sheets consist of  $\beta$ -strands connected laterally by at least two or three backbone hydrogen bonds, forming a generally pleated sheet. A  $\beta$  strand is a stretch of polypeptide chain, typically three to ten amino acids long, with the backbone in an a fully extended conformation. In an antiparallel arrangement, the adjacent  $\beta$  strands alternate directions so that the amino terminus of one strand is adjacent to the carbonyl terminus of the next strand as shown in Figure 7.

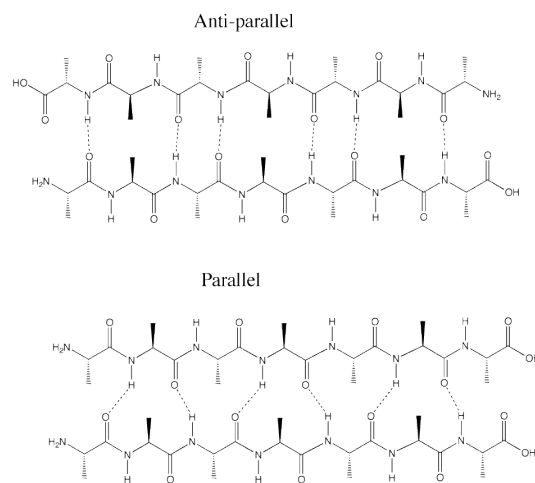


**Figure 7.** Structure of anti-parallel and parallel beta sheets showing hydrogen bonding between amine and carbonyl groups. Adapted from White.<sup>43</sup>

This arrangement, as compared to the parallel structure, produces the strongest inter-strand stability because it allows the inter-strand hydrogen bonds between carbonyls and amines of adjacent strands to be planar. An amorphous loop is simply a secondary structure which cannot be classified as any type of other known secondary structure.<sup>43</sup>

In general, short amino acid chains do not exhibit much  $\alpha$ -helical or  $\beta$ -sheet structure in solution since the entropic energy associated with folding the amino acid chain is not compensated for by a sufficient amount of stabilizing interactions. The backbone hydrogen bond interactions are considered weakened by the addition of hydrophilic molecules and are readily attacked by water molecules. However, in more hydrophobic environments, amino acid chains can adopt stable secondary structures. Furthermore, crosslinks or bridges can aid in conformationally stabilizing helices or sheets. Crosslinks stabilize the secondary structures through bonds which are stronger than the entropy related to unfolding. LSZ contains four disulfide bridges which stabilize the secondary structure as seen in Figure 8.

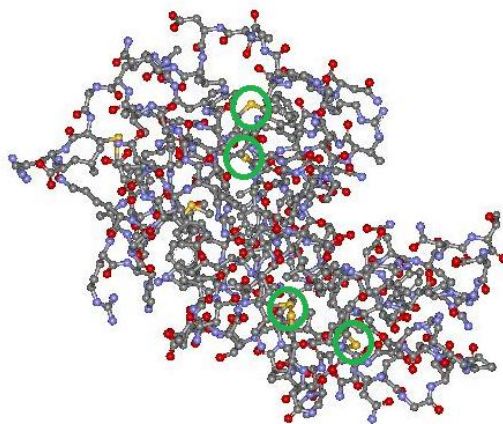


**Figure 8.** Ball-and-stick representation of LSZ structure highlighting the disulfide bridges at the core. All protein atoms are shown as balls, and bonds between atoms are shown as a stick. Carbon, nitrogen, oxygen and sulfur atoms are colored grey, blue, red and yellow, respectively. Adapted from Szymanska et al.<sup>41</sup>

Because of these disulfide bridges, it is difficult for LSZ to completely lose its globular shape. Disulfide bridges are a covalent bond, derived by the coupling of two thiol groups. In the case of LSZ, the disulfide bridges are formed between the thiol groups of cysteine residues.<sup>43</sup> The disulfide bond stabilizes the folded form of LSZ in several ways. First, it holds two portions of LSZ together, biasing the protein towards the folded morphology. More simply, the disulfide bond destabilizes the unfolded form of the protein by lowering its entropy. Second, the disulfide bond helps to form the nucleus of a hydrophobic core. Essentially, local hydrophobic residues condense around the disulfide bond and onto each other through hydrophobic interactions within the core of the LSZ. Third, the disulfide bond links two segments of the LSZ chain increasing the effective local concentration of protein residues and lowers the effective local concentration of water molecules in solution. Since water molecules attack hydrogen bonds and break up secondary structure, the disulfide bonds stabilize the secondary structure.<sup>44</sup> Also, due to the disulfide bridges, LSZ is reasonably stable over a wide range of pH and temperature, with the isoelectric point of LSZ being 11 and the denaturation temperature being 76°C. Having such a high isoelectric point makes solutions of LSZ a very good electrostatic solvent having a charge of +8 at neutral pH.<sup>45</sup> It should be noted that the other sulfur-containing amino acid, methionine, cannot form disulfide bonds.

### **2.2.2. LYSOZYME ENZYMATIC ACTIVITY**

In addition to all the structural properties associated with LSZ that make it a good surfactant, the advantage of LSZ as a SWNT dispersant is the natural antibacterial activity LSZ possess. LSZ catalyzes the hydrolysis of 1,4- $\beta$ -glycosidic linkages between N-acetylmuramic acid (NAM) and N-acetylglucosamine (NAG) which are components of the cell wall

peptidoglycan of bacteria, as shown in Figure 9.<sup>46</sup> As such, LSZ is an enzyme which is an efficient antibacterial agent against Gram-positive bacteria.

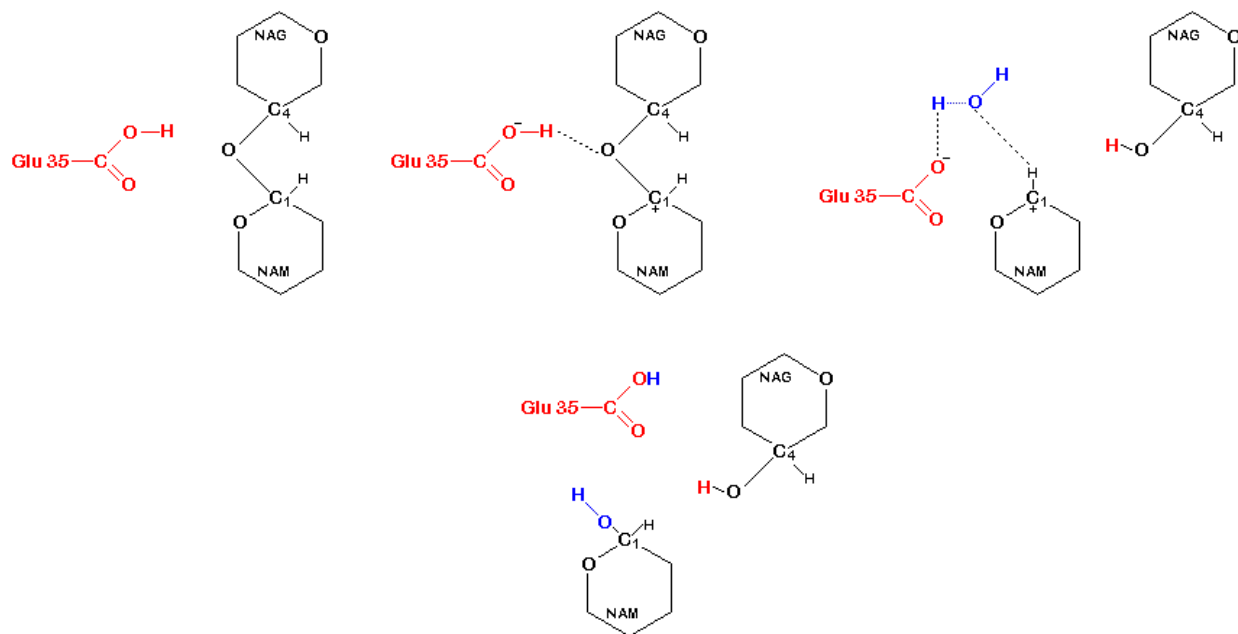


**Figure 9.** Schematic mechanism of LSZ hydrolyses. Glu35 is the active site of Glutamic Acid, however, it could also be represented by Asp52; N-acetylglucosamine is represented as NAG, and N-acetylmuramic acid is represented as NAM. Adapted from White.<sup>43</sup>

LSZ belongs to the hydrolases enzymatic class. Hydrolases catalyze the hydrolysis or hydrolytic cleavage of a chemical bond resulting in the formation of water. This class of enzymes is usually classified by the nature of the hydrolyzed bond, the chemical nature of the substrate, and finally by the enzyme. Within the class of hydrolases, LSZ belongs to the glycosylases family due to its reaction with the glycosidic bond between NAM and NAG. This reaction takes place in a long, deep cleft, which contains the active sites of LSZ. The active sites of LSZ are glutamic acid at residue 35 and aspartic acid at residue 52. The activity cleft is a very

specific active site, which can bind only six sugar rings from a polysaccharide chain and hydrolyze them into a disaccharide and a tetrasaccharide subunit.<sup>43</sup>

LSZ can be inhibited from antibacterial activity by sodium dodecyl sulfate, alcohols, and oxidizers. However, LSZ activity can also be enhanced by the activator ethylene diamine tetraacetic acid due to its strong antioxidant properties. Unlike many antibacterials, LSZ has enzymatic activity in both its native and partially denatured states. Thus, making LSZ useful in processes which require some form of heat treatment.<sup>8</sup>

### **2.2.3. LYSOZYME PHASE BEHAVIOR**

The strong bonding nature of LSZ allows for multiple phases to be created in an aqueous environment. Fully solvated LSZ in water is an isotropic liquid, showing very little difference from the solvent. As water is evaporated from the aqueous LSZ solution, the increasing concentration of LSZ causes the system to become a weakly linked gel, which is hypothesized to be held together via hydrophobic covalent bonding. Adding a co-solvent or using a solvent other than water can lead to the formation of other gels or liquid crystalline phases.<sup>40, 47</sup>

In general terms, a gel transition of a polymeric system may be thought of as a nucleation process in which colloidal particles grow through condensation of macromolecular components into large clusters. Links between neighboring clusters then begin to occur until a network of clusters having developed with distinct interstices having developed between clusters. Distinct factors may induce these events, such as temperature, pH, or concentration conditions, or specific reactions leading to bond cleavage and cross-linking. In such cases, a new chemical or physical structure occurs. Solvent-induced LSZ gels are physically structured gels brought about by addition of the correct solvent to cause pH or ionic strength changes which can modify aspects of the three dimensional folding of the protein.<sup>40, 45, 48</sup> This process usually takes place at

high LSZ concentrations and involves different kinds of interactions – electrostatic and hydrophobic – as well as intermolecular disulfide bridging formation. The specific behavior in each case is unique to the solvent and method of unfolding. However, the general behavior associated with most solvent-induced LSZ gels is that of translation of  $\alpha$ -helices into  $\beta$ -sheets via hydrogen bond transfer.<sup>45</sup> Common solvents and co-solvents used to create LSZ gels include flouroalcohols, tetramethylurea, and dimethyl sulfoxide.<sup>40, 49-50</sup>

LSZ is known to form amyloid fibrils when incubated at low pH and elevated temperatures. Amyloid fibrils are polymeric  $\beta$ -sheet aggregates of a protein consisting of relatively stiff, nonbranching fibrils that are approximately a few microns long and few nanometers wide. These fibrils can be considered to be long and rigid. In this respect, they are comparable to rod-like synthetic and biological polymers which are known to form liquid crystalline phases. The amyloid fibrils formed by LSZ do in fact form liquid crystal phases similar to that of DNA.<sup>47</sup> The low pH needed for fibril formation is achieved through addition of a salt, generally sodium chloride. After addition of the salt, the LSZ solution is allowed to incubate which causes unfolding of the LSZ in such a way as to create stacked, order sheets of fibrils creating small domains of liquid crystals. Although liquid crystalline domains are evident due to the alignment of the amyloid fibrils, in literature, the distance over which the ordering occurs is debated.<sup>41, 47</sup>

### **2.3. LYSOZYME DISPERSIONS OF CARBON NANOTUBES**

Throughout the literature there are various systems containing SWNT and LSZ. All the systems are aimed at combining SWNT properties with those of LSZ and other molecules. However, the solvent or solvents that are used to dissolve the LSZ into solution vary. The three most common systems are aqueous, gel, and liquid crystalline systems. Each of these solution

systems has their own unique reasons for research, properties, advantages, and disadvantages. Aqueous and liquid-crystalline systems will be covered in depth. Gelled systems will only be sparsely covered due to the amount of conflicting data in current literature.

### **2.3.1. AQUEOUS LYSOZYME – CARBON NANOTUBE DISPERSIONS**

Aqueous LSZ-SWNT dispersions are made with the initial LSZ solution solvent being water. The use of water as the primary solvent for the LSZ-SWNT dispersion is primarily three-fold. First, water is a readily available solvent in which LSZ is extremely soluble. Second, there are little to no health and safety risks with handling or use of water. Third, since water is readily available, the cost impact of using water as a solvent is small in comparison with some more exotic solvents.

Although, the use of water as the primary solvent seems practical, there are some unique properties of water and LSZ systems which give it advantages and disadvantages. LSZ is extremely soluble in water, however, over extended time periods (>1 week) at room temperature LSZ will aggregate to form macroscopic aggregates and fibrils. This aggregation makes the eventual dispersion of SWNT very difficult; a non-homogenous LSZ solution will not properly disperse individual tubes as will be discussed later. There is the possibility that LSZ is stable in water for longer periods at a lower temperature. However, this could reduce the ease with which processing can occur and could increase the economic capital for processing due to the need to refrigerate the solution below ambient conditions. Aggregation of LSZ in water has the possibility to occur, however, the use of water as the primary solvent does not reduce the antibacterial activity of the enzyme. Circular dichroism measurements in the far- and near-UV regions have been done to show that in water, LSZ does not change conformation of either the

secondary or tertiary structure.<sup>10, 51</sup> The ability of water to maintain the antibacterial activity of LSZ is critical for the final desired properties.

The advantages of using water as the primary solvent are akin to why it is used for research: it is economically viable, it has no health, safety, or environmental risks, it makes processing easier, and it maintains the antibacterial activity of LSZ. Water being used as the solvent helps for scale-up by reducing the initial capital expenditure and also by possibly reducing the operational expense of processing. The general inertness of water also creates favorable aspects of processing and handling. The use of materials that are a low risk for health and environmental issues reduces the capital expenditure of processing because less interlocks and safety precautions are needed. The wide use of water in commercially available and currently used processes makes design and acquisition of processing equipment much easier. Using other solvents that are volatile or flammable increases design and acquisition difficulty due to special precautions that must be taken. Finally, water's ability to maintain the activity of LSZ makes it a great and practical solvent. If use of the water reduced or eliminated the enzymatic activity the justification for using LSZ as a dispersant would be questioned – why use a relatively expensive biological molecule as a dispersant when many other organic surfactants could be used at lower cost. The ability for final products to be antibacterial is what justifies the use of LSZ as a dispersant. It is important to note, that the addition of SWNT to the LSZ solution does not eliminate the antibacterial activity of LSZ.<sup>8</sup> Turbidimetric analysis was done for LSZ-SWNT systems to show that the enzymatic activity of LSZ was maintained in the presence of SWNT, as seen in Figure 10.

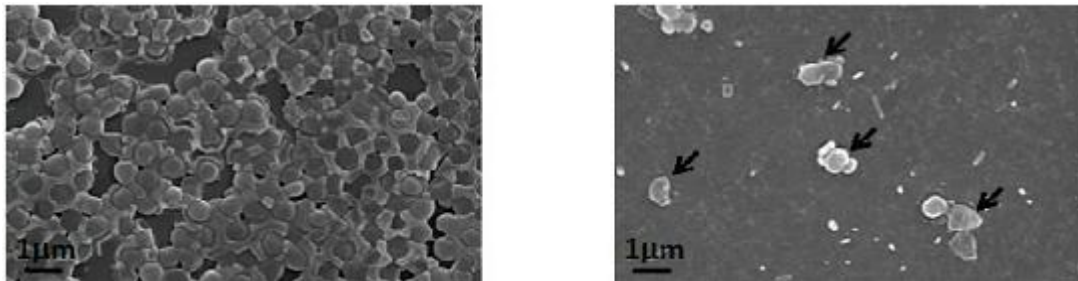


**Figure 10.** Scanning electron micrographs of colony growth showing a control substrate still dense with *Staphylococcus aureus* on the left and a substrate coated with LSZ-SWNT that shows little evidence of *S. aureus* on the right. Adapted from Nepal et al.<sup>8</sup>

In Figure 10, the difference in colony growth of the *S. aureus* shows that the LSZ-SWNT dispersion does in fact maintain antibacterial activity. The analysis shows that LSZ-SWNT maintains 92% of native LSZ activity.<sup>8</sup> The disadvantage of using water is the short time frame of kinetic stability of LSZ in water. The short time scale before LSZ in water aggregates could make continuous, scaled-up processing and application difficult.

### **2.3.2. LIQUID CRYSTALLINE LYSOZYME – CARBON NANOTUBE DISPERSIONS**

Liquid crystalline LSZ-SWNT dispersions are made with the initial LSZ solution solvent being composed of a liquid crystalline mesophase, shown in Figure 11, and a secondary solvent. The secondary solvent can range from water to ethers. These solutions are made by first making, or purchasing, the liquid crystalline phase and then making a solution of LSZ with a solvent.<sup>52</sup> Although not discussed in the literature, in order to choose an adequate solvent for the LSZ it must be a good solvate for the LSZ and also be compatible with the liquid crystal. In general this requires that LSZ be soluble in the solvent and the solvent must be structurally similar to the liquid crystalline mesophase. After the liquid crystalline and LSZ solutions are made, they are

combined to form a ternary system in which the LSZ is held in between the mesophases in the solvent as shown in Figure 12.

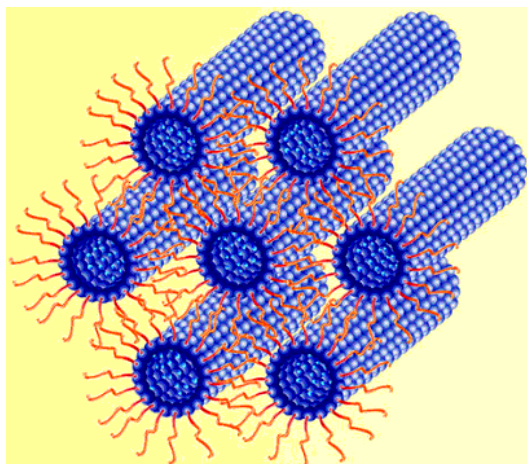


**Figure 11.** A schematic of a general liquid crystal showing order and orientation. The LSZ and SWNT integrate between the liquid crystalline structures adding greater stability. Adapted from Mishraki et al.<sup>53</sup>

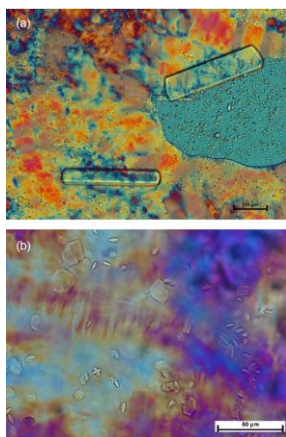


**Figure 12.** Photomicroscope images of LSZ crystals in hexagonal liquid crystalline mesophases. Adapted from Mishraki et al.<sup>53</sup>

After formation of the ternary system, SWNT is added. The exact interaction between SWNT and the ternary system are not known, but are the areas of current research.<sup>41</sup> The best possible

explanation for incorporation of SWNT is that the tubes disperse individually within the lattice spacing created by the ordered alignment of the liquid crystalline phase. By having a liquid crystalline phase, it would, in theory, be easy to individually disperse SWNT – but not just disperse them individually, also have them align with little to no external force. Thinking geometrically, if the liquid crystalline phase is aligned rods facing parallel to a director with their mass centers randomly dispersed, such as a nematic liquid crystal, and SWNT were incorporated, it would be spatially impossible to incorporate the SWNT without having them be in alignment with the liquid crystal. For this reason, liquid crystals combined with other solvents for LSZ dispersions is a very desirable area of research. There are three major advantages to using liquid crystals for LSZ-SWNT dispersions: LSZ thermal stability, SWNT ordering, and ease of macroscopic assembly.<sup>52</sup> The thermal stability of LSZ across a wide range of concentrations and pH was studied to determine if the liquid crystalline phase had any significant impact. It was found by Mishraki et. al. that not only does the denaturation temperature shift higher, but the pH dependent denaturation mechanism is virtually lost with only a 10% reduction in antibacterial activity. These findings prove that LSZ can be properly stabilized in such a way as to maintain proper activity while also being able to withstand higher temperatures; not only does this increase the range of applications but also decreases the difficulties in processing as described in the aqueous solutions section. Practical theory would lead to the idea that auto-alignment must occur if the tubes are indeed incorporated. Although there has been no documented research specifically on the auto-alignment of SWNT within the liquid crystalline-LSZ-solvent phase, there is research on the inclusion of SWNT and other nanorods in other liquid crystalline phases. The ease of macroscopic assembly is also an area that was not covered in literature, however, the order of alignment of liquid crystalline phases makes fluid phase processing of dispersions much

easier than isotropic solutions. The alignment also has the ability to increase the structural integrity of the final material.

The disadvantages of using liquid crystalline phases in dispersing LSZ-SWNT are two-fold: health, environmental, and process economics, and loss or drastic reduction of antibacterial activity. The health and environmental concerns of using liquid crystalline phases are mainly centered around the solvent used. If water were used as the secondary solvent, these concerns would not be viable. However, in the literature solvents such as glycerol monooleate, diethyl ether, and tetrahydrofuran are used.<sup>52-53</sup> Each of these solvents introduces processing risks such as flammability, reactivity, and low level toxicity which increases the risk of processing and in turn the capital cost of processing as previously described. Another economic concern is the cost of the raw material used in operation. Use of exotic and expensive materials to produce the initial ternary system of liquid crystalline-LSZ-solvent could render the macroscale assembly processing not cost effective, and therefore not viable. Along with the economic concern, exotic solvents will reduce the overall applicability of using LSZ. Although the liquid crystalline phase has been shown to stabilize LSZ from temperature and pH, there are many other compounds that can cause the protein to denature such as alcohols and peroxides. If diethyl ether is used as a solvent, it can readily react to form peroxides which then denature the LSZ eliminating the antibacterial activity. Loss of the antibacterial activity renders the use of LSZ as a SWNT dispersant. The use of liquid crystalline phases with LSZ as a dispersant for SWNT has both advantages and disadvantages that would need to be weighed against what the final desired properties and applications are prior to choosing it as a method of dispersion.

### 2.3.3. GEL LYSOZYME – CARBON NANOTUBE DISPERSIONS

Gelled LSZ – SWNT dispersions are made with the initial LSZ solution solvent being composed of a gelled polymer or a binary solvent-solvent system which induces gelling. The most commonly used polymer is glycerol.<sup>42</sup> The combination of LSZ with glycerol shows many of the same affects as the combination of LSZ with liquid crystalline mesophases – the structure of LSZ in the glycerol matrix is highly ordered and is therefore more thermally stable than in water.<sup>42</sup> The combination of LSZ with a gelled solvent-solvent mixture, such as tetramethyl urea and water or dimethyl sulfoxide and water, shows similar attributes of thermal stability.<sup>48, 50</sup> Although there are some discernible differences between polymer gels and solvent-solvent gels, from this point forward the properties and aspects discussed will be common to both types of systems. The justification for using gelled systems is similar to that of using liquid crystalline systems: ordering and stability of the LSZ and SWNT. In theory, increased order will increase the stability, both kinetic and thermal, of the system. However, in the current literature, researchers are finding conflicting viewpoints as if stabilization occurs, why it occurs, and if the properties of LSZ are or are not affected. da Silva et al. have published that the stabilization of LSZ occurs due to the physical containment of the LSZ within the viscoelastic matrix of the gel.<sup>45</sup> However, Knubovets et al. believe that the stability of LSZ is a localized effect and offers no macroscopic property enhancement.<sup>42</sup>

Although the literature has conflicting view points, there are distinct advantages and disadvantages to working with a gelled system. The major advantage is order of the dispersion. If the LSZ – SWNT is able to be ordered within a gel – something that is inherent about the matrix of a gelled network – then processing of the dispersion would be much easier as described previously. The primary disadvantage is the loss or suppression of antibacterial activity of the

LSZ. The confinement of LSZ within a gel matrix restricts the expression of the activity. By not allowing the LSZ to maintain or move into the native conformation, the matrix itself could prevent the active cleft from being exposed which prevents the activity of LSZ. On an elementary level, this could be thought of as putting a black coating on a light bulb; although the bulb may be capable of putting off light, it will not be able to do so because of the actions acted upon it with the paint. More research needs to be done in the area of gelled systems of LSZ – SWNT in order to determine the actual affects of the gel on the system. Until such time, gel systems will remain intriguing because of their theoretical advantages.

## **2.4. COLLOID THEORY**

CNT excellent material properties including low density and high aspect ratio make CNT desirable for many applications. However, in order to take advantage of their excellent properties, they must first be separated from themselves. It is CNT poor solubility characteristics that have hindered their manipulation and use in some applications.<sup>54</sup> Colloidal forces at the interface of particles are important in determining, and in turn tailoring, characteristics of dispersions. Therefore, manipulation of the forces between CNT can lead to improved solubility, and the ability to optimize the attractive and repulsive forces within the dispersion.

### **2.4.1. VAN DER WAALS FORCES**

The same forces that allow a gecko to scale horizontal walls are also responsible for the aggregation and binding of nanotubes to one another.<sup>55</sup> Both are a result of van der Waals forces which have long been understood to cause negative deviations from Boyle's law of ideal gases. For a closed system, this deviation is interpreted as an attractive force between particles or atoms reducing the force exerted on the container in a manner which is inversely proportional to the square of the system volume.<sup>56</sup> This is intuitively explained by considering an air piston. As the

closed volume is compressed, the force needed to compress the fixed mass is reduced as particles become attracted to one another. These forces allow condensed phases to form and are stronger within solids and liquids than in gases. However, what is important to note is that the observance of what is deemed the van der Waals pressure indicates that even electrically neutral bodies attract.<sup>57</sup>

The empty space between two atoms is actually a constant omni-directional sea of electromagnetic waves. This is a result of continuous interaction of charges in matter leading to spontaneous and transient electromagnetic fields. The additive effects of coordinated interactions of electromagnetic stimuli are what create van der Waals forces. Consider an atom surrounded by electromagnetic waves travelling in all directions. Now, allow the presence of a neighboring atom with omni-directional electromagnetic waves to interrupt fluctuations between the two bodies. The net interaction is that the atoms are pushed together by each atom's uninterrupted electromagnetic waves.<sup>57</sup>

In order to extend this idea to describe bodies larger than atoms or molecules, Hamaker introduced the concept of pairwise-summation for particles.<sup>58</sup> The coefficient of interaction between objects is known as the Hamaker constant,  $A$ , and is a function of the materials involved. The Hamaker constant given by Equation 2.3 is typically on the order of  $10^{-19}$  to  $10^{-21}$  J.<sup>58-59</sup>

$$A = \pi^2 C \rho_1 \rho_2 \quad (2.3)$$

In Equation 2.3,  $C$  is the coefficient in the atom-atom pair potential,  $\rho_1$  is the number of atoms per unit volume in body 1, and  $\rho_2$  is the number of atoms per unit volume in body 2.<sup>59</sup> The atom-atom pair potential is given by Equation 2.4.

$$W = -\frac{C}{D^6} \quad (2.4)$$

The potential,  $W$ , is the work required to bring the two atoms from infinite separation to a distance,  $D$ , apart and is negative due to the sign convention used for attraction.<sup>60</sup> The idea of correlation to curved, nonlinear surfaces was termed the Derjaguin Approximation and took the attractive potential for planar surfaces and adapted it to describe curved surfaces at small separations. Interactions between cylindrical CNT are of interest in this research, therefore, only curved planar geometries are considered. For the non-retarded van der Waals interaction free energy between parallel cylinders of differing radii, the interaction potential is given by Equation 2.5.<sup>59</sup>

$$W = \frac{-AL}{12\sqrt{2}D^{\frac{3}{2}}} \left( \frac{R_1 R_2}{R_1 + R_2} \right)^{\frac{1}{2}} \quad (2.5)$$

This expression for parallel cylinders gives the energy per unit length,  $L$ . The distance of separation between the two surfaces is given by  $D$  and the cylinder radii are given by  $R_1$  and  $R_2$ . The attractive force between the two cylinders can then be derived by taking the derivative of the work with respect to separation distance. In general, for parallel cylinders the force is inversely proportional to  $D^{5/2}$  as shown by Equation 2.6.

$$F \propto -ALD^{-\frac{5}{2}} \quad (2.6)$$

If the cylinders are orthogonal instead of parallel, the expression for interaction potential yields the energy of separation with no dependence on length as given by Equation 2.7.

$$W = \frac{-A\sqrt{R_1 R_2}}{6D} \quad (2.7)$$

Correspondingly, for orthogonal cylinders the attractive force is inversely proportional to  $D^2$  as shown in Equation 2.8.

$$F \propto -AD^{-2} \quad (2.8)$$

In contrast to the determination of pairwise atom interactions, the Hamaker constants are typically determined from experimental data. Because of this, the properties of the bulk material are averaged instead of examining individual constituents. Regardless of methods of determination, the van der Waals potential functions are useful for determining the attractive potential as a function of radial dependence and separation distance.

#### 2.4.2. D.L.V.O. THEORY

If the van der Waals forces acted alone in nature, it could be expected that all dispersed particles would fall out of solution immediately. However, this is not the case since particles suspended in media are often charged and stabilized electrostatically.<sup>59</sup> Derjaguin, Landau, Verwey, and Overbeek (DLVO) considered particle and colloidal interactions as a function of two separable forces: van der Waals attractive forces and electrostatic repulsive forces. The total interaction potential for electrostatically stabilized particles is represented as the sum of the electrostatic repulsive forces and van der Waals attractive forces. Although the shape of the sum will vary with the magnitude of the contributions from each repulsive and attractive forces, Figure 13 displays a possible net energy curve as a function of interparticle separation.

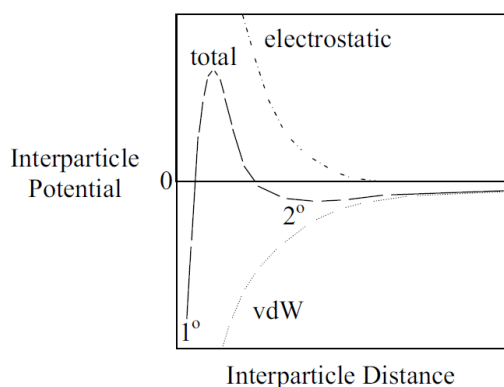


**Figure 13.** Schematic representation of the interaction potential for van der Waals attraction, electrostatic repulsion, and the total interaction potential showing metastable behavior. The primary ( $1^\circ$ ) and secondary ( $2^\circ$ ) minima are highlighted. Reproduced from Israelachivili.<sup>59</sup>

In this representation, the total interaction potential shows metastable behavior with a secondary energy minimum,  $2^\circ$ , at intermediate separation and a primary energy well,  $1^\circ$ , at close distances. The shape of the primary minimum is not highlighted well, but, in general, hard sphere behavior is shown at particle contact with the potential energy diverging to infinity which is consistent with the Pauli Exclusion Principle for atomic orbitals. The attractive behavior dominates at both small and large distances away from the  $2^\circ$  minimum. However, at small distances, the van der Waals attraction must always dominate due to the power law as given in Equation 2.3 which is not matched by any double-layer interaction.<sup>57, 59</sup> If the  $2^\circ$  minimum is accompanied by a large enough potential energy barrier (the peak in the total energy curve) particles are kept from falling in the  $1^\circ$  well and forming irreversible aggregates. Typically, the energy at the  $2^\circ$  minimum, estimated at only a few  $k_B T$ , is small enough that Brownian motion is enough to breakup particle flocculation.<sup>61</sup>

The electrostatic force was introduced by the theory of an electric double layer which results from the charging of particle surfaces. This repulsive force explains why all particles in solution do not aggregate and precipitate out. In general, the charging of a surface results from the adsorption of ions from solution to a surface of oppositely charged ions or from the ionization or dissociation of surface groups.<sup>59</sup> The result of an adsorbed surface charge is an oppositely charged region of counterions around the particle. In close proximity to the surface a narrow layer of bound ions develops and is known as the Stern layer. Surrounding the Stern layer is an atmosphere of loosely associated ions known as the diffuse double layer. To this end, like charged particles or surfaces will electrostatically repel each other in solution.

Another important force that can contribute to suspension stability is that of steric forces. These are short range forces resulting from adsorbed surface groups on a particle or molecule

which physically prevent overlapping and mixing. If the interparticle separation approaches the dimensions of the adsorbed group then the space between the particles is depleted due to entropic effects causing flocculation. Essentially, the adsorbed group gains entropy by being free of constraint of the interparticle dimension causing the particles to be forced together by a depletion interaction.<sup>61</sup>

### 2.4.3. BINDING ENERGY OF CARBON NANOTUBES

It has been shown that in their natural, as produced state, SWNT self-organize into crystalline ropes 0.5 to 20 nm in diameter and tens to hundreds of microns in length.<sup>2</sup> The van der Waals intertube bonding holds the individual tubes in a triangular lattice with a lattice separation constant of 1.7 nm as shown in Figure 14.<sup>2</sup>

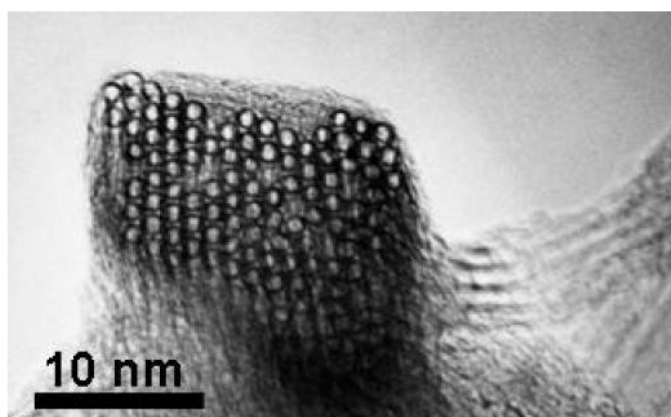


**Figure 14.** A single SWNT rope made up of approximately 100 SWNT as it bends through the image plane of the microscope, showing uniform diameter and hexagonal packing of the tubes within the rope. The diameter of the individual SWNT were determined to be approximately 1.38 nm. Adapted from Thess et al.<sup>2</sup>

The parallel alignment seen is a consequence of the highly polarizable and pristine nature of the  $sp^2$  hybridized carbon interface of SWNT.<sup>62</sup> The pairwise interaction potential has been modeled

for parallel CNT revealing a deep potential energy well at equilibrium separation on the order of  $100 \text{ meV nm}^{-1}$ .<sup>63-64</sup> Due to the high SWNT aspect ratio, the van der Waals attractive force becomes the obstacle for achieving stable dispersions as tubes tend to exist in ropes or arrangements of bundles. For tube-tube interactions, the binding energy of SWNT is approximately  $0.5 \text{ eV nm}^{-1}$ , making them inherently difficult to process into individuals or small bundles.<sup>2, 62</sup> It should be noted that this value is smaller but on the same order of magnitude as what is estimated by simulation.<sup>63</sup> This discrepancy is likely due to the presence of defects on the sidewalls of tubes and solvent interactions. The lower value could also reflect the peeling of an outermost SWNT from the bundle rather than a SWNT centered in the rope.

A continuum approach was taken in order to calculate the intertube interaction potential for CNT pairs.<sup>63</sup> By this method, the interaction energy was determined over an effective area occupied by a carbon atom. The intertube potential for two structures was then calculated by integrating the Lennard-Jones potential over the surface of the tubes.<sup>65</sup> From this model, the potential energy well depth was characterized at equilibrium spacing. Considering the symmetry of hexagons, the cohesive energy was calculated for a tube centered in a rope interacting with six nearest neighbors as three times the potential energy of the well depth.<sup>64</sup> From these calculations, conclusions can be drawn as to how the van der Waals forces in roped or tube pairs scale with tube diameter. As tube diameter and separation distance are increased, the binding energy increases. The increase in binding energy with increasing diameter and separation distance may seem counterintuitive from the perspective of colloidal interactions modeled via Hamaker functions. However, it is important to note that the larger diameter tubes have more carbon atoms interacting per unit length than smaller diameter tubes. Thus, even though the separation between larger diameter tubes is larger, the models account for the presence of more carbon

atoms whose extra pull seems to outweigh the separation.<sup>63</sup> In the same manner, one must also adjust the Hamaker constant to account for the presence of more C atoms. Because of this shortfall it should be noted that the van der Waals models based on Hamaker are of little utility in comparing interactions between CNT of different diameters and chiralities. In order to determine what manner CNT can be separated from one another, two modes of separation were compared: radial displacement and array peeling.<sup>65</sup> Through theoretical arguments, results showed that array peeling of individual tubes from the outer diameter of a rope requires much smaller forces than dilation. Therefore, the likely mode of separation is array peeling as it can be accompanied by delivering much lower intensity energy density to the CNT as compared to dilation.<sup>65-66</sup>

## **2.5. THERMODYNAMICS OF CARBON NANOTUBE SOLUTIONS**

Thorough thermodynamic analysis of SWNT dispersions and solutions are rare in literature. To date, only two exhaustive studies have been completed that try to describe the free energy of mixing, with each work taking a different approach. Sabba and Thomas published the first thermodynamic description of CNT solutions.<sup>67</sup> Specifically, this approach was based on Onsager's theory for anisotropic particles, and was used to describe the Helmholtz energy of mixing. The conclusion drawn from this work was that due to the large van der Waals attraction and poor solvents, a negative value for the free energy of mixing may only be obtained at low CNT concentration.<sup>67</sup> However, further research has shown that stable solutions of CNT can be obtained at higher concentrations.<sup>5, 68-70</sup> Bergin et al. published research to formulate a description of the Gibbs free energy of mixing, however it has since been strongly contradicted.<sup>70-71</sup> It should therefore be noted that although a number of polymer models have been extended to CNT through theory, there have been a limited number of CNT systems for

which experimental data follows a CNT-specific model.<sup>71</sup> From this it can be surmised that modeling of CNT systems is difficult, at this point in time. However, to present the information that is available this section will show the important thermodynamic properties of CNT dispersions.

### **2.5.1. CYLINDRICAL PARTICLE THEORY**

Onsager and Isihara who theorized that the separation of an ordered phase of highly asymmetric particles will occur even in the absence of repulsive molecular forces.<sup>72-74</sup> Similar conclusions were also made by Flory who considered the role of polymer chain inflexibility in polymer crystallization.<sup>75</sup> It was argued that if one were to imagine placing long, stiff molecules one at a time into the volume, after a certain fraction was added it would be impossible to find space for additional molecules without relaxing the chain stiffness. It was then hypothesized that only through the development of order could additional molecules be added.<sup>75</sup> Flory later extended these theories to semi-flexible and rod-like polymers.<sup>76</sup> However, it has been argued that Flory's lattice approach does not adequately describe liquid crystalline ordering due to restrictions placed on chain flexibility. Therefore, initially, Onsager's theory was deemed more appropriate for studying liquid crystalline phases while Flory's theory was deemed more useful for describing concentrated solutions.<sup>77</sup> However, since the discovery of CNT, Onsager theory has been shown to be equally applicable for liquid crystalline and concentrated solution phases.<sup>68, 78</sup>

Flory's semi-flexible model considered polymer chains having many segments arranged on a two dimensional lattice. As a result of the constraint of chain stiffness, chain segments had to be placed co-linearly with adjacent segments of the molecule; with the assumption that the chains exist in a configurational arrangement that is energetically favorable as compared to others but still defined by the lattice. This assumption and treatment restricts the placement of

subsequent chain segments. With the geometrical constructs in place and considering the molecules already on the lattice, the next step was to estimate the possible number of vacant sites accessible as the next chain segment was added. This type of exercise was independently developed by Flory and Huggins for a two component liquid mixture of polymers in solvent assuming no change in the volume of mixing.<sup>75-76, 79-80</sup> Flory then extended this treatment for semi-flexible polymers by including the degree of chain bending. The result of that exercise was an expression for the total number of possible lattice configurations and subsequently the partition function. To address the situation where the solute behaves as a rigid rod, where chain bending is zero, with no preferred chain orientation, the model for semi-flexible molecules was modified by pushing the flexibility and interaction parameters to zero giving two extreme cases. The partition function for athermal systems of rigid rods was then extracted.<sup>80</sup> At one extreme, the system existed in complete disorder, whereas at the other extreme the rods existed in parallel alignment. However, neither extreme was able to adequately describe the intermediate arrangement of rods in concentrated solutions.

In development of theory for the intermediate orientations, the lattice model was modified to overcome the inability to accommodate a rod in a continuously varying range of orientations.<sup>76</sup> Figure 15 displays a molecule inclined at an angle  $\theta$  with respect to the principal axis of the lattice.<sup>76</sup> Instead of treatment as a continuous rod, Flory divided each molecule into a series of smaller molecules having parallel arranged segments as seen in Figure 16.<sup>81-82</sup>

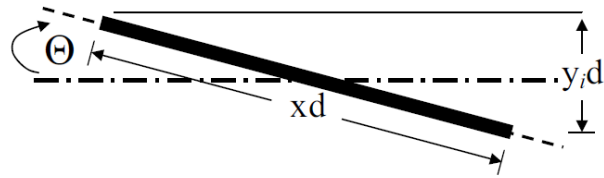


**Figure 15.** A rigid rod in the Flory lattice tilted at angle  $\theta$  to the director. The rod length is taken to be  $x d$  so that  $x$  plays the role of the aspect ratio where  $d$  is the characteristic dimension of the cubic lattice cell. Reproduced from Beris and Edwards, Ciferri, and Wang and Zhou.<sup>77, 81-82</sup>

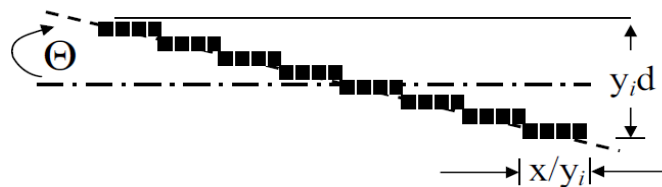


**Figure 16.** A rod divided into  $y_i$  submolecules having  $x/y_i$  segments per submolecule and tilted at angle  $\theta$  to the director. The term  $y_i d$  represents the height with respect to the director with units of lattice cell number. Reproduced from Beris and Edwards, Ciferri, and Wang and Zhou.<sup>77, 81-82</sup>

Introduction of the parameter  $y_i$ , known as the disorder index defined by Equation 2.9, requires that  $x$  be the rod aspect ratio with a diameter equivalent to the lattice size. Therefore, a total of  $y_i$  submolecules are taken to have  $x/y_i$  segments per submolecule aligned along the principle axis with each submolecule occupying one lattice site.<sup>81</sup>

$$y_i = x \sin \theta \quad (2.9)$$

The omission of the index on the rod length  $x$  indicates that all solute molecules are taken to be of uniform length. In this case, with  $j$  molecules already in place, the number of sites accessible to an additional molecule inserted into the lattice must be considered along with the molecule orientation. This was achieved by estimating the probability of finding a vacant site while

inserting each of the subsequent submolecules one at a time, row by row.<sup>77</sup> A conditional probability allowing for the necessary lattice sites in adjacent rows must also be upheld. What results is the partition function for disordered rods in an athermal solution with a solvent. Both of Flory's extreme cases for semi-flexible rods can be recovered from this treatment. In perfect alignment, the angle of inclination would disappear and there would be only one submolecule per rod. More simply, for perfect order the disorder index is unity and approaches the molecule aspect ratio for complete disorder. The partition function,  $Z$ , for rods of random disorder is displayed by Equation 2.10 where Stirling's approximation has been used to treat the logarithm of combinatory factorials.<sup>77</sup>

$$-\ln Z = n_s \ln v_s + n_x \ln \frac{v_x}{x} + n_x(x - 1) - n_x \ln \sigma \quad (2.10)$$

In Equation 2.10,  $n_s$  and  $n_x$  represent the number of solvent and solute molecules, respectively, with  $v_s$  and  $v_x$  representing the volume fraction of solvent and solute molecules, respectively. The rod aspect ratio is taken to be  $x$  and  $\sigma$  manifests itself as the rotational degeneracy factor which is an arbitrary constant.

### 2.5.1.1. CYLINDRICAL PARTICLE ENTROPY OF MIXING

The partition function can be related to the nanotube-solvent system by using more convenient factors suitable for experiment. The nanotube loading is an independent variable defined by the volume fraction,  $\phi$ , and the aspect ratio,  $\alpha$ . With these conventions, and combining terms, the partition function can be written in a more useful form shown in Equation 2.11.<sup>83</sup>

$$-\ln Z = n_s \ln(1 - \phi) + n_{CNT} \ln \left( \frac{\phi}{\sigma \alpha} \right) + n_{CNT}(\alpha - 1) \quad (2.11)$$

This expression in itself contains the statistical configuration information for the isotropic array of nanotubes approximated as rigid rods in an athermal solution. The change in entropy upon

mixing  $\Delta S_{mix}$  can then be obtained by using the Boltzman relation as shown in Equation 2.12 where  $k_B$  represents Boltzman's constant.<sup>83</sup>

$$\Delta S_{mix} = k_B \ln Z = -k_B \left( n_s \ln(1 - \phi) + n_{CNT} \ln \left( \frac{\phi}{\sigma \alpha} \right) + n_{CNT} (\alpha - 1) \right) \quad (2.12)$$

### 2.5.1.2. CYLINDRICAL PARTICLE ENTHALPY OF MIXING

When describing the enthalpy of mixing, it is first necessary to consider the existence of CNT at their natural state. Evidence of crystalline ropes on CNT was shown with hexagonal close packing.<sup>2</sup> Consider CNT having density of  $\rho_{CNT}$  existing in bundles of radius  $R_1$  and length  $L_1$ , then the number of bundles  $N_1$  in a fixed mass of CNT can be defined by Equation 2.13.

$$N_1 = \frac{m_{CNT}}{\rho_{CNT} \pi R_1^2 L_1} \quad (2.13)$$

Bergin et al. considered this system and determined the enthalpy of mixing for a solvent-CNT dispersion by calculating the energy required to separate all molecules to infinity less the energy required to bring them back arranged in a dispersed phase.<sup>84</sup> Here a dispersed phase is considered one in which the final solute bundle size has been reduced with respect to the bulk starting material. This was treated by dividing the contributions into five energetic components.<sup>84</sup> The first component being the energy required to create the surfaces associated with the individual nanotubes,  $E_1^{CNT}$ . This is a direct function of the intertube attractive potential. A second component was derived considering the energy required to remove all solvent molecules to infinity,  $E_1^{Sol}$ . This was taken as the difference between the solvent energy of cohesion less the solvent interfacial energy, and is by definition a function of the pure solvent only. In order to arrange the CNT in a dispersed state, a third term  $E_2^{CNT}$  was used in the exact same way as  $E_1^{CNT}$  but differing in the bundle size,  $R_2$ , when the CNT are redispersed. In theory,  $R_2$  will be smaller than the original bundle size. The fourth component,  $E_2^{Sol}$ , takes the solvent molecules

from infinite separation to a molecular packing appropriate for the liquid specific volume while leaving voids for the newly dispersed CNT bundles. The term  $E_2^{Sol}$  is identical to  $E_1^{Sol}$  less the solvent interfacial surface energy interacting with the surface of the dispersed bundles. The final component is the interfacial energy associated with the placement of CNT in the voids,  $E_2^{CNT-Sol}$ . The value of this energy is estimated as twice the solvent-CNT binding energy,  $E_{Inter}^{CNT-Sol}$ . Combining all the above terms yields an equation for the enthalpy of mixing shown in Equation 2.14.<sup>84</sup>

$$\Delta H_{mix} = E_1^{CNT} + E_1^{Sol} - (E_2^{CNT} + E_2^{Sol} + E_{Inter}^{CNT-Sol}) \quad (2.14)$$

In this analysis, the magnitude of attraction was taken to be positive by convention. Bergin et al. then assumed the solvent external surface area was the same before and after mixing and that the bundle size was much reduced compared to the original state leading to an approximate solution as shown in Equation 2.15.<sup>84</sup>

$$\Delta H_{mix} \approx 2 \frac{m_{CNT}}{R_2 \rho_{CNT}} (E_{Sur}^{CNT} + E_{Sur}^{Sol} - E_{Inter}^{CNT-Sol}) \quad (2.15)$$

Next, the solute-solvent binding energy can be approximated by Equation 2.16 using the identity in Equation 2.17.<sup>84</sup>

$$E_{Inter}^{CNT-Sol} \approx (E_{Sur}^{CNT} E_{Sur}^{Sol})^{\frac{1}{2}} \quad (2.16)$$

$$\delta_i \approx (E_{Sur}^i)^{\frac{1}{2}} \quad (2.17)$$

In relation to traditional polymer science,  $E_{Sur}^i$  can be thought of as cohesive energy density, and  $\delta_i$  can be considered as a solubility parameter. By relating the CNT loading to the total solution volume,  $V_{mix}$ , the enthalpy of mixing can be a function of more experimental variables as shown in Equations 2.18 and 2.19.<sup>84</sup>

$$\phi = \frac{m_{CNT}}{\rho_{CNT}V_{mix}} \quad (2.18)$$

$$\frac{\Delta H_{mix}}{V_{mix}} \approx 2 \frac{\phi}{R_2} (\delta_{CNT} - \delta_{Sol})^2 \quad (2.19)$$

Inspection of these equations shows that in order to minimize the enthalpy of mixing, the surface solvent parameters for the CNT and solvent should be nearly equal. The origin of  $R_2$  in the denominator is a result of estimating the tube or bundle number density,  $N_2$ , in the final state from the SWNT tube density and bundle size. It is important to note that these parameters are similar to, but not identical to the regular solubility parameters used in Scatchard-Hildebrand solution theory. In Equation 2.19, the solute and solvent parameters are a function of the surface energy whereas Scatchard-Hildebrand uses the cohesive energy density.<sup>56</sup> Hence, from here on the parameters defined by Equation 2.17 are referred to as surface-solubility parameters. It is important to point out that approximation introduced in Equation 2.16 allows the surface solubility parameters to be estimated from the pure component interaction energy using Equation 2.17. From these equations, it can be seen that to minimize enthalpy of mixing, the surface tension must be minimized.<sup>84</sup>

Alternatively, the enthalpy of mixing can be defined by using the Flory-Huggins parameter,  $\chi$ . The Flory interaction parameter is dimensionless and describes the interaction energy between solute-solute, solute-solvent, and solvent-solvent.<sup>56</sup> For ideal solutions,  $\chi$  is zero and can take positive or negative values for real solutions. For chemically similar mixtures,  $\chi$  is small compared to unity.<sup>56</sup> Additionally,  $\chi$  is inversely related to the temperature but independent of solute concentration.<sup>83, 85</sup> Equation 2.20 expresses the enthalpy of mixing as a function of  $\chi$ .<sup>83</sup>

$$\Delta H_{mix} = \chi RT n_s \phi \quad (2.20)$$

This expression was originally adapted from the van Laar heat of mixing by Flory.<sup>85</sup> In the case for the CNT-solvent system it is more useful to write  $n_s$  in terms of the solvent volume fraction. Equation 2.21 introduces the solvent molar volume in order to link these terms.

$$n_s = \frac{(1 - \phi)V_{mix}}{\bar{V}_s} \quad (2.21)$$

Inserting the expression for  $n_s$  into the equation for the enthalpy of mixing yields Equation 2.22.

$$\frac{\Delta H_{mix}}{V_{mix}} = \chi \frac{RT}{\bar{V}_s} \phi(1 - \phi) \quad (2.22)$$

By taking advantage of Equation 2.22, the enthalpy of mixing can be measured more accurately than by Equation 2.19, and this was used by Bergin et al. to validate the estimation for the enthalpy of mixing.<sup>84</sup> In order to minimize the enthalpy of mixing,  $\chi$  should be small or negative.<sup>56</sup> In addition,  $\chi$  can be directly related to the solubility parameters and the solvent molar volume by Equation 2.23.<sup>56</sup>

$$\chi = \frac{v_1}{RT} (\delta_{CNT} - \delta_{sol})^2 \quad (2.23)$$

Inspection of Equation 2.22 again supports the minimization of  $\chi$ , and therefore  $\Delta H_{mix}$ , by matching  $\delta_i$  for the solute and solvent. However, the form of Equations 2.19, 2.23, and any solubility parameter based expression contains a shortcoming for estimating the enthalpy of mixing in a real solution. The square of the difference in these equations cannot yield an enthalpy of mixing less than zero.<sup>83</sup> Thus, exothermic mixing cannot be effectively predicted or described.

### 2.5.1.3. CYLINDRICAL PARTICLE FREE ENERGY OF MIXING

The driving force behind dissolution of a solute into a solvent can be defined by the Gibbs free energy. Equation 2.28 gives the free energy of mixing at constant temperature and pressure.<sup>83, 86</sup>

$$\Delta G_{mix} = \Delta H_{mix} - T\Delta S_{mix} \quad (2.24)$$

In the absence of metastabilities, dissolution into a single phase occurs only if the change in free energy upon mixing can be decreased. Criteria for dissolution can be displayed as shown in Equation 2.25

$$\Delta G_{mix} = \Delta H_{mix} - T\Delta S_{mix} < 0 \quad (2.25)$$

From this, dissolution can be viewed as competition between the enthalpy and entropy of mixing as shown by Equation 2.26.<sup>84</sup>

$$\Delta H_{mix} < T\Delta S_{mix} \quad (2.26)$$

From Equation 2.26 it can be deduced that at constant temperature and pressure, minimizing  $\Delta H_{mix}$  and maximizing  $\Delta S_{mix}$  will help drive solubility. For typical small molecule solutions then enthalpy of mixing is small and positive whereas the entropy of mixing is of a large magnitude resulting in an overall negative free energy of mixing which drives dissolution in the solvent. As a result of their inherent properties and structure, CNT behave differently than such an ideal small molecule system. It has been generalized that in most CNT dispersions, the large intertube van der Waals attractive potential is expected to result in a positive enthalpy of mixing.<sup>84</sup> This is manifested in a contribution to  $\Delta H_{mix}$  via the  $E_2^{CNT}$  term of Equation 2.14. Furthermore, the CNT stiffness and high molecular weight generally result in small, positive entropy of mixing.<sup>84</sup> By comparison, Flory-Huggins theory for a system of low molecular weight solute and solvent to that of a low molecular weight solvent and a high molecular weight solute, one finds the entropy of mixing becomes smaller as the aspect ratio increases. This is a result of the loss in conformational entropy.<sup>83</sup> Therefore, a positive free energy of mixing results in CNT-solvent systems which prevents spontaneous dissolution. Whereas a negative free energy of mixing can

result in the spontaneous exfoliation of CNT in solution leading to a dynamic equilibrium between individual tubes and small bundles.<sup>84</sup>

### **2.5.2. CYLINDER-SPHERE PARTICLE THEORY**

Numerous studies have investigated the phase behavior, thermodynamics, and structure of suspensions of rod-like colloids and spherical colloids, independently. However, far fewer studies have been conducted on colloidal suspensions of rod-like particle with spherical particles. The theory of hard rod fluids are better understood and developed than hard sphere systems. This was recognized by Onsager who realized that the isotropic to nematic transition in rod-like colloids occurs at such a low concentration that only two-body interactions were necessary to quantitatively explain the phase transition.<sup>87</sup> This is in contrast to theory of phase transitions of hard spheres, for which no experimentally validated theory exists.<sup>88</sup> Rigorous combination of hard rod theory with hard sphere theory for binary mixtures has been limited. However, the limited research has shown that manipulation of rod theory to account for spheres is capable of producing simulated results which mimic experimental data of ideal systems of monodisperse hard spheres and hard rods with no interactions. It should therefore be noted that the modeling of cylinder-sphere systems at this time is mostly theoretical with little application toward interacting, polydisperse systems such as LSZ-SWNT. The overall generalizations of the ideal, theoretical systems are good indications though of what could happen in complex systems. Of particular interest in rod-sphere systems are the free energy of mixing and excluded volume interactions which determine the equilibrium phase behavior for rod-sphere suspensions.<sup>87, 89</sup>

#### **2.5.2.1. CYLINDER-SPHERE EXCLUDED VOLUME INTERACTION**

The free volume of a suspension composed of a binary mixture of macromolecules is maximized when the two components phase separate. Increasing the free volume, or reducing the

excluded volume, raises the translational entropy of the macromolecules, but does so at the expense of lowering the entropy of mixing. At low concentrations, the mixing entropy dominates and the solution is miscible, but with increasing concentration, if the gain in free volume is sufficient, phase separation will occur, as shown in Figure 17. This effect is known as depletion. The depletion effect may cause like particles to flocculate, known as depletion attraction, or it may cause like particles to separate, known as depletion repulsion.<sup>90</sup>

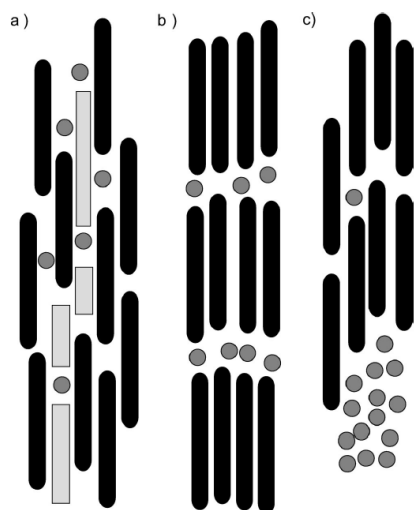


**Figure 17.** a.) A schematic illustration of excluded volume effects in a miscible, nematic phase of rods and spheres, b.) A schematic illustration of transition to a layered phase, the large excluded rod-sphere volume vanishes, c.) Illustration of the immiscible phase where the system bulk phase separates into a rod-rich phase and sphere-rich phase. Adapted from Dogic et al.<sup>89</sup>

Theoretical and experimental studies of depletion interactions between two charged spherical colloids have been presented by Walz and are expected to be qualitatively similar to the case of charged rods.<sup>91</sup> The total potential of mean force between rods suspended in spheres is the sum of an attractive potential caused by the depletion force, and a repulsive potential arising from the electrostatic repulsion. The range of the depletion attraction is the effective sphere diameter, and

the depth of the attractive interaction is proportional to the number density of the depletant. If the rods are sufficiently charged and strongly repel each other, then the rods will never come close enough to each other to exclude the spheres from the region between the rods, and thus will never feel the depletion force. Altering the electrostatic repulsion and allowing the rods to come within the sphere diameter of one another, and the depletion force will be felt.

In order to properly determine the phase dependence of depletion interactions, the physical volume of space mutually excluded between pairs,  $v_{i,j}$ , was determined as shown in Equations 2.27, 2.28, and 2.29.<sup>92</sup>

$$v_{rod-rod} = 2L^2 d \sin(\gamma) + 2\pi d^2 L + \frac{4}{3}\pi d^3 \quad (2.27)$$

$$v_{rod-sphere} = \pi \left[ \frac{(D+d)^3}{6} + \frac{(D+d)^2}{4} L \right] \quad (2.28)$$

$$v_{sphere-sphere} = \frac{4}{3}\pi D^3 \quad (2.29)$$

In the above equations for excluded volume,  $L$  and  $d$  stand for the length and diameter of the rods, respectively,  $D$  is the diameter of the sphere, and  $\gamma$  is the angle between the axes of the interacting rods. The physical excluded volume is shown in Figure 18.

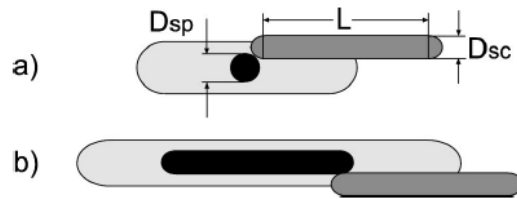


**Figure 18.** (a) Volume excluded to the center of mass of a rod (spherocylinder – sc) due to the presence of a sphere (sp) is indicated by light shading. (b) Volume excluded to the center of mass of a second rod due to the presence of a first rod. Adapted from Dogic et al.<sup>89</sup>

### 2.5.2.2. CYLINDER-SPHERE FREE ENERGY

In hard particle fluids all allowed configurations have the same energy, and therefore it is the number of states, or equivalently the entropy of a system that determines the equilibrium phase. The concept that entropy alone is sufficient to drive a transition from a disordered to ordered phase is an old idea in colloid sciences.<sup>90</sup> The physical origin of the entropically driven phase transition in colloidal mixtures is both extremely simple and general. Most colloidal suspensions consist of particles whose interactions are dominated by steric repulsion, and so it is natural to consider the simplified case of hard particles as a model system. The phase behavior of a colloidal suspension of hard particles is found by minimizing the free energy, where the interaction enthalpy is zero for sterically repelled particles. Thus, the phase behavior of hard particles is determined by maximizing the entropy. Examples of entropically driven ordering are the liquid crystalline phases exhibited by hard rods or the fluid-crystal transition of hard spheres. These phase transitions have been studied extensively with theory and computer simulations, but experimental data of rod-sphere colloidal suspensions is scarce. Another class of entropically driven ordering arises in rod-sphere mixtures where a demixing transition occur. The usual scenario is that if the shape of the two components is different enough, bulk phase separation will occur for an appropriate composition of components.<sup>89</sup> For entropically determined ordering, phase transitions or demixing are driven by differences in physical properties, such as shape, which can create bulk or microphase separation.<sup>90</sup> For rod-sphere systems, the physical and thermodynamic origin of this separation can be explained in terms of the depletion interaction between molecules which is entropically driven by the sum of electrostatic and steric repulsive forces, and van der Waals attractive forces as previously described.<sup>93-95</sup> Bulk phase separation, which is common to rod-sphere systems, occurs when the rods and spheres

completely separate (in the absence of any interaction) forming a rod-rich and sphere-rich phase.<sup>89</sup> Another less common type of separation seen in rod-sphere systems is that of microphase separation. In microphase separation the system starts demixing into regions which are either rod- or sphere-rich. However, unlike bulk separation, the liquid-like regions grow to a critical size at which point they can form kinetically stable three-dimensional equilibrium structures.<sup>89-90</sup>

Onsager theory, despite its' inherent limitations with a second virial approximation, provides a natural framework for the understanding of the physical rod-sphere problem in terms of the steric effects associated to the particular molecular geometries considered. For finite size molecules, Onsager theory tends to become inaccurate at high concentrations typical in phase transitions, and the scaled particle theory of Parsons and Lee can be adapted.<sup>92</sup> Application of Onsager and Parsons-Lee theories to the case of rod-sphere systems have received considerable attention within the context of the stability of colloidal suspensions. Although the properties of these binary mixtures have been determined theoretically, experimental data of rod-sphere systems is not extensively available. What little experimental data is available of phase behavior and thermodynamics of rod-sphere systems is to a large extent unexplained by theory, although some relevant effects have been reproduced in theoretical and computer simulations.<sup>92</sup> However, the Onsager and Parsons-Lee theories show capability for predicting, both quantitatively and qualitatively, the phase behavior and thermodynamics of rod-sphere systems. Onsager theory uses the probability distribution for the orientation of rod-like particles with respect to a fixed reference frame is determined by a single-particle distribution function, and Parsons-Lee theory uses the scaling approximation which takes into account higher virial coefficients. Combination

of the Onsager and Parsons-Lee theories leads to Equations 2.30, 2.31, and 2.32 for the free energy of a rod-sphere mixture.<sup>92</sup>

$$G = f_{iso}^{id} - \left\{ 1 - \ln(\rho) - (x_c \ln(x_c) + x_c \sigma[f]) - x_s \ln(x_s) - \frac{\rho}{2} (x_c^2 (2ag[f] + v_{rod-rod}) + 2x_c x_s v_{rod-sphere} + x_s^2 v_{sphere-sphere}) \right\} \quad (2.30)$$

$$\sigma[f] = \int \ln[4\pi f(\Omega)] f(\Omega) d\Omega \quad (2.31)$$

$$g[f] = \frac{4}{\pi} \int |\sin \gamma| f(\Omega) d\Omega \quad (2.32)$$

Here,  $f_{iso}^{id}$  is the concentration-independent portion of the free energy per particle,  $\rho$  is the particle density,  $x_c$  and  $x_s$  are the molar fractions of rod and sphere particles, respectively,  $a$  is the aspect ratio of the rods,  $\gamma$  is the angle between rod axes,  $v_{i,j}$  is the pairwise excluded volume as discussed previously, and  $f(\Omega)$  is the particle distribution function. In the isotropic phase, all orientations for the particle distribution function are equally probable, mathematically shown in Equation 2.33a. However, in the liquid crystalline phase the orientation is dependent of the axial symmetry and the director angle,  $\gamma$ , which is the angle between the molecule and the nematic director vector, mathematically shown in Equation 2.33b.<sup>92</sup>

$$f(\Omega) = \begin{cases} \frac{1}{4\pi} & (\mathbf{a}) \\ \frac{\gamma}{2\pi} & (\mathbf{b}) \end{cases} \quad (2.33)$$

From the Equations 2.30 through 2.33 it can be seen that the equilibrium phase behavior in a rod-sphere mixture is determined by four parameters: the aspect ratio of the rod, the ratio of the diameter of the rod to the diameter of the sphere, the total volume fraction of spheres and rods, and the partial volume fraction of spheres.

### 2.5.2.3. CYLINDER-SPHERE PHASE BEHAVIOR

The physical origin of the phase behavior of spheres and rods can be explained in terms of the depletion interaction which is entropically driven by steric repulsive interactions between the rod and sphere particles. A dilute particle solution can be treated as an ideal gas of hard spheres, whose mean size is given by the radius of gyration,  $R_g$ , of the spherical particle.<sup>96</sup> In the rod-sphere mixture, the center of the rod cannot penetrate into the shell with thickness  $R_g$  surrounding each spherical particle, called the depletion zone. When two colloidal particles approach each other, these depletion zones will overlap. The translational entropy of the particle then increases. Due to these interactions, mixtures of rods and spheres can form miscible isotropic, immiscible isotropic, miscible nematic, and immiscible nematic phases. Miscible phases are those which the rod and sphere are homogenous within the mixture. Immiscible phases are those which contain rod-rich and sphere-rich regions. In recent years, mixtures of colloidal rods and nonadsorbed polymers have been investigated from experimental, theoretical, and computer simulation points of view. Mixtures of rod-like colloidal particles, such as bacteriophage  $f_d$  virus or tobacco mosaic virus, and flexible polymers, such as polyethylene oxide, exhibit various phase behaviors as a function of the concentration of constituents.<sup>96</sup> These phase behaviors can be explained by the concept of the depletion interaction as well as the concentration and size of the spherical and rod colloidal particles.

The effect of rod concentration and size on mixtures of rods and spheres has been theoretically determined. At low concentrations of rods, the mixing entropy dominates and the spherical particles are miscible with the rods particles. With increasing rod concentration, the increase of the translational entropy compensates for the decrease of mixing entropy and phase separation occurs, although the interaction between constituents is purely repulsive.<sup>96</sup> At smaller

rod length, the miscible, isotropic phase persists to much higher concentrations until an eventual transition is made to a miscible, nematic phase, as predicted by Onsager and Flory theories. As the rod length is increased, the transition from miscible, isotropic to miscible, nematic occurs at a much lower rod concentration. With increasing rod length, the excluded volume due to the rod-sphere interaction grows proportionally to the rod length and consequently the rod-sphere and rod-rod excluded volume increases which allows formation of a miscible, nematic phase at lower concentrations.<sup>89</sup>

The effect of sphere concentration and size on mixtures of rods and spheres is rather counterintuitive. While holding the concentration of the rods constant, increasing the concentration of small spheres will transform the system from miscible, isotropic to miscible, nematic as shown in Figure 19.

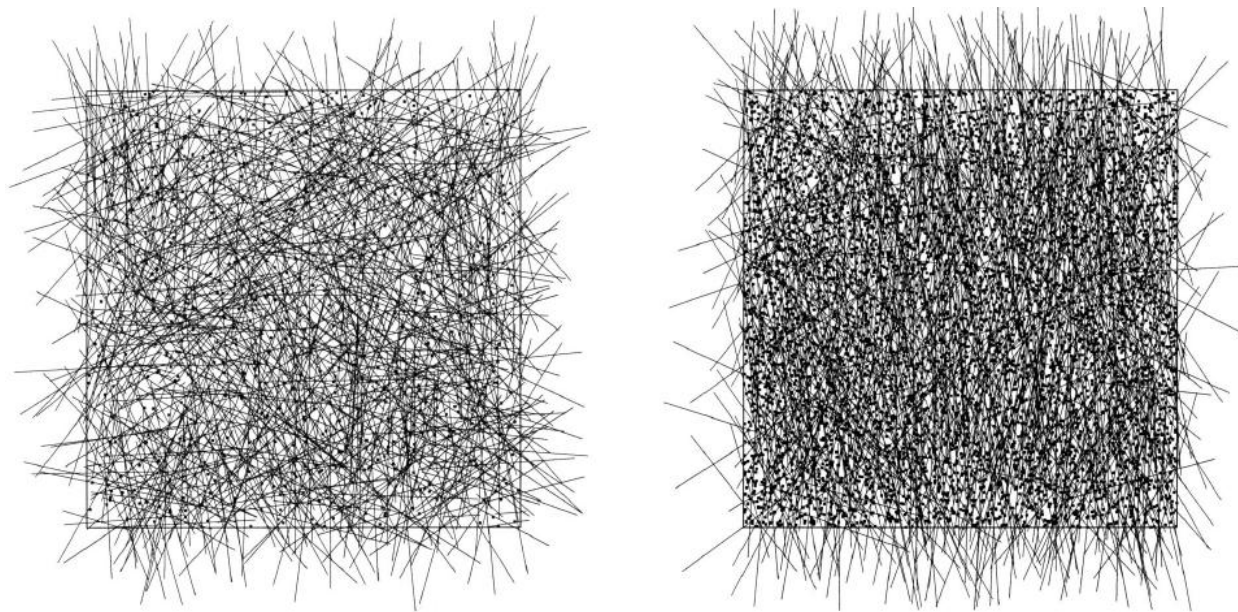


**Figure 19.** Simulation results for addition of small spheres. Phase behavior changes from isotropic (left) to nematic (right) by increasing concentration of small spheres. Adapted from Dogic et al.<sup>89</sup>

If the sphere radius is halved while keeping the volume fraction of spheres constant, then the number of spheres is increased by a factor of eight. At the same time, the result of reducing the sphere size is a decrease in the excluded volume of the rod-sphere system. However, the eightfold increase in the number of rod-sphere interactions more than compensates for the decrease in the excluded volume between the rods and spheres. This leads to the increased stability of the nematic phase with decreasing sphere size.

While holding the concentration of rods constant, increasing the concentration of large spheres will transform the system from a miscible, isotropic to an immiscible isotropic phase. Further increasing the sphere concentration will cause the rod rich phase to transform from isotropic to nematic, as shown in Figure 20.

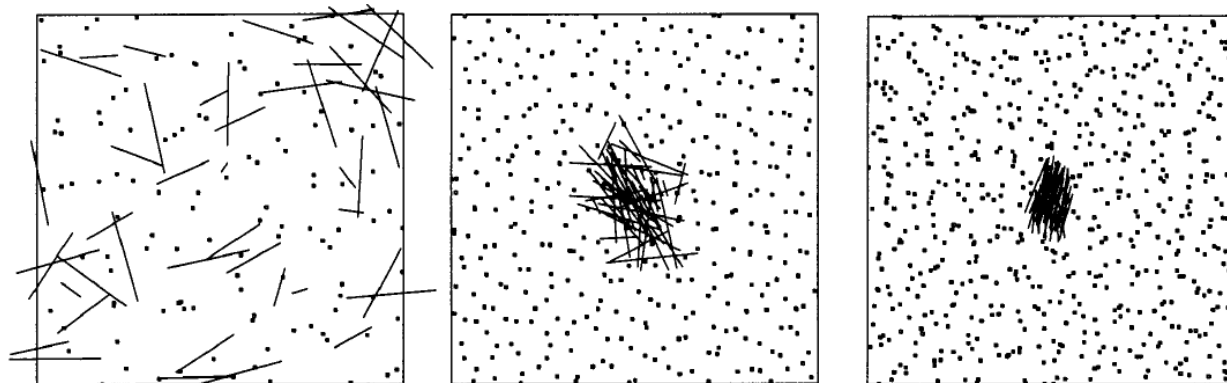


**Figure 20.** Diagrams of three phases of rod-large sphere mixtures with increasing large sphere concentration from left to right – miscible, isotropic (left), immiscible, isotropic (middle), immiscible, nematic (right). Adapted from Urakami et al.<sup>96</sup>

At low volume fractions of large spheres where the mixture directly bulk phase separates, the ratio of rod-sphere excluded volume to rod-rod excluded volume is much greater than unity. This indicates that demixing very effectively reduces the unfavorable rod-sphere interactions. These results give a physical picture of the excluded volume effect. Unlike small spheres, large

spheres cannot fit into the gap between rod layers. Consequently there is no way to gain free volume by transitioning to an ordered phase. Thus, to gain free volume, the system bulk phase separates at the lowest volume fraction of spheres possible.<sup>78, 89</sup>

When the sphere size is small, the overlap volume of the depletion zones is small because the depletion zone surrounding a rod is thin. In this case, the gain of translational entropy cannot compensate for the decrease of mixing entropy, resulting in the miscible state even when the isotropic-nematic transition of rods takes place. On the other hand, when the sphere size is large, the overlap volume of the depletion zones exceeds a threshold value. Then the increase of the translational entropy of spheres compensates for the decrease of the mixing entropy, and the system transforms to the phase separated state.<sup>89-90, 92, 96</sup>

## **2.6. RHEOLOGY THEORY**

Rheology is the field of science that studies the flow and deformation of matter.<sup>97</sup> Of particular interest to this research is the study of complex fluids. Complex fluids show behavior that is intermediate between classical solids and liquids. Classical materials show either viscous, liquid-like behavior or elastic, solid-like behavior, which will be discussed in later sections. For reference, a classical solid will maintain its shape indefinitely whereas a classical liquid will take the shape of its container.<sup>98</sup> In general, many complex fluids will show intermediate behavior in that they will maintain their shape for a certain time, but eventually flow. A fluid of this type is termed viscoelastic, as it behaves like an elastic solid over short timescales and a viscous liquid over long time scales. Interestingly, a material does not have to be out of the ordinary to be considered complex. Mayonnaise, paints, ice cream, and even blood are common examples of complex fluids. Many common complex fluids are engineered to have a complex rheological response such as the yield stress of toothpaste or ketchup.<sup>98</sup>

A variety of instruments are available to measure rheological properties of fluids. Simple flow indexers and capillary viscometers are commonplace in industrial settings. However, research grade rotational rheometers are available and are capable of measuring both steady state and transient flow properties of materials under controlled stresses and strains. In addition, temperature and pressure controlling capabilities are available with many research grade rheometers.<sup>97</sup>

### 2.6.1. CONE AND PLATE RHEOLOGY

The features of a cone and plate rheometer are displayed in Figure 21 utilizing a spherical coordinate system of  $(r, \theta, \phi)$ . A flat, circular plate of radius  $R$  is opposed by a linearly concentric upper cone. The tip of the cone is flattened so that no physical contact is made with the lower plate. The cone angle,  $\alpha$ , is typically only a few degrees, and the rotation of the cone occurs at an angular speed of  $\Omega$ . Derivation of the velocity profile, shear stress, first normal stress, and torque can be found in Macosko which start from the equations of motion in spherical coordinates.<sup>61, 99</sup>

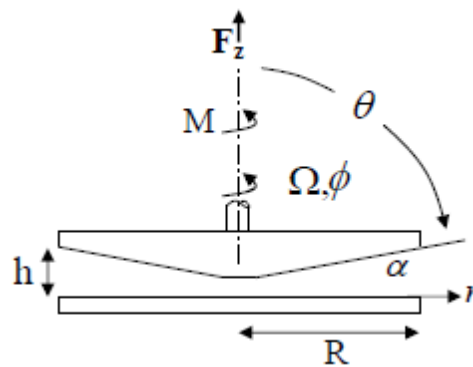


**Figure 21.** Coordinate system and geometric parameters describing the cone and plate measuring geometry. Adapted from Macosko.<sup>61</sup>

Assuming that the velocity is a function of  $r$  and  $\theta$  only, and the only non-diminishing component is in the  $\varphi$  direction, the shear stress can be measured from the raw torque as shown in Equation 2.34.

$$\tau = \frac{3M}{2\pi R^3} \quad (2.34)$$

During an experiment, the rheometer measures the raw torque from the torque transducer, required to maintain the set test variable which is commonly the shear rate of the angular frequency at a set strain amplitude. It is important to note that there is no  $\theta$  angular dependence on the shear stress due to the small magnitude of  $\alpha$ . Thus, the shear stress imposed on the fluid is essentially constant and uniform, and therefore the shear strain and shear rate are uniform.<sup>61</sup> The shear strain in cone and plate geometry is measured by introducing the angular displacement,  $\theta_d$ . Equation 2.35 represents the angular displacement under steady shear.

$$\theta_d = \Omega t \quad (2.35)$$

The definition of shear strain can then be rewritten as shown in Equation 2.36.

$$\gamma = \frac{\theta}{\alpha} \quad (2.36)$$

Likewise, the expression for shear rate in a cone and plate geometry can be rewritten as shown in Equation 2.37.

$$\dot{\gamma} = \frac{\Omega R}{h} = \frac{\Omega}{\tan \alpha} \approx \frac{\Omega}{\alpha} \quad (2.37)$$

Here the angular speed of the cone is given by  $\Omega$  and the cone angle is represented by  $\alpha$ . The first normal stress difference is measured directly in cone and plate geometry by the total thrust on the plate. The value of  $N_1$  as well as its interpretation can be derived from Equation 2.38.

$$N_1 = T_{\varphi\varphi} - T_{\theta\theta} = \frac{2F_z}{\pi R^2} \quad (2.38)$$

Here  $N_I$  is taken to be the difference between the normal stress in the direction of flow and the direction orthogonal to the lower plate. The quantity  $F_z$  is the normal force measured by the rheometer force transducer taken to be the force required to hold the apex of the cone at the center of the lower plate.<sup>97-98</sup> As displayed in Figure 21, the rheometer used in this study measures the normal force in the upward direction. Thus, the magnitude of Equation 2.38 must be adjusted for the coordinate system as displayed in Equation 2.39.

$$N_1 = \frac{-2F_z}{\pi R^2} \quad (2.39)$$

### 2.6.2. PARALLEL PLATE RHEOLOGY

Since the cone and plate geometry provides a uniform stress it is the preferred geometry for many rheologists. However, if suspensions of particles have dimensions comparable to the small gap between the cone and plate, a parallel plate geometry must be used. In many ways, the two geometries are similar, with the largest difference being that the flow between the parallel plates is non-homogenous and a function of the radial distance  $r$ . Figure 22 displays the geometrical constructs of the parallel plate geometry. A cylindrical coordinate system is used to describe the plates in  $(r, \theta, z)$ . Two identical and coaxial flat parallel disks are rotated to impose flow. Typically, the upper plate is rotated with an angular speed  $\Omega$  in the direction of  $\theta$ . The gap between the plates,  $h$ , is held constant and can be adjusted throughout testing. An adjustable gap is advantageous for correcting sample edge defects or checking for sample slip, whereas with the cone and plate geometry the gap is fixed and requires reloading upon edge failure. Derivation for the velocity profile, shear stress, first normal stress, and torque can be found in Macosko which starts from the equations of motion in cylindrical coordinates.<sup>61, 99</sup>

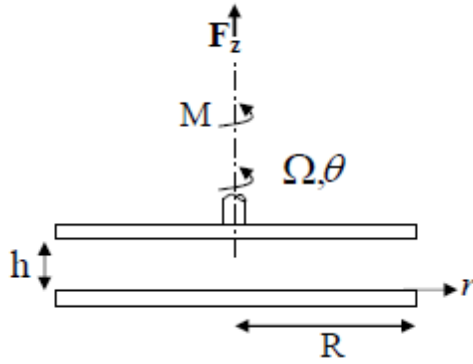


**Figure 22.** Coordinate system and geometric parameters used to describe the parallel plate measuring geometry. Adapted from Macosko.<sup>61</sup>

Assuming that the velocity is a function of  $r$  and  $z$  only and the only non-diminishing component is in the  $\theta$  direction, then the shear stress can be measured from the raw torque as shown in Equation 2.40.

$$\tau(r) = \frac{M}{2\pi R^3} \left( 3 + \frac{d \ln M}{d \ln \dot{\gamma}_R} \right) \quad (2.40)$$

Through examination of Equation 2.40 it shows that the derivative of the natural log of the torque with respect to the natural log of the plate edge shear rate,  $\dot{\gamma}_R$ , cannot be determined accurately without sufficient data to correlate the two variables.<sup>61</sup> However, if the fluid is Newtonian, the derivative equals unity and the shear stress is defined as the apparent shear stress,  $\tau_a$ . Equation 2.41 shows the expression for the apparent shear stress.

$$\tau_a(r) = \frac{2M}{\pi R^3} \quad (2.41)$$

Often, the apparent shear stress is simply used to calculate an apparent viscosity since only the raw torque measurement is required. Inaccuracies may be contained within measurements but this is often not addressed in the literature. However, in the case of sinusoidal varying measurements within the linear viscoelastic regime, the derivative in Equation 2.40 also

diminishes to unity, and the apparent shear stress given by Equation 2.41 is exact.<sup>61</sup> In both cases, Equation 2.40 and Equation 2.41 are functions of the radius of observation. This is a result of the shear rate being a function of the angular speed which varies with radial distance from the center of the plate, which can be mathematically corrected. Equation 2.42 displays the shear rate for the parallel plate geometry.

$$\dot{\gamma}(r) = \frac{r\Omega}{h} \quad (2.42)$$

Equation 2.43 gives the shear rate for the parallel plate geometry at the plate edge.

$$\dot{\gamma}_R = \frac{R\Omega}{h} \quad (2.43)$$

As with the shear rate, the shear strain also varies with radial position and can be calculated from Equation 2.44.

$$\gamma(r) = \frac{r\theta_d}{h} \quad (2.44)$$

To evaluate the viscoelastic moduli, the strain must also be measured at the plate edge as given by Equation 2.45.

$$\gamma_R = \frac{R\theta_d}{h} \quad (2.45)$$

In contrast to the cone and plate geometry, the first normal stress difference cannot be measured alone for a parallel plate geometry. Instead what is obtained is the difference between the first and second normal stress differences as shown by Equation 2.46.

$$(N_1 - N_2)|_{\gamma_R} = \frac{F_z}{\pi R^2} \left( 2 + \frac{d \ln F_z}{d \ln \dot{\gamma}_R} \right) \quad (2.46)$$

The normal force is represented by  $F_z$  and is taken to be positive, consistent with Figure 22. Again, as with the cone and plate geometry, consideration must be taken for the coordinate system of the instrument being used and properly accounted for in determination of magnitude.

In order to completely decompose the difference between  $N_1$  and  $N_2$ , measurements must be made in both parallel and cone and plate geometries and then compared.

### 2.6.3. LINEAR VISCOELASTICITY

A classic example which illustrates how the behavior of complex and ideal fluids differ in response under applied strain is stress relaxation. The shear strain is a measure of the sample deformation due to an applied force,  $F$ . Figure 23 illustrate a sliding plate model where the sample is placed in the gap of height  $h$ .<sup>100</sup>

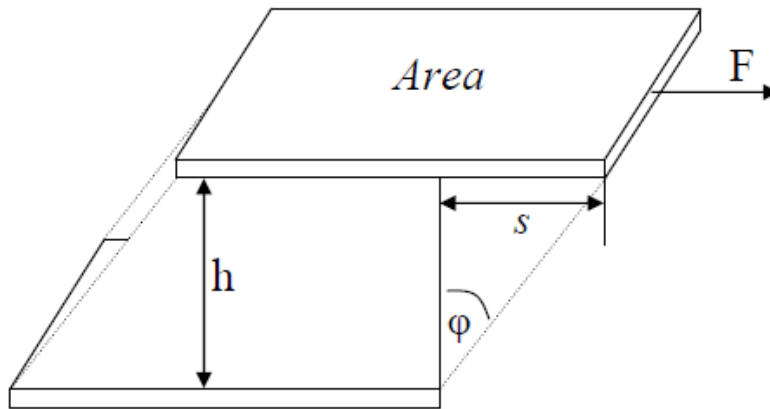


**Figure 23.** Illustration of important terms used in describing the shear strain of a fluid between two parallel sliding plates. Reproduced from Mezger.<sup>100</sup>

In Figure 23, the lower plate is stationary and the deflection of the upper plate is shown by the distance  $s$ . Equation 2.47 defines the strain as the ratio of deflection distance to gap height.

$$\gamma = \frac{s}{h} \quad (2.47)$$

The shear strain, by definition, is a dimensionless number, and is equivalent to the tangent of the deflection angle  $\phi$ . For a point of reference, a deflection angle of  $45^\circ$  corresponds to a strain of 1 or 100%. Often, the strain set points are quite small – less than 5% - and therefore the deflection is small enough to consider the microstructure of the material to be undisturbed. While operating

the rheometer in strain-controlled mode, the user sets the strain and therefore the deflection angle. The deflection angle is then fixed by the instrument throughout the test.

Figure 24 illustrates various response types when a step increase in strain is imposed on a fluid and the dissipation of relaxation of the stress is measured.

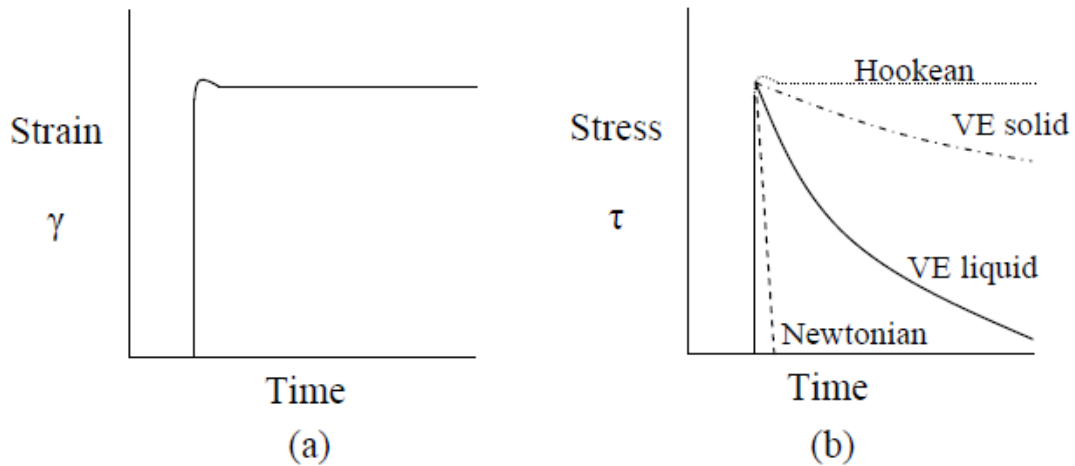


**Figure 24.** Illustration of a stress relaxation experiment. (a) The step increase in strain, and (b) the stress vs. time response of various fluid types. Reproduced from Macosko.<sup>61</sup>

Figure 24(a) shows the step strain imposed on the fluids. Figure 24(b) shows the typical relaxation response for various types of fluid. The Newtonian fluid relaxes as soon as the strain reaches a constant value characteristic of a prototypical viscous liquid. Conversely, the Hookean solid shows prototypical elastic behavior with no stress relaxation. Intermediate behavior is seen for both the viscoelastic liquid and viscoelastic solid where the stress relaxes over some given time. The difference being that the viscoelastic liquid will eventually relax to zero stress whereas the viscoelastic solid approaches an equilibrium value.<sup>61</sup>

The stress relaxation data can be easily converted into a modulus by taking the stress to strain ratio. This modulus, the stress relaxation modulus, is defined in Equation 2.48.

$$G(t, \gamma) = \frac{\tau(t, \gamma)}{\gamma} \quad (2.48)$$

Typically, for imposed step strains larger than unity, the stress is both a function of time and the imposed strain. The behavior is known as nonlinear viscoelasticity. On the other hand, for small strains, typically less than unity, log-log plots of the stress relaxation modulus superimpose. This region of strain showing independent stress modulus is known as the linear viscoelastic regime. Equation 2.49 defines the linear relaxation modulus.

$$G(t) = \frac{\tau(t)}{\gamma} \quad (2.49)$$

Both  $G$  and  $\tau$  are only functions of time in the linear viscoelastic regime. This is a fundamental observation and can be exploited to further characterize the material.

#### 2.6.4. OSCILLATORY FLOW

In the linear viscoelastic regime, all measurements made at small strains less than the critical strain,  $\gamma_c$ , of that material are related to one another. To this end, small-amplitude oscillatory shear measurements provide important structural information without significantly deforming the fluid's microstructure. Furthermore, by changing the frequency of strain, one can vary the timescale of observation. Typically a sinusoidal wave in stress or strain is imposed on the fluid with the frequency measured in cycles per second or more commonly as angular frequency,  $\omega$ , in units of radians per second. The strain relationship can be represented by Equation 2.50 where  $\gamma_0$  represents the strain amplitude.

$$\gamma = \gamma_0 \sin \omega t \quad (2.50)$$

In addition, the strain rate is found by taking the time-derivative of the strain as shown in Equation 2.51.

$$\frac{d\gamma}{dt} = \dot{\gamma} = \gamma_0 \omega \cos \omega t \quad (2.51)$$

At steady state, the stress will also oscillate sinusoidally with the same frequency but shifted by the phase angle,  $\delta$ , in regards to the strain wave as shown in Equation 2.52.<sup>61</sup>

$$\tau = \tau_0 \sin(\omega t + \delta) \quad (2.52)$$

The graphical representation of the applied strain wave and the resultant strain wave are shown in Figure 25. The stress will be out of phase with the strain rate unless the fluid is Newtonian. In that case,  $\delta$  will shift the stress by  $45^\circ$  and the trigonometric functions will be of equal value.

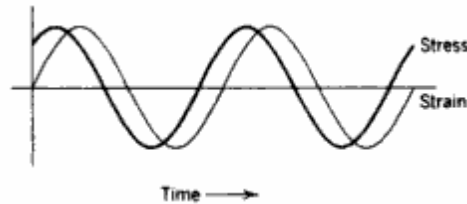


**Figure 25.** The imposed strain wave and resulting steady-state stress wave under simple shear flow. The stress wave is in frequency with the strain but shifted in phase by angle  $\delta$ . Reproduced from Ferry.<sup>101</sup>

The stress wave can be decomposed further by applying the sum-difference identity which leads to Equation 2.53. The first term of the equation represents the stress component in phase with the strain wave and the second represents the stress component out of phase with the strain. Both components oscillate on the same frequency but do not necessarily have to be of the same magnitude.

$$\tau_0 \sin(\omega t + \delta) = \tau_0 (\cos \delta \sin \omega t + \sin \delta \cos \omega t) \quad (2.53)$$

Equation 2.53 holds true regardless of the deformation mode, provided that the strain amplitude does not exceed the limit of linear viscoelasticity.<sup>97</sup> The components of Equation 2.53 are graphically shown in Figure 26.

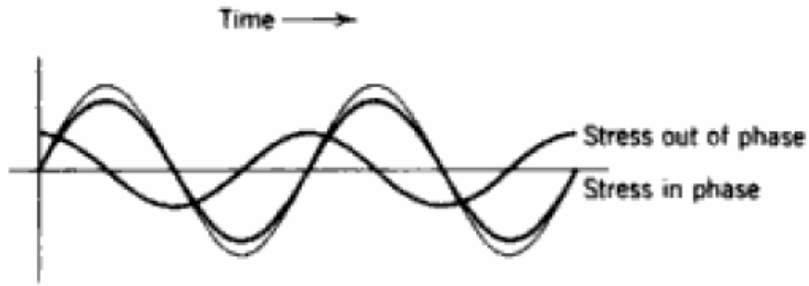


**Figure 26.** Trigonometric deconvolution of the steady-state stress wave in to its in-phase and out-of-phase components. Reproduced from Ferry.<sup>101</sup>

Taking the ratio of Equation 2.53 to the strain amplitude, two independent moduli can be defined by Equation 2.54 and Equation 2.55.<sup>101</sup>

$$G' = \left(\frac{\tau_0}{\gamma_0}\right) \cos \delta \quad (2.54)$$

$$G'' = \left(\frac{\tau_0}{\gamma_0}\right) \sin \delta \quad (2.55)$$

Equation 2.54 displays the in-phase modulus, more commonly referred to as the storage or elastic modulus, which represents the storage of elastic energy in the material. Equation 2.55 displays the out-of-phase modulus, more commonly referred to as the loss or viscous modulus, which represents the loss of viscous energy through the material.<sup>98</sup> For a perfectly elastic solid, the phase angle is close to zero and all energy is stored in the material as indicated by  $G''$  having no value. For a perfectly viscous liquid, the phase angle is approximately  $45^\circ$  and all energy is dissipated through the sample with  $G'$  having a magnitude of zero. Figure 27 displays typical linear viscoelastic responses of storage and loss moduli.<sup>98</sup>

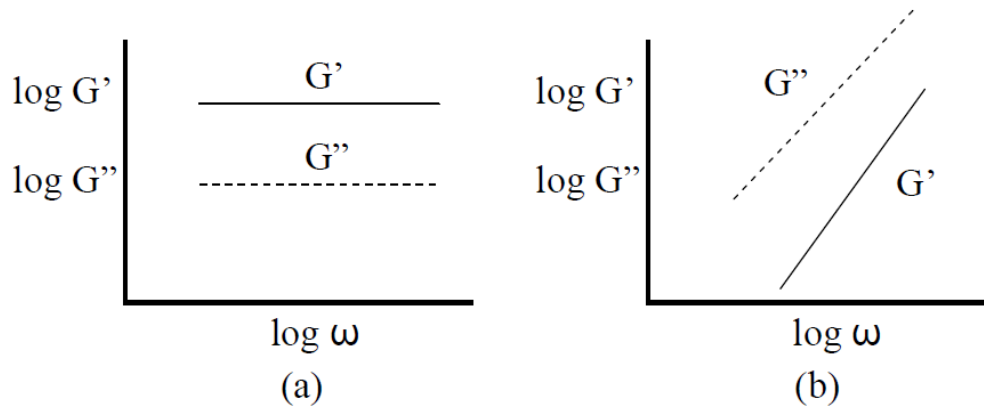


**Figure 27.** The prototypical linear viscoelastic response in terms of frequency dependent storage modulus,  $G'$ , and loss modulus,  $G''$ , for (a) a “solid-like” fluid and (b) a “liquid like” fluid. Reproduced from Larson.<sup>98</sup>

For “solid-like” response shown in Figure 27(a),  $G'$  is much greater than  $G''$  in magnitude, and  $G'$  is also nearly or completely frequency independent.  $G''$  does not necessarily have to be frequency independent and may show some upturn at low frequency as a result of aging.<sup>102</sup> For the “liquid-like” response in Figure 27(b),  $G''$  dominates in magnitude and both moduli scale with frequency in a power-law fashion. As previously discussed, real complex fluids are expected to show some behavior intermediate to the two ideal responses.

Taking advantage of Equations 2.54 and 2.55 the expression for the stress wave can be written in a more convenient form as shown in Equation 2.56.

$$\tau = \gamma_0(G' \sin \omega t + G'' \cos \omega t) \quad (2.56)$$

Another useful parameter is defined by taking the ration of the loss modulus to the storage modulus as shown in Equation 2.57.

$$\tan \delta = \frac{G''}{G'} \quad (2.57)$$

Equation 2.57 is also known as the loss tangent or damping factor. The magnitude of this equation is greater than unity for materials behaving more as liquids, and less than unity for materials behaving more as solids. More simply, the behavior of a material as solid or liquid can be inferred from the dominant modulus at a given frequency. The loss tangent is simply another means to measure energy dissipation in viscoelastic materials.<sup>97</sup>

The complex modulus,  $G^*$ , is defined by considering the amplitude of the stress waveform as a whole and taking its ratio to the strain amplitude.<sup>98</sup> Its magnitude is defined by Equation 2.58.

$$|G^*| = \left( G'^2 + G''^2 \right)^{\frac{1}{2}} = \frac{\tau_0}{\gamma_0} \quad (2.58)$$

The magnitude of  $G^*$  can be interpreted as a measure of the overall resistance to deformation. This measurement takes no consideration in to how the energy is dissipated via  $G'$  and  $G''$  individually. Finally, dividing the complex modulus by the angular frequency gives the magnitude of the complex viscosity,  $\eta^*$ , as shown in Equation 2.59. The complex viscosity is a measure of a materials resistance to flow under oscillatory shear.

$$|\eta^*| = \frac{|G^*|}{\omega} = \left[ \left( \frac{G'}{\omega} \right)^2 + \left( \frac{G''}{\omega} \right)^2 \right]^{\frac{1}{2}} \quad (2.59)$$

In many cases, the complex viscosity can be related to the shear or apparent viscosity by means of the Cox-Merz rule. The Cox-Merz rule does not hold for liquid crystals and many non-ideal, multicomponent, or interacting systems. This relationship is strictly empirical and states that shear viscosity of a fluid at steady state is equivalent to the complex viscosity of that fluid in the linear viscoelastic regime provided that they are measured at equivalent magnitudes of rotational shear rate and angular frequency.<sup>61</sup> Mathematically this can be expressed by Equation 2.60 with the condition of Equation 2.61.

$$\eta(\dot{\gamma}) = |\eta^*(\omega)| \quad (2.60)$$

$$\dot{\gamma} = \omega \quad (2.61)$$

Again, the Cox-Merz rule only holds true if the conditions of matching shear rate and angular frequency are met. It is important to note the  $\dot{\gamma}$  used in Equation 2.61 is intended to represent the shear rate, but its' meaning still holds true as the rate of deformation. The difference is that under steady rotational shear the shear strain and therefore shear rate is held constant whereas under oscillatory flow it remains a function of time.

### 2.6.5. SHEAR FLOW

All the geometries of various measuring systems may vary, however, all are similar in that they impose a drag flow by a controlled motion along the system boundary. Figure 28 shows a simple sliding plate geometry where the bottom boundary is stationary and the top plate moves at a set velocity of rotation. All motion is along one coordinate direction,  $x_1$ , with velocity varying in a second coordinate direction,  $x_2$ , orthogonal to the shear.<sup>97</sup>

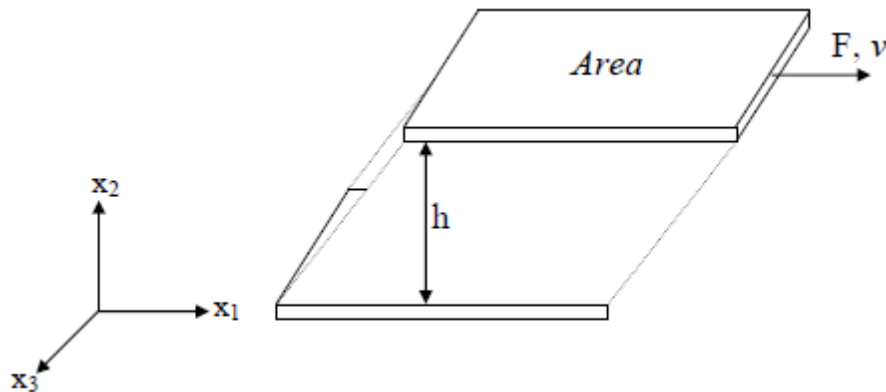


**Figure 28.** The sliding plate model, and relative coordinate system for simple shear. Adapted from Gupta and Mezger.<sup>97, 100</sup>

The upper plate in Figure 28 moves along the positive  $x_1$  direction with velocity  $v$  while the sample remains between the gap of height  $h$ . Mathematically, viscometric flow translates to there being only one non-zero velocity component,  $v_1$ , and therefore one zero component to the velocity gradient tensor.<sup>61</sup> This non-diminishing component is known as the shear rate,  $\dot{\gamma}$ , and can be represented by Equation 2.62.

$$\dot{\gamma} \equiv \frac{\partial v_1}{\partial x_2} \quad (2.62)$$

It should be noted that the shear rate is simply the velocity gradient, and is often referred to as the rate of deformation or strain rate. For sliding plate geometries, the magnitude of the shear rate is the velocity divided by the gap as shown by Equation 2.63.

$$\dot{\gamma} = \frac{v}{h} \quad (2.63)$$

The force that the flowing fluid is exerting on the surface in the direction parallel to flow is known as the shear stress,  $\tau$ . After imposing a steady shear to a fluid from a state of rest, the shear stress does not reach steady state immediately.<sup>98</sup> Rather, the stress goes through a transient period where it varies with time. The ratio of the instantaneous stress to the imposed steady shear rate gives the transient start-up viscosity as shown by Equation 2.64.

$$\eta(\dot{\gamma}, t) = \frac{\tau(\dot{\gamma}, t)}{\dot{\gamma}} \quad (2.64)$$

After a certain period of time in which the steady shear has been applied, the shear stress will then come to a steady state. Thus, the shear stress is no longer a function of time, and the shear viscosity can be defined as shown by Equation 2.65.

$$\eta(\dot{\gamma}) = \frac{\tau(\dot{\gamma})}{\dot{\gamma}} \quad (2.65)$$

The behavior of the shear stress as a function of various shear rates is one way to define the type of material or fluid. The simplest response is that of a Newtonian fluid in which the shear stress is directly proportional to the shear rate and the viscosity is therefore constant. Deviation from this behavior indicates a shear rate dependence on viscosity and materials exhibiting this type of response are classified as non-Newtonian.

A common phenomenon with complex fluids is that of a yield stress. Fluids with some solid-like character will not flow initially upon the initiation of shear. Instead, the stress grows linearly with the shear rate up to a critical value, above which the material yields or flows at a constant shear stress. It is noteworthy to point out that the yield stress describes the point at which flow begins.<sup>98</sup>

In general, a fluid is a material that cannot support a shear stress without flowing.<sup>61</sup> Consider a fluid element as displayed in Figure 29. If at rest all surface stresses on the element act orthogonal to the surface – normal stresses – and are not only equal in magnitude but independent of orientation of the element. This type of normal stress is known as the hydrostatic pressure and is compressive in nature. The absence of motion within the element also implies the absence of shear stresses. Thus, for a fluid in motion it follows that there must be either shear stresses present or normal stresses that are unequal. These shear stresses are known as viscous or extra stresses because they act on a fluid in addition to the fluid pressure.

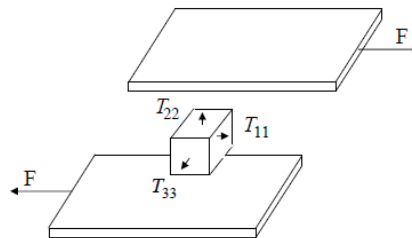


**Figure 29.** Schematic diagram showing the notation for normal stresses in a shear field. Adapted from Gupta.<sup>97</sup>

The tensor  $T_{ii}$  contains the contributions of the pressure and the extra stress as shown by Equation 2.66.

$$T_{ii} = -p + \tau_{ii} \quad (2.66)$$

As a consequence of most liquids being considered incompressible, the application of equal normal stresses along the three coordinate directions shown in Figure 29 does not lead to deformation or change in volume. Therefore, it is only unequal normal stress that may cause motion or strain in liquids.<sup>97</sup> This means that one cannot determine the absolute value of the normal stresses from controlled strain experiments, but only normal stress differences because the value of  $p$  is indeterminate. Equation 2.67 gives the expression for the first normal stress difference,  $N_1$ , and Equation 2.68 gives the expression for the second normal stress difference,  $N_2$ .

$$N_1 = T_{11} - T_{22} = \tau_{11} - \tau_{22} \quad (2.67)$$

$$N_2 = T_{22} - T_{33} = \tau_{22} - \tau_{33} \quad (2.68)$$

Subtraction of normal stresses eliminates the pressure term leaving only the difference between the extra stresses. A negative first normal stress difference tends to force the plates together and the positive first normal stress difference tends to push them apart. A negative second normal stress difference tends to bulge the fluid at the edges of the plate.<sup>86</sup> The most common instance of a positive first normal stress difference is the die swell experienced by a melt extruded polymer emerging into the atmosphere. In general, if the fluid being sheared is polymeric in nature, the normal stresses become unequal in magnitude, and if the fluid is Newtonian their magnitudes remain equal.<sup>97</sup>

## 2.6.6. RHEOLOGY OF PARTICULATE SUSPENSIONS

Suspensions consist of discrete particles dispersed in a liquid medium.<sup>61</sup> The hydrodynamic disturbance resulting from the presence of particles was first determined by Einstein in 1906. The presence of particulates can not only drastically change the measured viscosity, but can also introduce non-Newtonian behavior to the fluid under study. The particle will modify the velocity distribution in the flowing liquid. Extra energy dissipation will arise because of this and will be reflected in a proportional increase in viscosity. The stability of these types of fluids are of primary concern if one is to measure the rheological responses of a dispersion. A rigorous examination of important assumptions and criteria that need to be met for accurate rheological measurements can be found in Macosko.<sup>61</sup> In general, for reproducible results, the fluid structure or dispersion state should not change over the time-scale of the experiment.

Particle settling is the primary cause for concern as particles larger than approximately one micron tend to settle under the influence of gravity alone.<sup>98</sup> This can be circumvented by either matching the density of the suspending medium to that of the particle or by using a medium that is viscous enough to prevent sedimentation. By matching the density of the particle and fluid, the buoyant force can be exploited to support the particles in suspension. Similarly, if the particles are Brownian, the ratio of gravitational to Brownian forces should be less than unity indicating stability from thermal motion. Brownian motion is the name given to the irregular movement of pollen in water as observed by Robert Brown.<sup>103</sup> If the particle dimensions are small enough then the random thermal motion of solvent molecules can transfer momentum to the particle. By this analysis, a density difference of greater than  $1 \text{ g mL}^{-1}$  leads to the sedimentation of particles greater than two microns in diameter.<sup>98</sup> On the other hand, if the

medium is viscous enough, the rate of particle settling can be slowed considerably. Depending on the viscosity of the solvent, this may be enough to allow for stable measurements to be taken over the duration of the testing. An approximate criterion for neglecting the effect of settling in spherical particles can be obtained from Stoke's law.<sup>61</sup>

### 2.6.7. RHEOLOGY OF NON-SPHERICAL PARTICULATE SUSPENSIONS

The rheology of non-spherical suspensions depends on the particle loading, aspect ratio, distribution, and rheology of the suspending medium.<sup>97</sup> To begin to understand how elongated particles flow, single, non-interacting particles in dilute suspensions were considered. At these conditions, the suspension can be essentially thought of under the constraints of an ideal gas. Jeffery considered non-interacting particles dispersed in a Newtonian fluid in the absence of Brownian motion. Solving the appropriate equations of motion he concluded that non-spherical, non-Brownian particles not only translate but rotate indefinitely under the influence of a shearing flow.<sup>97-98</sup> The rotation was discovered to be periodic with time, known as the Jeffery orbit. Particles with large aspect ratios were predicted to rotate rapidly when their longest dimension is orthogonal to flow and slowly when it is parallel to flow. The consequence of this type of behavior is that the viscosity is also periodic and cycles with time.<sup>97</sup>

If Brownian motion cannot be neglected, deviations from the Jeffery orbit for particles are observed and must be accounted for probabilistically. In absence of flow, an important Brownian phenomena known as the dilute-solution rotary diffusivity,  $D_{r0}$ , can be calculated. The rotary diffusivity is a measure of the rate at which a particle reorients by Brownian motion. For rods of length  $L$  and diameter  $d$ , the rotary diffusivity can be estimated from the theory of Doi and Edwards and that of Kirkwood and Auer, as shown in Equation 2.69.<sup>98, 104-105</sup>

$$D_{r0} = \frac{3k_B T \left( \ln \left( \frac{L}{d} \right) - 0.8 \right)}{\pi \eta_s L^3} \quad (2.69)$$

From Equation 2.69, it can be seen that there is a logarithmic dependence on the aspect ratio. The viscosity of the suspending fluid or solvent is represented  $\eta_s$ , the temperature  $T$ , and the Boltzmann constant  $k_B$ . If the solvent is non-Newtonian then the viscosity should be taken in the limit of zero-shear as  $\eta_0$ .

Under the application of shear, the crossover from Brownian to non-Brownian behavior for a flowing suspension can be calculated by the magnitude of the rotational Peclet number.<sup>98</sup> Equation 2.70 displays the dimensionless Peclet number,  $Pe$ .

$$Pe \equiv \frac{\dot{\gamma}}{D_r} \quad (2.70)$$

The shear rate in the numerator should be taken as the lowest value imposed in experiment in order to characterize the lower transition limit. Similarly, the rotary diffusivity in the denominator can be taken as the dilute solution rotary diffusivity. A value of  $Pe$  greater than unity indicates a dominating contribution by the imposed shear rate and thus a non-Brownian behavior. On the other hand, a value of  $Pe$  less than unity indicates that the rotary diffusivity dominates and thus Brownian motion is relevant in the imposed shear field. Identifying Brownian and non-Brownian behavior is important for interpretation of particle dispersions as the stress tensor contains an elastic contribution from Brownian motion.<sup>98</sup> In the absence of Brownian motion, this contribution is simply neglected.

Relaxing the criterion for dilute dispersions brings in some additional considerations in describing particulate suspensions. To this end, the rheology of rod-like particles is defined by unique concentration regimes as shown in Figure 30.

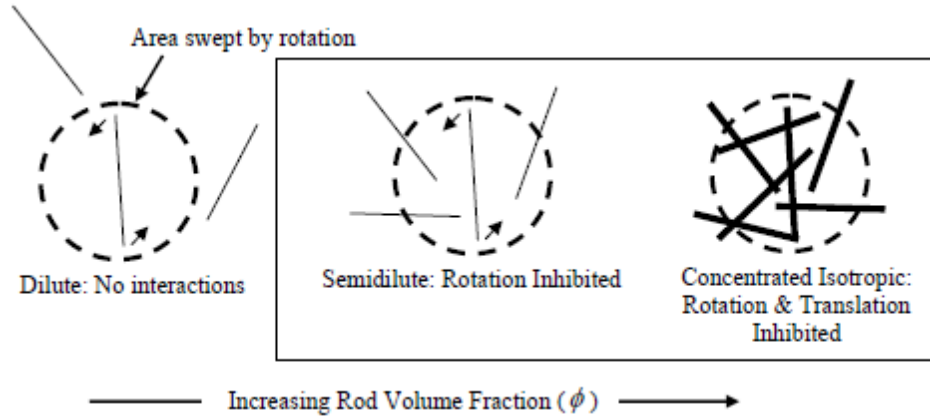


**Figure 30.** Concentration regimes used to describe rod-like particles. Adapted from Larson, and Doi and Edwards.<sup>98, 104</sup>

The major assumption is that the rods are rigid and inflexible with the absence of attractive interactions.<sup>104</sup> In the dilute regime the rods are able to rotate freely without interacting with neighboring rods. Considering a rod of length  $L$  rotating about its center of mass there is a volume of approximately  $L^3$  that must be free of nearest neighbors. Equation 2.71 shows the relationship between the number concentration,  $\nu$ , and volume fraction of rods,  $\phi$ .

$$\phi = \frac{\pi d^2 L \nu}{4} \quad (2.71)$$

From this equation, one can define transitions between each regime. Rod-rod interactions can be assumed to occur when the number density approaches  $L^{-3}$  but experiment has shown disagreement with this prediction. The volume fraction which delineates semi-dilute behavior can be seen in Equation 2.72.

$$\phi_0 \approx 24 \left( \frac{d}{L} \right)^2 \quad (2.72)$$

As shown by Figure 30, the semi-dilute regime is characterized by having neighboring rods impeding the rotation of one another, but still allowing translation through the suspending fluid.

Therefore at rod concentrations somewhat above  $\phi_0$  a rod may be inserted with negligible probability of intersecting another and therefore excluded volume is not a factor.<sup>98</sup> The effect of the rod volume is indicated in Figure 30 by the size of the lines used to represent each rod. While increasing concentration in the semi-dilute regime, there lays a point in which the rods have trouble isotropically arranging themselves due to excluded volume interactions. This condition delineates the semi-dilute from the concentrated isotropic regime as calculated by Equation 2.73.

$$\phi'_0 \approx \frac{\pi d}{4L} \quad (2.73)$$

In practice, for both rigid and flexible rod-like particles and polymers, these naming conventions for various concentration regimes are used. The logic being that in the case of flexibility, the swept area would be smaller. Therefore, the transitions predicted for rigid rods would be conservative estimates on the higher end of each concentration regime. For non-Brownian rods the interpretation of when the crossover from the dilute to semi-dilute occurs is physically taken to be the point when the rods begin to influence each other hydrodynamically. It is important to note that the crossover is not necessarily at the same concentration that Brownian motion of one rod would be affected by its nearest neighbors.<sup>98</sup>

Other deviations between Brownian and non-Brownian behavior can be seen in the shear viscosity of suspensions. At low shear rates, the theory of Doi and Edwards predicts a large increase and domination of the stress contribution from Brownian motion as the concentration is taken from dilute to semi-dilute.<sup>98</sup> However, in non-Brownian solutions this is not the case and the same dramatic viscosity increase is not expected. The modest particle contribution to the viscosity was experimentally and theoretically confirmed for fibers with large aspect ratios by Yamane et al. and Bibbo.<sup>106-107</sup> This occurs because in the absence of Brownian motion the fibers readily rotate to align, with the shear flow contributing little to the shear viscosity which is

especially true at large  $Pe$ . Therefore, the shear history must be considered when measuring the rheological properties on non-Brownian suspensions and is of the utmost importance for reproducible results. For repeatability, it is necessary to allow sheared suspensions to relax back to isotropic ordering before characterization.

As the concentration of the particles is increased through the semi-dilute regime there is a critical point where three-dimensional network formation occurs known as percolation. This onset of network formation is interpreted differently depending on the mode of percolation. Rheological percolation occurs when the particle network is sufficient to impede the motion of the solvent. If the solvent is a high molecular weight polymer, then percolation occurs when the size of the polymer chain is large compared to the separation between the rods or particles.<sup>108</sup> Depending on the length of the polymer, percolation may be a result of entanglement instead of molecular contact. This is initially characterized by a solid-like, viscoelastic response over short timescales. A second mode of percolation exists in which electrical conductivity can be recognized. However, the formation of conductive networks occurs on a different length scale. It has been shown that physical contact does not need to occur in CNT systems since the intertube distances only need to be close enough for electrons to jump from one tube to another. This distance has been estimated to be less than five nanometers.<sup>108-109</sup> Being that CNT are comprised of some non-metallic tubes, not all particles contribute to network conductivity. Thus, in CNT systems electrical percolation can be assumed to occur at higher concentration of CNT than rheological percolation. Furthermore, CNT with sidewall defects contribute little to the electrical conductivity of the network.<sup>108</sup> In general, the larger the aspect ratio, the less packing density of the particles and the lower one would expect to find the critical volume concentration.<sup>110</sup>

### 3. EXPERIMENTAL DETAILS

#### 3.1. RAW MATERIALS

Two types of SWNT were used in the current research: Unidym (Sunnyvale, CA) 187.1, 187.2, and 187.3 and Southwest Nanotechnologies (SWeNT) (Norman, OK) CG200-L100 and L014. Unidym, are high pressure carbon monoxide process (HiPco) SWNT and have a purity of 99% as determined by thermogravimetric analysis, non-SWNT carbon content of 3%, average length and diameter of 1042 nm and 1.24 nm, respectively, as determined by AFM, and D/G ratio of 0.1 on both 514 nm and 785 nm lasers. SWeNT CG200 are cobalt-molybdenum catalyst process (CoMoCat) SWNT and have a purity of 93% as determined by thermogravimetric analysis, non-SWNT carbon content of 14%, average length and diameter of 860 nm and 1.36 nm, respectively, as determined by AFM, and average D/G ratio of 0.06 and 0.09 on 514 nm and 785 nm lasers, respectively. The HiPco SWNT will have impurities such as amorphous carbon and iron from catalysts, and the CoMoCat SWNT will have impurities such as amorphous carbon, cobalt and molybdenum from catalysts, and other non-SWNT carbonaceous material.

Dialyzed, lyophilized LSZ from chicken egg white was purchased from Sigma Aldrich (St. Louis, MO) and used as delivered. All the following data is given from the manufacturer. The molecular mass was calculated as 14,307 Da as determined by the specific amino acid sequence. The isoelectric point was given as 11.35, and the extinction coefficient at 280 nm was given as 36. The LSZ was determined to be 90% pure via spectroscopy with the impurities being buffer salts of sodium acetate and sodium chloride. Powdered TTAB was purchased from Sigma Aldrich and used as delivered. The molecular mass was calculated as 336.4 Da as determined by the molecular structure. Powdered hydroxypropyl methylcellulose (HPMC) was purchased from Sigma Aldrich with approximately 28 to 30 % methoxy groups and 7 to 12 % hydroxypropoxy groups and used as delivered. Hydrolized poly(vinyl alcohol) (PVA) with an average molecular

mass of 195 kDa and 99.3% purity was purchased from Sigma Aldrich and used as delivered. It should be noted that all solutions and dispersions were made using deionized (DI) water.

## **3.2. METHODS OF PREPARATION**

Preparation of LSZ-SWNT dispersions requires two primary techniques. First, sonication is used to disperse SWNT within the LSZ solution. Second, if needed, the bulk mixture will be centrifuged to remove any excess material. Other initial steps of preparation were attempted. However, due to the large van der Waals force of attraction between SWNT, tip sonication was necessary to disperse them with no visible aggregates seen via optical microscopy at 50x magnification.

### **3.2.1. SONICATION**

Sonication is the technique of applying sound energy to disturb particles within a sample. Sonication energy is applied using either an ultrasonic bath or an ultrasonic probe. It can be used to disperse or dissolve materials by breaking intermolecular interactions. In this research, sonication was used specifically for preparing the initial dispersions of LSZ-SWNT. More specifically, it was used to break apart large bundles of CNT being held together via van der Waals forces to allow LSZ to intercalate and disperse the SWNT. The sonicator used in this research was a Sonics and Materials Inc. (Newtown, CT) Vibra Cell VC 750 operated at 60% amplitude with a sonication sequence of 5 s on and 2 s off for 30 minutes.

### **3.2.2. CENTRIFUGATION**

Centrifugation is a technique that uses centrifugal force for the separation of mixtures. More dense components of the mixture migrate away from the axis of rotation, and less dense components of the mixture migrate towards the axis of rotation. The material which collects at the bottom of the test tube is known as the precipitate, while the remaining material is called the

supernatant. The precipitate falls to the bottom due to higher density and a larger sedimentation coefficient, which is a function of sedimentation velocity and centrifugal acceleration.

The rate of centrifugation is specified by the acceleration which needs to be applied to the sample. This is measured in revolutions per minute or gravitational equivalence. The acceleration at which particles precipitate is a function of their size and shape, the size, shape, and interaction of the solvent molecule, the density difference between the particles and the liquid, and the solvent viscosity. The acceleration of centrifugation can range from 1 to 100,000 times gravity.

In this research, centrifugation was used to remove excess LSZ and bundles or aggregates of SWNT from the bulk dispersions. The centrifuge used in this research was a Fisher Scientific (Pittsburgh, PA) accuSpin Micro 17 with capabilities of holding 24 microcentrifuge tubes with 2 mL volumes and reaching accelerations from 300 to 17,000 x g. For this research the centrifuge was operated at 17,000 x g for 3 hours.

### **3.3. METHODS OF CHARACTERIZATION**

Characterization of LSZ-SWNT dispersions was carried out via four primary characterization methods: microscopy, spectroscopy, rheology, and thermal analysis. Each method was used to determine or probe an aspect of the dispersion state. Many of the methods overlap and were used as validation to support other methods results.

#### **3.3.1. MICROSCOPY**

Microscopy is the scientific field of using microscopes to view samples that cannot be seen within the resolution range of the human eye. The three branches of microscopy used in this research are optical, electron, and probe microscopy. Optical and electron microscopy involve the diffraction, reflection, or refraction of light or electron beams interacting with the specimen and the subsequent collection of this scattered light or electron signal in order to create an image.

Probe microscopy can involve the physical contacting or close contacting of a sample where the topography is mapped.

### **3.3.1.1. ATOMIC FORCE MICROSCOPY**

Atomic force microscopy (AFM) is a form of high-resolution scanning probe microscopy. The demonstrated resolution is on the order of fractions of a nanometer. Binnig, Quate, and Gerber invented the first AFM in 1986.<sup>111</sup> The AFM is used primarily for imaging and measuring materials at the nanoscale.

The AFM consists of a cantilever with a probe tip at its end that is used to scan the material surface. When the probe tip is lowered toward the material surface, forces between the tip and the sample lead to a deflection of the cantilever. Depending on the material being scanned and the scanning mode, forces that are measured in AFM include mechanical contact force, van der Waals forces, capillary forces, chemical bonding, electrostatic forces, or magnetic forces. The deflection of the cantilever is measured by a laser reflected from the probe tip surface to an array of detectors which measures the changes in cantilever position to develop an image.<sup>111</sup> If the tip scanned at a constant height above the sample, there would be a risk that the tip would collide with the surface and not capture relevant data. Therefore, dynamic feedback mechanisms are employed to adjust the probe tip-to-sample distance. This feedback is accomplished by maintaining a constant force between the tip and the material being scanned.<sup>112</sup>

In the current research, the AFM was operated in a static, non-contact mode. In static mode, the probe tip is rastered across the surface of the sample, and the contours of the surface are measured directly using the deflection of the cantilever. In non-contact mode, the tip of the cantilever does not contact the sample surface. The cantilever is instead oscillated at a frequency slightly above its resonant frequency where the amplitude of oscillation is typically a few

nanometers. van der Waals and electrostatic forces, which are strongest directly above the surface, act to decrease the resonance frequency of the cantilever. This decrease in resonant frequency combined with the feedback loop system maintains a constant oscillation amplitude or frequency by adjusting the average tip-to-sample distance. Measuring the tip-to-sample distance at each raster point allows the AFM to develop a topographic image of the material surface.<sup>112</sup>

AFM was specifically used in this research to determine whether SWNT are dispersed as individuals or small bundles, and to determine the average aspect ratio of the SWNT while in dispersion. The AFM used in this research was a Pacific Nanotechnology (Berkley, CA) Nano-R SPM.

### **3.3.1.2. OPTICAL MICROSCOPY**

The optical microscope, also known as a light microscope, uses visible light and a system of lenses to magnify images. Optical microscopes are popular because the use of visible light allows the sample to be viewed directly by the human eye rather than needing detectors and signal transducers. Anton van Leeuwenhoek is credited with bringing the microscope to broad use in scientific fields around the middle of the 16<sup>th</sup> century.

All optical microscopes designed for viewing samples by transmitted light share the same basic components of the light path: light source, diaphragm, condenser lens, objective, and ocular lens. In addition, the microscope used in the current research contains variable angle polarizers, dark and bright field capabilities, and multiple condenser lenses for different viewing modes.

Optical microscopy was specifically used in this research to study the phase behavior and transitions of LSZ-SWNT dispersions. The optical microscope used in this research was a Nikon (Melville, NY) Eclipse 80i with transmitted light.

### 3.3.1.3. SCANNING ELECTRON MICROSCOPY

The scanning electron microscope (SEM) is a type of electron microscope that images the sample surface by scanning it with a high-energy beam of electrons in a raster scan pattern. The electrons interact with the atoms that make up the specimen producing scattering signals that contain information about the sample's surface topography. The signals result from interactions of the electron beam with atoms at or near the surface of the sample. The SEM was developed over several decades by various researchers including Max Knoll, Manfred von Ardenne, Charles Oatley, and Gary Stewart.<sup>113</sup>

A field emission SEM uses a field emission cathode in the electron gun to provide a narrower probing beam. This results in both improved spatial resolution and higher magnification capabilities.<sup>113</sup> In the field emission SEM used for this research, an electron beam is thermionically emitted from an electron gun fitted with a tungsten filament cathode. The electron beam is focused by two condenser lenses then passes through a pair of deflector plates in the electron column, which deflect the beam allowing it to raster over the sample surface.

When the electron beam interacts with the sample, the electrons lose energy by repeated random scattering and absorption within the specimen, which can extend from 0.1  $\mu\text{m}$  to 5  $\mu\text{m}$  into the surface. The energy exchange between the electron beam and the sample results in the reflection of high-energy electrons by elastic scattering, emission of secondary electrons by inelastic scattering and the emission of electromagnetic radiation, each of which are picked up by detectors. Electronic amplifiers are then used to amplify the detector signal which is displayed as variations in brightness. Therefore, the resulting signal from the detectors is a distribution map of the intensity of the electrons being emitted from the scanned area of the specimen.<sup>114</sup>

Magnification in an SEM is unlike optical or transmission electron microscopes. Magnification in the SEM is not a function of the power of the objective lens. Rather, magnification results from the ratio of the dimensions of the raster on the specimen. Therefore, higher magnification results from reducing the size and speed of the raster on the specimen.<sup>114</sup>

SEM was specifically used in this research to determine qualitatively if there was a molecular interaction between LSZ and SWNT, and to aid in determining quantitatively whether SWNT are dispersed aggregates or small bundles. The SEM used in this research was a JEOL (Tokyo, Japan) 7000F FE-SEM with energy dispersive X-ray spectroscopy capabilities.

#### **3.3.1.4. TRANSMISSION ELECTRON MICROSCOPY**

Transmission electron microscopy (TEM) is an electron microscopy technique where a beam of electrons is transmitted through a specimen. The beam of electrons interacts with the specimen as it passes through, and an image is formed from the interaction of the electrons transmitted through the specimen. The image is then magnified and focused onto an imaging detector. The first TEM was built by Max Knoll and Ernst Ruska in 1931.<sup>115</sup>

The TEM is capable of imaging at a significantly higher resolution than light microscopes, owing to the small frequency wavelength of electrons. At lower magnifications TEM image contrast is determined by the absorption of electrons in the sample. This is due to the thickness and composition of the sample material. At higher magnifications, complex wave interactions will modulate the intensity of the image.<sup>116</sup> TEM can be used to identify or observe modulations in chemical identity, crystal orientation, and electronic structure, as well as transmission imaging.

The TEM used for this research consists of a tungsten emission source connected to an electron gun. By connecting this emission source to a high voltage source the electron gun emits

electrons by thermionic electron emission. Electromagnetic lenses are then used to bend the electrons allowing for variable focusing power. Also, electrostatic fields can be used to cause the electrons to be deflected at a constant angle. After the electron beam has been properly transmitted through the sample, an electron imaging detector signal is focused and magnified for the image.

TEM was used specifically in this research to aid in characterizing LSZ-SWNT dispersions as well as qualitatively imaging the interaction between LSZ and SWNT. The TEM used in this research was Zeiss (Thornwood, NY) EM 10 TEM.

### **3.3.2. RHEOLOGY**

Rheology is the scientific field that studies the deformation and flow of materials. It is a branch of physics due to the fact that many of the variables used are from the field of mechanics. Rheology studies both the flow behavior of fluids and the deformation behavior of solids. The connection between the two is that at after long relaxation times, even solid-like materials will flow or deform, such as the creeping of stained glass windows. The behavior of real materials is based on the combination of the ideal behavior of fluids and solids. When a material such as rubber is loaded in shear or extension an instantaneous deformation is followed by a continuous deformation or “creep”. When the load is removed, part of the deformation recovers instantly while some deformation recovers with time and still other deformation is permanent. The time dependant response is known as viscoelasticity. When defined by stress relaxation, the stress of a purely viscous liquid will instantly relax to zero after the subjected strain, while a purely elastic solid will show no relaxation.<sup>61</sup> In this research, rheology was used to determine the molecular structure by probing the dispersion state using four different tests: amplitude sweep, frequency sweep, transient or start-up flow test, and flow curve or steady shear test. The rheometer used in

this research was an Anton Paar (Ashland, VA) Physica MCR 301 with attachments for temperature control. Rheology for this research was run at 10°C over three separate loads with three runs of each test for each load. To prevent evaporation a water-cooled Peltier hood was used, and all data was collected above the torque transducer limit of 0.1 μNm.

### 3.3.2.1. AMPLITUDE SWEEP TEST

An amplitude sweep test is an oscillatory test with variable wave amplitude and constant wave frequency. An amplitude sweep is used to determine the linear viscoelastic range and limit of linear viscoelasticity of a material. The linear viscoelastic range is determined by range of amplitudes of strain for which the storage and loss moduli show a constant plateau value. Linear-elastic behavior is found whenever Hooke’s law applies as shown in Equation 3.1, and linear-viscous behavior is found whenever Newton’s law applies as shown in Equation 3.2.<sup>100</sup>

$$\frac{\tau_A}{\gamma_A} = \text{Constant} \quad (3.1)$$

$$\frac{\tau_A}{\dot{\gamma}_A} = \text{Constant} \quad (3.2)$$

In these equations,  $\tau_A$  is the variable stress amplitude,  $\gamma_A$  is the variable strain amplitude, and  $\dot{\gamma}_A$  is the variable shear amplitude. The limit of the linear viscoelastic range is the point at which the storage modulus deviates significantly from the plateau of the linear viscoelastic range. The significance of the limit of linear viscoelasticity is that at strain amplitudes lower than the limit, the structure of the material is stable or undisturbed. However, at strains above the limit, the structure of the sample could be deemed to have been irreversibly changed or disrupted.

The microstructural behavior of a material can also be elucidated from the linear viscoelastic range. If the storage modulus is larger than the loss modulus, then elastic behavior dominates over viscous behavior and the material is a viscous solid; indicating the microstructure

has a certain amount of rigidity. Even materials with low viscosity will show this type of response if they have a stable chemical network which gives it rigidity. If the loss modulus is larger than the storage modulus, then viscous behavior dominates elastic behavior and the material shows liquid or sol character. Materials which are highly viscous will even show this behavior if they are lacking the chemical or physical network of forces which would stabilize the material.<sup>100</sup> For this research, the amplitude test was run at an angular frequency of  $10 \text{ s}^{-1}$  from 0.01% to 100% strain.

### **3.3.2.2. FREQUENCY SWEEP TEST**

A frequency sweep test is a measure of the viscoelastic oscillatory response with variable wave frequency and constant wave amplitude. The importance of the frequency sweep is that it probes the time-dependant shear behavior of materials. Short-term behavior is probed at high frequency by rapid movements, and long-term behavior is probed at low frequency by slow movements. Prior to running a frequency sweep, an amplitude sweep must be run in order to determine what constant wave amplitude (strain) to run that is not greater than the strain limit of linear viscoelasticity.

Interpretation of frequency sweep data can be counterintuitive unless the mathematics behind each variable is understood. In general, the storage and loss moduli will increase as frequency increases indicating the material becomes more rigid. The dominance of either the storage or loss moduli at each frequency will indicate the character of the material; whether or not it is more solid or more fluid. At the same time as the storage and loss moduli increase, the complex viscosity decreases indicating the resistance to flow of the material decreases with increasing frequency. Mathematically, the complex viscosity is the quotient of the complex

modulus divided by the frequency. Therefore, as the frequency is increased, the complex viscosity will decrease.

With increasing frequency, the internal structure of the physical network becomes more inflexible and rigid. In this rigid structure, more deformation energy is stored than lost so the elastic behavior becomes increasingly dominant, thus the storage modulus will become more dominant. At the same time, the portion of the lost deformation energy decreases, therefore reducing the importance of the viscous behavior and causing the loss modulus to become less important. Due to the intermolecular interaction in dispersions, such as those in this research, the elastic behavior dominates over the viscous and the sample shows elastic character. For a stable dispersion, the loss modulus and storage modulus will be relatively parallel straight lines with shallow slopes.<sup>100</sup> For this research, frequency sweep tests were run at 2% strain from an angular frequency of  $0.01\text{s}^{-1}$  to  $100\text{s}^{-1}$ .

### **3.3.2.3. TRANSIENT TEST**

A transient test is a flow test with constant shear rate. This test is used to find the time necessary to overcome transient effects and reach a steady state viscosity at the given shear rate. For a transient test, the time of the test must be sufficiently long enough. Otherwise, start effects or time-dependent transition effects will result in the transient viscosity rather than the steady-state viscosity, which is needed to develop flow curves.

Transient tests can also be used to identify phenomena such as low shear aggregation or low shear flocculation. Aggregation and flocculation both result in molecules “sticking” to one another. However, aggregates require a large amount of energy to be broken apart and are seen as a primary energy well in DLVO theory, whereas flocs can be broken easily and are seen as a secondary energy minimum in DLVO theory; in the remainder of this section, aggregates will be

described. For some dispersions or suspensions, the amount of energy needed to move the molecular constituents close enough to one another to have them aggregate, or stick to one another, is very low. Low shear aggregation occurs when the shear energy causes constituents within the dispersion or suspension to overcome solvation or repulsive forces and attract to one another. As molecules begin to attract to one another, a snow ball effect occurs where small aggregates continuously join to eventually form macroscopic aggregates. This is rheologically seen by increasing viscosity with time at a constant, low shear rate. The viscosity will slowly increase then begin to exponentially increase as larger and larger aggregates are formed. For this research, the transient test was run at a shear rate of  $0.1 \text{ s}^{-1}$  for 1,000 s.

#### **3.3.2.4. FLOW CURVE TEST**

A flow curve test is a flow test with specific variable shear rates taken over a specific varying time frame. As discussed in the previous section, transient effects can invalidate the steady-shear viscosity measurements. Therefore, transient test are run at the lowest applicable shear rate to determine the longest time needed for the shear rates tested. After determination of this testing period, the time frame can be reduced as the shear rate is increased. As a general rule of thumb, the time to sample the viscosity at a specific shear rate is equal to the reciprocal of the shear rate.

From the data collected of viscosity at certain shear rates, viscosity or flow curves are developed which show the dependence of viscosity for a material on shear rate. There are four common responses of viscosity versus shear rate: Bingham plastic, shear thinning or pseudoplastic, shear thickening or dilatants, and Newtonian. A Bingham plastic initially responds to an applied shear stress by deforming but not flowing. However, when the shear stress exceeds a critical value, known as the yield stress, the material will flow in the same way as a Newtonian

fluid. Pseudoplastic fluids are those where viscosity is a decreasing function of shear rate, or more simply offer less resistance to flow at higher shear rates. Dilatant fluids are those where the viscosity is an increasing function of shear rate, or more simply, the fluids resistance to shearing becomes larger the faster it is sheared. Finally, a Newtonian fluid viscosity is independent of shear rate. It should be noted that for all testing methods temperature is a variable which can alter the microstructure of the material. For this research, flow curves were run with a time sampling interval dependent upon the results from the transient tests from shear rates of  $0.01 \text{ s}^{-1}$  to  $100 \text{ s}^{-1}$ .

### **3.3.3. SPECTROSCOPY**

Spectroscopy is the study of the interaction between materials and radiated energy. Spectroscopy originated through the study of visible light dispersed according to its wavelength by a prism. However, the concept has expanded to comprise any interaction with radiative energy. Spectroscopy types are distinguished by the type of radiative energy involved in the interaction, such as, electromagnetic radiation, particle radiation, and acoustic radiated pressure waves. Types of spectroscopy can also be distinguished by the nature of the interaction between the energy and the material, such as, absorption, emission, elastic scattering, inelastic scattering, and impedance.

#### **3.3.3.1. ULTRAVIOLET – VISIBLE SPECTROSCOPY**

Ultraviolet-visible spectroscopy (UV-vis) refers to absorption spectroscopy in the ultraviolet-visible spectral region. This means it uses light in the visible and adjacent near-UV range. The absorption or reflectance in the visible range directly affects the perceived color of the chemicals involved. In this region of the electromagnetic spectrum, molecules undergo electronic transitions meaning absorption measures transitions from the ground state to the excited state of the sample.

UV-vis is routinely used in the quantitative determination of solutions of biological macromolecules. The quantitative determination of solutions is done via the Beer-Lambert Law. The Beer-Lambert law states that the absorbance of a solution is directly proportional to the concentration of the absorbing species in the solution and the path length, as shown in Equation 3.3.

$$A = \ln \frac{I_0}{I} = \epsilon cL \quad (3.3)$$

In Equation 3.3,  $A$  is the measured absorbance,  $I_0$  is the reference intensity of the incident light,  $I$  is the transmitted intensity,  $L$  the pathlength through the sample, and  $c$  the concentration of the absorbing species. For each species,  $\epsilon$  is a constant known as the molar absorptivity or extinction coefficient and is a fundamental molecular property. Thus, for a fixed path length and known concentration, UV-vis can be used to determine the extinction coefficient of the absorbent molecule in the solution. This allows for development of calibration curves showing absorbance versus concentration.<sup>117</sup>

UV-vis was used specifically in this research to characterize the LSZ solutions used, develop calibration curves, determine the enzymatic activity of LSZ solutions and LSZ-SWNT dispersions, and determine interactions changes in dispersions. The UV-vis used for this research is a Cary (Santa Clara, CA) 3E UV-Vis Spectrophotometer.

### **3.3.3.2. CIRCULAR DICHROIC SPECTROSCOPY**

Circular dichroism (CD) refers to the differential absorption of left and right circularly polarized light. This phenomenon is exhibited in the absorption bands of optically active chiral molecules. CD spectroscopy has a wide range of applications in many different fields. Most notably, ultraviolet CD is used to investigate the secondary structure of proteins. Ultraviolet-visible CD is used to investigate charge-transfer transitions. Near-infrared CD is used to

investigate geometric and electronic structure. Infrared circular dichroism is used for structural and vibrational studies.<sup>118</sup>

CD is exhibited by biological molecules, because of their dextrorotary (right-handed) and levorotary (left-handed) constituents. More importantly, secondary and tertiary structure will impart a distinct CD spectrum to its respective molecule. Therefore, the alpha helix of proteins and the double helix of nucleic acids have CD spectral signatures unique to their structures, much like a human finger print.<sup>118</sup>

CD spectra can be readily used to estimate the fraction of a molecule that is in the alpha-helix conformation or the beta-sheet conformation. It can also be used to study how the secondary structure of a molecule changes as a function of temperature; in this way it can reveal important thermodynamic information about the molecule, such as the enthalpy or Gibbs free energy of denaturation.<sup>118</sup>

CD was specifically used in this research to determine the effect that the molecular interaction between LSZ and SWNT has on the secondary and tertiary structure, and thereby the activity, of LSZ. The CD used in this research was a JASCO (Easton, MD) J-810 Spectropolarimeter.

### **3.3.3.3. FOURIER-TRANSFORM INFRARED SPECTROSCOPY**

Fourier transform infrared spectroscopy (FT-IR) is a spectroscopic technique which is used to obtain an infrared spectrum of absorption or emission of a solid, liquid, or gas. An FT-IR spectrometer simultaneously collects raw spectral data in a wide spectral range. The Fourier-Transform algorithm is required to convert the raw data collected into the actual spectrum.

Rather than shining a monochromatic beam of light at the sample, FT-IR shines a beam containing many different frequencies of light at once, and measures how much of that beam is

absorbed by the sample. Then, the beam is modified to contain a different combination of frequencies, giving a second data point. This process is repeated many times. Afterwards, a computer takes all the data and works backwards using the Fourier-Transform to infer what the absorption is at each wavelength.<sup>119</sup>

The FT-IR beam is generated by starting with a broadband light source containing the full spectrum of wavelengths to be measured. The light shines into a certain configuration of mirrors that allows some wavelengths to pass through but blocks others. The beam is then modified for each new data point by moving one of the mirrors thereby changing the set of wavelengths that pass through. Computer processing then turns the raw data into the desired result of light absorption for each wavelength.<sup>120</sup>

FT-IR was specifically used in this research to study the chemical bonding structure found in the LSZ-SWNT dispersions. The material used for FT-IR was loaded in two separate methods; either as effluent from the thermogravimetric analysis oven, or as an undisturbed solid or liquid sample for transmission or ATR. The FT-IR used in this research is a Thermo Scientific (Waltham, MA) Nicolet iS10 FT-IR with SMART iTR and ATR.

#### **3.3.3.4. RAMAN SPECTROSCOPY**

Raman spectroscopy, named after Sir Chandrasekhara Venkata Raman, is a spectroscopic technique used to study vibrational, rotational, and other low-frequency modes in a system. It relies on inelastic, or Raman scattering, of monochromatic light. The monochromatic light is usually from a laser in the spectral range needed during experimentation. The laser light interacts with molecular vibrations, phonons, or other excitations in the system, resulting in the energy of the laser photons being shifted up or down. The shift in energy gives information about the vibrational modes in the system.<sup>121</sup>

Spontaneous Raman scattering is typically very weak, and as a result the main difficulty of Raman spectroscopy is separating the inelastically scattered light from the elastically, Rayleigh, scattered light. Modern instrumentation typically uses filters for laser rejection and spectrographs – axial transmissive, Czerny-Turner, or Fourier-Transform detectors. There are also a number of advanced types of Raman spectroscopy to enhance the weak inelastic scattering signal, including surface-enhanced Raman, resonance Raman, tip-enhanced Raman, polarized Raman, stimulated emission Raman, transmission Raman, spatially offset Raman, and hyper-Raman.<sup>121-122</sup>

The Raman effect occurs when light impinges upon a molecule and interacts with the electron cloud and the bonds of that molecule. For the spontaneous Raman effect, a photon excites the molecule from the ground state to a virtual energy state. When the molecule relaxes it emits a photon and it returns to a different rotational or vibrational state. The difference in energy between the original state and this new state leads to a shift in the emitted photon frequency away from the excitation wavelength. If the final vibrational state of the molecule is more energetic than the initial state, then the emitted photon will be shifted to a lower frequency in order for the total energy of the system to remain balanced. This shift in frequency is designated as a Stokes shift. If the final vibrational state is less energetic than the initial state, then the emitted photon will be shifted to a higher frequency, and this is designated as an Anti-Stokes shift. Raman scattering is an example of inelastic scattering because of the energy transfer between the photons and the molecules during their interaction. It should be noted that the Raman effect is a light scattering phenomenon which should not be confused with absorption where the molecule is excited to a discrete, real energy level.<sup>121</sup>

Raman spectroscopy was specifically used in this research to study the changes which occur to the SWNT through addition of LSZ elucidating interactions, charge transfer, and possible processing fractionation. A Renishaw (Gloucestershire, UK) in Via microRaman was used for Raman spectroscopy. Samples were prepared by drying in a vacuum over for 24 hours. The samples were then placed on a glass slide by suspending on double-sided tape. Prior to running test on all samples, each laser was calibrated using a silicon reference. Each sample was scanned by a 514 nm and 785 nm laser to probe both the semi-conducting and metallic CNT present. Each run by each laser consisted of 10 scans over a Raman shift from  $100\text{ cm}^{-1}$  to  $3200\text{ cm}^{-1}$ .

### **3.3.3.5. FLUORESCENCE SPECTROSCOPY**

Fluorescence spectroscopy is a type of electromagnetic spectroscopy which analyzes the fluorescence from a sample. It involves using a beam of light that excites the electrons in molecules of certain compounds and causes them to emit light, or fluoresce. Fluorescence spectroscopy is primarily concerned with electronic and vibrational energy levels within a molecule or compound. Generally, the species being examined has a ground electronic state and an excited electronic state of higher energy. Within each of these electronic states are various vibrational states.<sup>123</sup>

In fluorescence spectroscopy, the species is first excited from its ground electronic state to one of the various vibrational states of a higher energy level. Collisions with other molecules cause the excited molecule to lose vibrational energy until it reaches the lowest vibrational state of the excited energy level. The molecule then drops down to one of the various vibrational levels of the ground electronic state which emits a photon in the process. As molecules may drop down into any of several vibrational levels in the ground state, the emitted photons will have

different energies, and thus frequencies. Therefore, by analyzing the different frequencies of light emitted in fluorescent spectroscopy, along with their relative intensities, the structure of the different vibrational levels can be determined.<sup>123-124</sup>

Fluorophores are more likely to be excited by photons if the transition moment of the fluorophore is parallel to the electric vector of the photon. For fluorophores in solution this means that the intensity and polarization of the emitted light is dependent on rotational diffusion. Therefore, anisotropy measurements can be used to investigate how freely a fluorescent molecule moves in a particular environment, and is of particular use in determining binding events of biological molecules.<sup>123-124</sup>

In a typical experiment, the different wavelengths of fluorescent light emitted by a sample are measured using a monochromator, holding the excitation light at a constant wavelength. This is called an emission spectrum. An excitation spectrum is the opposite, where the emission light is held at a constant wavelength, and the excitation light is scanned through many different wavelengths. Both types of experiments use the same setup. The light from an excitation source passes through a filter and strikes the sample. A portion of the incident light is absorbed by the sample and results in the fluorescence of any molecules at the excitation wavelength. The fluorescent light is emitted in all directions. Some of this fluorescent light passes through a second filter and reaches a detector, which is usually placed at 90° to the incident light beam to minimize the risk of transmitted or reflected incident light reaching the detector. Various light sources may be used as excitation sources, including lasers, photodiodes, and lamps.<sup>123</sup>

Fluorescence spectroscopy and anisotropy were used in the current research to determine the specific interaction between LSZ and SWNT as well as their direct binding interaction. A

Perkin Elmer (Waltham, MA) LS 55 Luminescence Spectrometer was used for fluorescence measurements. Emission spectra were taken at room temperature scanning from 300 nm to 500 nm with a 0.5 nm resolution and a scan rate of 500 nm/min with an incident angle of 90°. The excitation wavelength was set to 280 nm to probe the quenching of the tryptophan within LSZ when coupled with SWNT. Anisotropic fluorescence data was collected at an excitation wavelength of 295 nm with an emission wavelength of 345 nm. The excitation and emission slits were each set at 15 nm where a G-factor was calculated at 1.581.

### **3.3.3.6. ENERGY DISPERSIVE X-RAY SPECTROSCOPY**

Energy-dispersive X-ray spectroscopy (EDS) is an analytical technique used for the elemental analysis or chemical characterization of a sample. It relies on the investigation of an interaction of some source of X-ray excitation and a sample. Its characterization capabilities are due in large part to the fundamental principle that each element has a unique atomic structure allowing unique set of peaks on its X-ray spectrum. To stimulate the emission of characteristic X-rays from a specimen, a high-energy beam of charged particles such as electrons, protons, or a beam of X-rays, is focused into the sample being studied. At rest, an atom within the sample contains ground, unexcited state electrons in discrete energy levels.<sup>114</sup> The incident beam excites an electron in an inner shell, ejecting it from the shell while creating a void where the electron was. An electron from an outer, higher-energy shell then fills the hole, and the difference in energy between the higher-energy shell and the lower energy shell may be released in the form of an X-ray.<sup>114</sup> The number and energy of the X-rays emitted from a specimen can be measured by an energy-dispersive spectrometer. The energy of the X-rays are characteristic of the difference in energy between the two shells, and of the atomic structure of the element from which they were emitted, this allows the elemental composition of the specimen to be measured.

The four primary components of the EDS setup are the excitation source, the X-ray detector, the pulse processor, and the analyzer.<sup>114</sup>

Accuracy of EDS spectrum can be affected by various factors. Many elements will have overlapping peaks so the accuracy of the spectrum can also be affected by the nature of the sample. X-rays can be generated by any atom in the sample that is sufficiently excited by the incoming beam. These X-rays are emitted in any direction, and so they may not all escape the sample. The likelihood of an X-ray escaping the specimen, and thus being available to detect and measure, depends on the energy of the X-ray and the amount and density of material it has to pass through. This can result in reduced accuracy in inhomogeneous and rough samples.<sup>114</sup>

The EDS in this research was used to determine molecular constituents of complex mixtures of LSZ-SWNT, LSZ-TTAB-SWNT, and other compounds. A JEOL (Tokyo, Japan) 7000F FE-SEM with energy dispersive X-ray spectroscopy was used for performing EDS analysis.

#### **3.3.4. THERMOGRAVIMETRIC ANALYSIS**

Thermogravimetric analysis (TGA) is a testing method performed on materials which determine changes in weight with relation to changes in temperature. TGA is most commonly used for determination of characteristics of materials or mixtures such as degradation temperatures, concentration of mixture components, and determination of crystallization of components with a mixture among others.

The analyzer consists of a high-precision balance with a pan for loading the sample. The sample is placed in a small electrically heated oven with a thermocouple to accurately measure the temperature. The atmosphere within the oven may be an inert gas, to prevent oxidation or other undesired reactions, or air to allow for complete combustion of all components. A

computer is used to control the instrument. Analysis is carried out by raising the temperature of the sample gradually and plotting mass, or weight percent, against temperature.

The TGA used in this research was used to characterize the SWNT and determine concentrations of LSZ and SWNT in evaporated samples prior to fiber spinning or film coating. The effluent vapor could then be sent to an FT-IR for further analysis. The TGA used in this research was a TA Instruments (New Castle, DE) TGA Q50.

### **3.3.5. TURBIDIMETRIC ANALYSIS**

Turbidimetry or turbidimetric analysis is the process of measuring the loss of intensity of transmitted light due to the scattering effect of particles suspended in it. Turbidimetry can be used in biology to find the number of cells in a solution and is usually carried out in a UV-vis spectrophotometer. For processing, light is passed through a filter creating a light of known wavelength which is then passed through a cuvette containing a solution of interest. A detector then collects the light which passes through the cuvette. A measurement is then given for the amount of absorbed or transmitted light.<sup>125</sup>

The turbidimetric analysis was used to determine the lytic activity of all dispersions and macroscopic assemblies. A Cary (Santa Clara, CA) 3E UV-vis Spectrophotometer was used for the turbidimetric analysis of this research. First, a 66mM solution of potassium phosphate buffer was adjusted to a pH of 6.24 with potassium hydroxide at room temperature. Next, a bacterial cell suspension in the potassium phosphate buffer containing 0.015 wt. % *Micrococcus lysodeikticus* (Sigma Aldrich) was prepared. Next, 1 cm path length quartz cuvettes were filled with 2.5 mL of bacterial suspension, at which point 0.1 mL of buffer solution or liquid dispersions are added. Finally UV-vis is performed on the buffered bacterial suspension followed

by UV-vis of a buffered bacterial suspension containing the liquid dispersions where kinetic scans are at 450 nm for 5 min.

### **3.3.6. ULTIMATE TENSILE STRENGTH ANALYSIS**

Ultimate strength tensile testing is a fundamental materials science test in which a sample is subjected to uniaxial tension until failure. Properties that are directly measured via a tensile test are the load and the elongation. From these measurements the following properties can also be determined: Young's modulus, Poisson's ratio, yield strength, tensile strength, maximum elongation, toughness, and strain-hardening characteristics, among others.

The most common testing machine used in tensile testing is the universal testing machine. This type of machine has two crossheads. One is adjusted for the length of the specimen and the other is driven to apply tension to the test specimen. The machine must have the proper capabilities for the test specimen being tested. There are three main parameters: force capacity, speed, and precision and accuracy.<sup>126</sup> Force capacity is important for ultimate strength testing because the machine must be capable of generating enough force to fracture the specimen. The crosshead speed is also important as it must be able to be set fast or slow enough to properly mimic the actual application. Finally, the machine must be able to accurately and precisely measure the gauge length and forces applied; for instance, a large machine that is designed to measure long elongations may not work with a brittle material that experiences short elongations prior to fracturing. Alignment of the test specimen in the testing machine is critical, because if the specimen is misaligned the testing machine will exert a non-linear force on the specimen creating data capable of being misinterpreted.<sup>126</sup>

The test process involves placing the test specimen in the testing machine and applying tension to it until it fractures. During the application of tension, the elongation of the gauge

section is recorded against the applied force. The data is manipulated so that it is not specific to the geometry of the test sample. The elongation measurement is used to calculate the engineering strain,  $\epsilon$ . The force measurement is used to calculate the engineering stress,  $\sigma$ . The machine does these calculations as the force increases, so that the data points can be graphed into a stress-strain curve.

Tensile testing was used in this research to determine the mechanical properties of the macroscopic assemblies produced in this research. An Instron (Norwood, MA) 5565 Calibration Lab was used as the testing machine. After the fibers were spun, samples were glued into a testing frame with a gauge length of 26 mm. The load cell used for this testing was 100 cN with a cross-head separation speed of 1.0 mm/min. The load and gauge length were balanced and zeroed before each run. Test data collected for each sample were load, extension, time, and strain. Analysis to determine specific mechanical properties was done using Excel.

### **3.3.7. ELECTRICAL RESISTIVITY ANALYSIS**

Electrical resistivity is an electrical property of a material that quantifies how strongly the material opposes the flow of electric current. A low resistivity indicates a material that readily allows the movement of electric charge whereas a high resistivity indicates a material that will not allow the movement of an electric charge.

Quantum mechanics states that electrons in an atom cannot take on any arbitrary energy value. Rather, there are fixed energy levels which the electrons can occupy, and values in between these levels are impossible.<sup>127</sup> When a large number of such allowed energy levels are spaced close enough together then it can be said that the energy levels together form an "energy band". There can be many such energy bands in a material, depending on the atomic number and their distribution.<sup>128</sup> Two such bands important in the discussion of resistivity or conductivity of

materials are the valence band and the conduction band. Electrons in the conduction band may move freely throughout the material in the presence of an electrical field. In insulators and semiconductors, the atoms influence each other in such a way that between the valence band and the conduction band there exist a band-gap of energy levels, which the electrons cannot occupy. In order for a current to flow across this band-gap, a relatively large amount of energy must be furnished to an electron for it to leap across into the conduction band. Thus, large voltages can yield relatively small currents. Therefore, the measure of electrical resistivity of a material is influenced by the molecular make-up of the material, the surroundings of the material, and the power of the electrical charge.<sup>127-128</sup>

The electrical resistivity of the macroscopic assemblies in this research were measured by the 2-wire Ohms test method using an HP 34401A Multimeter (Palo Alto, CA). The fibers were placed on slides and Pelco® colloidal silver paste from Ted Pella, Inc. (Reading, PA) was used to create the lead contacts which were separated about ~ 1mm apart.

### **3.4. METHODS OF MACROSCOPIC ASSEMBLY**

Macroscopic assembly of nanomaterials can be carried out in a myriad of methods: fiber spinning, film drying, charge layering, spray coating, chemical layering, etc. In each method, it is desired to maintain the nanostructured properties of each system through processing. Therefore, it is necessary to understand how each processing method affects and changes the dispersion state. In the current research, wet and dry fiber spinning and film drying have been completed.

#### **3.4.1. FIBER SPINNING**

Traditional fiber spinning techniques include melt and solution spinning which can be dry or wet spun. In addition, techniques such as solid state drawing, solid state extrusion, gel spinning, and a combination of solid state drawing and tensile drawing have been used

successfully to obtain mechanically stable fibers. In order to process these fibers, solvents are used to cause solidification of the fiber solution, and after solidification the solvent must be dried off. However, most solvents used for these solutions are not sufficiently volatile to be easily removed. To prevent this problem, wet solution spinning uses a non-solvent (coagulant) to extract the solution solvent in a process known as coagulation. After coagulation of the fiber, it can be washed and/or heat treated in order to achieve desired properties.<sup>129</sup>

By adequately understanding the physical process of fiber formation, the physical properties of the fiber will be able to be determined by the chemical nature of the solution rather than by the coagulation process. Wet solution spinning involves the investigation of two problems: the structure formation in various processing conditions, and the relationship between structure and macroscopic properties.<sup>129</sup> Understanding these problems is very difficult since heat and mass transfer accompany phase transition in the coagulation, drying, and heat treatment processes.

Fiber solidification occurs through the coagulation process. The spinning solution undergoes a change in composition depending on the outward flux of the solvent and the inward flux of the coagulant. Thus, the coagulation process and the resulting morphology and mechanical properties are controlled by thermodynamic and transport effects, such as phase boundary shifts and flux ratios. These complex issues are both difficult to model and difficult to predict. Therefore, rather than study these directly, research has been done on variables which influence each to determine final fiber properties.<sup>129</sup> Temperature and coagulant concentration are the two most common variables. Increasing temperature of the spinning bath will increase the solubility of the system and also increase the diffusion coefficients and fluxes. It was found that with increasing temperature fibers possessed better mechanical properties despite surface

defects.<sup>129</sup> This indicates the internal structure of the fiber was quickly coagulated not allowing for void formation. Increasing concentration of the coagulant will speed the mass transfer by increasing the inward coagulant flux and outward solvent flux. It has been shown that with increasing coagulant concentration fibers were more homogenous at the surface and had mechanical properties that were dependant on the temperature of the coagulant.<sup>129</sup> This indicates that the increased concentration of the coagulant creates a skin at the outer most layer which prevents voids and pits from forming. It was also proposed by Hancock et al. that the mechanism of surface void formation was a function of interfacial instability due to capillary forces between the solvent and coagulant. Fiber post-treatments have also been studied to determine changes in morphology or mechanical stability. However, it has been thoroughly documented that when using a volatile coagulant, post-treatment does not result in morphological or mechanical changes to the fiber.<sup>129-130</sup> Therefore selection of coagulants is important and should be determined through experimentation.

In the current research fibers were spun by wet and dry spinning. For each, dispersions were extruded through a 21-gauge, stainless steel needle using a Harvard apparatus syringe pump with a stainless steel, 10 mL syringe at a volumetric rate of 0.5 mL per minute. Wet spinning of fibers was carried out by extrusion of dispersions into a PVA solution at room temperature. The coagulant solution speed varied from 50 to 150 revolutions per minutes. After coagulation, the fibers were removed from the PVA bath and washed in DI water. The fibers were then hung to be dried at room temperature. Dry spinning of fibers was carried out by extrusion of dispersions onto a Teflon mold. The dispersions were then allowed to dry at room temperature prior to removal from the mold. Post-processing of dry spun fibers was carried out by submersion of the fiber in methanol at room temperature for 24 hours. After submersion, the fibers were removed

and drawn at a ratio of 6:1. Drawing was carried out by taping the ends of a 3 cm section of fiber to posts on a measured rail system. The posts were then separated to a distance of 18 cm.

### **3.4.2. FILM DRYING**

Film drying of dispersions is a key processing technique for macroscopic assembly of nanomaterials. Film drying can consist of single drop-dried layers of solution or multiple layers of solution created via multiple drying steps or through layer interactions holding each layer separately. Regardless of the type of film, the structure and properties of the final product are influenced by the dynamics which take place when being processed.

Similar to the process of fiber spinning, film drying is theoretically governed by the thermodynamics and transport phenomena of the multicomponent system. The removal of solvents from a film is a complex heat and mass transfer process. Temperature and concentration, therefore, are of critical importance in creating robust films. Temperature will directly affect the thermodynamics and kinetics of transport. Increasing the temperature of a drying system will increase the diffusion rate thereby reducing the drying time of the film. However, increases in diffusion rate will cause internal forces between the evaporating solvent and non-evaporating mixture to be strained which could adversely affect the final structure of the film.<sup>131</sup> Increasing diffusion rate will also cause the vapor-liquid phase boundary to move at a more rapid pace causing non-homogeneity in the finalized film. Altering the concentration of the system is an even more complex problem. The concentration of the solvent, film mixture, or ambient air could be altered which will change the way in which the film dries. Increasing the concentration of the solvent at a fixed dispersion concentration will lead to less mechanically stable films which are more homogenous. This is due to the reduced mass of film mixture which eventually becomes the film, and it is for this reason the film is more homogenous; there is not a

sufficient film material to impede evaporation which creates homogenous layering effects.<sup>132</sup> Increasing the concentration of the film mixture will be not as homogenous as the aforementioned increased solvent film but will be more structurally sound films up to a critical concentration of diminishing returns. At this critical concentration, the amount of film mixture will be great enough that entrapment of the solvent occurs creating a complex gelled network rather than a dry film.<sup>131</sup> Therefore, the concentration of the film should be increased to the critical concentration which depends upon the solvent molecule size and volatility. Although it is possible to alter the atmosphere in which the film is drying, most research has steered away from this opting for completely dry conditions due to the complexity involved in maintaining a steady-state transport condition.

In the current research, films were created by drying of single layers on a glass or Teflon substrate. The concentrated mixtures were extruded on to the substrate via a syringe. After being placed on the substrate the films are dried on an orbital mixer in a fume hood.

### 3.5. MATHEMATICAL CONVERSIONS

Preparation of LSZ-SWNT dispersions was carried out on a weight basis. This is the most practical and most convenient from an experimental stand point. However, understanding of phase behavior and dispersion kinetics is based on volume, or more importantly position which is a basis of volume. Therefore, mathematical analysis was carried out to determine various important properties of constituents of LSZ-SWNT dispersions.

The density of LSZ is needed in order to determine the volume fraction present in a LSZ solution. Since LSZ is a globular protein, it was modeled as a sphere with a diameter of 3 nm in order to obtain the volume of a single LSZ molecule,  $V_{LSZ}$ , as shown in Equation 3.4.

$$V_{LSZ} = \frac{4}{3}\pi r^3 = \frac{4}{3}\pi \left(\frac{3nm}{2}\right)^3 = 1.41 \times 10^{-20} \frac{cm^3}{molecule\ of\ LSZ} \quad (3.4)$$

After determination of  $V_{LSZ}$ , the specific volume of LSZ,  $\hat{V}_{LSZ}$ , was determined using Avogadro's number,  $N_A$ , as shown in Equation 3.5.

$$\begin{aligned}\hat{V}_{LSZ} &= V_{LSZ}N_A = 1.41 \times 10^{-20} \frac{cm^3}{molecule\ of\ LSZ} \cdot 6.02 \times 10^{23} \frac{molecules\ of\ LSZ}{mol\ of\ LSZ} \\ &= 8,510 \frac{cm^3}{mol\ of\ LSZ}\end{aligned}\quad (3.5)$$

After determination of the specific volume of LSZ, the density of LSZ,  $\rho_{LSZ}$ , can be determined by using the molecular weight of LSZ,  $MW_{LSZ}$ , as shown in Equation 3.6.

$$\rho_{LSZ} = \frac{MW_{LSZ}}{\hat{V}_{LSZ}} = \frac{14,300 \frac{g\ of\ LSZ}{mol\ of\ LSZ}}{8,510 \frac{cm^3}{mol\ of\ LSZ}} = 1.68 \frac{g}{cm^3}\quad (3.6)$$

Determination of volume fraction of rods, SWNT, or spheres, LSZ, in a solution was carried out by knowing the mass fraction of each in solution or dispersion. The formula for determining the volume fraction of LSZ,  $\phi_{LSZ}$ , from the mass fraction of LSZ is shown in Equation 3.7.

$$\phi_{LSZ} = \frac{Volume\ of\ LSZ}{Volume\ of\ H_2O + Volume\ of\ LSZ} = \frac{\frac{m_{LSZ}}{\rho_{LSZ}}}{\frac{m_{H_2O}}{\rho_{H_2O}} + \frac{m_{LSZ}}{\rho_{LSZ}}} = \frac{\frac{\rho_{H_2O}}{\rho_{LSZ}} \cdot \omega_{LSZ}}{1 + \left(\frac{\rho_{H_2O}}{\rho_{LSZ}} - 1\right) \omega_{LSZ}}\quad (3.7)$$

In the above equation,  $m_{LSZ}$  is the mass of LSZ,  $m_{H_2O}$  is the mass of water,  $\rho_{H_2O}$  is the density of water, and  $\omega_{LSZ}$  is the mass fraction of LSZ. Equation 3.7 can be further simplified since the density of water and LSZ are constants. The resulting equation, shown in Equation 3.8 gives the volume fraction of LSZ as only a function of the mass fraction of LSZ.

$$\phi_{LSZ} = \frac{\frac{\rho_{H_2O}}{\rho_{LSZ}} \cdot \omega_{LSZ}}{1 + \left(\frac{\rho_{H_2O}}{\rho_{LSZ}} - 1\right) \omega_{LSZ}} = \frac{\frac{1}{1.68} \cdot \omega_{LSZ}}{1 + \left(\frac{1}{1.68} - 1\right) \omega_{LSZ}} = \frac{0.595 \cdot \omega_{LSZ}}{1 - 0.405 \cdot \omega_{LSZ}}\quad (3.8)$$

After determination of the volume fraction of LSZ in solution, the volume fraction of SWNT,  $\phi_{SWNT}$ , can be determined as shown in Equation 3.9.

$$\begin{aligned}\phi_{SWNT} &= \frac{\text{Volume of SWNT}}{\text{Volume of LSZ Solution} + \text{Volume of SWNT}} = \frac{\frac{m_{SWNT}}{\rho_{SWNT}}}{\frac{m_{LSZ-H_2O}}{\rho_{LSZ-H_2O}} + \frac{m_{SWNT}}{\rho_{SWNT}}} \\ &= \frac{\frac{\rho_{LSZ-H_2O}}{\rho_{SWNT}} \cdot \omega_{SWNT}}{1 + \left(\frac{\rho_{LSZ-H_2O}}{\rho_{SWNT}} - 1\right) \omega_{SWNT}}\end{aligned}\quad (3.9)$$

In the above equation,  $\rho_{LSZ-H_2O}$  is the density of the LSZ solution,  $m_{SWNT}$  is the mass of SWNT,  $\rho_{SWNT}$  is the density of SWNT, and  $\omega_{SWNT}$  is the mass fraction of SWNT. By examination of Equation 3.9, it can be seen that in order to determine the volume fraction of SWNT the LSZ solution density, SWNT density, and SWNT mass fraction must be known. The density is estimated for the SWNT being used, and the LSZ solution density is known through experimentation. Therefore, Equation 3.9 can be simplified to show the volume fraction of SWNT as only a function the mass fraction of SWNT as shown in Equation 3.10.

$$\phi_{SWNT} = \frac{\frac{\rho_{LSZ-H_2O}}{\rho_{SWNT}} \cdot \omega_{SWNT}}{1 + \left(\frac{\rho_{LSZ-H_2O}}{\rho_{SWNT}} - 1\right) \omega_{SWNT}} = \frac{\frac{1.01}{1.45} \cdot \omega_{SWNT}}{1 + \left(\frac{1.01}{1.45} - 1\right) \omega_{SWNT}} = \frac{0.697\omega_{SWNT}}{1 - 0.303\omega_{SWNT}} \quad (3.10)$$

Any further mathematical analysis which was performed was done on a singular basis and did not encompass the entire scope of research. It will, therefore, be discussed on an individual basis as it arises.

### 3.6. PREPARATION OF LYSOZYME – CARBON NANOTUBE DISPERSIONS

Preparation of LSZ-SWNT dispersions is straight forward and many papers present preparation methods which are very similar.<sup>3, 8, 10, 51, 133-134</sup> Each preparation method contains four basic steps: preparation of a solution of LSZ and a solvent or solvents, after the solution has

stabilized, introduction of SWNT into the LSZ solution, sonication of the LSZ-SWNT dispersion, and when needed, centrifugation of the sonicated solution of LSZ-SWNT.

Preparation of the LSZ-solvent solution is required prior to the addition of SWNT to ensure the LSZ has had adequate time to homogenize within the solution. If the LSZ solution is not homogenous then there will be areas of high, and consequently low, concentrations which will reduce the effectiveness of the LSZ in dispersing the SWNT. The timing and method of homogenization is also critical in achieving a dispersion with no visible aggregation via optical microscopy. If stirring rods are used, too little time will lead to a non-homogenous solution. Addition of SWNT to the LSZ solution has similar caveats as the LSZ-solvent solution. The SWNT must be added to the solution and allowed to homogenize, to the greatest possible extent by magnetic or physical stirring methods, allowing the most intimate contact between SWNT and LSZ. If proper mixing of the SWNT in the LSZ is not allowed there will be areas of high SWNT concentration with LSZ concentration possibly below that need to individually disperse the SWNT, which will adversely affect the dispersion. Therefore, the time of mixing and type of mechanical agitation used to mix must be taken into account as variables affecting the final dispersion state. Sonication of the LSZ-SWNT dispersion is done either using a bath or tip sonicator. Sonication is the application of high energy sound waves to a dispersion in order to break apart particles; if the amplitude and frequency of the waves can be controlled they should be optimized so as to minimize the damage to the SWNT and LSZ, but still allow enough energy to overcome the van der Waals forces of attraction between SWNT allowing the LSZ to intercalate between the individual tubes. Sonication is done specifically to overcome the van der Waals forces between SWNT allowing them to separate, at which time the LSZ is able to move between the tubes, interact, and stabilize them as individuals. Along with the frequency and

amplitude of the sonicating waves, time is also an important variable of sonication. Since the waves are high energy, the portion of the wave energy that is remaining after use for mechanical separation is dissipated as heat and sound energy. If the sonication is allowed to carry on for too long, the heat energy can cause damage to the LSZ and also cause evaporation of the solvent, which in turn changes the dynamics of the system and affects the final dispersion state. Therefore the duration of sonication and the wave characteristics must be accounted for in variables affecting the final dispersion state. Centrifugation of the sonicated dispersion is done in order to separate the kinetically unstable SWNT and LSZ from the supernatant which is typically the desired phase of individually dispersed SWNT. Figure 31 shows a schematic representation of the process which occurs during sonication.

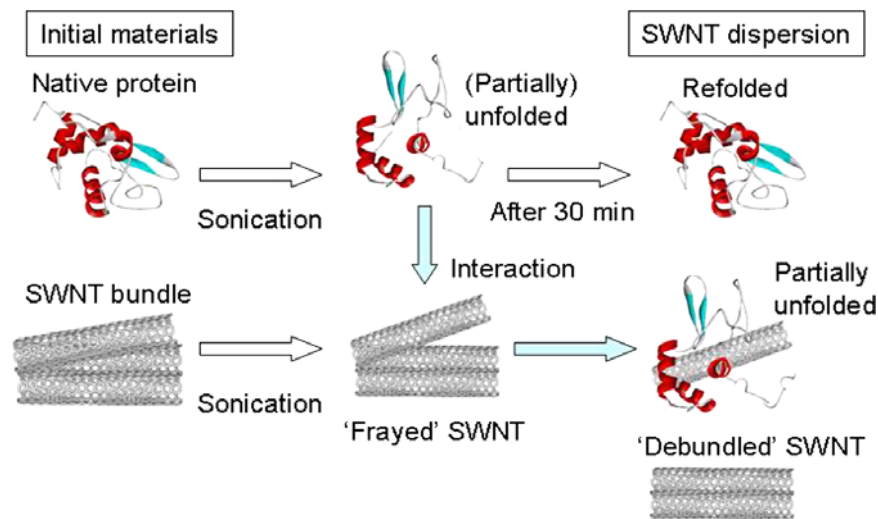


**Figure 31.** Possible mechanism where sonication leads to dispersion. SWNT bundles are ‘frayed’ and LSZ partially unfolds. The unfolded LSZ then adsorbs onto the ‘frayed’ SWNT. Any remaining LSZ returns to native conformation and any non-LSZ-adsorbed SWNT rebundle to form aggregates.<sup>51</sup>

Centrifugation rate and duration are both variables which affects what SWNT and LSZ which are deemed to be kinetically unstable. Depending on the stabilization of the individually dispersed SWNT, centrifugation rates can range from 300 x g to 100,000 x g with time ranging from 30 minutes to 72 hours. If the centrifugation rate is very high, then SWNT which may not be perfectly kinetically stable may precipitate out of the dispersion because the centrifugal force overcomes the stabilizing and van der Waals forces. Although long durations and high speeds seem to be bad, low times and low speeds will not do the proper job of removing the unstable constituents. If the rate is too low then the centrifugal force is not great enough to pull aggregated SWNT to the bottom of the centrifuge tube. In parallel, if the duration is not long enough then the time for the SWNT and LSZ to navigate the tortuous path to the bottom of the centrifugation will not be met and the final dispersion will be left with unstable SWNT and LSZ – mainly aggregates of each. The major difference between papers is the concentrations of LSZ and SWNT that are used to achieve stable dispersions. Although, many research groups use various initial concentrations of both SWNT and LSZ, they all use greater amounts of LSZ than is theoretically needed. This is because if a mixture is mixed so that the exact amount of LSZ is added to individually disperse a set amount of SWNT, there are possibilities that LSZ will not properly intercalate to give individual SWNT. Therefore, by adding additional LSZ (or any dispersant), there are statistically greater chances of having LSZ intercalate since the concentration is so high that if some LSZ does not intercalate there is excess in order to fill that void. However, as will be discussed, the excess LSZ has a role in the phase behavior of LSZ-SWNT dispersions through depletion interactions. Regardless of all the variables that must be accounted for in preparation of the dispersion and the differing initial concentrations that can be used, the end goal is to achieve a stable dispersion of individually dispersed SWNT.

In the current research, LSZ-SWNT dispersions are prepared following a similar method as the one described above. The desired amount of LSZ is weighed and poured into a beaker. The appropriate amount of deionized water is then added to the beaker along with a magnetic stirring rod; the beaker is then covered with Para-Film to prevent evaporation. For this research, all dispersions were made with 100 mL total volumes. The LSZ solution is stirred at approximately 100 repetitions per minute for thirty minutes to allow for solvation and complete mixing. The correct amount of SWNT are weighed and poured into the LSZ solution. The solution is then stirred with a spatula to incorporate all of the SWNT. The LSZ-SWNT dispersion is then magnetically stirred for one hour at approximately 100 repetitions per minute to allow for complete mixing of SWNT within the LSZ solution. The LSZ-SWNT dispersion is then tip sonicated for thirty minutes at 60% amplitude, which equates to approximately 55 J. After sonication, the LSZ-SWNT is termed to be a mixture or bulk dispersion. If desired, the LSZ-SWNT uncentrifuged dispersion is then centrifuged for three hours at 17,000 times gravity. Depending on the size of the initial dispersion, multiple batches of centrifugation must occur to process all of the material. After centrifugation, the liquid supernatant is removed via pipette and stored. It should be noted that LSZ-SWNT dispersions, both centrifuged and uncentrifuged, are stored at approximately 5°C in order to help maintain the activity of LSZ and prevent any thermal energy from causing unwanted enzyme interactions. Dispersions of LSZ-SWNT stabilized with TTAB were prepared analogous to LSZ-SWNT. TTAB and LSZ were added to DI water and magnetically stirred for 10 minutes at which point SWNT was added and tip sonicated. Again, two sample preparation methods were used to create mixture and supernatant dispersions. After sonication, the mixture was processed by centrifugation at 1,000 x g for 30 minutes and removing the supernatant, whereas the supernatant was centrifuged for 3 hours at

17,000 x g. Evaporation of the LSZ-TTAB-SWNT dispersions was used to create concentrated samples for analysis and fiber spinning. Solutions of LSZ-SWNT or LSZ-TTAB-SWNT in PVA were created by combining dilute mixture or supernatant dispersions with solutions of 185 kDa PVA. The PVA solution was 4.10 vol.% in DI water mixed via magnetic stir bar at 50°C for 3 days. After combination of the dispersions with the polymer solution, the resultant solutions were mixed via magnetic stir bar for 20 minutes then concentrated via evaporation on an orbital mixer for fiber spinning.

## **4. RESULTS AND DISCUSSION**

### **4.1. LYSOZYME SOLUTION CHARACTERIZATION**

Prior to using LSZ as a dispersant for SWNT, the aqueous LSZ solution was characterized independently. This was done in order to determine changes due to the inclusion of SWNT. Understanding the original LSZ state along with any changes will allow for the determination of the concentration in dispersed SWNT, and also allowing for the elucidation of changes in secondary and tertiary structure, LSZ-SWNT binding sites, and changes in enzymatic activity.

#### **4.1.1. ULTRAVIOLET – VISIBLE SPECTROSCOPY**

UV-vis was used to develop calibration curves for LSZ in order to determine concentrations of unknown LSZ samples. UV-vis was also used to indicate a molecular interaction between SWNT and LSZ. LSZ has a characteristic absorption peak at a wavelength of 280 nm. This characteristic peak, shown in Figure 32, is due to the hydrophobic tryptophan residue located within the core of LSZ. As shown in Figure 32, processing of LSZ analogous to that used in processing the LSZ-SWNT dispersions does not significantly alter the absorption spectra. The slight difference between the unprocessed solution, and the sonicated and sonicated, centrifuged solutions is due to the partial unfolding and refolding of LSZ before and after sonication. Changes in the absorbance of a solution, especially protein solutions, are primarily due to the change in the environment surrounding the primary absorbing chromophore.

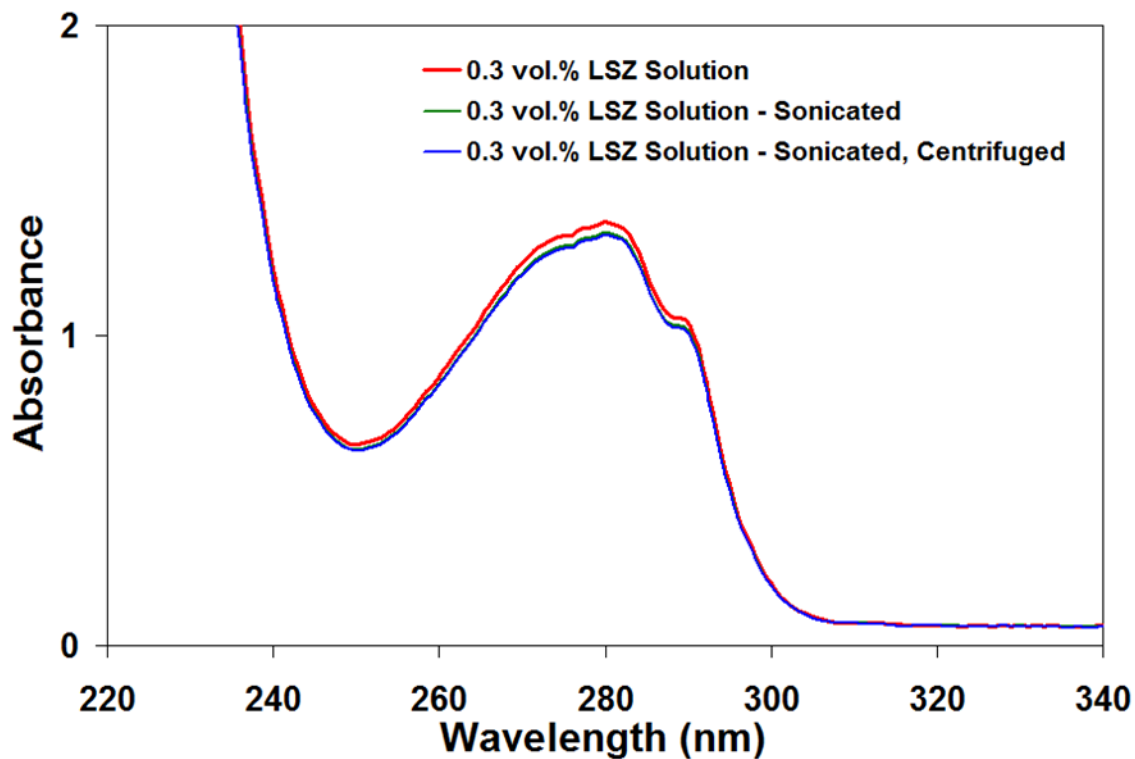


**Figure 32.** Absorbance spectrum of 0.30 vol. % LSZ solutions at various stages of processing.

After determination that processing of LSZ does not alter the absorption spectrum, a calibration curve was constructed. In order to construct the calibration curve, serial dilution was used to cover a range of 1.20 vol. % LSZ to 0.01 vol. % LSZ. The absorption spectrum of LSZ solution at various concentrations is shown in Figure 33.

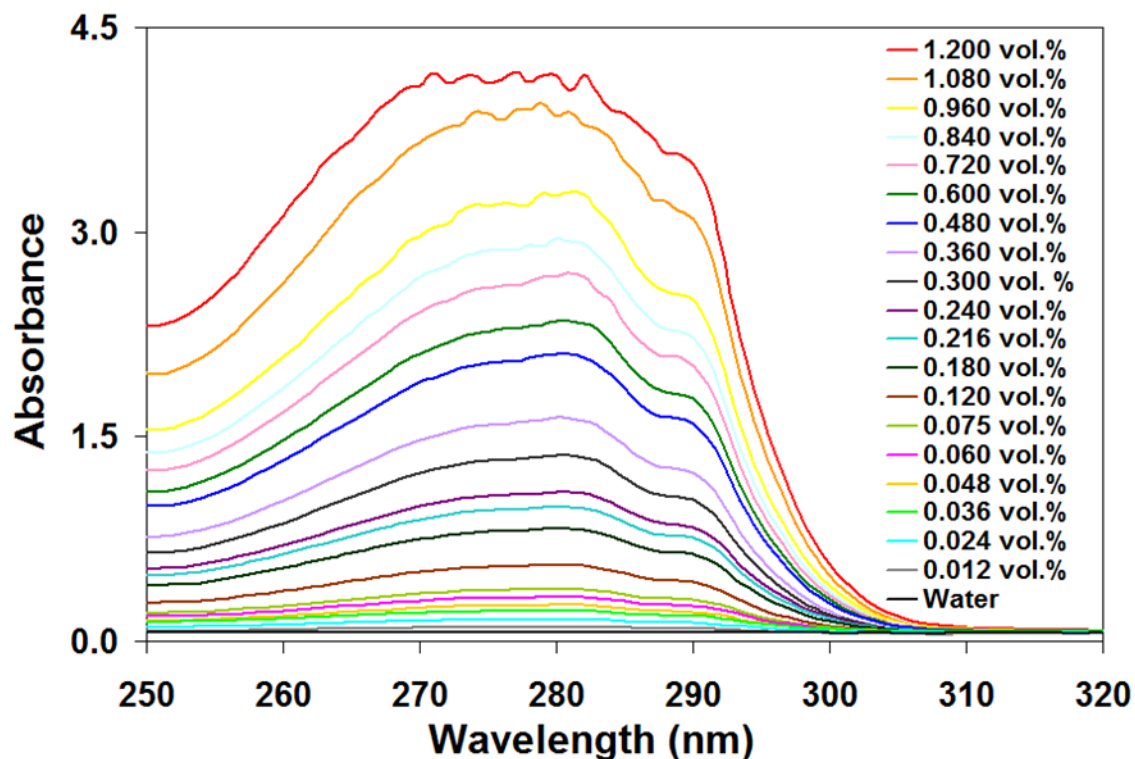


**Figure 33.** Absorbance spectrum of LSZ solutions with the water baseline removed at concentrations ranging from 1.20 vol. % to 0.01 vol. %. Subtraction of the water baseline is essential in determining the actual absorbance of LSZ corresponding to the known concentration.

At LSZ concentrations above 0.48 vol.%, absorption flattening occurs. At sufficiently high concentrations, the absorption bands will saturate and show absorption flattening. The absorption peak appears to flatten because close to 100% of the light is being absorbed. The concentration at which this occurs depends on the particular compound being measured. Solutions that are not homogeneous can show deviations from the Beer-Lambert law because of absorption flattening.<sup>117</sup> This can happen, for instance, where the absorbing chromophore is located within suspended particles, as is the case with LSZ solutions. For clarity, Figure 34 shows the deviation of from the Beer-Lambert law for LSZ solutions at concentrations above 0.48 vol.%. Figure 35

shows the calibration curve of LSZ given in volume percent with the extinction coefficient of  $4.31 \text{ mm}^{-1} \text{ vol.}\%^{-1}$  or  $36,669 \text{ cm}^{-1} \text{ M}^{-1}$ .

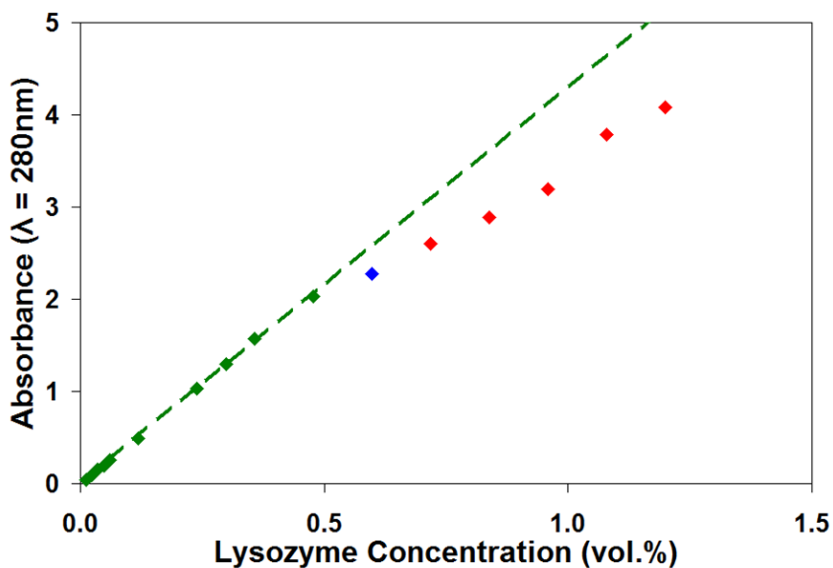


**Figure 34.** Calibration curve for LSZ showing deviation from the Beer-Lambert law at a concentration above 0.48 vol. % LSZ.

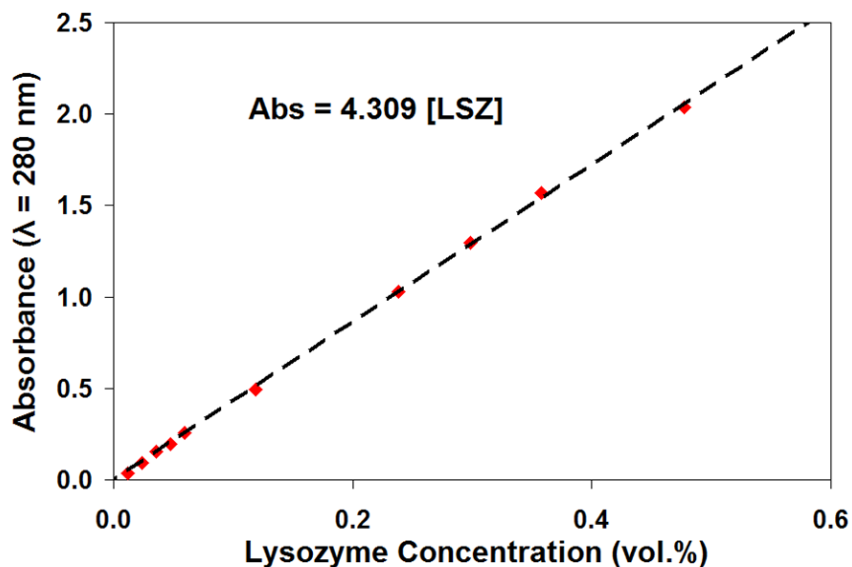


**Figure 35.** Calibration curve for LSZ showing only usable concentrations and calibration equation from linear data fit with statistical  $R^2$  of  $>0.99$ .

#### 4.1.2. CIRCULAR DICHROIC SPECTROSCOPY

CD was used to determine the initial secondary and tertiary structure of LSZ in order to compare it to LSZ-SWNT dispersions to determine any alterations that occur during the binding of LSZ to SWNT. Secondary structure can be determined by CD spectroscopy in the far-UV spectral region from 190 nm to 250 nm. At these wavelengths, the chromophore is the peptide bond, and the signal arises when it is located in a regular, folded environment. Alpha-helix, beta-sheet, and random coil structures each give rise to a characteristic shape and magnitude of CD spectrum. Alpha helices show characteristic peaks between 200 nm and 230 nm. Beta sheets show a characteristic peak centered at 215 nm. Random coils show a characteristic peak centered at approximately 200 nm.<sup>118</sup> Figure 36 shows the secondary structure of LSZ at various processing conditions to be dominated by the alpha helix with an unsmoothed bimodal response between 200 nm and 230 nm. The alpha helix rich secondary structure of LSZ is important for the enzymatic activity of the protein. The CD spectrum of a protein in the near-UV spectral region from 250 nm to 350 nm can be sensitive to certain aspects of tertiary structure. At these wavelengths, the chromophores are the aromatic amino acids and disulfide bonds, and the CD signals they produce are sensitive to the overall tertiary structure of the protein and the environment surrounding them.<sup>118</sup> Signals in the region from 280 nm to 300 nm are attributable to tryptophan and those from 310 nm to 330 nm are attributable to disulfide bonds. Figure 37 shows the near-UV spectrum for LSZ solution after various processing steps.

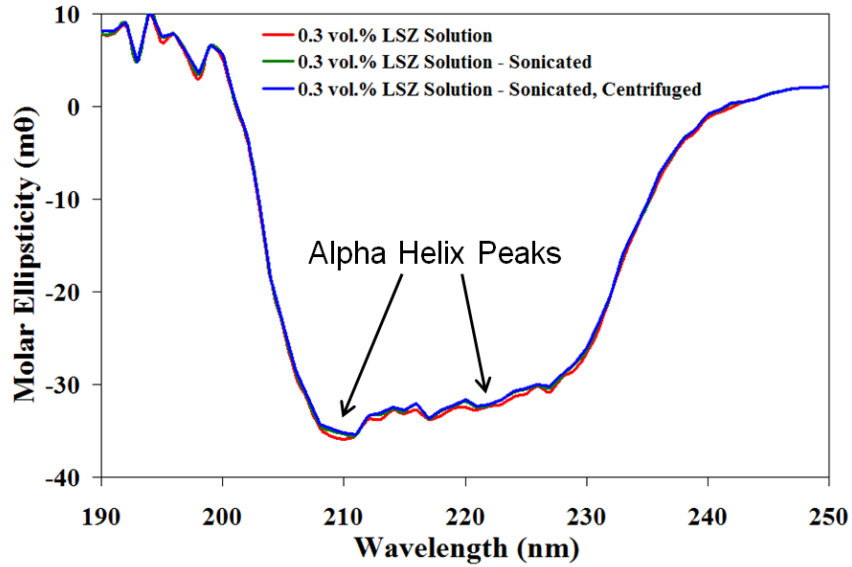


**Figure 36.** Far-UV CD spectrum of 0.30 vol. % LSZ solution both before and after processing. The lack of deviation of the sonicated and sonicated, centrifuged solutions shows that processing does not fully disrupt the secondary structure of LSZ.

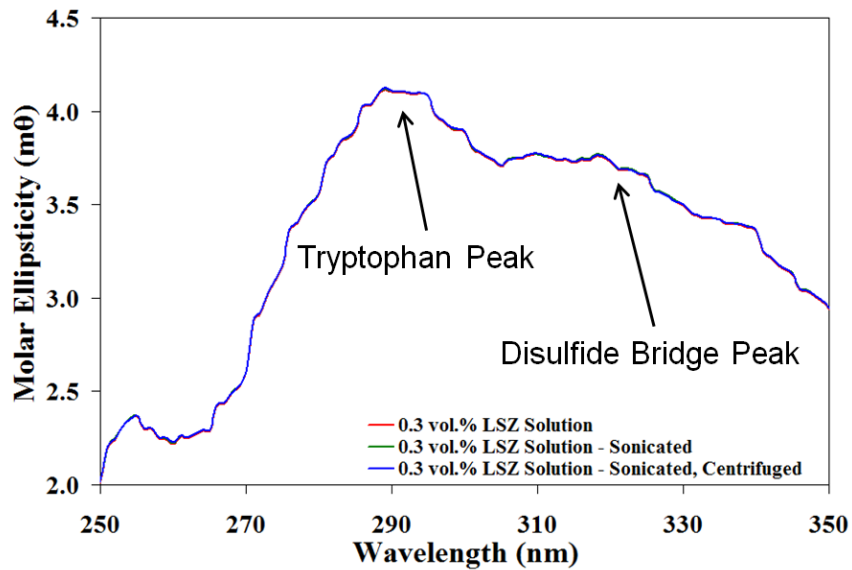


**Figure 37.** Near-UV CD spectrum of 0.30 vol. % LSZ solution both before and after processing. The lack of deviation of the sonicated and sonicated, centrifuged solutions shows that processing does not disrupt the tertiary structure of LSZ.

### 4.1.3. ENZYMATIC ACTIVITY ANALYSIS

The enzymatic activity of LSZ is derived from its' secondary structure of alpha helices and is predominantly active against Gram-positive bacteria. In order to quantify the activity of LSZ, turbidimetric analysis was done. Turbidity is the haziness or cloudiness of a suspension resulting from light scattering around colloidal entities. The turbidity of the bacterial suspension predominantly occurs at the cell surface because of the high refractive gradient between the fluid and the cell surface. Turbidimetric analysis is the application of measuring antibacterial activity of reacting agent in the presence of a known bacterial agent. A bacterial culture during the log phase of growth is relatively homogeneous and each cell is actively metabolizing and dividing at about the same rate. Consequently if a chemical agent is added to a culture in the log phase then any change in growth rate may be attributed to the action of the reacting agent. The turbidimetric analysis used in this research uses a UV-vis spectrophotometer to measure the increase of light transmitted at 450 nm through a sample containing *Micrococcus lysodeikticus* and LSZ, which is the standard method of activity analysis for LSZ.<sup>117</sup> Figure 38 shows the turbidimetric analysis of several solutions of LSZ. Reduction in the absorbance of transmitted light at 450 nm shows that LSZ lyses the *M. lysodeikticus* making the solution clearer (less turbid). As shown in Figure 38, the different processing methods – none, sonicated, and sonicated,centrifuged – do not show significant differences. This indicates that the processing methods for creating the LSZ-SWNT dispersions do not affect the inherent activity of LSZ. The trendlines shown for each processing method are fitted to the linear cell death region of the bacterial solution as described by Michaelis-Menten kinetics. The slope from each trendline can be used to determine the specific activity of LSZ using Equation 4.1.

$$Activity = \frac{\frac{\Delta Abs_{Enzyme}}{\Delta t} - \frac{\Delta Abs_{Ref}}{\Delta t}}{0.001 \cdot V} \quad (4.1)$$

The activity from equation 4.1 is given in active units per volume of LSZ where the  $\Delta\text{Abs}_{\text{Enzyme}}$  is the linear cell death region trendline slope,  $\Delta\text{Abs}_{\text{Ref}}$  is the trendline slope from the water reference as given in Figure 39, V is the volume of LSZ present in the injected solution, and 0.001 is the definition of LSZ activity in units of  $\text{Abs active unit}^{-1} \text{ min}^{-1}$ .

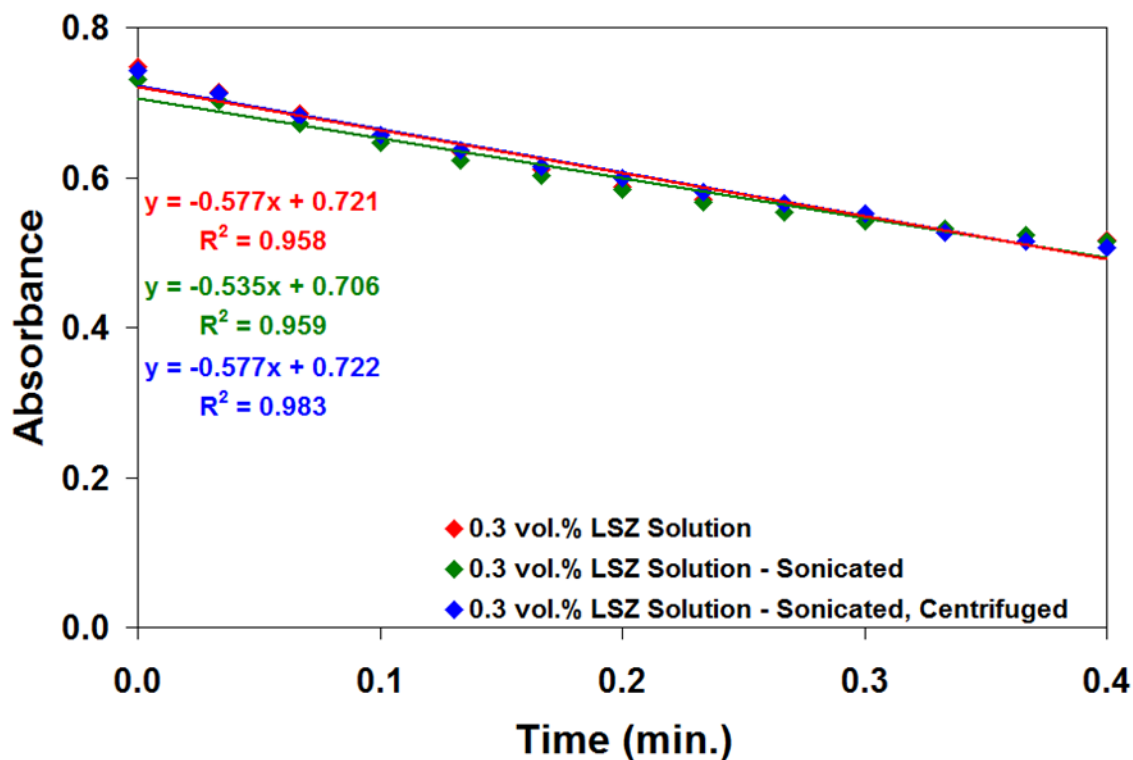


**Figure 38.** Turbidimetric analysis of 0.3 vol.% LSZ solutions at various processing conditions. Linear fit of cell death region shown for each processing method with the slope of the line equation used to calculate activity.

The specific activity of LSZ can be calculated from Equation 4.1 and the data given in Figure 38, it is possible to calculate the specific activity of LSZ at each processing methods. The LSZ solutions maintained  $5630 \pm 140$  active units per mL LSZ through processing. For reference, Figure 39 shows the turbidimetric analysis of *M. lysodeikticus* with the addition of water.

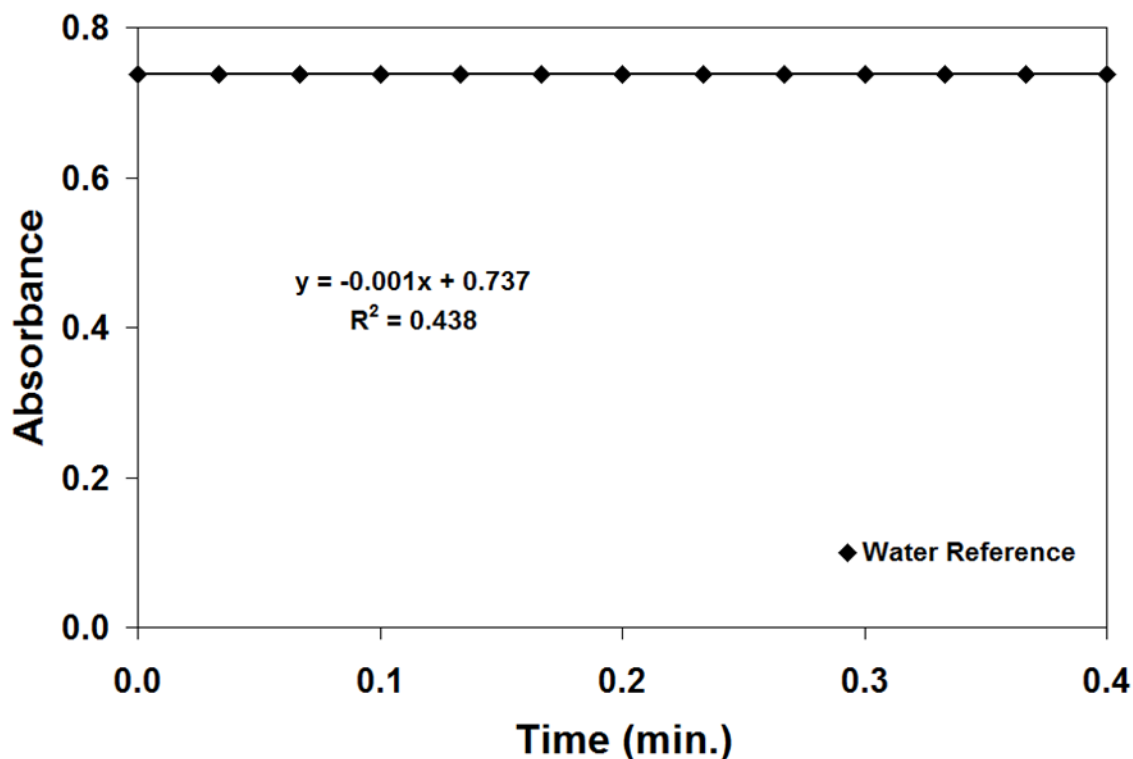


**Figure 39.** Turbidimetric analysis of *M. lysodeikticus* and water as a reference.

#### 4.1.4. THERMOGRAVIMETRIC ANALYSIS

TGA was done in both air and argon for LSZ and SWNT dispersions and solid assemblies to determine the thermal decomposition behavior. The thermal decomposition temperature,  $T_d$ , should not be confused with the denaturation temperature.  $T_d$  is the temperature at which a molecule chemically decomposes into its' constituent components and is primarily exothermic. Thermal denaturation is the act of a protein or enzyme losing its' structure and unfolding due to the application of heat. There are three stages of protein thermal denaturation prior to thermal decomposition. Quaternary structure denaturation is the dissociation or spatial movement of protein subunits; tertiary structure denaturation involves the disruption of covalent interaction between amino acids, such as disulfide linkage breaks and dipole-dipole interaction

disruption; and secondary structure denaturation is responsible for the loss of all regular repeating patterns of alpha helices and beta sheets adopting a random coiled structure.<sup>135</sup> It should be noted that the primary structure denaturation cannot occur because denaturation is the unfolding of the protein, and after losing all secondary structure it is completely unfolded. Rather, the primary structure is disrupted by the act of thermal decomposition when the thermal energy input is large enough to disrupt the covalent peptide bonds which hold together the protein.

LSZ has a characteristic  $T_d$  at approximately 270°C in argon and 255°C in air as determined by the onset point of decomposition. It has a  $T_d$  at approximately 323°C in argon and approximately 305°C in air as determined by the derivative weight loss curve. The onset point  $T_d$  was determined to be the intersection of the tangent line from the initial LSZ dry weight and the inflection point of the loss curve, which is the peak maximum of the weight loss derivative curve. The weight loss derivative curve is calculated by determining the slope between points using the least-squares method; the peak maximum of the weight loss derivative curve shows an alternative method of determining  $T_d$ . The TGA weight loss curve and weight loss derivative curve for LSZ in air and argon can be seen in Figure 40 and Figure 41, respectively.

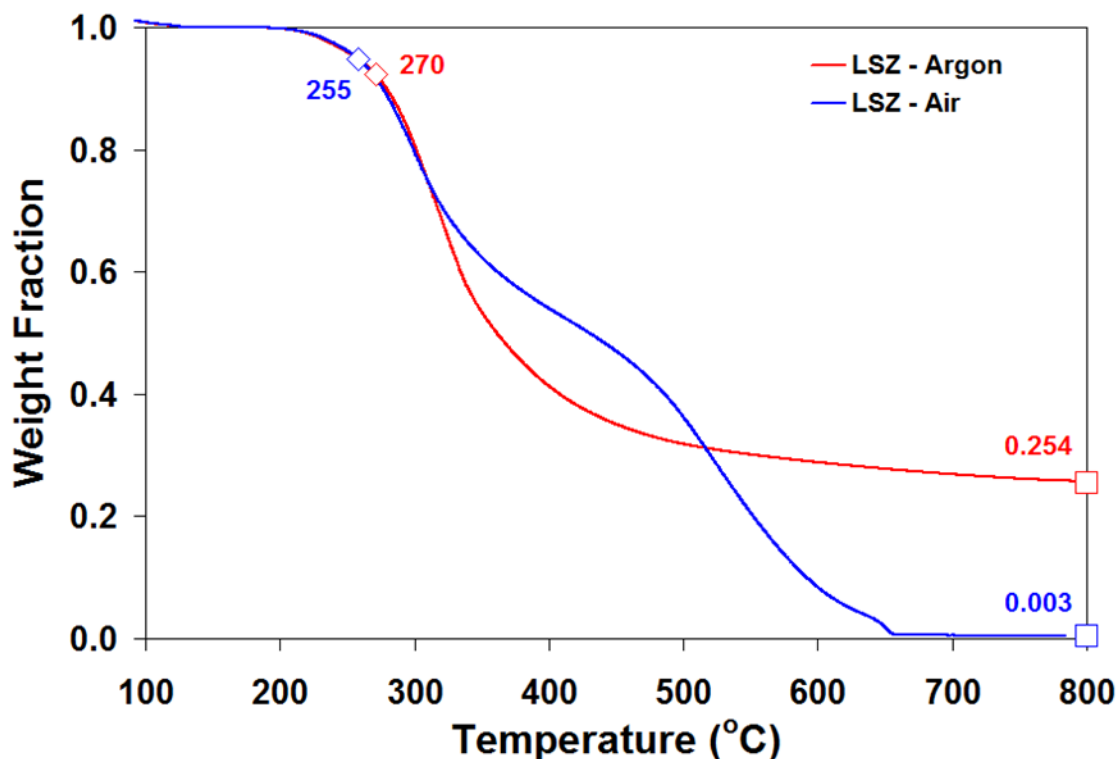


**Figure 40.** TGA weight loss curve versus temperature for LSZ in argon (red) and air (blue). Curves are averages of three runs of each air and argon; error for LSZ in argon is 0.61% and error for LSZ in air is 1.01%. Diamond markers indicate the decomposition onset temperature and the square markers indicate the residual weight fraction.

Figure 40 shows that LSZ has a characteristic weight loss curve from approximately 220°C to 350°C in both air and argon. The difference of 15°C in onset point  $T_d$  is due to the mechanism by which decomposition takes place in each atmosphere. In air, combustion takes place to thermally decompose the molecules, whereas in argon, thermal cracking takes place to thermally decompose the molecules. Figure 40 also shows that in air LSZ has a second and third loss from approximately 400°C to 550°C and 620°C to 670°C, respectively, which are not seen in argon. These losses are attributed to the buffering materials in the raw LSZ, sodium acetate and sodium

chloride. The buffering salts are also the difference for the residual difference between air and argon. In air, the buffer salts break down leaving a residue of 0.3 wt.%, whereas in argon, the buffer salts do not break down leaving a residue of 25.4 wt.%.

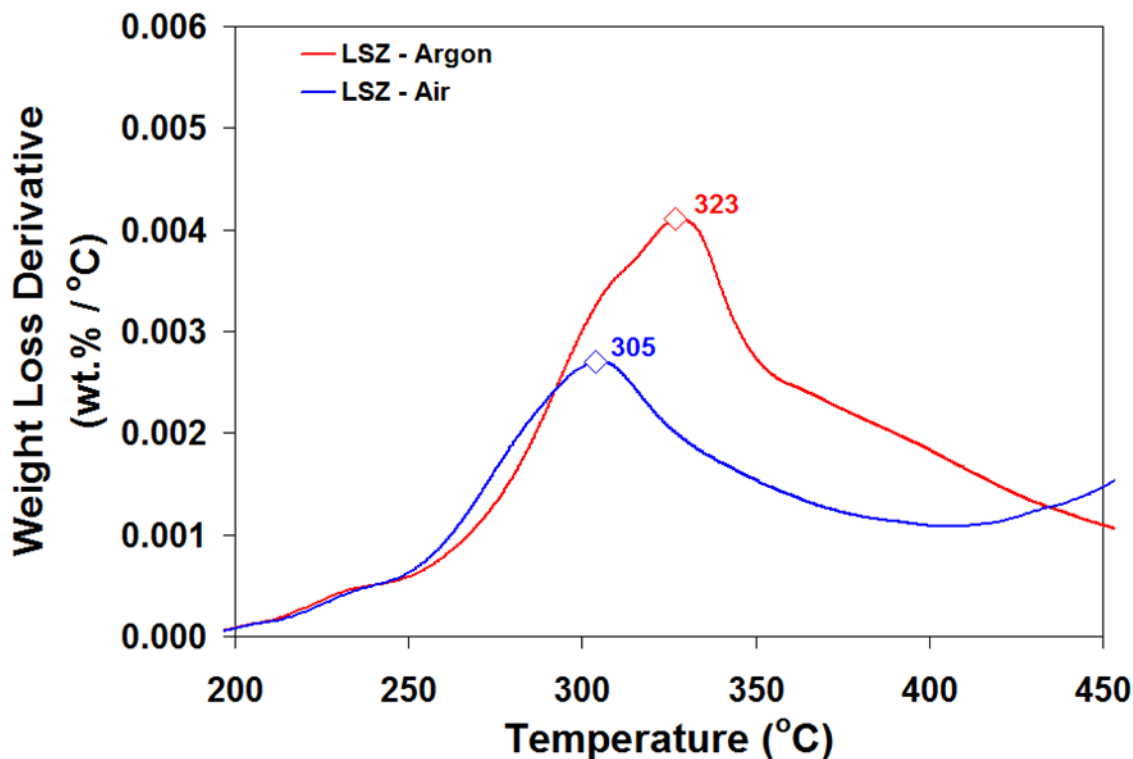


**Figure 41.** TGA weight loss derivative curve versus temperature for LSZ in argon (red) and air (blue). Curves are averages of three runs of each air and argon; error for LSZ in argon is 0.61% and error for LSZ in air is 1.01%. Diamond markers indicate the decomposition temperature.

Figure 41 shows that for the derivative curve method LSZ has a  $T_d$  of 323°C in argon and 305°C in air. The difference of 18°C is analogous to that of the differences in the onset point  $T_d$ . The shape of the air and argon curves after the decomposition temperatures are different due to the second and third losses which occur in air but not in argon. The difference in onset point  $T_d$  and derivative  $T_d$  show that each method can consistently measure change in  $T_d$  with both giving

consistent differences between air and argon for LSZ. It should be noted that the heating rate can alter  $T_d$ , therefore, to compare data between runs the same heating rate must be used.

#### **4.1.5. RHEOLOGICAL BEHAVIOR**

Rheology of aqueous LSZ solutions was done in order to determine the microstructural response and viscosity to increasing LSZ concentrations. The importance of determining the solution rheological characteristics is in order to mathematically remove the effects of LSZ and water in the LSZ-SWNT dispersions. As previously discussed, concentrating LSZ solutions at ambient conditions leads to aggregate and fibril formation. Therefore, the various concentrations of LSZ were individually made by combining the desired amount of LSZ with DI water and mixing to create homogenous solutions. The concentration range tested was from 0.30 vol.% to 9.50 vol.% with a total of eight concentrations being tested. The elastic effect of LSZ was not seen in aqueous solutions until approximately 2.5 to 3.0 vol.% LSZ. Therefore, data below these concentrations is sparse due to the torque detection limits of the rheometer used. It should also be noted that each data set was collected over three separate loadings with three runs per loading for a total of nine runs per test.

The solutions were first subjected to an amplitude sweep in order to determine the limit of linear viscoelasticity. The limit of linear viscoelasticity was determined by graphical analysis where the correlation in the direction of the tangent line of the low-strain plateau was lost. The critical strain was determined via graphical analysis to be approximately 1.6%. Another interesting note is to see that increase in LSZ concentration of approximately three-fold only leads to an approximate one order of magnitude increase in the solid-like response of the solution. Figure 42 shows the storage modulus of LSZ solutions as a function of amplitude strain.

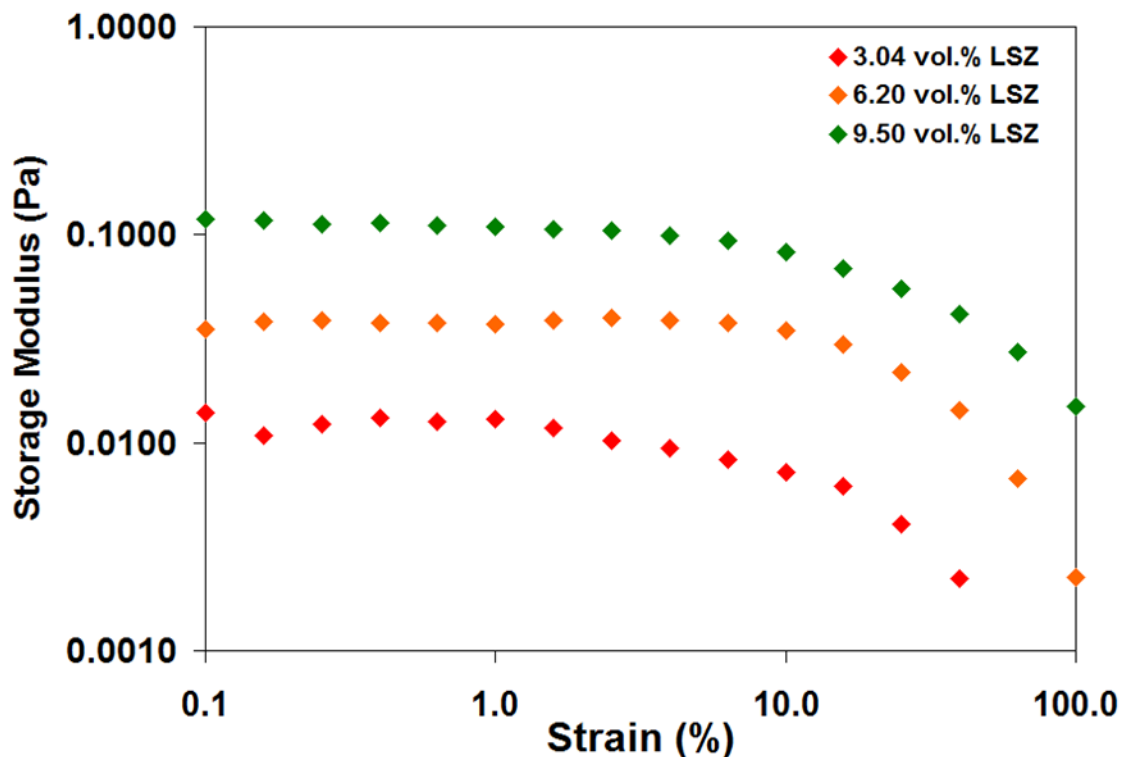


**Figure 42.** Amplitude sweep test data showing storage modulus as a function of amplitude strain for concentrations of 3.04 vol.% LSZ, 6.20 vol.% LSZ, and 9.50 vol.% LSZ. The critical strain was determined to be 1.6% by graphical analysis where the correlation in the direction of the tangent line of the low-strain plateau was lost. Error for each concentration is less than +/- 3%.

After determination of the critical strain, the linear viscoelastic oscillatory response of the dispersions was tested to probe the time-dependent behavior of increasing concentrations of LSZ. Figure 43 shows the storage modulus for increasing concentrations of LSZ as a function of angular frequency. As expected, the elastic behavior increases for increasing concentration of LSZ. However, the slope of the storage modulus versus angular frequency does not drastically change with increasing concentration. This indicates that the elasticity of the gel network created by LSZ does not increase in strength with increasing concentration of LSZ. The linear slope for

each concentration can be found by taking the exponential function of the slope from the logarithmic fit of each data set – 1.00 for 3.04 vol.% LSZ and 1.01 for 6.20 vol.% LSZ and 9.50 vol.% LSZ.

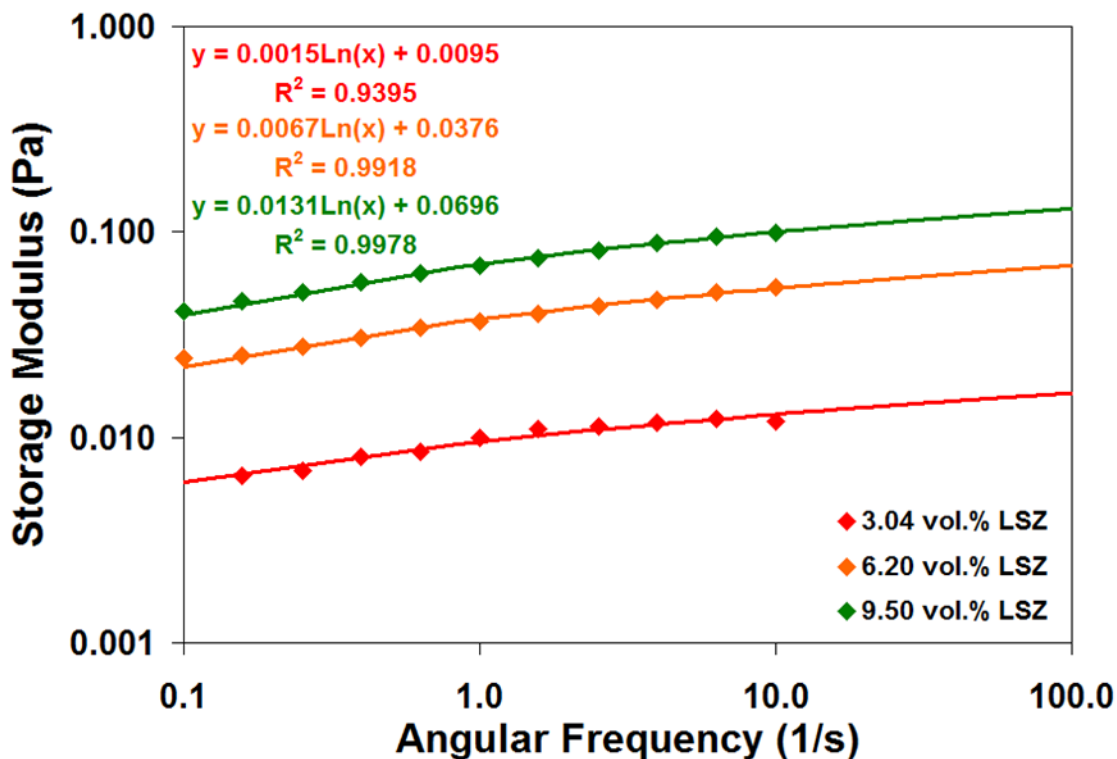


**Figure 43.** Linear viscoelastic oscillatory response showing the storage modulus as a function of angular frequency for concentrations of 3.04 vol.% LSZ, 6.20 vol.% LSZ, and 9.50 vol.% LSZ. Error for each concentration is less than +/- 3%.

After determination of the elastic response as a function of frequency, storage modulus was plotted versus LSZ concentration to determine the effect of LSZ concentration on the elasticity of the solution. Figure 44 shows the storage modulus scales with LSZ concentration by a power law function.

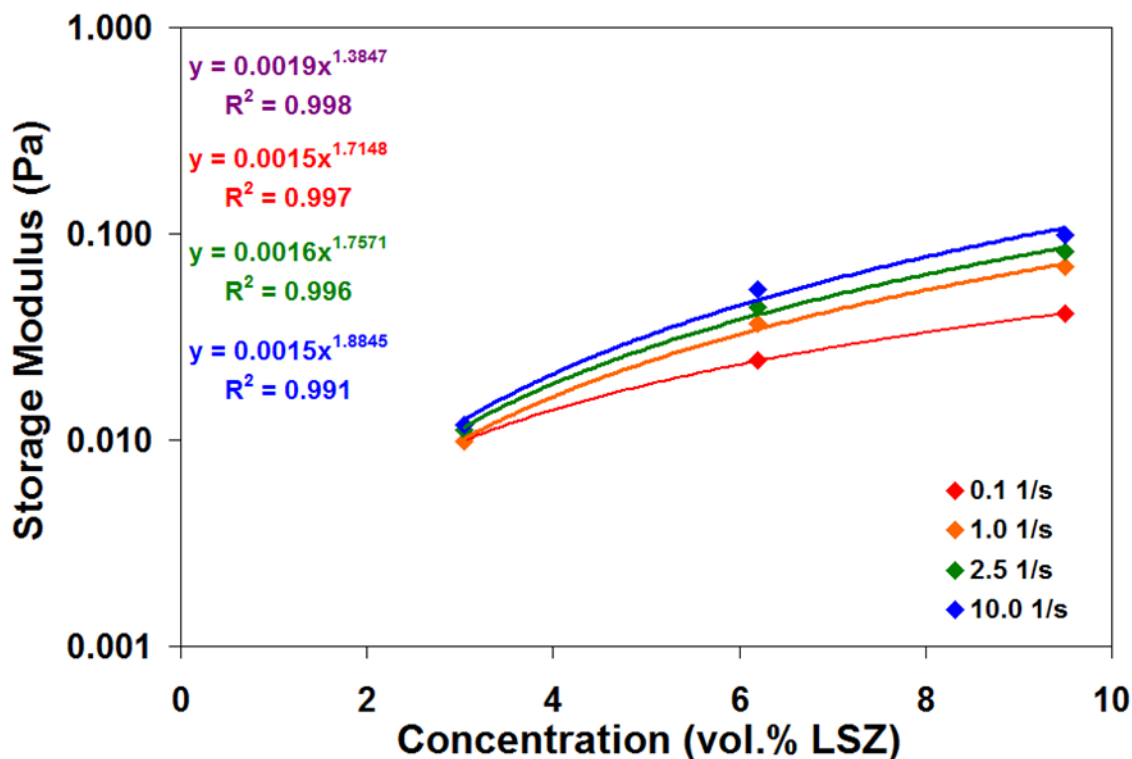


**Figure 44.** Linear viscoelastic oscillatory response showing the storage modulus as a function of LSZ concentration for angular frequencies of  $0.1 \text{ s}^{-1}$ ,  $1.0 \text{ s}^{-1}$ ,  $2.5 \text{ s}^{-1}$ , and  $10.0 \text{ s}^{-1}$ . Error for each concentration is less than  $\pm 3\%$ .

After the microstructure was probed by oscillatory testing, the viscosity of the solutions was determined via steady shear flow curve testing. The flow characteristics of each dispersion varied for each concentration as seen in Figure 45. At concentrations below 0.60 vol.% LSZ, the solutions acted as Newtonian fluids. This indicates that there was not yet any interaction between LSZ molecules to induce any kind of shear response. At concentrations above 0.60 vol.% LSZ, the solutions show differing slopes of shear thinning behavior. This shows that above this concentration, there was a physical interaction between LSZ molecules creating a system which

shows a shear response. As the shear rate is increased, however, the network attractive force is overcome by shear force causing the viscosity to decrease.

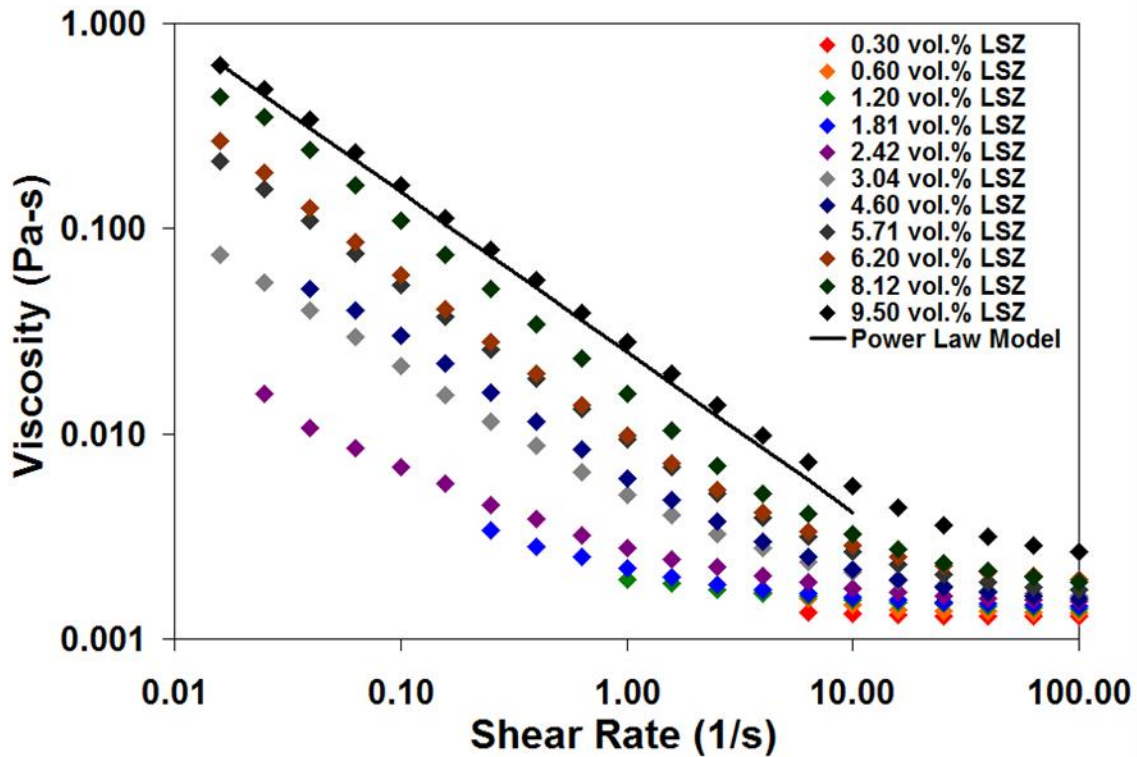


**Figure 45.** Flow curve showing viscosity versus shear rate for concentrations of 0.30 vol.% LSZ to 9.50 vol.% LSZ, and a power law model fit. The power law model shown has  $K = 0.025 \text{ Pa}\cdot\text{s}^2$  and  $n = 0.220$ . Error for each concentration is less than  $\pm 4\%$ .

The viscosity continues to decrease with shear rate with a power law nature until approximately  $10 \text{ s}^{-1}$  when the shear thinning behavior begins to level off into an infinite shear viscosity plateau. The power law nature of the shear thinning behavior is shown by the power law model in Figure 45, as described by Equation 4.2.

$$\eta = K\dot{\gamma}^{(n-1)} \quad (4.2)$$

For the entire concentration range studied  $K$  varies from 0.0013 Pa-s<sup>2</sup> to 0.0250 Pa-s<sup>2</sup> and  $n$  varies from 0.22 to 1.00. After determining the shear nature of the LSZ solutions, the viscosity was plotted as a function of LSZ concentration as shown in Figure 46a. The LSZ solution viscosity is integral to determine the specific and inherent viscosity of LSZ-SWNT dispersions as will be discussed in detail later. Third-order polynomial fits were chosen to determine the function of LSZ solution viscosity versus LSZ concentration. The fit was controlled by dictating that at zero LSZ concentration the viscosity would be 1.308 mPa-s which is the viscosity of water at 10°C to ensure the generated equation had a true physical meaning for the system they were describing.

The rheological behavior of particulate suspensions of hard spheres is well documented by Russel et al., Hiemenz and Rajoagopalan, Kim and Karrila, Mackosko, Brady, Mellema, and Larson.<sup>61, 136-140</sup> At concentrations below 3 vol.%, the shear viscosity of a hard sphere suspension can be predicted by Equation 4.3 which Einstein calculated from the viscous dissipation produced by the flow around a single sphere.<sup>98</sup>

$$\eta = \eta_s(1 + 2.5\phi) \quad (4.3)$$

As shown in Figure 45, concentrations below 3 vol.% follow a power law function as described in Equation 4.2 and would therefore deviate significantly from the linear function of Equation 4.3. Taking the effect of multibody interactions into account, Batchelor, was able to adapt Equation 4.3 for hard spheres with rigid repulsion interactions to generate Equation 4.4 which has been shown to be valid for concentrations below 10 vol.%.<sup>98</sup>

$$\eta_r = 1 + 2.5\phi + 6.2\phi^2 \quad (4.4)$$

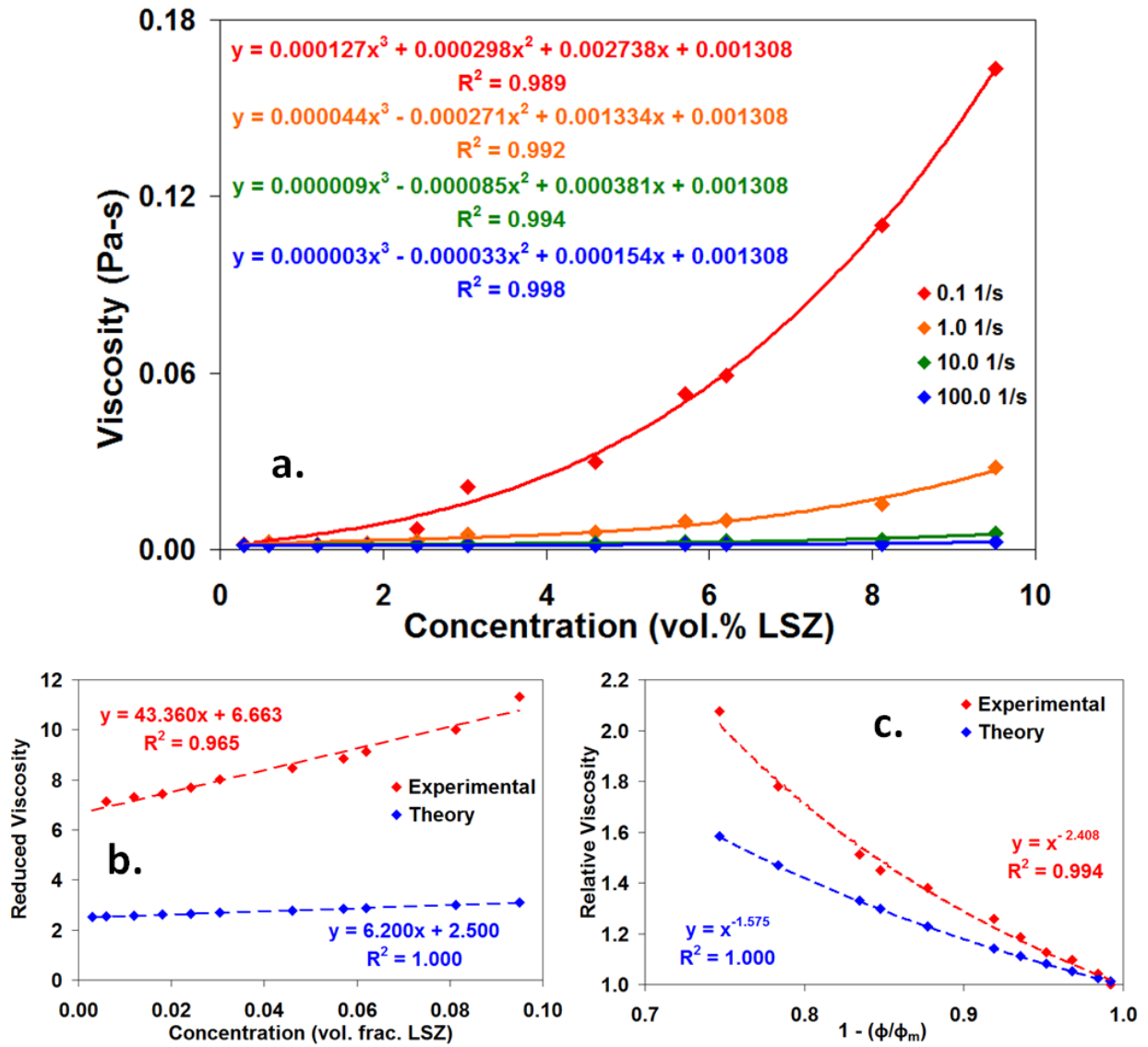


**Figure 46.** a.) LSZ solution viscosity as a function of LSZ concentration for shear rates of  $0.1 \text{ s}^{-1}$ ,  $1.0 \text{ s}^{-1}$ ,  $10.0 \text{ s}^{-1}$ , and  $100.0 \text{ s}^{-1}$ . Third-order polynomial fits are used to create the equations for LSZ viscosity contribution and are shown with the corresponding statistical  $R^2$  values, b.) reduced viscosity as a function of LSZ concentration (red) with a linear fit showing deviation from the Batchelor expansion of the Einstein equation (blue), and c.) relative viscosity versus  $1 - \phi/\phi_m$  (red) with a power law fit showing deviation from the Krieger-Dougherty equation (blue).

By manipulating Equation 4.4 to show reduced viscosity – subtracting one and dividing by  $\phi$  – it is possible to see that the slope of the reduced viscosity versus concentration curve should be 6.2, however, this slope for LSZ solutions is 40.5, as shown in Figure 46b. The higher slope for the reduced viscosity versus concentration curve is an indication of the non-spherical nature of LSZ, which is validated by x-ray diffraction data showing a globular structure with two main axes with slightly different lengths: 3.08 nm and 2.95 nm.<sup>39</sup> Furthermore, hard-sphere rheology theory would dictate that for high-shear relative viscosity versus concentration the curve would follow the Krieger-Dougherty equation shown in Equation 4.5 and Figure 46c with an intrinsic viscosity of approximately 2.5 where  $\phi_m$  is the maximum packing volume of hard spheres, which is approximately 0.63.<sup>98</sup>

$$\eta = \eta_s \left(1 - \frac{\phi}{\phi_m}\right)^{-[\eta]\phi_m} \quad (4.5)$$

For LSZ solutions to fit Equation 4.5,  $\phi_m$  must be set to 0.37 which is significantly lower than the 0.63 for hard spheres. The lower packing volume is also an indication of the ellipsoidal or globular nature of LSZ. Furthermore, after fitting of the Krieger-Dougherty equation, the intrinsic viscosity is determined to be 6.56 for LSZ which is approximately 2.6 times greater than that of hard spheres; another indication that LSZ is not purely spherical but elongated on one axis. LSZ solutions clearly do not follow hard-sphere rheology in which the only interactions between particles were rigid repulsions that would occur only when particles come into contact. Therefore it should be noted that for LSZ-SWNT rheology, the cylinder-sphere phase behavior theory was used as a starting point for the determination of what could happen in the system.

## 4.2. LYSOZYME – CARBON NANOTUBE INTERACTION

Aqueous dispersions of LSZ and SWNT are only possible because the LSZ and SWNT interact with one another on a molecular level to produce a kinetically stable dispersion. The

interaction between LSZ and SWNT was probed using a combination of methods including TEM, SEM, UV-vis, Raman spectroscopy, CD, and fluorescence spectroscopy and anisotropy.

There are two common approaches to immobilizing proteins on SWNT: covalent and non-covalent. Several researchers have used EDC/NHS chemistry to covalently attach enzymes such as LSZ,<sup>141-142</sup> horseradish peroxidase,<sup>44</sup> and organophosphate hydrolase<sup>7</sup> to SWNT. However, covalent attachment of proteins to CNT has the disadvantages of increasing processing time and cost. In addition, covalent functionalization disrupts the intrinsic sp<sup>2</sup> bond structure that is responsible for the unique properties of SWNT. Therefore, understanding the non-covalent interactions between proteins and pristine SWNT is important for producing materials that combine protein function with the intrinsic properties of pristine SWNT. However, while there have been several studies on LSZ-SWNT dispersions, the details of the interaction are not well understood. It has been hypothesized that the size of SWNT facilitated SWNT fitting into LSZ's hydrophobic pocket and that the primary interaction was therefore  $\pi$ - $\pi$  stacking between hydrophobic residues.<sup>143</sup> Other research has echoed this hypothesis and further suggested that partial unfolding during sonication facilitated dispersion.<sup>51, 144</sup> In this section evidence is provided of the importance of hydrophobic interactions and  $\pi$ - $\pi$  stacking, and that the binding mechanism is between tryptophan (aromatic amino acid residue) and the aromatic SWNT sidewall.<sup>9</sup> LSZ contains three hydrophobic residues within its core: methionine, phenylalanine, and tryptophan. Of these three amino acids, it is less likely that methionine interacts with the SWNT sidewall since it does not possess any aromatic rings to enable  $\pi$ - $\pi$  stacking with SWNT. Phenylalanine and tryptophan both possess aromatic rings, but phenylalanine's benzene group is less likely to interact than tryptophan's aromatic indole group due to its larger size and higher electrostatic potential.<sup>145</sup>

The close association between LSZ and SWNT was visualized using TEM and SEM. TEM imaging of LSZ SWNT dispersions show a thin polymer boundary surrounding SWNT bundles, as show in Figure 47. The disparity in transparency between the outer boundary and the encapsulated material clarify that the outer material is much more susceptible to electron transmission, as is the case with biological polymers such as LSZ.

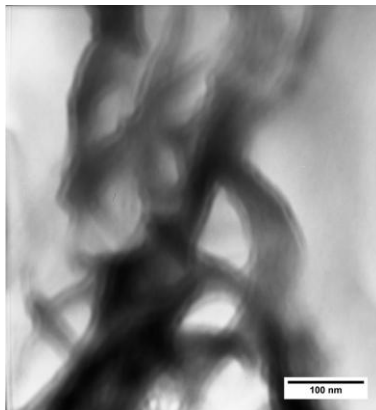


**Figure 47.** TEM micrograph at 160,000x of 0.30 vol.% LSZ – 0.07 vol.% SWNT dispersion showing an interaction between LSZ and SWNT with SWNT bundle sizes of approximately 25 nm to 50 nm.

Although SEM is primarily intended for scanning the surface of molecules, a certain amount of transmission occurs. The ability of electrons to scan a surface versus transmit through the surface is dependent upon the electronic conductivity of the molecules being imaged. If the material is highly conductive, then the electrons will scan the surface giving a high resolution, opaque image. If the material is not conductive the electrons can transmit through the material giving a low resolution, partially translucent image. Since the SWNT are significantly more electrically conductive than LSZ, SWNT appear opaque under SEM while LSZ appears translucent. As shown in Figure 48, small SWNT bundles are intimately surrounded by LSZ; no other materials

were present in the sample. In addition, as the electrical energy from the electrons was transferred to the LSZ in the form of thermal energy, the LSZ began to swell. This is a common effect in SEM of proteins and biological polymers. Figure 48(a) was taken last sequentially, and it can be seen by comparison with Figure 48(b) and 48(c) that the empty spaces between the coated SWNT have been filled in by the swelling of the bound LSZ. Further evidence of this effect is shown by the size ratio of LSZ to SWNT increasing by approximately three-fold from Figure 48(b) to 48(d). The exact bundle size cannot be determined from this image due to the limits of resolution, but previous studies have shown that dispersions prepared by the same method dispersed SWNT as individuals and small bundles.<sup>8</sup> Since drying can affect both morphology and the specificity of interaction, additional methods were used to confirm the nature of the SWNT-LSZ interaction.

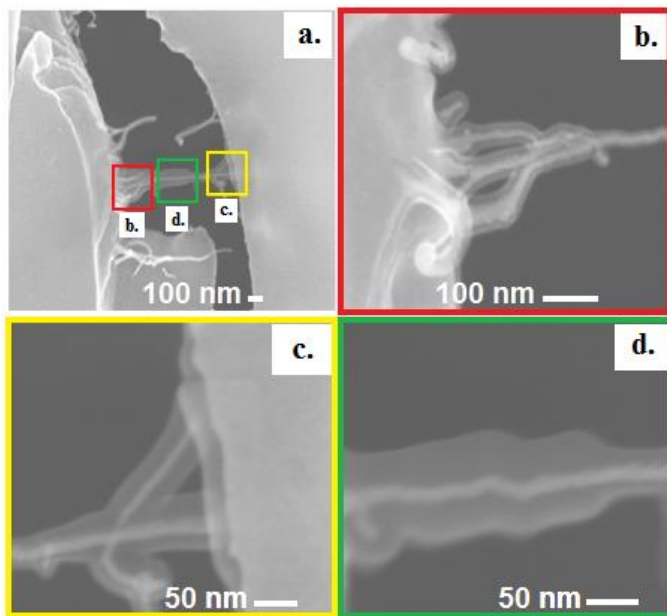


**Figure 48.** Scanning electron micrograph of a dried 0.30 vol.% LSZ – 0.07 vol.% SWNT aqueous supernatant illustrating the direct interaction between SWNT (opaque) and LSZ (translucent) along with swelling of biopolymer LSZ layer; (a) 50,000x, (b) 200,000x, (c) 300,000x, and (d) 400,000x.

Immobilization of LSZ on SWNT was also evidenced by attenuated total reflectance Fourier transform Infrared Spectroscopy (ATR-FTIR) and Raman spectroscopy. Figure 49 shows the ATR-FTIR spectra of dried samples of SWNT, LSZ, the aqueous LSZ-SWNT mixture prior to centrifugation, and the resulting LSZ-SWNT supernatant. The LSZ, LSZ-SWNT mixture and resulting supernatant show the characteristic amide I ( $\sim 1650\text{ cm}^{-1}$ ) and amide II ( $\sim 1535\text{ cm}^{-1}$ ) peaks characteristic of proteins and enzymes. In addition, the LSZ-SWNT mixture and supernatant overlay the LSZ peak at  $\sim 3300\text{ cm}^{-1}$  which is the overtone to the amide I peak and is characteristic of amino radicals present in each sample.

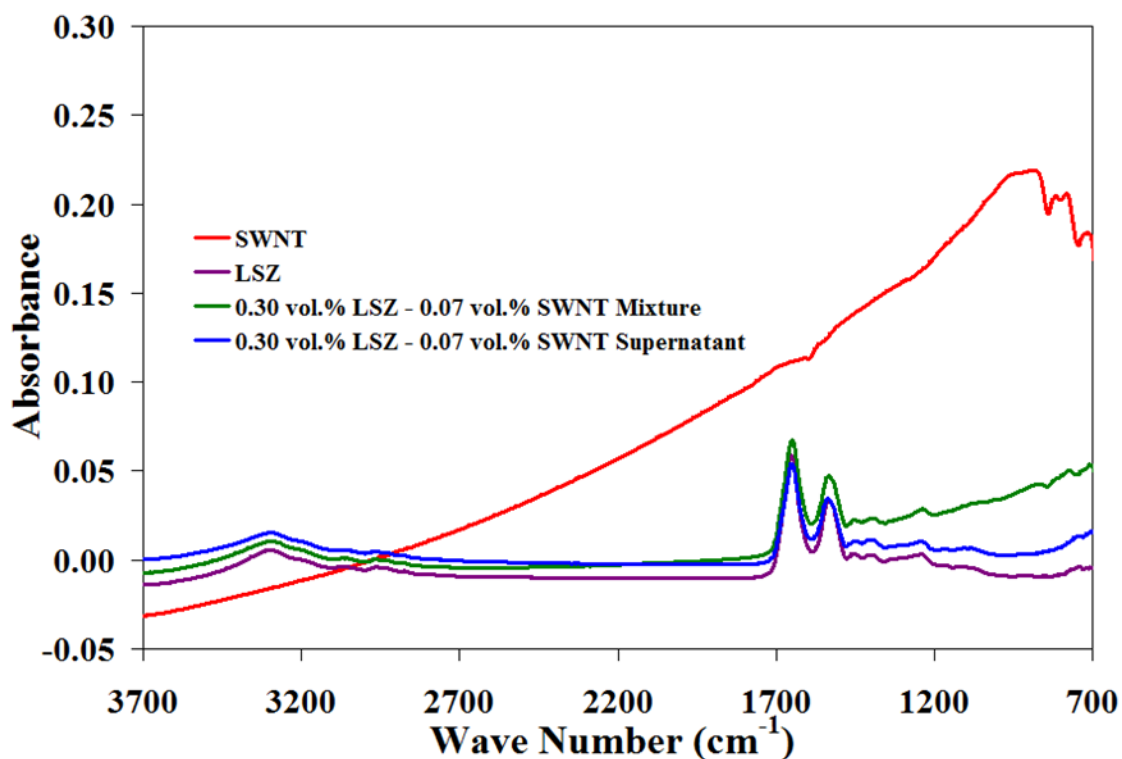


**Figure 49.** ATR-FTIR spectrum of SWNT, LSZ, 0.5 wt.% LSZ – 0.1 wt.% SWNT mixture and the resulting supernatant. The LSZ and LSZ-SWNT dispersions show the amide I and II peaks as well as the characteristic amino radical peak characteristic of LSZ confirming adsorption of LSZ to SWNT.

Furthermore, the LSZ-SWNT mixture and supernatant show increasing absorbance from  $\sim 1500\text{cm}^{-1}$  to  $\sim 700\text{cm}^{-1}$  similar to that seen in pristine SWNT. This result clearly indicates that SWNT were stabilized in solution by the presence of LSZ, and thus carried over into the dry sample, in agreement with previous work.<sup>8, 51, 134, 146</sup> The data also shows that a portion of SWNT was lost during centrifugation, but the relative increase between  $1200\text{cm}^{-1}$  and  $700\text{cm}^{-1}$  in the supernatant (compared to the pure LSZ) shows that LSZ-stabilized SWNT are still present in the supernatant. Interestingly, the peak ( $1000$  to  $900\text{cm}^{-1}$ ) in the SWNT IR absorption band is red-shifted in the dispersed SWNT, where there is a constant increase through  $700\text{cm}^{-1}$ . This is an effect of the aqueous dispersion of LSZ since the dispersed SWNT spectrum is distinctly different from the spectra of non-interacting, dry mixed LSZ and SWNT (see supporting information). This ATR-FTIR data thus supports that there is an interaction between LSZ and SWNT, and this interaction is further interrogated below using other spectroscopic methods.

Figure 50 shows the Raman spectra ( $514$  &  $785\text{nm}$  excitation), of the LSZ-SWNT mixture and supernatant as well as the initial SWNT material. Several facets of these spectra support the existence of noncovalent functionalization of individual SWNT with LSZ. The spectra show characteristic radial breathing modes (RBM) from  $100\text{cm}^{-1}$  to  $400\text{cm}^{-1}$ , the D peak due to  $\text{sp}^3$  hybridized carbons at  $\sim 1335\text{cm}^{-1}$ , the G peak due to tangential  $\text{sp}^2$  hybridized carbons at  $\sim 1589\text{cm}^{-1}$ , and the G' peak at  $\sim 2645\text{cm}^{-1}$  which is the second overtone of the D peak. It has been previously reported that LSZ preferentially adsorbs to larger diameter nanotubes.<sup>144, 147</sup> The inset of Figure 50(a) & (b) shows the RBM peaks. All obvious RBM peaks present for SWNT used in the dispersions are present in both the mixture and supernatant with similar relative intensities. This suggests that in this work there was no significant fractionation based on diameter. The D/G ratios vary only slightly between SWNT (0.13), LSZ-SWNT mixture (0.14),

and LSZ-SWNT supernatant (0.16). This indicates that the immobilization is through a noncovalent interaction; covalent functionalization would significantly increase the D:G ratios. The noncovalent interaction is further evidenced by the linearity of the data of  $I_D/I_{RBM}$  vs.  $I_D/I_G$  of each excitation laser (see supplementary information).<sup>148</sup> As shown in Figure 50(b), the LSZ-SWNT supernatant Raman spectra shows significant luminescence interference from  $600\text{ cm}^{-1}$  to  $3200\text{ cm}^{-1}$ . The observation of luminescence is associated with individual, non-covalently functionalized SWNT. As the concentration of individual SWNT increases within a dispersion, the luminescence intensity increases dramatically and the Raman scattering signal will essentially be buried under the luminescence.<sup>149-151</sup> Therefore, the Raman spectra of LSZ-SWNT supernatant at  $785\text{ nm}$  excitation further validates the non-covalent functionalization of SWNT dispersed as individuals by LSZ.

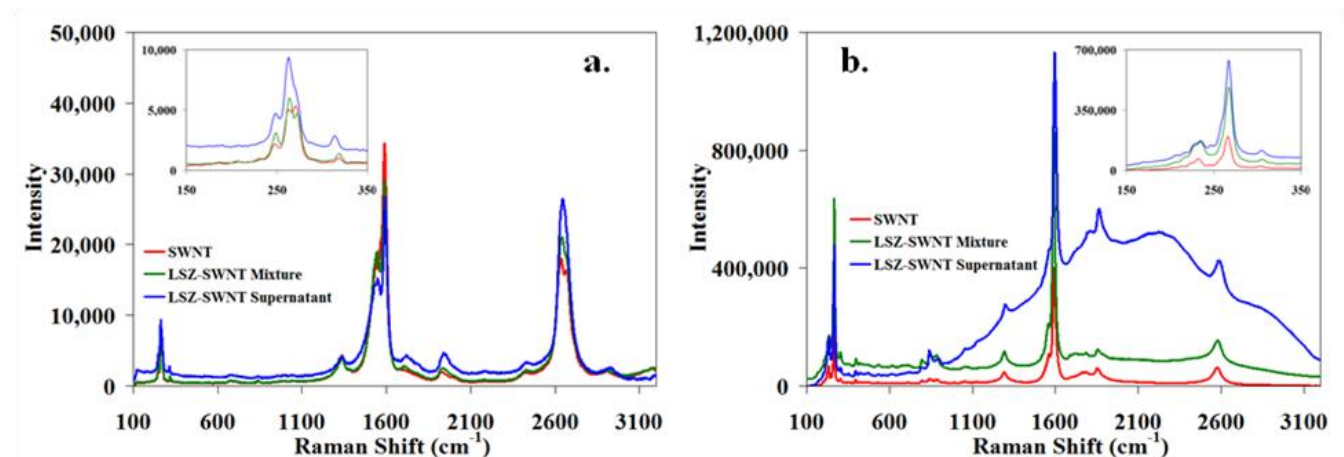


**Figure 50.** Raman spectra with a)  $514\text{ nm}$  and b)  $785\text{ nm}$  excitation of SWNT, the LSZ-SWNT mixture, and the resulting supernatant. The full spectra show the RBM, D-, G-, and G'-peaks characteristic of stretching modes within SWNT; the inset highlights the RBM peaks.

Several features of the Raman spectra are indicative of charge transfer between the LSZ and SWNT via non-covalent bonding.<sup>23, 152-154</sup> Another interesting facet of the Raman spectra is the

suggestion of charge transfer between the LSZ and SWNT in both the mixture and supernatant. Both the  $G^{153-154}$  and  $G'^{23, 152}$  peaks have been used to elucidate doping effects. While luminescence prevents accurate determination of differences in peak location and intensity using 785 nm excitation, the spectra using 514 nm supports charge transfer (see Table 1). Compared to the pristine SWNT, the mixture and supernatant show an upshift in the  $G'$ -peak, from  $2636\text{ cm}^{-1}$  to  $2654$  and  $2645\text{ cm}^{-1}$  respectively. In contrast, the  $G/G'$  ratio for the pristine SWNT was 1.9 but only 1.4 for the mixture and 1.0 for the supernatant which indicates doping.<sup>152</sup> No G-band shift was observed between the SWNT LSZ-SWNT mixture, but there was a  $5\text{ cm}^{-1}$  shift between the pristine SWNT and LSZ-SWNT supernatant. These results are in contrast to those of Xie et al. who found that the frequency of  $G'$  did not shift and who stated that no charge transfer is expected due to the lack of a metallic center in LSZ.<sup>144</sup> The difference in these charge transfer results are likely due to the different starting materials and processing methods used to produce the respective dispersions

514 nm Laser							
Sample	Raman Shift ( $\text{cm}^{-1}$ )				Intensity Ratios		
	RBM	D	G	$G'$	D/G	$G/G'$	D/RBM
SWNT	263	1338	1589	2636	0.126	1.899	0.861
LSZ-SWNT Mixture	263	1335	1589	2654	0.136	1.374	0.657
LSZ-SWNT Supernatant	263	1333	1594	2645	0.157	1.008	0.449

**Table 1.** Peak positions of RBM, D, G, and  $G'$  for each dispersion tested along with the D/G,  $G/G'$ , and D/RBM ratios from the Raman spectra of 514 nm excitation laser. The shifts in G and  $G'$ , and the decrease of  $G/G'$  are indicative of charge transfer between the LSZ and SWNT.

In an attempt to increase the adsorption of LSZ to SWNT through hydrogen bond interactions between hydroxyl and amine or carboxyl groups, SWNT were functionalized via acid oxidation to introduce carboxyl and hydroxyl groups and increase SWNT hydrophilicity. It

is well established that the introduction of carboxyl, hydroxyl and other hydrophilic groups as a result of oxidation significantly increases SWNT dispersibility in water.<sup>155-157</sup> Counterintuitively, the dispersibility of SWNT-Ox with LSZ was much poorer than for pristine SWNT. In fact, the SWNT-Ox supernatant was virtually clear whereas the pristine SWNT supernatant was characteristically black. Comparing the relative changes in absorbance for the initial mixtures and supernatants elucidated the marked difference between SWNT-Ox and pristine SWNT dispersed with LSZ. The ratio of  $[\text{SWNT-Ox}]_{\text{supernatant}}:[\text{SWNT-Ox}]_{\text{mixture}}$  was 23% and the ratio  $[\text{SWNT}]_{\text{supernatant}}:[\text{SWNT}]_{\text{mixture}}$  was 34% at 506 nm. Assuming no significant change in the extinction coefficients for SWNT-Ox and SWNT in aqueous LSZ, the supernatant concentration of SWNT-Ox was 27.0 mg/L compared to 108.0 mg/L for pristine SWNT. The possibility that the reduced dispersibility of the SWNT-Ox was due to isoelectric effects was explored based on Nepal and Geckler's finding that the dispersion limit of individual SWNT in aqueous LSZ was pH-dependent.<sup>143</sup> For the SWNT used in their work, the dispersion limit was nearly constant at 89 mg/L for  $1.4 < \text{pH} < 8.2$  using similar centrifugation conditions of 3 hours at 18,000 g. Near the isoelectric point,  $\text{pH} = 10.2$ , virtually no SWNTs could be dispersed. However, SWNT dispersibility increased again above the isoelectric point. The SWNT mixtures and supernatants in the present work had very similar pH values of 5.3 and 5.6 respectively. For SWNT-Ox, the mixtures and supernatants had pH values of 7.4 and 7.2 respectively. Buffering the SWNT-Ox mixture with 66mM  $\text{KH}_2\text{PO}_4$  to obtain a pH of 5.2, similar to the pristine SWNT, resulted in a supernatant with pH of 5.3 but an even lower SWNT-Ox concentration of 19.0 mg/L, which is contrary to the expectations. Therefore, electrostatic effects are not the primary reason for SWNT-Ox having a lower supernatant concentration than pristine SWNT. Most likely, the reduced dispersibility was due to SWNT-Ox's reduced potential for hydrophobic interaction with

LSZ. This indicates that the hydrophobic interaction between LSZ and SWNT is more important to dispersion stabilization than favorable hydrophilic interactions with water.

UV-vis of the supernatants of LSZ-SWNT dispersions show the characteristic, sharp van Hove singularities which are indicative of the presence of individual or small bundle SWNT, as shown in Figure 51. van Hove singularities are discontinuities in the one-dimensional electronic structure of SWNT. The discontinuities arise from overlapping electronic transitions in the repeating structure of SWNT. Since UV-vis probes the electronic structure of materials, the van Hove singularities are easily seen as peaks in the absorbance between wavelengths of approximately 450 nm and 800 nm. The van Hove singularities can also be used to qualitatively describe the dispersion state of SWNT. Large, jagged peaks occur when SWNT are dispersed as individuals or small bundles, whereas small, broad peaks occur due to absorbance quenching when SWNT are dispersed as large, aggregated bundles. Previous investigations further confirmed individual dispersion using AFM and ellipsometry.<sup>158</sup>

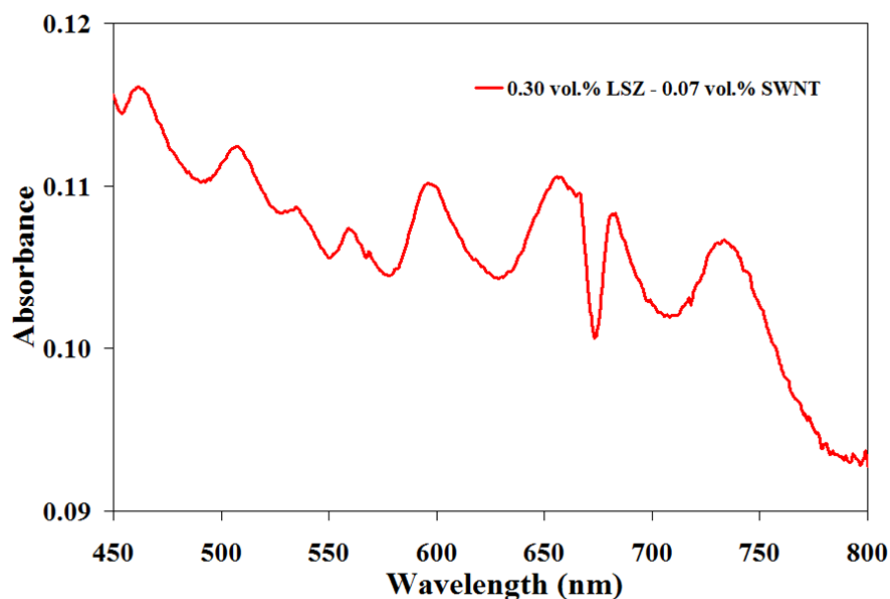


**Figure 51.** UV-vis absorbance spectrum of 0.30 vol.% LSZ – 0.07 vol.% SWNT supernatant showing van Hove singularity peaks characteristic of individually dispersed SWNT.

Comparing aqueous LSZ solutions and LSZ-SWNT dispersions of equal LSZ concentrations show changes in the LSZ spectral profile in the presence of SWNT. As apparent from the black color of the dispersions, SWNT-dependent increases in absorbance at all wavelengths were significant and could overshadow changes in the LSZ spectrum. Therefore, difference spectra, shown in Figure 52, were obtained by subtracting the absorbance spectrum of the 0.30 vol.% LSZ solution without SWNT. This enabled changes in the LSZ spectrum resulting from the LSZ-SWNT interaction to be extracted. At 280 nm, the wavelength where tryptophan absorbs,<sup>159</sup> the data show an increased absorbance of approximately 0.09 for the LSZ-SWNT supernatant and approximately 0.31 for the LSZ-SWNT mixture. In addition, a hyperchromic shift was observed which was likely due to two phenomena. First, the partial unfolding of LSZ during sonication could cause the shift.<sup>51</sup> When LSZ intercalates between and partially envelops SWNT, the environment surrounding the hydrophobic core of the protein is altered. More specifically, the tryptophan chromophore in the hydrophobic core is no longer buried within the LSZ core. The emergence of the chromophore from the hydrophobic core could increase the absorbance of light at 280 nm. Second,  $\pi$ - $\pi$  stacking of an aromatic ring with the sidewall of SWNT can change the electronic structure of the chromophore. Consequently, an increase in absorbance intensity of the chromophore at a given wavelength could also be due to the overlap of p-orbitals excited by UV-light.<sup>160</sup>

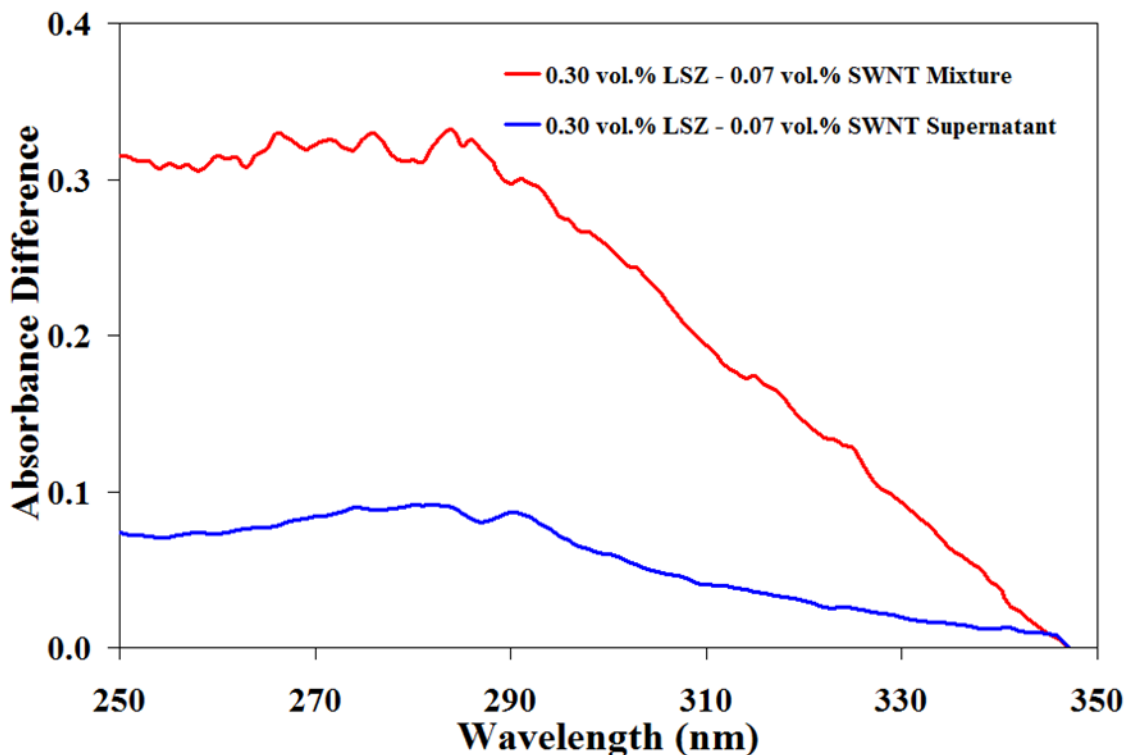


**Figure 52.** UV-vis absorbance difference spectra of 0.30 vol.% LSZ – 0.07 vol.% SWNT mixture and 0.30 vol.% LSZ – 0.07 vol.% SWNT supernatant. The absorbance difference intensities have been down shifted to the LSZ solution (zero) beginning at 348 nm to highlight the hyperchromic shift due to the adsorption of LSZ to SWNT.

Of the three amino acids showing Cotton effects between 250 nm and 350 nm in CD spectra (tryptophan, tyrosine, and phenylalanine), tryptophan is twice as abundant in LSZ and absorbs about four-fold more light at 280 nm compared to tyrosine; phenylalanine is also less abundant and has negligible absorbance at 280 nm.<sup>161</sup> This allows CD to be used for relatively selective examination of the interaction between tryptophan and the sidewall of SWNT. Specifically, CD was used to show that the addition of SWNT causes a definitive change in the optical polarity of LSZ. The supernatant of LSZ-SWNT dispersion was used to compare the CD

spectra to enhance the spectral changes due to binding which could be masked by excess LSZ present in the mixtures. Due to its electronic structure and chirality, the tryptophan within LSZ will naturally absorb more left polarized light than right leading to a slight increase between 280 nm and 300 nm wavelengths.<sup>161</sup> As shown in Figure 53, even after sonication and centrifugation, the aqueous LSZ solutions show a tryptophan peak between wavelengths of 280 nm and 300 nm; this is consistent with literature values for LSZ.<sup>162</sup> However, the addition of SWNT quenches the optical polarity at these wavelengths by approximately 23% in the supernatant. The change in structure observed in the CD spectrum upon interaction with SWNT is believed to be due to the electronic structure and hydrophobic core environment of LSZ, specifically tryptophan, being altered as a result of the a hydrophobic,  $\pi$ - $\pi$  stacking interaction between the LSZ and SWNT.

The final methods used to elucidate the specific interaction between LSZ and SWNT were fluorescence spectroscopy and anisotropy. The dominant fluorophore within LSZ is tryptophan which has an excitation of 280 nm. Tryptophan's maximum emission wavelength is highly sensitive to the polarity of the surrounding environment, but is generally around 335 nm. In addition to effects of solvent polarity on the fluorescence of tryptophan, binding can cause two changes: shifts in the emission maximum wavelength and in fluorescence intensity.<sup>163-164</sup> Horsely et al.<sup>30b</sup> were able to determine the quenching constant for bound LSZ by probing the tryptophan excitation and showed that it increased when bound to variously charged silica surfaces. Therefore, it would be expected that the tryptophan emission fluorescence intensity would decrease, or quench, in LSZ-SWNT dispersions if the tryptophan residue was bound to SWNT.

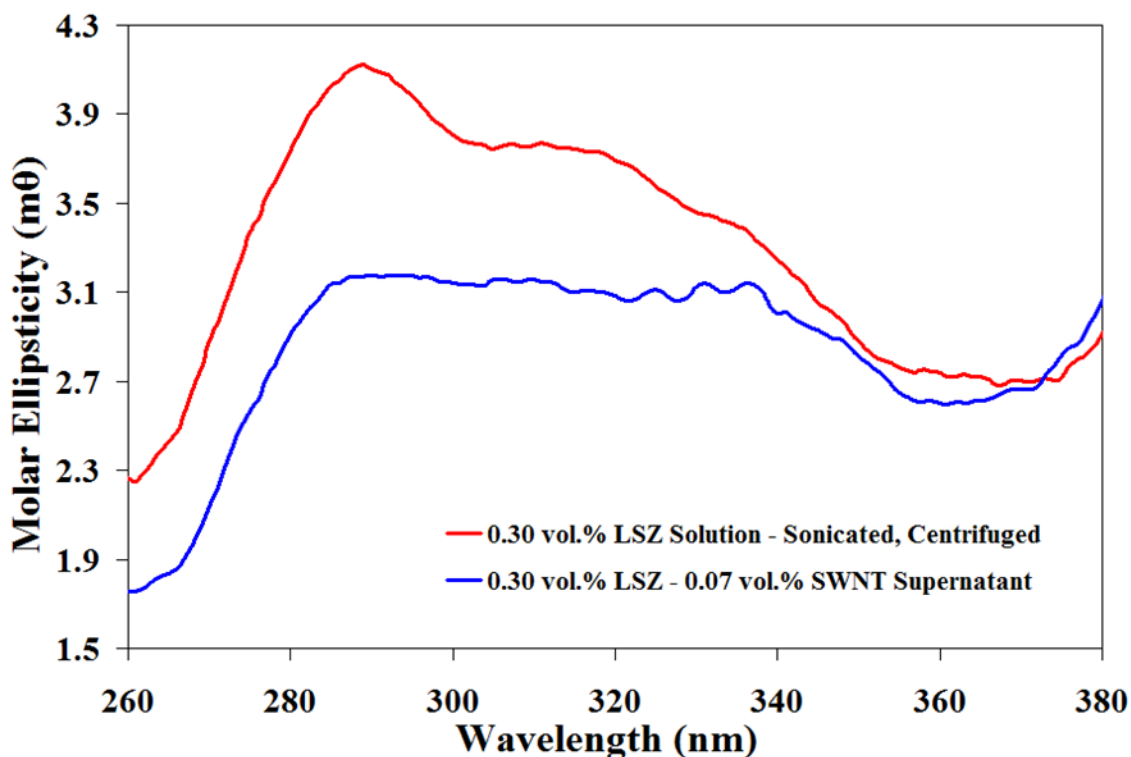


**Figure 53.** Circular dichroism spectrum of 0.5 wt.% LSZ solution and 0.5 wt.% LSZ – 0.1 wt.% SWNT supernatant which shows the loss of the tryptophan peak between wavelengths of 280 nm and 300 nm due to the interaction between the LSZ tryptophan and the sidewall of SWNT. The molar ellipticity of the LSZ solution has been upshifted to that of the LSZ-SWNT supernatant for clarity.

The LSZ and LSZ-SWNT supernatant were excited at 280 nm to specifically probe the tryptophan fluorescence within LSZ for proof of LSZ interaction with SWNT and specific interaction of tryptophan with SWNT. Since the absorption of excitation light at 280 nm by SWNT could result in false interpretation of fluorescence quenching, the extinction coefficients of both LSZ and SWNT were determined through differential absorbance at varying dilution factors (see supporting information) and used to obtain a corrected LSZ-SWNT supernatant

emission spectrum. Figure 54 shows the fluorescence emission spectrum of the LSZ solution and the corrected spectrum of the LSZ-SWNT supernatant dispersion. Even after sonication, the fact that the tryptophan fluorescence within the LSZ-SWNT dispersion is still quenched by approximately 13% relative to the processed LSZ solution provides further evidence of tryptophan-SWNT interaction. It is hypothesized that the quenching of the tryptophan fluorescence results from  $\pi$ - $\pi$  stacking interaction which occurs between the tryptophan residue and the sidewall of SWNT.<sup>165</sup> To further illuminate the interaction between LSZ and SWNT, anisotropic fluorescence measurements were performed. Fluorescence anisotropy is concentration independent and ideally suited for measuring binding events, especially the association of proteins with other molecules.<sup>123</sup> Due to changes in rotational freedom, binding of proteins to other molecules increases the dependence of their fluorescence on the polarity of the excitation light. Based on the concentration of LSZ and SWNT present in the sample used for anisotropy measurements, for every individual SWNT present there were approximately 1800 LSZ molecules present. Even if full coverage of each SWNT is assumed, only 400 LSZ molecules bind to SWNT, leaving an excess of 1400 LSZ molecules in solution. Therefore, the change in anisotropy of LSZ bound to SWNT was not very pronounced due to the presence of unbound LSZ. Tracking the fluorescence emission at 345 nm, the anisotropy of LSZ solutions was observed to be 0.160 and that of the LSZ-SWNT supernatant solutions was 0.166, as shown in the inset of Figure 54. Although this difference of 0.006 seems small, the result was consistent over all tests and statistically significant. A t-test of the data collected for each solution revealed  $p < 0.0001$  indicating that the means were distinctly different. In conjunction with the fluorescence quenching, the anisotropy increase shows a direct, binding interaction between LSZ

and SWNT that was shown through emission quenching to be tryptophan interacting with the SWNT sidewall.

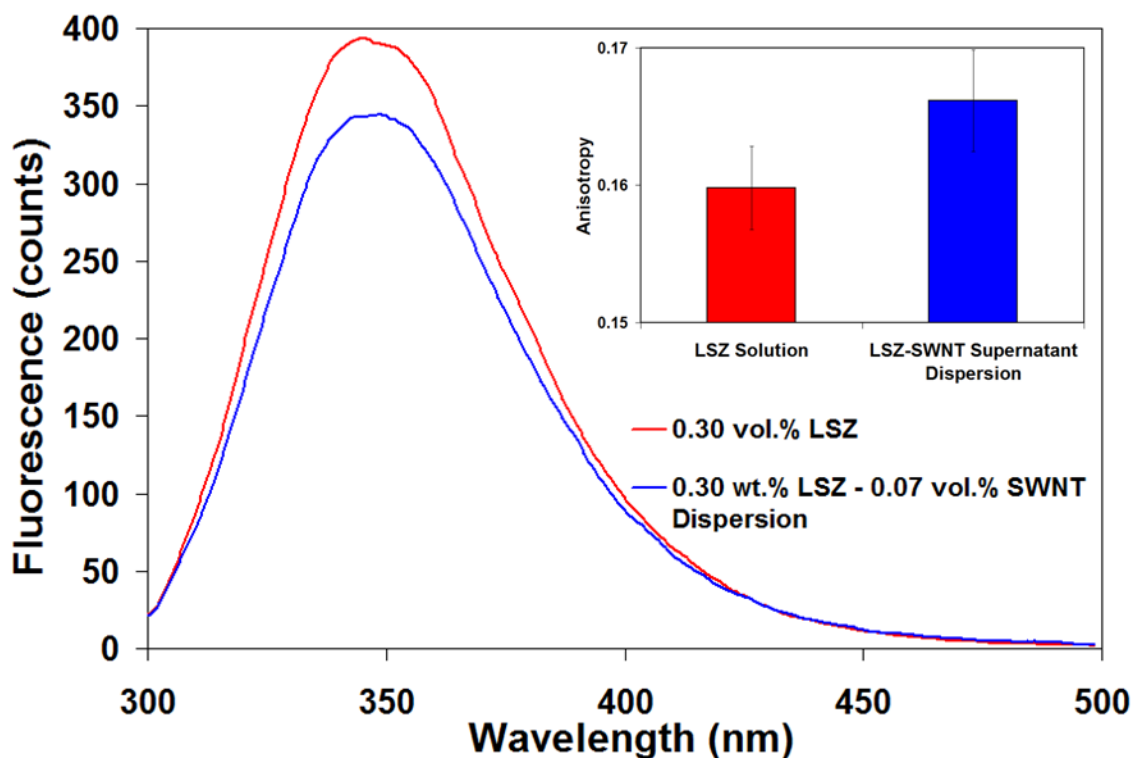


**Figure 54.** UV-vis fluorescence spectra of 0.5 wt.% LSZ solution and 0.5 wt.% LSZ – 0.1 wt.% SWNT supernatant excited at 280 nm showing the quenching of the fluorescence intensity of the LSZ-SWNT supernatant due to the binding of excitation-probed tryptophan within LSZ with SWNT. The inset shows the results of the anisotropy measurements with error.

For this research it was imperative to be able to determine the dilute and concentrated concentrations. For concentrated samples, TGA can be used to directly determine the concentrations. In order to determine the concentration of LSZ and SWNT in the dilute phase, UV-vis was used. First, bulk mixtures of LSZ-SWNT were analyzed to determine absolute LSZ and SWNT absorbance, at 280 nm and 506 nm respectively, as a function of concentration and a

calibration curve was formed for both SWNT absorbance versus concentration and LSZ absorbance versus concentration as shown in Figure 55 and Figure 56. Second, supernatants of LSZ-SWNT were analyzed to determine the absorption of both LSZ and SWNT. Finally, the supernatant LSZ-SWNT absorption at both 280 nm and 506 nm was super imposed on the bulk mixture calibration curves to give the actual concentration of LSZ and SWNT in the supernatant. It should be noted that the initial volume for each dispersion was 100 mL. From this analysis it was determined that after centrifugation approximately 92% of the SWNT is centrifuged out, and approximately 49% of the excess LSZ is centrifuged out. Table 2 and Table 3 show the data used in this analysis.

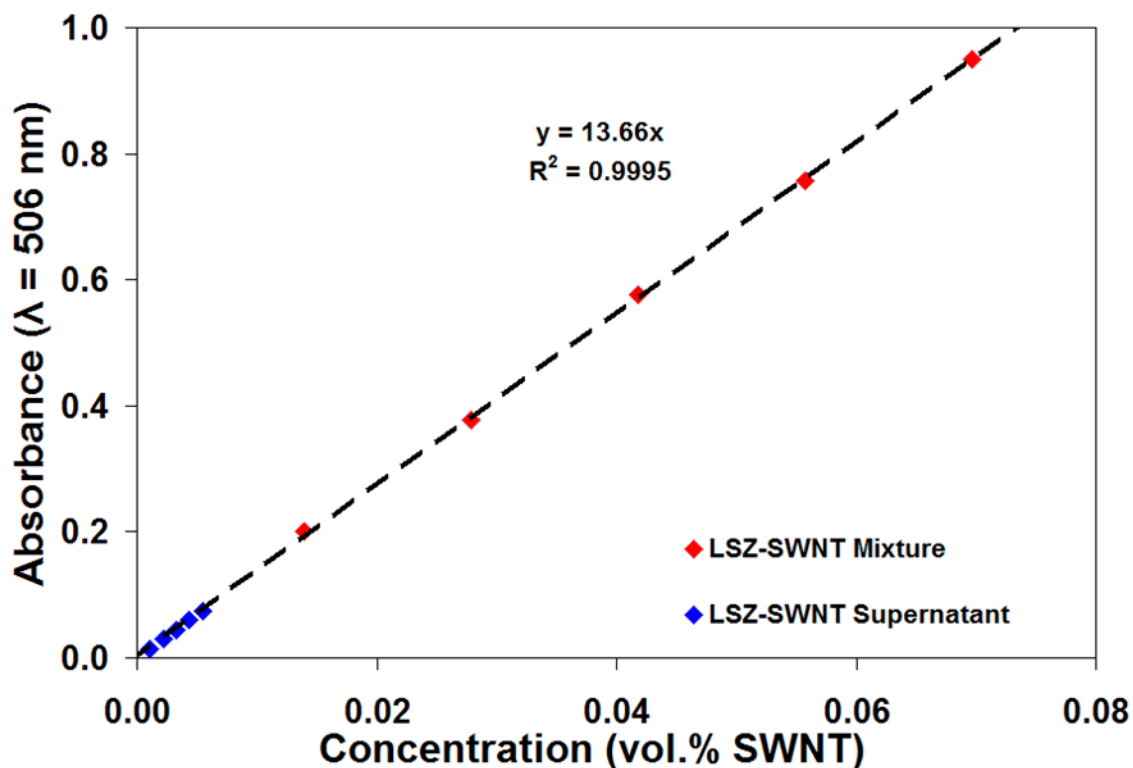


**Figure 55.** SWNT calibration curve for mixture and supernatant showing absorbance at 506 nm versus volumetric concentration of SWNT. As can be seen the supernatant curve super imposed perfectly onto mixture curve. Data for this figure can be seen in Table 2.

	Initial SWNT Concentration (vol. %)	Actual SWNT Concentration (vol. %)	Absorbance ( $\lambda = 506$ nm)
Mixture	0.0697	0.06967	0.9495
	0.0557	0.05573	0.7578
	0.0418	0.04179	0.5770
	0.0279	0.02786	0.3780
	0.0139	0.01393	0.2015
Supernatant	0.0697	0.00545	0.0741
	0.0557	0.00436	0.0602
	0.0418	0.00327	0.0442
	0.0279	0.00218	0.0304
	0.0139	0.00109	0.0143
Mixture Trendline Slope		13.66	
Supernatant Trendline Slope		1.07	
Relative Coefficient		0.08	

**Table 2.** UV-Vis SWNT calibration curve data. Supernatant SWNT concentration determined via superposition of absorption data onto SWNT mixture calibration curve.

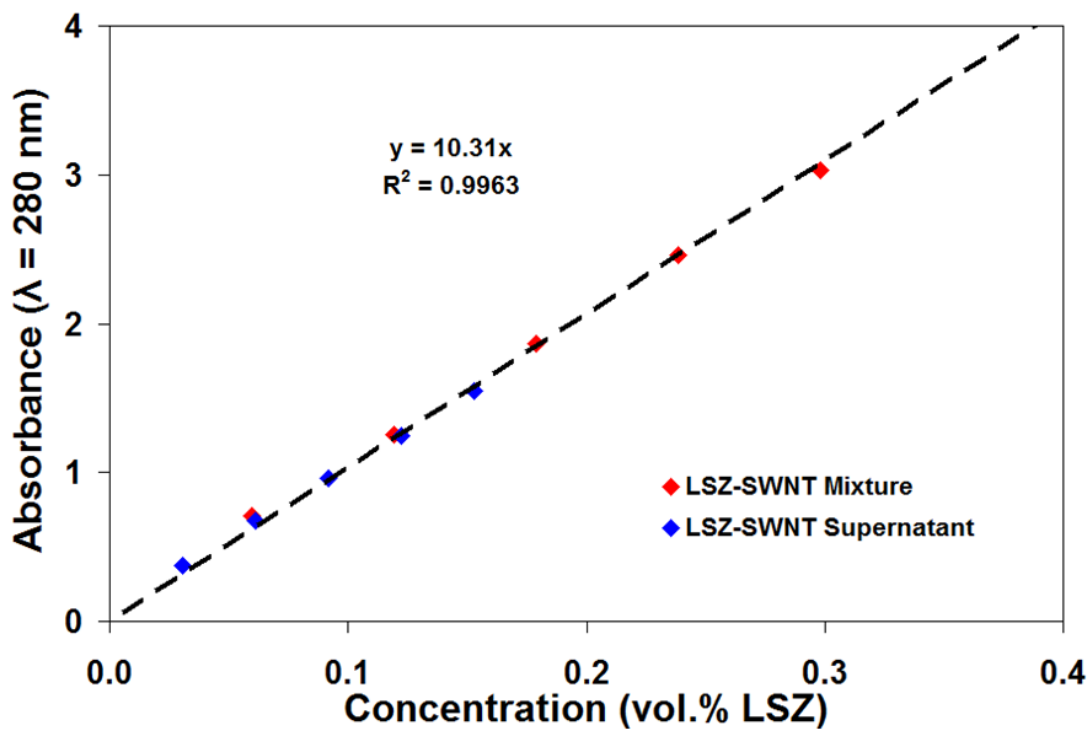


**Figure 56.** LSZ calibration curve for mixture and supernatant showing absorbance at 280 nm versus volumetric concentration of LSZ. The supernatant curve super imposed directly onto mixture curve. Data for this figure can be seen in Table 3.

	<b>Initial LSZ Concentration (vol. %)</b>	<b>Actual LSZ Concentration (vol. %)</b>	<b>Absorbance (<math>\lambda = 280</math> nm)</b>
<b>Mixture</b>	0.2981	0.29813	3.0315
	0.2384	0.23841	2.4607
	0.1787	0.17874	1.8621
	0.1191	0.11911	1.2584
	0.0595	0.05953	0.7121
<b>Supernatant</b>	0.2981	0.15279	1.5465
	0.2384	0.12218	1.2482
	0.1787	0.09160	0.9606
	0.1191	0.06104	0.6728
	0.0595	0.03051	0.3767
<b>Mixture Trendline Slope</b>		10.32	
<b>Supernatant Trendline Slope</b>		5.29	
<b>Relative Coefficient</b>		0.51	

**Table 3.** UV-Vis LSZ calibration curve data. Supernatant LSZ concentration determined via superposition of absorption data onto LSZ mixture calibration curve.

This section has provided additional evidence of the close interaction between LSZ and SWNT and not only supported but refined previously reported hypotheses that the interaction is a hydrophobic one involving  $\pi$ - $\pi$  stacking. The results of this work verify that there is a direct molecular interaction between LSZ and SWNT through the indole moiety of tryptophan and the aromatic sidewall of SWNT. These results shed light on the interactions between LSZ and nanotubes and reveal important information for the molecular design and manipulation of nanomaterials and biopolymers. Furthermore, these results provide a foundation for additional work on elucidating the interactions between pristine carbon materials and other proteins.

#### **4.3. LYSOZYME – CARBON NANOTUBE PHASE BEHAVIOR**

Aqueous solutions of LSZ have been shown to be an effective dispersant of low concentrations of individual SWNT, however, there were no previous studies on the rheological characterization or phase behavior of higher concentration dispersions. This section, describes

the application of optical microscopy and rotational rheology to dilute to concentrated LSZ-SWNT dispersion rheology and phase behavior. It should also be noted that each data set was collected over three separate loadings with three runs per loading for a total of nine runs per test. The LSZ-SWNT dispersions were shown to have a defined phase transition where an increase in the number and size of SWNT aggregates was seen and the elasticity of the dispersions was increased due to the formation of physical LSZ networks. The depletion effect and network formation were further validated by the increase of viscosity with concentration after aggregation of SWNT. Finally, various ratios of LSZ:SWNT supernatant and mixture dispersions were shown to collapse onto a master viscosity curve after accounting for the presence of LSZ. The ability to produce and tailor the unique properties of biomolecule-SWNT dispersions through changes in processing method represents a significant advancement in the future development of functional materials with synergistic properties of biomolecules and SWNT. This was achieved by first understanding, the microstructure and aqueous phase behavior of LSZ-SWNT dispersions. LSZ-dispersed SWNT show unique interactions,<sup>9</sup> and the LSZ activity is maintained throughout fiber and film processing methods; this will be discussed further in later sections. To fully understand the structure-property-processing relationship between initial dispersions of LSZ-SWNT and the final macroscopic assembly properties, rheological characterization of each constituent of the system was completed in addition to the combined dispersion. Previous rheological characterization of LSZ solutions to this point have consisted primarily of interfacial rheology<sup>166-168</sup>, rheology of LSZ within gel<sup>40, 42, 45, 48, 50</sup> or liquid crystalline<sup>52-53</sup> systems, or computational simulation of aqueous LSZ solutions.<sup>169</sup> Rheological characterization of SWNT dispersions has been ever evolving since their discovery to include the understanding of phase behavior for SWNT in superacids,<sup>68, 149, 170</sup> SWNT-polymer systems,<sup>6, 109, 171-173</sup> and even SWNT-

biomolecule dispersions.<sup>3-4, 174-175</sup> Although characterization of SWNT-biomolecule dispersions is available, they primarily consist of SWNT dispersed with other rod-like molecules such as hyaluronic acids or deoxyribonucleic acids which form liquid crystalline systems. Until now, no extensive experimental phase behavior or rheological characterization has been done on spherical biomolecule-dispersed SWNT solutions such as LSZ-SWNT.

In order to fully understand the phase behavior of LSZ-SWNT dispersions, it is first advantageous to understand the phase behavior theory of hard rods with hard spheres, as discussed previously. The phase behavior of any mixed colloidal system is found by minimizing the free energy of mixing. The particles present in LSZ-SWNT dispersions cannot interpenetrate and the interaction energy is constant as long as the particles maintain interaction.<sup>90, 176</sup> Therefore, the phase behavior is determined by maximizing the mixing entropy. For entropically determined ordering, phase transitions or demixing are driven by differences in physical properties, such as shape, which can create bulk or microphase separation.<sup>90</sup> For rod-sphere systems, the physical and thermodynamic origin of this separation can be explained in terms of the depletion interaction between molecules which is entropically driven by the sum of electrostatic and steric repulsive forces, and van der Waals attractive forces.<sup>93-95</sup> When a rod and sphere approach each other, their individual depletion zones will overlap increasing the translational entropy of the system at the expense of the mixing entropy.<sup>177</sup> At low sphere concentration, the mixing entropy dominates and the mixture is miscible. However, with increasing sphere concentration the mixing entropy decreases (due to the rise in translational entropy) and phase separation will occur.<sup>87, 92, 96, 177</sup> Bulk phase separation, which is common to rod-sphere systems, occurs when the rods and spheres completely separate (in the absence of any interaction) forming a rod-rich and sphere-rich phase.<sup>89</sup> Another less common type of separation

seen in rod-sphere systems is that of microphase separation. In microphase separation the system starts demixing into regions which are either rod- or sphere-rich. However, unlike bulk separation, the liquid-like regions grow to a critical size at which point they can form kinetically stable three-dimensional equilibrium structures.<sup>89-90</sup> Although demixing will occur for LSZ-SWNT systems, it is important to note that through variation of parameters such as sphere or rod diameter or concentration it is possible to create other types of phases and phase separation.<sup>87, 89-90</sup> LSZ-SWNT systems will inherently show some deviation from current theory for three primary reasons: 1. the aspect ratio of SWNT is significantly greater than rods typically used in the theoretical simulations,<sup>178</sup> 2. LSZ is not perfectly spherical nor considered a hard sphere,<sup>135, 161, 169</sup> and 3. LSZ and SWNT interact with one another.<sup>9</sup>

The phase behavior of LSZ-SWNT dispersions is complex and highly dependent upon constituent concentrations. LSZ-SWNT dispersions begin as an isotropic liquid and transition to a gel as the concentrations of LSZ and SWNT are increased. The increase in LSZ concentration is what causes the transition to a gel. Depletion of LSZ from between SWNT at a critical concentration creates an increased LSZ concentration surrounding the SWNT bundles or aggregates in a given volume. The increased concentration of LSZ leads to the formation of a physically networked gel structure, which increases elastic behavior.<sup>179</sup>

The aggregation state of the dispersions was first characterized by cross-polarized optical microscopy. The optical phase behavior transitions of LSZ-SWNT, shown in Figure 57, can be seen as the concentration where the number and size of SWNT aggregates increases. It should be noted that the clusters seen should also be flocs which have formed at the secondary energy minimum predicted by DLVO theory, however, the exact thermodynamic nature of the clusters is unknown and will henceforth be referred to as aggregates.

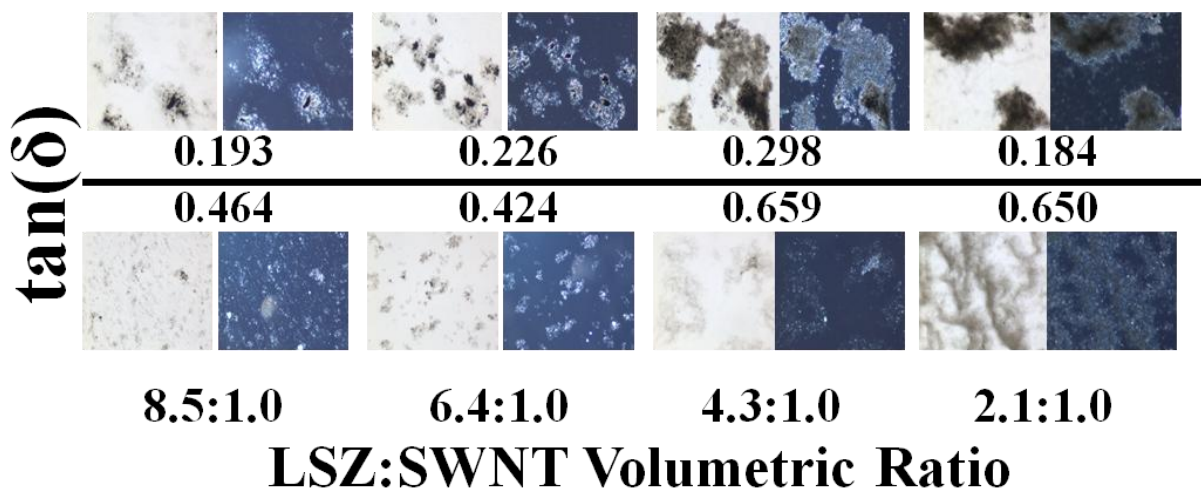


**Figure 57.** Phase transition diagram for LSZ-SWNT showing the LSZ and SWNT concentration at transition. In addition, the rheological parameter  $\tan(\delta)$  shows the increase in elasticity at each ratio across the transition indicating the formation of a physically gelled network.

The increase in aggregation is due to a depletion interaction between the spherical LSZ and cylindrical SWNT, which is similar to the depletion interactions of colloids and polymers. The depletion physically occurs as the concentration of LSZ and SWNT increase in a given volume causing the overlap of independent depletion zones. The LSZ acts as a depletant which causes attractive interactions between the SWNT. Depletion is effective at any concentration of SWNT, however this attractive interaction induces a phase separation of the SWNT only when the LSZ concentration is sufficiently large. The system phase separates between a SWNT rich phase and SWNT dilute phase. The loss of mixing entropy of the SWNT is compensated by the reduction of excluded volume of the LSZ as the SWNT are packed together. This leads to an increase of the translational entropy of LSZ. Here the SWNT rich phase does not reach true thermodynamic equilibrium. Instead this phase is in the form of amorphous aggregates. The system can be viewed as a kinetically arrested microphase separation. On the other hand, at significantly low

concentrations of LSZ, the electrostatic and steric stabilization of SWNT is reduced and the SWNT naturally reaggregate due to the strong van der Waals forces of attraction. As a consequence, there exist an optimum concentration range of LSZ to achieve homogenous dispersions of stabilized SWNT. This phase behavior is quantitatively seen through the rheological parameter  $\tan(\delta)$  as shown in Table 4;  $\tan(\delta)$  is the ratio of the viscous modulus to the elastic modulus and is therefore a measurement of the elasticity of a material. The decrease in  $\tan(\delta)$  across the transition at each volume ratio indicates an increase in the elasticity of the dispersion microstructure. This reflects the presence of a physical network created by the depletion induced aggregates of SWNT. As can be seen from Table 4, the concentration of SWNT at transition was approximately 0.1 vol.% for all ratios. This indicated a possible critical SWNT concentration at 0.1 vol.% SWNT at which the overlapping depletion zones of LSZ and SWNT create an interaction potential great enough to remove the intercalated LSZ and force SWNT reaggregation. Another interesting note from Table 4 is the increase in viscosity from the monophasic to the demixed phase. For dispersions of rigid rods, increasing the concentration up to or past the point of aggregation should cause a decrease in the elasticity and viscosity of the dispersion.<sup>61, 98, 104</sup> The decrease is due to the loss of rigid rod-solvent interactions and homogeneity within the dispersion which would decrease the elasticity and viscosity of the dispersion due to the loss in interfacial surface area of the rigid rods at aggregation leading to more fluid-like character of the dispersions.<sup>61, 98</sup> Therefore, the aggregated state of SWNT in the demixed phase would create a decrease in elasticity and viscosity. However, the creation of the physically networked LSZ after depletion aggregation causes the elasticity and viscosity of the dispersion to increase.

Dispersion (Volumetric Ratio)	Monophasic				Demixed			
	tan( $\delta$ )	Viscosity (Pa-s)	[SWNT] (vol.%)	[LSZ] (vol.%)	tan( $\delta$ )	Viscosity (Pa-s)	[SWNT] (vol.%)	[LSZ] (vol.%)
8.5:1.0 LSZ:SWNT Mixture	0.464	0.464	0.079	0.673	0.193	5.700	0.092	0.782
6.4:1.0 LSZ:SWNT Mixture	0.424	0.424	0.098	0.627	0.226	4.371	0.114	0.730
4.3:1.0 LSZ:SWNT Mixture	0.659	0.659	0.073	0.312	0.298	1.213	0.080	0.342
2.1:1.0 LSZ:SWNT Mixture	0.650	0.650	0.152	0.326	0.184	6.716	0.166	0.355

**Table 4.** Phase behavior transitions showing the increase in elasticity by the change in tan( $\delta$ ), the increase in viscosity, and the LSZ and SWNT concentrations for the monophasic and demixed regimes.

It should be noted that the supernatant, which is in equilibrium with the precipitate of SWNT aggregates, contains a low volume fraction of SWNT. Subsequently, evaporation of the supernatant did not result in any depletion. However, the supernatant should not be viewed as a separately processed dispersion of LSZ-SWNT but rather a LSZ-SWNT dispersion with a lower volume fraction of LSZ and SWNT present, which represents the dilute regime of the LSZ-SWNT phase behavior.

In order to probe the microstructure of LSZ-SWNT amplitude and frequency sweep oscillatory rheology tests were run. Figure 58 shows the storage modulus from an amplitude sweep for increasing concentrations of LSZ-SWNT. As would be expected for a system that transitions from isotropic liquid to gel, the elastic behavior increases as the concentration of SWNT and LSZ are increased. The important information gained from the amplitude sweep is that the critical strain and linear viscoelastic region are consistent among all concentrations tested. The critical strain was determined via graphical analysis to be approximately 2.5% to 3.9%. Another interesting note is that increases in SWNT concentration of approximately 0.5

vol.% can lead to increases in the solid-like response of a liquid of approximately four orders of magnitude.

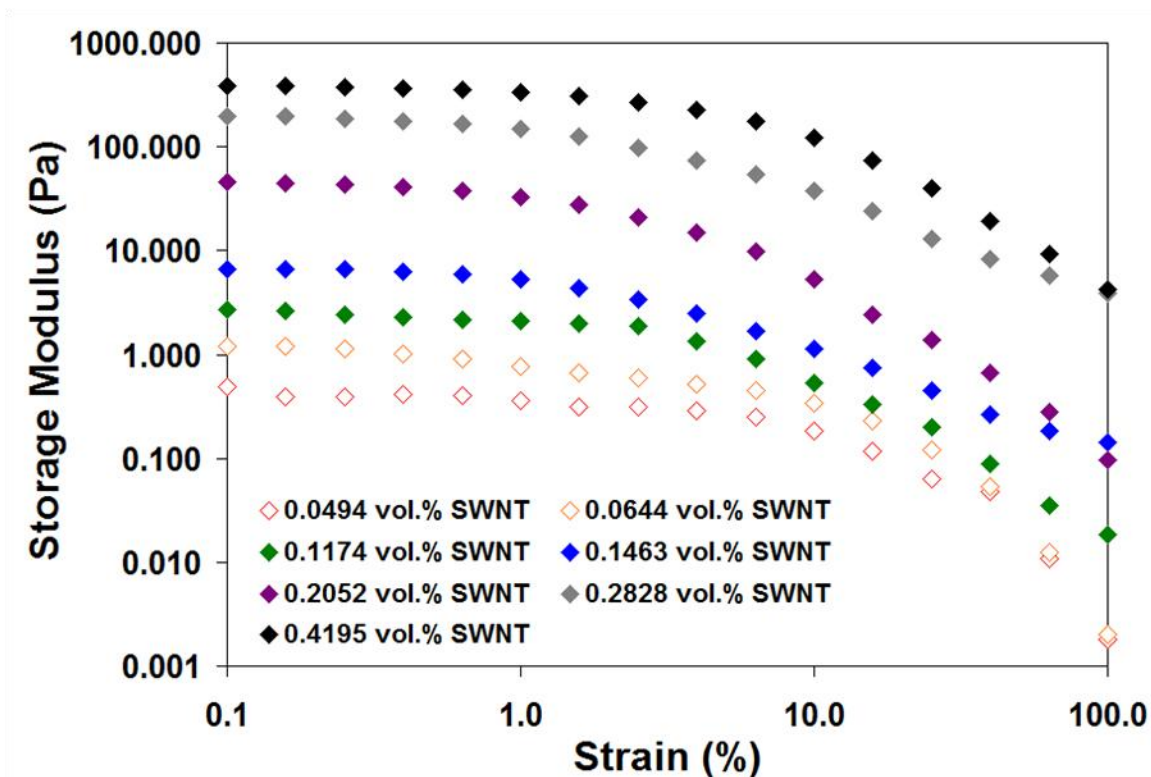


**Figure 58.** Amplitude sweep test data showing storage modulus as a function of amplitude strain for concentrations of 0.0494 vol.% SWNT, 0.0644 vol.% SWNT, 0.1174 vol.% SWNT, 0.1463 vol.% SWNT, 0.2052 vol.% SWNT, 0.2828 vol.% SWNT and 0.4195 vol.% SWNT. Error for each concentration was less than +/- 5%. Open symbols indicate supernatant dispersions.

After determination of the critical strain, the linear viscoelastic oscillatory response of the dispersions was tested to probe the time-dependent behavior of increasing concentrations of LSZ and SWNT. Figure 59 shows the loss and storage moduli for increasing concentrations of LSZ and SWNT. As expected, the elastic behavior increases with increasing concentration showing an important trend that the slope of the storage modulus decreases with increasing concentration.

The slope for 0.0494 vol.% SWNT was approximately 0.5, the slope for 0.2052 vol.% SWNT was approximately 0.1, and the slope for 0.4195 vol.% SWNT was approximately zero. This is an indication that with increasing concentration the elasticity of the dispersion becomes more frequency-independent and in addition the decreasing slope indicates that there was the formation of a percolated network. More specifically in the case of LSZ-SWNT the network was a physically gelled network created by LSZ in addition to the physical percolation of SWNT bundles and aggregates at high concentrations as shown in Figure 57.

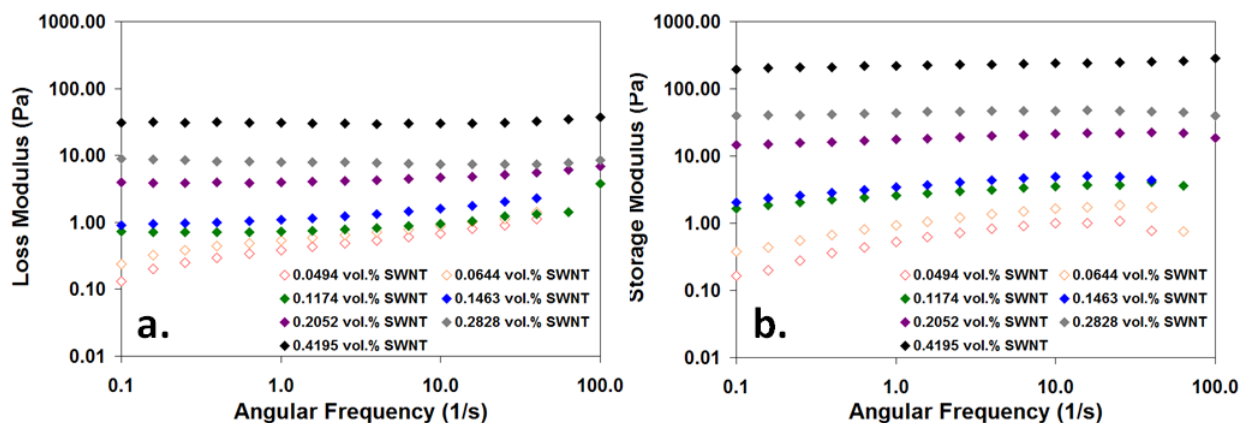


**Figure 59.** Linear viscoelastic oscillatory response showing a.) loss and b.) storage modulus as a function of angular frequency for concentrations of 0.0494 vol.% SWNT, 0.0644 vol.% SWNT, 0.1174 vol.% SWNT, 0.1463 vol.% SWNT, 0.2052 vol.% SWNT, 0.2828 vol.% SWNT and 0.4195 vol.% SWNT. Error for each concentration is less than +/- 5%. Open symbols indicate supernatant dispersions.

Figure 60 shows the storage and loss modulus of 0.0494 vol.% SWNT and 0.1174 vol.% SWNT versus angular frequency to show the crossover point from elastically dominated dispersion to viscous dominated dispersion. The crossover for 0.1174 vol.% SWNT was approximately 0.015

$s^{-1}$  indicating that at frequencies below that the dispersion will have more fluid-like character. However, the crossover for 0.0494 vol.% SWNT was approximately  $0.15 s^{-1}$ .

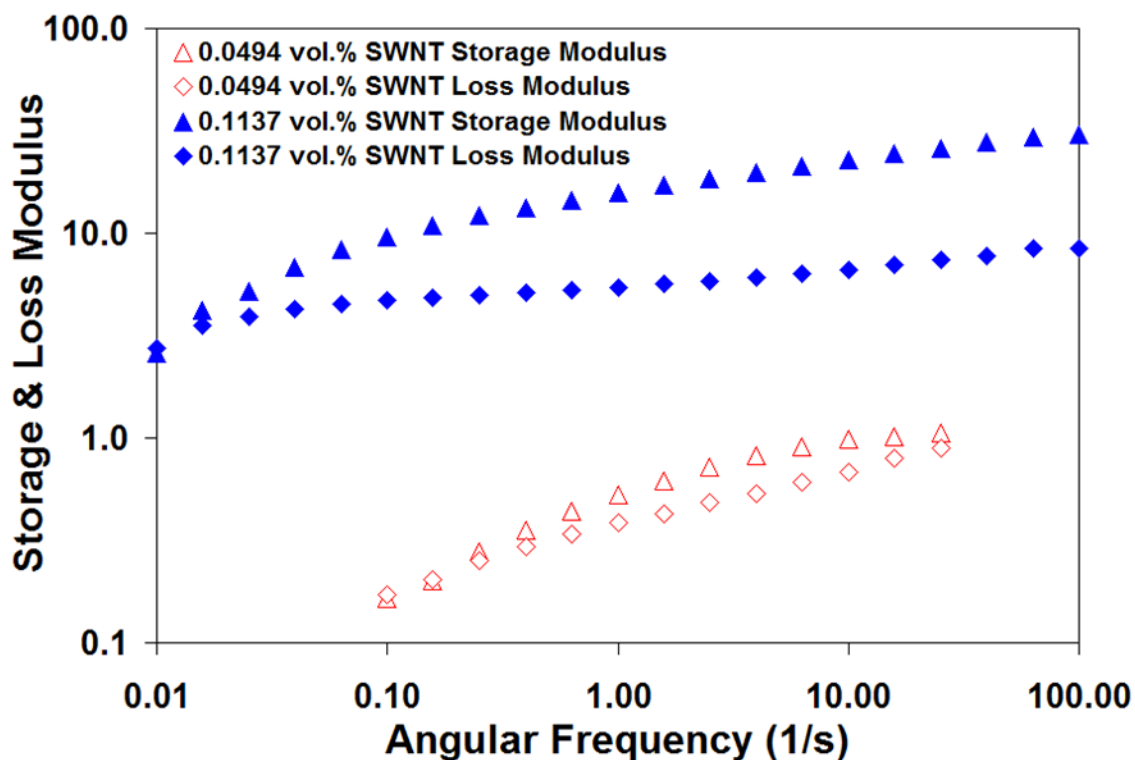


**Figure 60.** Linear viscoelastic response for the storage and loss modulus of 0.0494 vol.% SWNT and 0.1137 vol.% SWNT dispersions as a function of angular frequency showing the crossover point and how that point increases frequency with decreasing SWNT concentration until the fluid character of the dispersion completely dominates the elastic character over all frequencies. Error for each concentration is less than  $\pm 5\%$ . Open symbols indicate supernatant dispersions.

The increase of crossover frequency is indicative that the viscous character of the dispersion will increase until it completely dominates at lower LSZ and SWNT concentrations. To further elucidate the elastic response of each dispersion with increasing concentrations of LSZ and SWNT,  $\tan(\delta)$  was plotted versus angular frequency as shown in Figure 61a. This shows that for

all bulk LSZ-SWNT dispersions, the elastic nature of the dispersion dominated of the viscous nature. Furthermore,  $\tan(\delta)$  trended with SWNT concentration in a power law fashion as seen in Figure 61b.

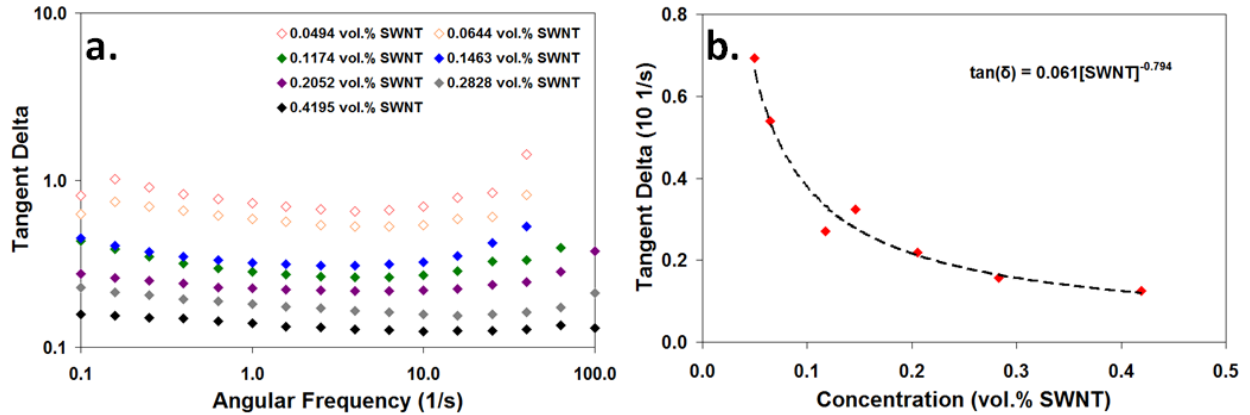


**Figure 61.** Graphical analysis of  $\tan(\delta)$  versus a.) angular frequency and b.) SWNT concentration showing that for LSZ-SWNT dispersions the elastic behavior typically dominates the viscous behavior, and that  $\tan(\delta)$  scales with concentration by a power law with a statistical  $R^2$  of 0.97. Error for each concentration is less than  $\pm 5\%$ . Open symbols indicate supernatant dispersions.

After the microstructure was probed by oscillatory testing, the viscosity of the dispersions was determined via steady shear flow curve testing. For all concentrations of LSZ-SWNT dispersions the flow characteristics were the same. Each concentration showed shear thinning behavior over the entire range of shear rates tested as shown in Figure 62.

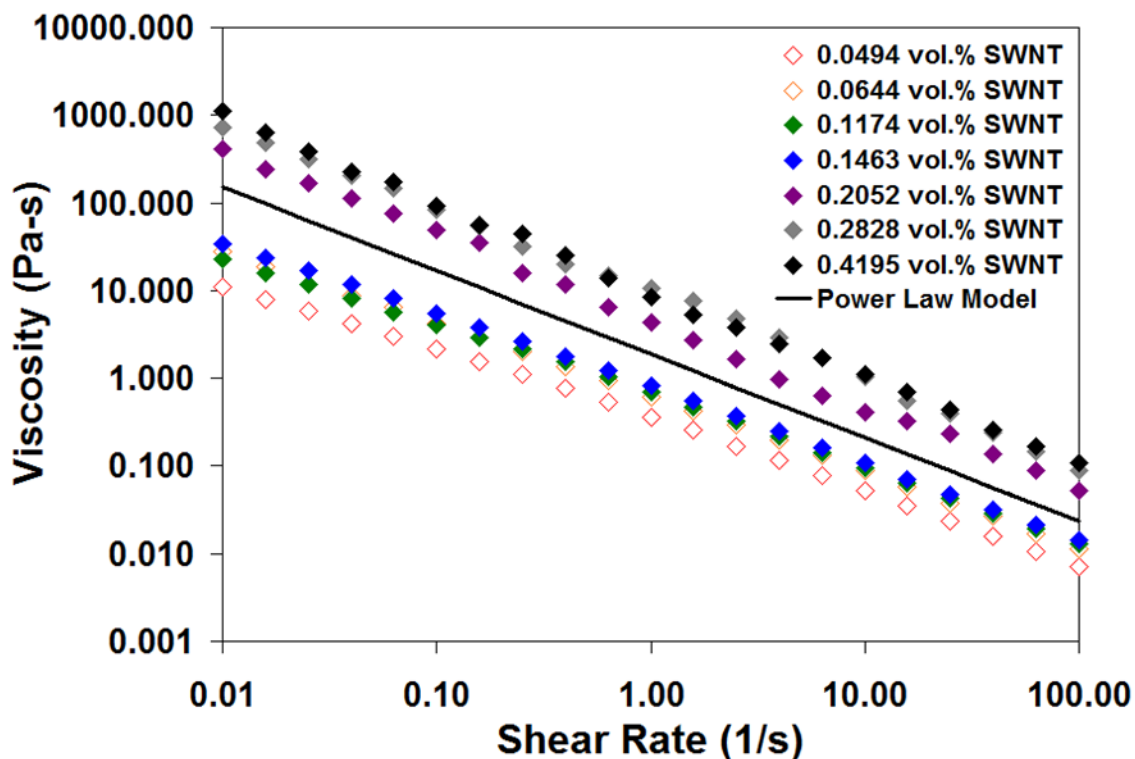


**Figure 62.** Flow curve showing viscosity versus shear rate for concentrations of 0.0494 vol.% SWNT, 0.0644 vol.% SWNT, 0.1174 vol.% SWNT, 0.1463 vol.% SWNT, 0.2052 vol.% SWNT, 0.2828 vol.% SWNT and 0.4195 vol.% SWNT, and a power law model fit. The power law model, as shown by Equation 4.2, has  $K = 1.88 \text{ Pa}\cdot\text{s}^2$  and  $n = 0.048$ . Error for each concentration is less than  $\pm 5\%$ . Open symbols indicate supernatant dispersions.

The shear thinning behavior of LSZ-SWNT indicates the tumbling and flow alignment of SWNT. With regard to actual nature of the dispersion, the gel nature of the concentrated LSZ-SWNT dispersion and the isotropic liquid nature of the initial dispersion follows a power law fluid as described by Equation 4.2. For the entire concentration range studied, from 0.0050 vol.% SWNT to 0.4195 vol.% SWNT,  $K$  varies from  $0.25 \text{ Pa}\cdot\text{s}^2$  to  $10 \text{ Pa}\cdot\text{s}^2$  and  $n$  varies from 0.01 to 0.25. From the flow curve data, it is important to note that there is no initial or final plateau over

the shear rates tested. When shear measurements are being taken, it is important to understand if any other forces are acting on the particles in the dispersion, as discussed in Section 2.6.7. Equations 2.69 and 2.70 were used to determine if the Brownian motion of the SWNT had any effect on the rheological shear data obtained. The calculations were done on the most dilute dispersions, 0.295 vol.% LSZ – 0.005 vol.% SWNT, at the lowest possible shear rate that was in torque, as required by Equations 2.69 and 2.70. The rotary diffusivity was calculated to be 17.16 s<sup>-1</sup> which generated a Peclet number of 0.0005 indicating that Brownian motion is in fact relevant in the dispersions under shear. This result was predicted by Larson who found that for particles whose longest dimension is less than 10 μm the Peclet number will be much less than unity, and therefore Brownian motion must be considered.<sup>98</sup> Considering the length of the SWNT used was on the order of 1 μm it holds that Brownian motion could create effects in the rheological data of the system.<sup>180</sup> To further show how dispersions, such as LSZ-SWNT, can deviate from classical systems the application of the Cox-Merz rule was determined for LSZ-SWNT dispersions. Deviations from the Cox-Merz rule can elucidate interactions among constituents in dispersions and show how systems deviate from idealized systems. The Cox-Merz rule, given in Equation 4.6, states that for corresponding values of shear rate,  $\dot{\gamma}$ , and angular frequency,  $\omega$ , the steady shear viscosity,  $\eta$ , and complex viscosity,  $\eta^*$ , will have the same values.<sup>100</sup>

$$\eta(\dot{\gamma}) = |\eta^*(\omega)| \quad (4.6)$$

Figure 63 shows the steady shear viscosity and complex viscosity versus shear rate and angular frequency, respectively, for various concentrations of LSZ-SWNT dispersions.

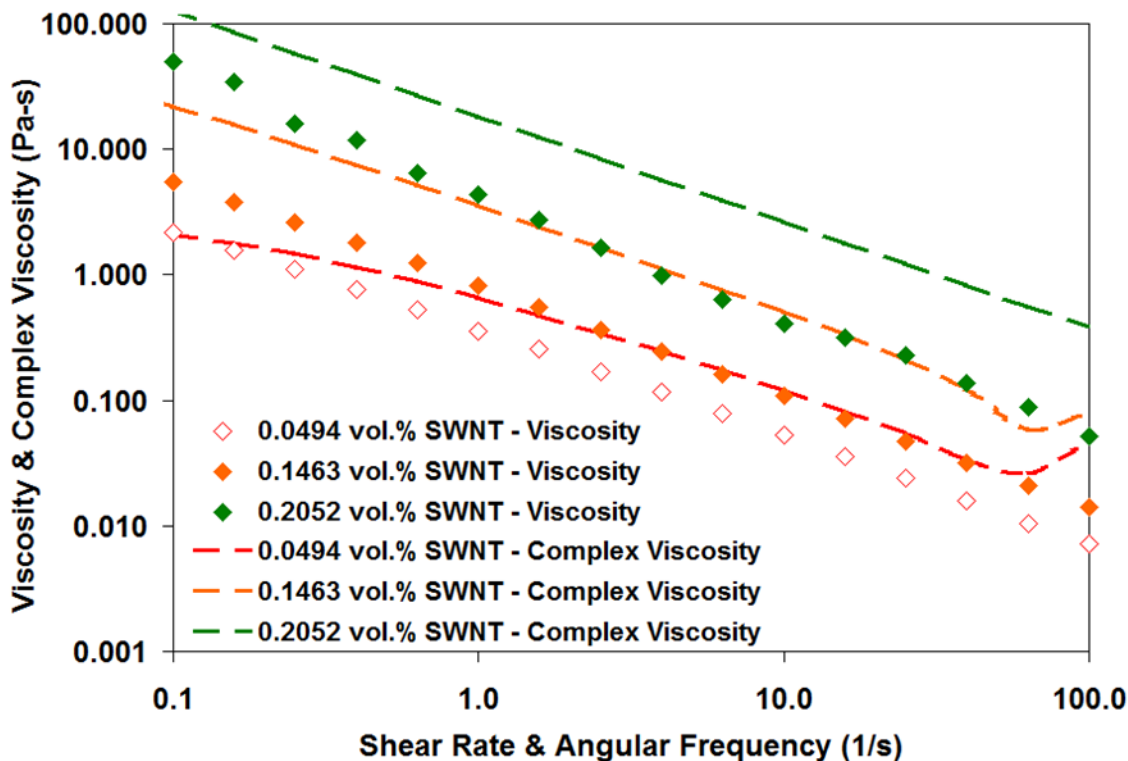


**Figure 63.** Deviation from the Cox-Merz rule for 0.0494 vol.% SWNT, 0.1463 vol.% SWNT, and 0.2052 vol.% SWNT dispersions. Deviation occurs due to the physical gel network formed after the depletion interaction present in LSZ-SWNT dispersions. Error for each concentration is less than +/- 4%. Open symbols indicate supernatant dispersions.

From Figure 63, it is obvious that LSZ-SWNT dispersions deviate from the Cox-Merz rule. This is due to the physical interactions that take place between LSZ and SWNT, and also due to the gel network that is forming as the concentration of LSZ and SWNT is increased. Of note in Figure 63 is that as the concentration of SWNT and LSZ increase, the deviation of the Cox-Merz rule increases. For 0.0494 vol.% SWNT the deviation is approximately 70%, for 0.1463 vol.% SWNT the deviation is approximately 76%, and for 0.2052 vol.% SWNT the deviation is approximately 83%, indicating that the elasticity of the gel network is increasing which is

causing the deviation to increase. Mezger affirms that the Cox-Merz rule holds for many polymer solutions, however, fails for most dispersions.<sup>100</sup> This is primarily due to the chemical and physical attractive and repulsive nature of the constituents of the dispersions which were not accounted for in the development of the Cox-Merz rule. The upturn at high frequencies is likely due to the inertia of the measuring system.

The interaction of LSZ with SWNT has been shown spectroscopically<sup>9, 181</sup> and now through rheological analysis. However, from Figure 62 it can be surmised that the viscosity of LSZ-SWNT dispersions does not scale linearly. In fact, after analysis of LSZ-SWNT viscosity versus LSZ and SWNT concentration independently, there is no definitive trend across all concentrations tested. This is likely due to the fact that the viscosity of the LSZ-SWNT dispersion is a function of not just LSZ or SWNT concentration but rather both. In order to account for the various concentrations of both LSZ and SWNT present at each data point, the reduced and inherent viscosity at each data point was determined. The reduced and inherent viscosities, shown in Equations 4.7 and 4.8, were used to compare the deviation of LSZ-SWNT dispersion rheology from that of typical rod rheology (reduced viscosity), and to show the trend of LSZ-SWNT viscosity data (inherent viscosity).

$$\eta_{Reduced} = \frac{\eta - \eta_s}{\eta_s \cdot \phi_{SWNT}} \quad (4.7)$$

$$\eta_{Inherent} = \frac{\ln \eta_r}{\phi_{SWNT}} \quad (4.8)$$

The relative viscosity,  $\eta_r$ , was calculated as the LSZ-SWNT dispersion viscosity,  $\eta$ , divided by the LSZ viscosity,  $\eta_s$ , for the specific concentration of LSZ present in the dispersion, where  $\phi_{SWNT}$  is the volume fraction of SWNT in the respective dispersion. By accounting for both the LSZ and SWNT present in each dispersion, it can be shown that the inherent viscosity of the full range of concentrations of LSZ-SWNT dispersions can be modeled as a power law versus

SWNT concentration, as shown in Figure 64a. Figure 64b show the reduced viscosity of dilute dispersions of LSZ-SWNT as a function of shear rate to show the deviation of LSZ-SWNT from typical rod rheology. The reduced viscosity versus shear rate for dilute dispersions of SWNT should follow the theory of Kirkwood and Plock at Weissenberg numbers above 1, which states that the log-log plot of reduced viscosity versus shear rate will have a slope of -0.5. This has been validated in experiment by Davis et al. who found that for SWNT in superacid, in the dilute phase, the reduced viscosity versus shear rate curve had a slope of -0.5.<sup>5</sup> The dashed line in Figure 64b is a slope of -0.50, but the data much more closely follows the solid line which has a slope of -0.74. This is a definitive indication that LSZ-SWNT dispersion rheology does not follow that of typical SWNT or rigid-rod rheology.

The dilute solution data – SWNT concentrations less than 0.01 vol.% as determined from the maximum of the dilute to semi-dilute transition for the SWNT used from Doi & Edwards<sup>104</sup> – for both reduced and inherent viscosity can be used to find the intrinsic viscosity of SWNT based on models developed for polymer solutions.<sup>182</sup> Although LSZ-SWNT does not follow the rigid rod rheology theory of Kirkwood and Plock, the dilute phase data was used to compare the intrinsic viscosity of LSZ-SWNT dispersions with the intrinsic viscosity of SWNT dispersions which follow rigid rod rheology. The reduced viscosity as a function of concentration, as shown in Equation 4.9, was used by Huggins to correlate the intrinsic viscosity where  $k'$  has been termed the Huggins constant.<sup>79-80</sup> For this equation, the viscosities should be taken at the lowest possible shear rate for extrapolation to zero concentration. Therefore each viscosity is from a shear rate of  $0.1 \text{ s}^{-1}$ .

$$\frac{\eta - \eta_s}{\eta_s \cdot \phi_{SWNT}} = [\eta] - k'[\eta]^2 c_{SWNT} \quad (4.9)$$

Figure 64c shows the dilute phase reduced viscosity as a function of concentration to determine the intrinsic viscosity.

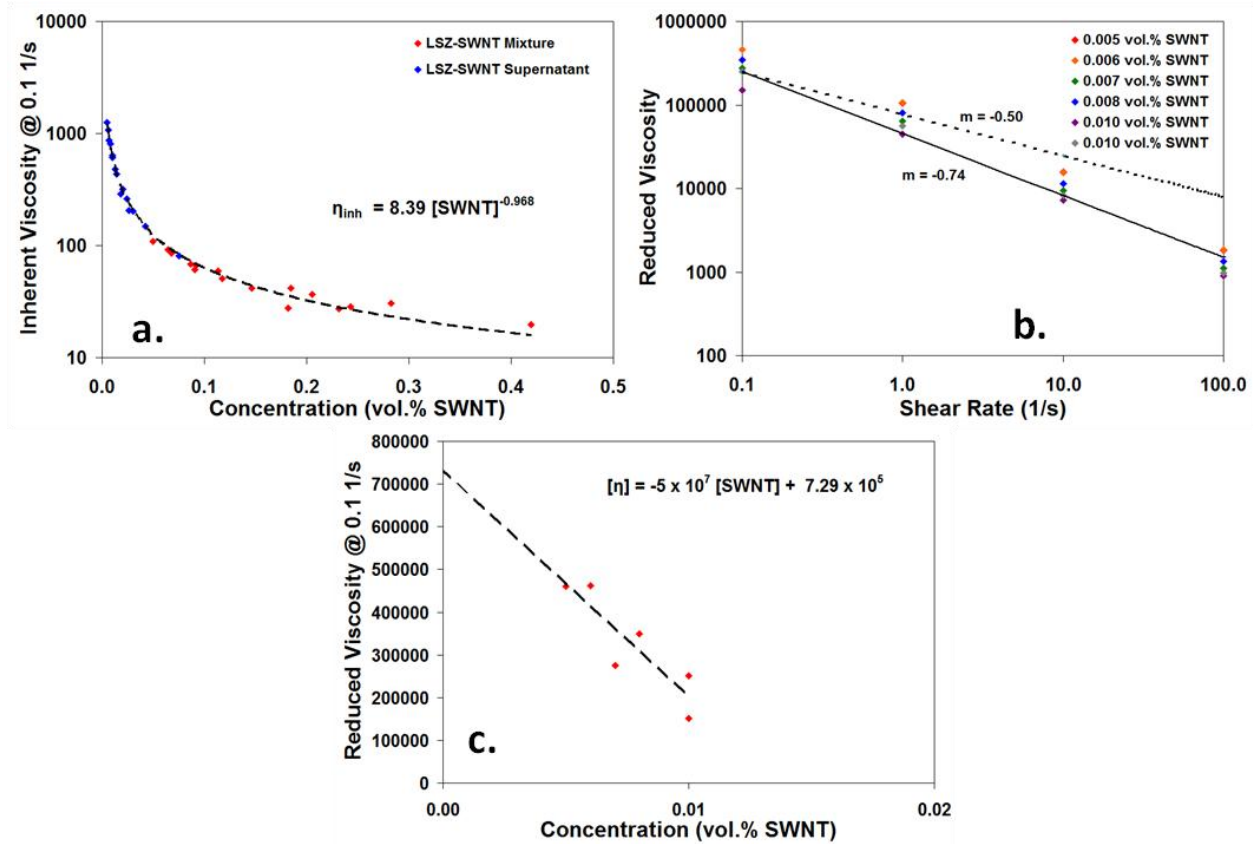


**Figure 64.** a.) Inherent viscosity versus SWNT concentration at a shear rate of  $0.1 \text{ s}^{-1}$  showing power law fit with a statistical  $R^2$  of 0.99, b.) reduced viscosity versus shear rate showing lines with slopes of -0.50 (dashed) and -0.76 (solid) (note all concentrations are supernatant dispersions), c.) the reduced viscosity linear fit of dilute, supernatant concentration data with a statistical  $R^2$  of 0.78. Error for each concentration is less than  $\pm 4\%$ .

By fitting a linear trendline through the dilute reduced viscosity solution data and extrapolating to zero concentration, it is possible to determine the intrinsic viscosity. The reduced viscosity gives an inherent viscosity of 7290. It is of distinct importance to note that the dilute solution

reduced viscosity data gives an intrinsic viscosity that is within 1% of the values in literature for SWNT intrinsic viscosity.<sup>149</sup>

The complex nature of LSZ-SWNT dispersions has been shown through oscillatory and steady-shear rheological analysis in addition to optical microscopy. Analysis of the viscoelastic oscillatory response indicates the physical networking of LSZ after the development of depletion induced aggregates with increasing LSZ and SWNT concentration. Furthermore, it shows that the elasticity of LSZ-SWNT dispersions scales by a power law with respect to SWNT concentration. Analysis of the steady shear viscosity shows shear thinning, power law nature of LSZ-SWNT dispersions versus shear rate, the complex interaction of LSZ-SWNT through the deviation from Cox-Merz, and the collapse of all LSZ-SWNT dispersions on to a master curve by accounting for the presence of both LSZ and SWNT through use of inherent viscosity. Understanding the rheological nature and phase behavior of LSZ-SWNT dispersions aids in their processing and macroscopic development.

#### **4.4. LYSOZYME - CARBON NANOTUBE PHASE BEHAVIOR ALTERATION**

Several groups have demonstrated that aqueous solutions of LSZ are an effective dispersant of low concentrations of individual SWNT. In this research, concentrated dispersions of LSZ-SWNT were shown to have a defined phase transition where an increase in the number and size of SWNT aggregates occurred. Increased aggregation in LSZ-SWNT dispersions decreases the opportunity to translate the unique properties of SWNT to practical applications by reducing the surface-to-volume ratio and by limiting processability. To decrease the size and number of aggregates, as well as shift the concentration at which aggregation occurs to a higher value, TTAB, a cationic surfactant, was added to the LSZ-SWNT dispersions. This section

describes how the addition of TTAB increased dispersion stabilization and increased the SWNT concentration at which aggregation occurred by an order of magnitude.

The cationic surfactant 0.34 vol.% TTAB was added to the initial mixtures of LSZ-SWNT. Surfactants have played a major role in the study and assembly of SWNT since their discovery.<sup>54, 183-185</sup> The likely mechanism of SWNT dispersion with surfactants for this system is based on the surface charging of SWNT.<sup>186</sup> Surfactants adsorb on SWNT by their hydrophobic tails. The hydrophilic heads of the surfactant create an effective charge on the SWNT surface. The surface charge then creates an electric double-layer. This double-layer induces an electrostatic repulsion and stabilizes the SWNT against aggregation from van der Waals forces as predicted by Derjaguin-Landau-Verwey-Overbeek (DLVO) theory.<sup>59</sup> However, zeta-potential studies of surfactants with SWNT have given insight into the possible interaction with SWNT.<sup>187-188</sup> Initial thoughts on surfactant interactions with SWNT were that of surfactant wrapping of the SWNT invoked the formation of cylindrical micelles around the SWNT with the hydrocarbon chains arranged along the SWNT sidewall. However, more recent studies using small-angle neutron scattering and density functional theory calculations suggest that the interaction is a random and disordered adsorption of surfactant molecule tails onto the SWNT surface. Regardless of exact interaction with SWNT, the stabilization mechanism remains that of electrostatic repulsion between surfactant molecules leading to colloidal stability as described by DLVO theory. TTAB is a cationic surfactant with a positively charged ammonium bromide head group and a 14-carbon tail, and was used because it showed a non-inhibitory effect toward the lytic activity when conjugated with LSZ. In theory, the TTAB will create a complex with both LSZ and SWNT to increase the stabilization of the dispersions.

The interaction of cationic surfactants with LSZ has been well studied.<sup>189-192</sup> It is generally accepted that the binding of TTAB to LSZ occurs by a combination of electrostatic and hydrophobic interactions. More specifically, Hayashi et al.<sup>190-191</sup> and Subramanian et al.<sup>192</sup> have shown through optical spectroscopy that the saturated TTAB tail binds with surface bound indole moieties of tryptophan and phenolic moieties of tyrosine amino acid residues along with exposed carboxyl groups which have been ionized by the aqueous environment. In addition to the interaction of TTAB with LSZ, there will also inherently be an interaction between TTAB and SWNT. However, there was no literature found on the interaction of cationic surfactants with biomolecule-SWNT complexes. Although the multiple interactions – LSZ-SWNT, LSZ-TTAB, TTAB-SWNT, and LSZ-TTAB-SWNT – are inherently complex and would be difficult to deconvolute, it is likely that the interactions are hydrophobic in nature and exist between the sidewall of SWNT, hydrophobic core of LSZ, and hydrophobic alkyl-tail of TTAB.

The addition of TTAB to the LSZ-SWNT dispersions increases the colloidal stability and alters the phase behavior transitions of the mixture and supernatant dispersions. Table 5 shows the phase behavior transitions of LSZ-TTAB-SWNT mixture and supernatant dispersions. The phase transition of LSZ-TTAB-SWNT is shown by the SWNT concentration at which the number and size of SWNT aggregates increases. The reason for this aggregation is believed to be analogous to that of LSZ-SWNT dispersions. Even in the presence of TTAB, depletion interactions can take place.<sup>183</sup>

Dispersion (Volume Ratio)	Demixed [SWNT] (vol.%)	Demixed [LSZ] (vol.%)
2.1:1.0 LSZ:SWNT Mixture	0.166	0.355
2.1:1.0 LSZ:SWNT Supernatant	0.075	1.057
0.9:1.2:1.0 LSZ:TTAB:SWNT Mixture	1.877	1.596
0.9:1.2:1.0 LSZ:TTAB:SWNT Supernatant	0.687	1.151

**Table 5.** The phase transition concentrations for volumetric each ratio showing the demixed concentration of SWNT and LSZ for LSZ-SWNT and LSZ-TTAB-SWNT dispersions.

Table 5 shows the demixed concentration for LSZ and SWNT for the LSZ-SWNT mixture containing the largest quantity of SWNT, and the LSZ-TTAB-SWNT mixture and their supernatant dispersions. For quantitative comparison, it should be noted that the concentration ratios of LSZ:SWNT for TTAB dispersions were significantly lower than original LSZ-SWNT dispersions. The LSZ-SWNT phase behavior, indicates that decreasing the LSZ:SWNT ratio would decrease the concentration at which aggregation occurs. However, for LSZ-TTAB-SWNT the concentration at which the transition occurs is an order of magnitude higher for the mixtures. Moreover, the use of TTAB as a stabilizing agent allowed the LSZ-TTAB-SWNT supernatant to maintain enough SWNT after centrifugation to show the depletion phase transition. This transition occurred approximately two orders of magnitude higher for the LSZ-TTAB-SWNT supernatant than the most concentrated LSZ-SWNT supernatant dispersion, which did not go through a phase transition. It should be noted that the original LSZ-SWNT supernatant dispersion had such a low SWNT concentration that analytical measurement of the exact concentration was not possible, therefore it was estimated from a dispersion mass balance. It is speculated that the increased size and total charge of the LSZ-TTAB complex compared with

LSZ contributes to the stabilization. This was supported by an increase in the zeta-potential of LSZ-TTAB-SWNT from LSZ-SWNT of +24 mV to +31 mV.

SEM on a dried LSZ-TTAB-SWNT supernatant dispersion qualitatively confirmed the presence of a continued interaction between LSZ and SWNT with the addition of TTAB. Figure 65 shows an opaque SWNT bundle surrounded by a semi-translucent layer of LSZ and TTAB. This layer appears similar to the LSZ layer previously reported in the absence of TTAB.<sup>9</sup>

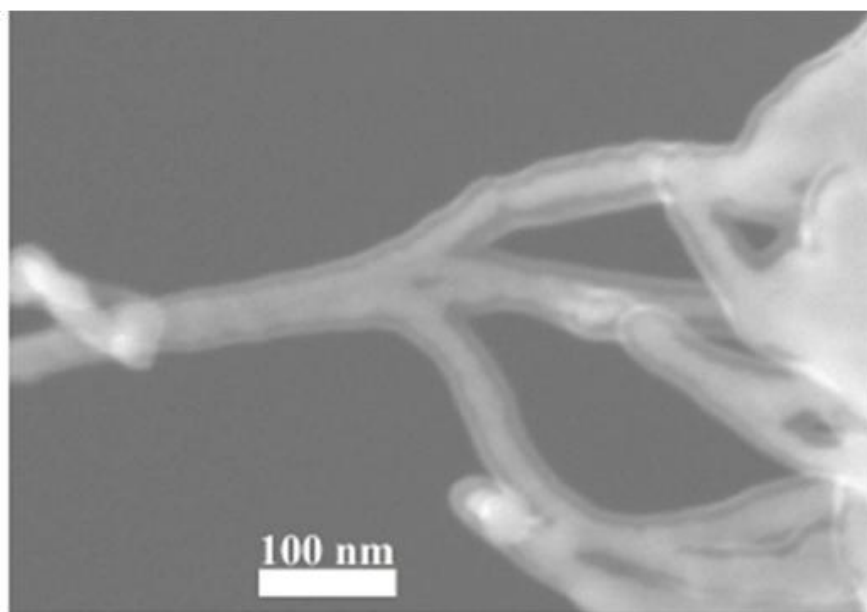


**Figure 65.** Scanning electron micrograph of an 0.24 vol.% LSZ – 0.34 vol.% TTAB – 0.28 vol.% SWNT supernatant dispersion illustrating the interaction between SWNT (opaque) and LSZ-TTAB (translucent); magnification is 190,000x.

The presence of TTAB in the translucent shell surrounding the SWNT was confirmed by EDS. Six scans of random locations within Figure 65 had an average elemental percentage of 11.8 % bromine. This supports the interaction between LSZ, TTAB, and SWNT. It is this cooperative interaction which allows for increased stabilization of SWNT.

UV-vis spectroscopy of LSZ-TTAB-SWNT was carried out in order to confirm the presence of individual or small bundle SWNT within the dispersion and reveal the difference in LSZ-SWNT and LSZ-TTAB-SWNT dispersions. Figure 66 shows UV-vis spectroscopy of the supernatant of a 0.24 vol.% LSZ – 0.28 vol.% SWNT and 0.24 vol.% LSZ – 0.34 vol.% TTAB – 0.28 vol.% SWNT dispersions.

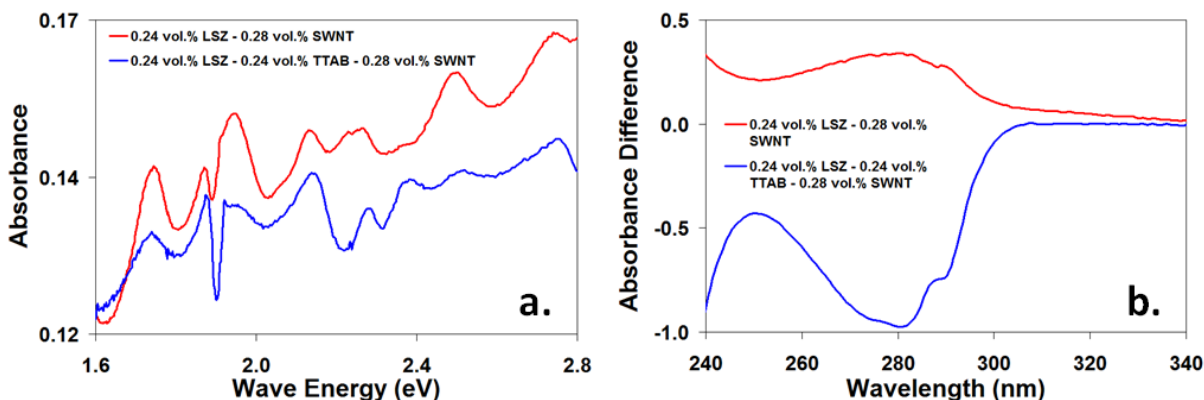


**Figure 66.** a.) UV-vis spectroscopy of the supernatant of a 0.24 vol.% LSZ – 0.28 vol.% SWNT and 0.24 vol.% LSZ – 0.24 vol.% TTAB – 0.28 vol.% SWNT dispersions showing sharp van Hove singularity peaks between 1.6 and 2.4 eV, elucidating the ability of LSZ-TTAB solutions to disperse SWNT as individuals or small bundles; LSZ-TTAB-SWNT down shifted by 0.065 to elucidate similarities, b.) UV-vis difference spectra of the supernatant of 0.24 vol.% LSZ – 0.28 vol.% SWNT and 0.24 vol.% LSZ – 0.24 vol.% TTAB – 0.28 vol.% SWNT dispersions showing a change in the surroundings of the LSZ tryptophan chromophore.

Figure 66a shows sharp van Hove singularity peaks between 1.6 and 2.4 eV for both dispersions, making clear the ability of LSZ-TTAB solutions to disperse SWNT as individuals or small bundles. The absorbance values of the LSZ-TTAB-SWNT dispersion at ~1.6 eV have been down shifted by 0.065 to coincide with the same wave energy absorbance values of the LSZ-SWNT

dispersions. Shifting of the absorbance by an offset value was chosen over normalization, because normalization of the data would lead to smoothing and quenching of the peaks. Alteration of the peak structure would then not illuminate the dispersibility of SWNT with LSZ-TTAB solutions. The offset was necessary due to the increased concentration of SWNT maintained in the LSZ-TTAB-SWNT supernatant, as described above. In addition to showing dispersibility, UV-vis also confirms that the solvent environment surrounding the LSZ is much different between the LSZ-SWNT and LSZ-TTAB-SWNT dispersion. Figure 66b shows the absorbance difference spectra of the supernatant of a 0.30 vol.% LSZ – 0.28 vol.% SWNT and 0.24 vol.% LSZ – 0.28 vol.% SWNT – 0.34 vol.% TTAB dispersions, where 0.30 vol.% LSZ solution absorbance values have been subtracted to clarify the difference in the solvent environment of the LSZ chromophore tryptophan. As can be seen from the figure, the LSZ-SWNT dispersions shows a hyperchromic shift whereas the LSZ-TTAB-SWNT dispersion shows a hypochromic shift. Shifting in the absorbance intensity of a chromophore is due to changes in the solvent surroundings.<sup>159-160</sup> Hyperchromic shifts of LSZ are due to the solvent surrounding of the LSZ chromophore tryptophan becoming more exposed to aqueous environments. This is the case for LSZ-SWNT dispersions when the LSZ hydrophobic core opens to bind with the hydrophobic sidewall of SWNT in the aqueous dispersion.<sup>9</sup> Hypochromic shifts also occur due to changes in the solvent surrounding of the chromophore. For LSZ-TTAB-SWNT, the hypochromic shift likely occurs due to encapsulation of LSZ or LSZ-SWNT within the hydrophobic core of a TTAB micelle. Although the interaction between LSZ, TTAB, and SWNT would be difficult to deconvolute, it still disperses SWNT as individuals or small bundles as evidence by Figure 65 and 66a.

For a comparative analysis, rheology of LSZ-TTAB-SWNT dispersions was carried out in a manner analogous to that of LSZ-SWNT dispersions. It should first be noted that although eight different concentrations of LSZ-TTAB-SWNT dispersions were run, the torque data for oscillatory test on six of them was too low to be considered valid data, therefore only the data for the two concentrations is shown for oscillatory tests. First, an amplitude sweep was run to determine the limit of linear viscoelasticity, as shown in Figure 67. The critical strain was determined to be approximately 4.0% as determined by graphical analysis where the correlation in the direction of the tangent line of the low-strain plateau was lost. In comparison to LSZ-SWNT dispersions, the critical strain is higher for dispersions with TTAB. The exact reason for this is unknown, however, it is hypothesized that the interactions between the constituents structurally stabilizes the dispersion better allowing for absorbance of higher amounts of energy prior to deformation.

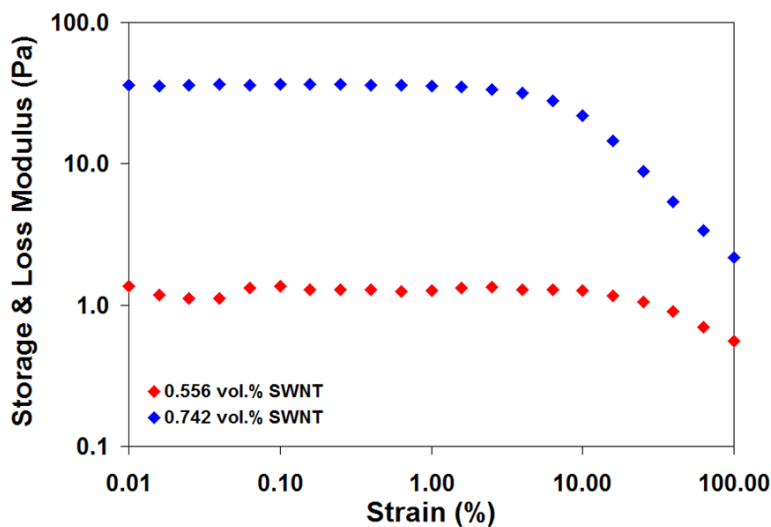


**Figure 67.** Amplitude sweep test data for LSZ-TTAB-SWNT dispersions showing storage modulus as a function of amplitude strain for concentrations of 0.556 vol.% SWNT and 0.742 vol.% SWNT. The critical strain was determined to be 4.0%. Error for each concentration is less than +/- 2.6%.

After determination of the limit of linear viscoelasticity, the linear viscoelastic oscillatory response was probed by a frequency sweep, as shown in Figure 68. Of interesting note for the frequency sweep data is that although there is a large jump in the magnitude of the storage modulus with the increase in concentration, the slope of the two lines remains similar – 0.25 for 0.556 vol.% SWNT and 0.23 for 0.742 vol.% SWNT. This indicates that there is no change in the elastic structure of the material, such as the physical networking seen with LSZ-SWNT dispersions.

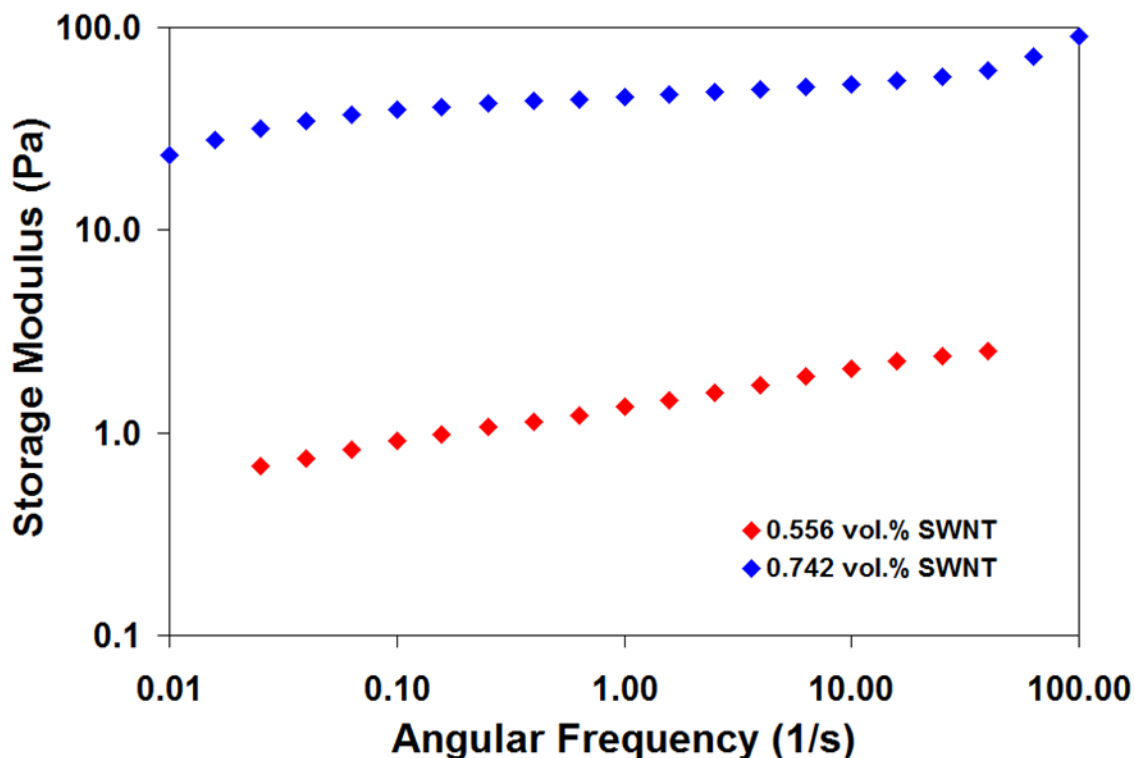


**Figure 68.** Linear viscoelastic oscillatory response for LSZ-TTAB-SWNT dispersions showing storage modulus as a function of angular frequency for concentrations of 0.556 vol.% SWNT and 0.742 vol.% SWNT. Error for each concentration is less than +/- 3.1%.

Finally the viscosity response of the dispersions was probed by steady-shear flow curve testing, as shown in Figure 69. Not all concentrations follow a shear-thinning pattern. For concentrations lower than 0.199 vol.% SWNT, the dispersions were nearly Newtonian as opposed to the shear-thinning response of the higher concentration dispersions. Moreover, the most dilute dispersions less than 0.1 vol.% SWNT have viscosities that are approximately 0.0014 Pa-s, only slightly higher than the viscosity of pure water at 10°C, 0.0013 Pa-s, and significantly lower than the LSZ-SWNT dispersion viscosity at the same concentration. Although the exact understanding for the difference in shear-thinning versus Newtonian behavior compared to LSZ-SWNT dispersions is not known it is likely due to the surface tension effects of adding TTAB to the dispersion. TTAB is a surfactant, and surfactants are compounds which decrease the surface tension, or interfacial tension, for liquid-liquid, solid-liquid, or liquid-gas systems.

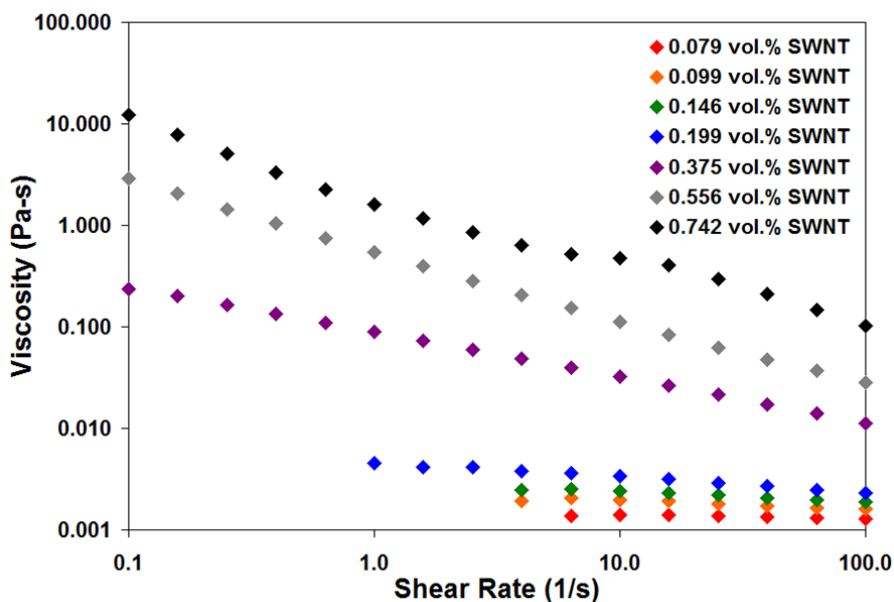


**Figure 69.** Viscosity response for LSZ-TTAB-SWNT dispersions showing viscosity as a function of shear rate for concentrations of 0.079 vol.% SWNT, 0.099 vol.% SWNT, 0.146 vol.% SWNT, 0.199 vol.% SWNT, 0.375 vol.% SWNT, 0.556 vol.% SWNT, and 0.742 vol.% SWNT. Error for each concentration is less than +/- 4.2%.

Surface tension is a contractive force of the surface of a liquid that allows it to resist external forces.<sup>193</sup> This property is caused by cohesion forces of similar molecules and is a measure of energy per unit area. The cohesive forces among liquid molecules are responsible for the phenomenon of surface tension. In the bulk of the liquid, each molecule is pulled equally in every direction by neighboring liquid molecules, resulting in a net force of zero. The molecules at the surface do not have other molecules on all sides of them and therefore are pulled inward creating an internal pressure forcing liquid surfaces to experience surface tension.<sup>193</sup> Another way to view surface tension is in terms of energy. A molecule in contact with a neighbor is in a lower energy state than if it were not in contact. More simply, interior molecules having more contacts have a lower energy, but the boundary (surface) molecules are missing neighbors and have a higher energy.<sup>193</sup> Therefore, reducing the surface tension of the dispersion will reduce the contractive force holding particles together which could account for the Newtonian-like behavior of the dispersions until the concentrations of LSZ and SWNT become significant enough to overcome the reduced surface tension.

The addition of TTAB was able to stabilize the aggregation of the dispersion to a higher concentration. However, the extensional properties of the concentrated LSZ-TTAB-SWNT dispersion were still not good enough to produce robust fibers. In order to improve the poor extensional properties of the LSZ-SWNT and LSZ-TTAB-SWNT dispersions, various synthetic and natural polymers, were combined with the dispersions to assist in fiber spinning. To fully understand the effect on the phase behavior of each dispersion with the addition of an elastic polymer, rheology of LSZ-SWNT in PVA and LSZ-TTAB-SWNT in PVA dispersions was completed.

An amplitude sweep was run to determine the limit of linear viscoelasticity, as shown in Figure 70. The critical strain was determined to be approximately 6.3% for LSZ-SWNT in PVA and 10% for LSZ-TTAB-SWNT in PVA as determined by graphical analysis where the correlation in the direction of the tangent line of the low-strain plateau was lost. In comparison to the LSZ-SWNT or LSZ-TTAB-SWNT dispersions, the critical strain is higher for dispersions containing PVA. This is due to the presence of the elastically robust polymer which structurally stabilizes the dispersions allowing for absorbance of higher amounts of energy prior to deformation.

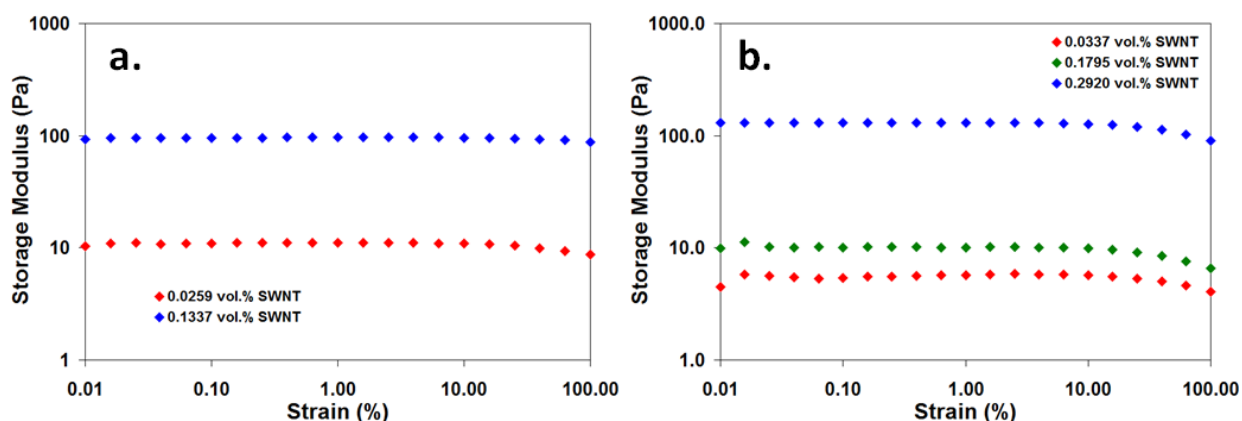


**Figure 70.** Amplitude sweep test data for a.) LSZ-SWNT in PVA and b.) LSZ-TTAB-SWNT dispersions showing storage modulus as a function of amplitude strain for various concentrations. The critical strain was determined to be a.) 6.3% and b.) 10%. Error for each concentration is less than +/- 2.4%.

After determination of the limit of linear viscoelasticity, the linear viscoelastic oscillatory response was probed by a frequency sweep, as shown in Figure 71. At concentrations below 0.18 vol.% SWNT, the slopes of the storage modulus lines ( $\sim 0.5$ ) remains similar for both LSZ-SWNT and LSZ-TTAB-SWNT. The lack of a change in slope between PVA containing

dispersions with different constituents (TTAB versus no TTAB) compared to the drastic differences in the absence of PVA indicates that PVA dominates the elastic response.

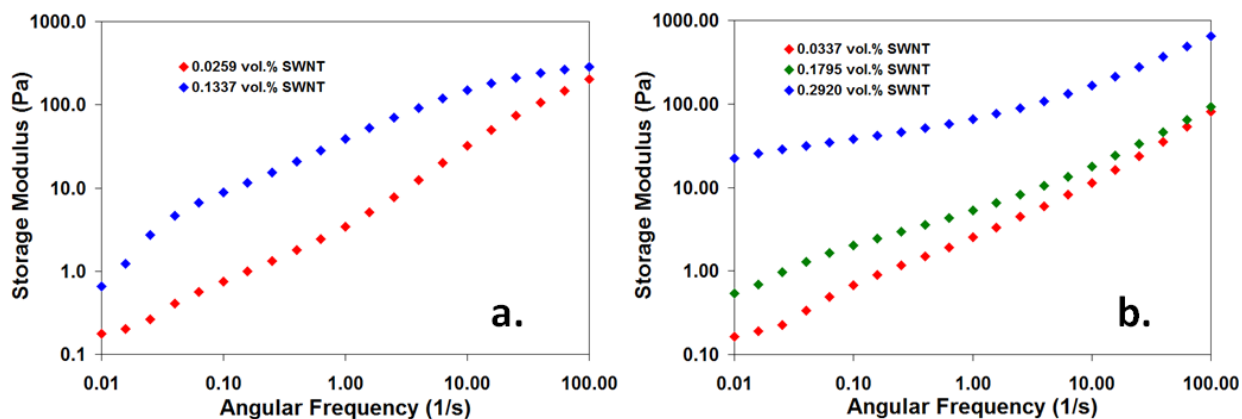


**Figure 71.** Linear viscoelastic oscillatory response for a.)LSZ-SWNT in PVA and b.) LSZ-TTAB-SWNT in PVA dispersions showing storage modulus as a function of angular frequency for various concentrations. Error for each concentration is less than +/- 2.6%.

The shear-thinning viscosity response of the dispersions is shown in Figure 72. As with the LSZ-SWNT and LSZ-TTAB-SWNT dispersions, the shear-thinning behavior of each concentration follows different power law parameters. It should be noted that the comparison of magnitudes of each dispersion modulus or viscosity will tell which dispersion may be more elastic or flow easier, however, the interactions involved in a five component system would need to be deconvoluted in order to tell exactly how or why the dispersions responded the particular way that they did.

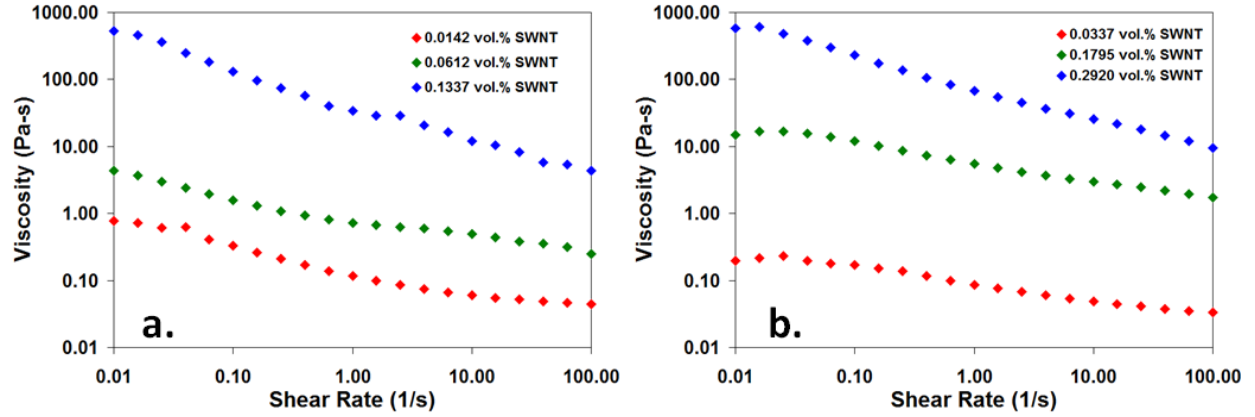


**Figure 72.** Viscosity response for a.) LSZ-SWNT in PVA and b.) LSZ-TTAB-SWNT in PVA dispersions showing viscosity as a function of shear rate for various concentrations. Error for each concentration is less than +/- 5.0%.

Finally, for a complete comparative analysis of all dispersions – LSZ-SWNT, LSZ-TTAB-SWNT, LSZ-SWNT in PVA, and LSZ-TTAB-SWNT in PVA – the inherent viscosity of each dispersion was determined by determining the relative viscosity of each dispersion. The relative viscosity equations for each dispersion are shown in Equations 4.10 through 4.13. For dispersions containing PVA, the relative viscosity included a correction factor which was the viscosity of PVA at the given concentration,  $\eta_{PVA}$ , to account for the viscosity of PVA in each dispersion.

$$\eta_r^{LSZ-SWNT} = \frac{\eta_{LSZ-SWNT}}{\eta_{LSZ}} \quad (4.10)$$

$$\eta_r^{LSZ-TTAB-SWNT} = \frac{\eta_{LSZ-SWNT}}{\eta_{LSZ}} \quad (4.11)$$

$$\eta_r^{LSZ-SWNT \text{ in PVA}} = \frac{\eta_{LSZ-SWNT}}{\eta_{LSZ} \cdot \eta_{PVA}} \quad (4.12)$$

$$\eta_r^{LSZ-TTAB-SWNT \text{ in PVA}} = \frac{\eta_{LSZ-SWNT}}{\eta_{LSZ} \cdot \eta_{PVA}} \quad (4.13)$$

The relative viscosity was then plugged in to Equation 4.8 to determine the dispersion inherent viscosity. From the relative viscosity it is also possible to determine the intrinsic viscosity of the dispersion as shown in Equation 4.9. However, for each dispersion except LSZ-SWNT, the dilute regime did not have enough concentrations (data points) to properly determine the intrinsic viscosity. The inherent viscosity for each dispersion was then plotted versus SWNT concentration; all the data collapsed onto a master inherent viscosity curve for SWNT dispersed with LSZ, as shown in Figure 73. To further show the trend, a power law trendline was fit to the data and it should be noted that the power law trend has a very similar equation for all dispersions to what was initially shown for LSZ-SWNT dispersions.

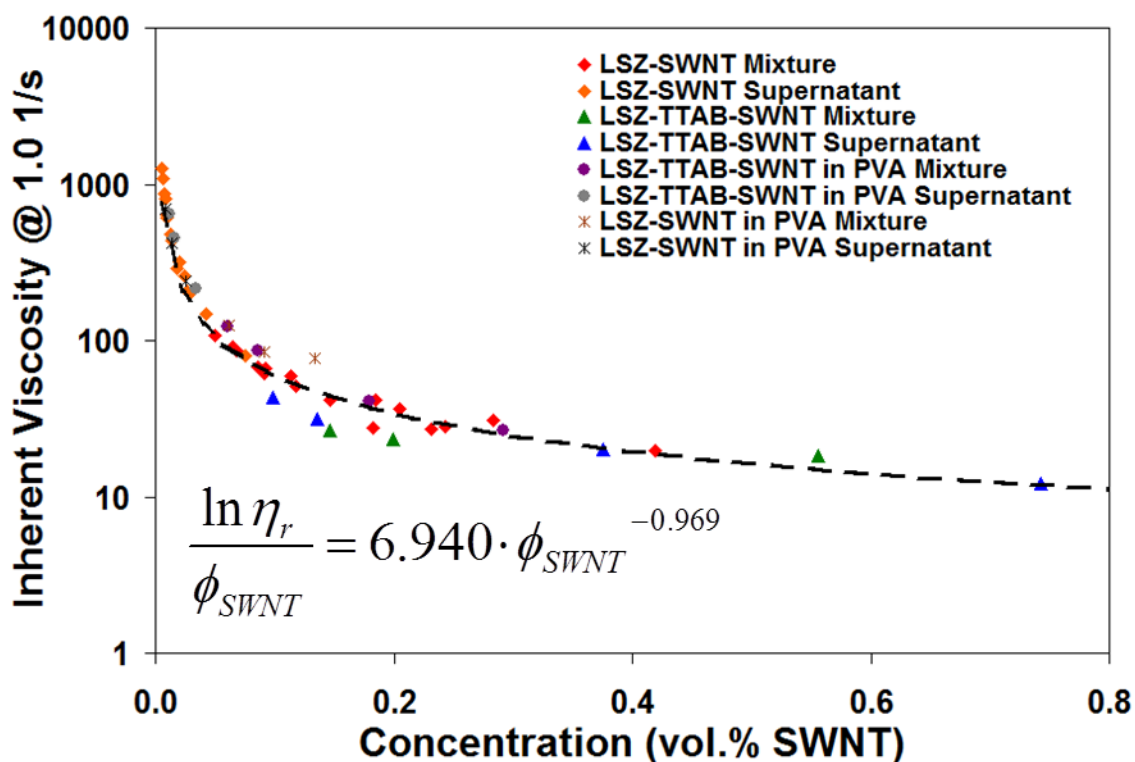


**Figure 73.** Inherent viscosity of LSZ-SWNT dispersions versus SWNT concentration at a shear rate of 1.0 s<sup>-1</sup> showing the collapse of all dispersions on to a master curve with a power law fit having a statistical R<sup>2</sup> of 0.97.

The addition of TTAB to LSZ-SWNT dispersions electrostatically stabilized the dispersion allowing for higher SWNT concentrations with reduced aggregation. The addition of natural or synthetic polymers then altered the phase of LSZ-SWNT or LSZ-TTAB-SWNT dispersions from an isotropic liquid to an elastic gel. Through stabilization and alteration of the LSZ-SWNT phase behavior, it was then possible to create robust and tailorable macroscopic assemblies.

#### **4.5. LYSOZYME CARBON NANOTUBE MACROSCOPIC ASSEMBLIES**

Processing of nanomaterial dispersions into macroscopic, solid materials is a challenging and active area of research. The two most commonly explored techniques are fiber spinning and film casting. In this work, wet and dry fiber spinning as well as film casting were investigated. Post-processing of fibers and films was attempted through drawing to attempt to increase the mechanical robustness and tailorability of the assemblies. Finally, each film and fiber was characterized for important properties including mechanical, electrical, optical, and antibacterial analysis.

##### **4.5.1. FIBERS**

Creating fibers from LSZ-SWNT dispersions was initially attempted by wet spinning. Wet solution spinning involves the injection of a concentrated dispersion into a rotating coagulation bath. It should be noted that coagulation does not require a rotating bath, however, with coagulation being a competitive diffusion event, the rotation allows for keeping constituents separated while promoting elongation. The rotation of the coagulation bath creates a drawing effect that when coupled with the injection of the dispersion creates a force balanced system between the shear force of extrusion and the rotational force of the coagulation bath. To ensure the most uniform fiber and the most consistent coagulation, the push and pull forces must be

nearly equal; in order for drawing to occur through coagulation the rotation rate should be slightly faster than the injection rate. Therefore the velocity of the injection rate must be nearly equal the tangential point velocity were the needle injects the dispersion. If the velocities do not closely match two differing discontinuities can occur. First, if the injection rate is too fast, coagulation cannot occur uniformly and the fiber will breakdown into small sections rather than a continuous fiber. Second, if the injection rate is too slow, then inhomogeneous sections of fiber will be formed creating fracture points in the structure due to the lack of adequate injection rate to create a homogenous fiber. To determine the correct injection rate, the tangential velocity can be calculated from Equation 4.14 where  $v$  is the tangential velocity,  $r$  is the radius from the center of the beaker, and  $n$  is the rotational speed at the center.

$$v = 2\pi rn \quad (4.14)$$

In order to match that velocity, the volumetric injection rate must have an equivalent velocity. The volumetric flow rate can be calculated from Equation 4.15 where  $\dot{V}$  is the volumetric flow rate,  $v$  is the tangential velocity from Equation 4.3, and  $d$  is the diameter of the needle.

$$\dot{V} = \frac{\pi v d^2}{4} \quad (4.15)$$

Attempts to wet solution spin LSZ-SWNT dispersions failed due to the presence of aggregates. While some small sections of fiber could be obtained by wet spinning into a stagnant 1-butanol coagulation bath, the mechanical properties were too poor to enable testing. The increased concentration at which aggregation occurs in LSZ-TTAB-SWNT dispersions enabled solution spinning. Initial wet spinning of a dilute LSZ-TTAB-SWNT dispersions into a PVA coagulation bath was performed in order to capitalize on the previous advances made for conventional PVA-SWNT fibers.<sup>183-184, 194</sup> Wet spinning of a dilute 0.24 vol.% LSZ – 0.28 vol.% SWNT – 0.34 vol.% TTAB dispersion into a rotating PVA coagulation bath resulted in fibers with smooth

surfaces and cylindrical geometries, and were mechanically robust enough to be tested for tensile properties as shown in Table 6. However, coagulation had the unintended consequence of eliminating the fiber's antibacterial activity. Since PVA does not inhibit LSZ activity, as will be shown later, it was surmised that the external layer of PVA masked the antibacterial activity of LSZ by physically covering the LSZ present on the surface of the SWNT. Dry spinning of a concentrated 3.17 vol.% LSZ - 4.63 vol.% TTAB - 3.71 vol.% SWNT dispersion resulted in fibers with antibacterial activity, as will be discussed later, but an order or magnitude lower Young's modulus and tensile strength. The dry solution spinning was carried out by injection of concentrated dispersions through 0.51 mm diameter needles into molds precut on a Teflon sheet at a volumetric rate of 0.5 mL/min. Each fiber was allowed to air dry. Following drying, the fibers were removed from the molds for characterization. The order of magnitude difference between the dilute LSZ-TTAB-SWNT wet spun (line 1) and concentrated LSZ-TTAB-SWNT dry spun (line 2) Young's modulus and tensile strength are due to the inclusion of PVA in the wet spun fibers. In order to gain the elastic and elongational benefits of PVA without completely overcoating the LSZ, PVA was incorporated directly into the dispersion. However, exploration of numerous solvents failed to coagulate the resultant dispersion; salts were not used since they could crystallize into the fiber matrix. Therefore, the resulting fibers were dry spun. Dry spinning of free-standing fibers from SWNT dispersions has typically failed due to either solvent volatility or a lack of extensional viscosity. In this case, however, dry spinning of continuous fibers onto Teflon surfaces was possible. In order to understand the influence of the dispersion state on fiber properties, four different dispersions were dry spun at the same conditions. Table 6 shows the tensile properties of the LSZ-SWNT and LSZ-TTAB-SWNT mixture and supernatant dispersions in PVA.

Sample	Young's Modulus (GPa)	Tensile Strength (MPa)	Strain at Failure (%)	Toughness (J/g)
LSZ-TTAB-SWNT Mixture 0.24 vol.% - 0.34 vol.% - 0.28 vol.% Wet Spun into 4.10 vol.% PVA	3.5 ± 0.5	49.1 ± 6.0	3.0 ± 0.7	-
LSZ-TTAB-SWNT Mixture 3.17 vol.% - 4.63 vol.% - 3.71 vol.% Dry Spun	0.4 ± 0.0	4.5 ± 0.6	1.9 ± 0.3	-
LSZ-SWNT Mixture in PVA 0.71 vol.% - 0.16 vol.% in 10.21 vol.% Dry Spun	22.3 ± 1.7	723.4 ± 47.5	3.7 ± 0.4	15.6
LSZ-SWNT Supernatant in PVA 0.36 vol.% - 0.03 vol.% in 9.99 vol.% Dry Spun	26.3 ± 1.6	774.5 ± 53.0	37.6 ± 0.8	268.4
LSZ-TTAB-SWNT Mixture in PVA 1.00 vol.% - 1.44 vol.% - 1.17 vol.% in 9.68 vol.% Dry Spun	32.0 ± 0.3	891.6 ± 30.5	61.2 ± 2.8	385.7
LSZ-TTAB-SWNT Supernatant in PVA 0.51 vol.% - 0.73 vol.% - 0.24 vol.% in 10.93 vol.% Dry Spun	47.0 ± 1.4	1718.6 ± 93.7	86.9 ± 13.2	660.9

**Table 6.** Mechanical test data for LSZ-SWNT and LSZ-TTAB-SWNT fibers from both wet and dry spun assembly methods illustrating the effect of dispersion state and processing method on the final mechanical properties.

The differences in strength, elasticity, and toughness is a function of the dispersion state from which each fiber was made. The respective supernatant fibers have greater strength and tensile properties than the respective mixture fibers. This is due to the larger number and size of aggregates present within the mixture fibers, which create non-homogenous sections easily torn by the stress during mechanical testing. The individual or small bundle SWNT present in the supernatant are more easily aligned through flow alignment during syringe-pump injection to the molds. This alignment, in addition to reduced aggregation, leads to the increased mechanical properties.<sup>195</sup> The removal of SWNT aggregates by centrifugation in the supernatant eliminates

discontinuities in the homogeneity of the fiber. It is these discontinuities (SWNT aggregates) within the mixture fibers which induce failure during the tensile testing of these fibers thereby reducing their overall strength.<sup>196</sup> Comparison of the 3.17 vol.% LSZ - 4.63 vol.% TTAB - 3.71 vol.% SWNT mixture dispersion dry spun not containing PVA shows that there is over a two order of magnitude difference in the tensile properties when compared to the 0.71 vol.% LSZ - 0.16 vol.% SWNT mixture in 10.21 vol.% PVA and 1.00 vol.% LSZ - 1.44 vol.% TTAB - 1.17 vol.% SWNT mixture in 9.68 vol.% PVA. It is the inclusion of PVA which creates a synergistic effect in increasing the mechanical properties of the fibers, as the contribution of pure PVA to the system is estimated at less than 1% of the mechanical strength.<sup>197-198</sup> The increased mechanical robustness of LSZ-TTAB-SWNT is due to the increased concentration of phase transition as seen in Table 5. The decrease in number and size of SWNT aggregates in the LSZ-TTAB-SWNT allows for better mechanical translation of SWNT properties.

In addition to ultimate strength and stiffness, particular attention should be given to toughness. It is probably one of the most critical parameters in many applications, including ballistic and aviation materials, as it is the total energy needed to rupture a fiber. It should first be noted that methods of improving toughness in CNT nanocomposite systems are not well-understood and have been achieved in the past mostly by rather accidental discoveries.<sup>199</sup> LSZ-TTAB-SWNT in PVA mixture and supernatant dry-spun fibers have a toughness of, 386 J/g and 661 J/g, which is approximately 2.7% and 38.7%, respectively, greater than any previously reported toughness values of SWNT composites.<sup>199</sup> For comparison, spider silk has a Young's modulus of 4 GPa and a toughness of 217 J/g. Overall, it is hypothesized that the strengthening and toughening mechanisms are likely to be a synergistic multiscale action of intermolecular interactions, improved load transfer, surface roughening, and energy dissipation. Of particular

interest to this research are previous studies on SWNT composite fibers have shown that PVA forms a coating on the nanotubes providing an important interphase region where the toughness arises from chain extension in amorphous regions between relatively rigid SWNT and amorphous PVA. In addition, slippage between individual nanotubes within bundles might also contribute to toughness.<sup>199-203</sup> The differences in mechanical properties, dispersion state, and processing methods demonstrates the ability for the complex LSZ-SWNT system to be adapted to overcome a myriad of obstacles.

Concentrated dispersions of LSZ-TTAB-SWNT in PVA were further characterized. SEM images of 1.00 vol.% LSZ - 1.44 vol.% TTAB - 1.17 vol.% SWNT in 9.68 vol.% PVA and 0.51 vol.% LSZ - 0.73 vol.% TTAB - 0.24 vol.% SWNT in 10.93 vol.% PVA dry spun fibers show varying surface morphology and mechanical robustness through the knot tied in each, as shown in Figure 74.<sup>183-184</sup> The maintenance of the relatively smooth surface with PVA may be due to the hydrogen bond interactions between PVA and the hydrophilic surfaces of LSZ and TTAB. It is this interaction which also play critical roles in the mechanical properties of the fibers.

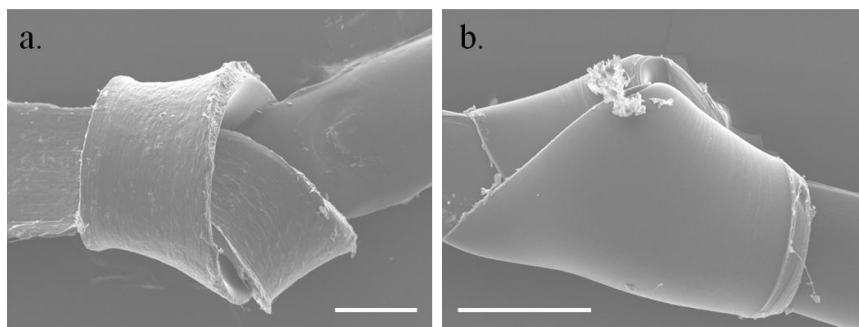


**Figure 74.** Scanning electron micrographs showing the mechanical robustness (knot) and smooth surface morphology of a.) 1.00 vol.% LSZ - 1.44 vol.% TTAB - 1.17 vol.% SWNT mixture in 9.68 vol.% PVA fiber extruded from a 0.84 mm diameter needle and b.) 0.51 vol.% LSZ - 0.73 vol.% TTAB - 0.24 vol.% SWNT supernatant in 10.93 vol.% PVA fiber extruded from a 0.26 mm diameter needle. The scale bar shown in each image is 500 nm.

The variations in the fiber surfaces shown in Figure 74 are likely due to differences in pressure drop associated with needle diameters used as well as the differences in the initial dispersion state. Pottick showed with poly(p-phenylene benzobisthiazole) that increasing the pressure drop during extrusion modifies the surface morphology of fibers.<sup>129</sup> In the case of these fibers, the increased pressure drop leads to smoother surfaces. However, the ribbon-like structure of these fibers is due to the drying process. As the water evaporated, the weight of the fiber caused it to collapse from a cylindrical fiber into a ribbon-like structure.

Figure 75 shows the Raman spectra (514 nm excitation), of the LSZ-TTAB-SWNT mixture and supernatant in PVA as well as the initial SWNT material. Raman spectroscopy was performed using both 514 nm and 785 nm excitation lasers. The 514 nm laser data is of particular interest as it probes the LSZ-SWNT system as well as the PVA polymer backbone. The spectra show characteristic radial breathing modes (RBM) from  $100\text{ cm}^{-1}$  to  $400\text{ cm}^{-1}$ , the D peak due to  $\text{sp}^3$  hybridized carbons at  $\sim 1335\text{ cm}^{-1}$ , the G peak due to tangential  $\text{sp}^2$  hybridized carbons at  $\sim 1589\text{ cm}^{-1}$ , and the G' peak at  $\sim 2645\text{ cm}^{-1}$  which is the second overtone of the D peak. Several facets of these spectra support the existence of noncovalent functionalization of individual SWNT with LSZ-TTAB complex. The D:G ratios vary only slightly between SWNT (0.13), LSZ-TTAB-SWNT mixture (0.15), and LSZ-TTAB-SWNT supernatant (0.12) indicating a noncovalent interaction. An interesting facet of the Raman spectra shown in Figure 4b is the evidence of charge transfer by the G'-peak. Both the  $\text{G}^{153-154}$  and  $\text{G}'^{23, 152}$  peaks have been used to indicate doping effects. However, for the data collected here, charge transfer is best elucidated by the G'-peak position shift as well as a decrease in G:G' as shown in Table 7 due to the G'-peak being independent of tensile load transfer.<sup>152, 204</sup> Charge transfer for the present system is expected due to the presence of the quaternary ammonium ion present in the cationic surfactant

TTAB. The lack of a shift in the G-peak could be explained by a combinatorial effect of charge transfer causing an upshift in frequency and tensile load transfer causing a downshift in frequency.<sup>205</sup> The presence of tensile load transfer is supported by the increase in mechanical data from LSZ-TTAB-SWNT to LSZ-TTAB-SWNT in PVA. Another interesting aspect of the Raman spectra is the shifting of the RBM peak positions as shown in the inset of Figure 75a. As previously described, the addition of TTAB to the LSZ-SWNT results in significant debundling of the SWNT as evidenced by the van Hove singularities shown in Figure 66a. This debundling of SWNT has been reported to result in shifting of RBM peaks.<sup>206</sup> In addition, it has been shown that changes in aggregation state result in different chirality SWNT being in resonance with a fixed-wavelength laser.<sup>207</sup> Furthermore, charge transfer has been linked to shifts in the RBM peaks.<sup>208</sup> It is not fully understood for this system the reason for the shifting, but is likely due to one of the aforementioned. Finally, Raman shows the polymer backbone of the PVA present in each fiber as shown by the peak for the supernatant and mixture at ~2910 seen in Figure 75a and b.<sup>209-210</sup>

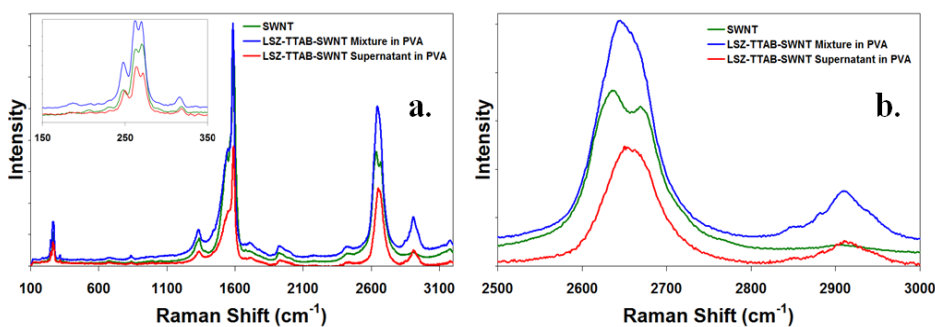


**Figure 75.** a.) Raman spectra of SWNT and LSZ-TTAB-SWNT mixture and supernatant fibers using a 514 nm excitation laser showing the characteristic RBM, D-, G-, and G'-peaks, as well as the CH<sub>2</sub> stretch associated PVA for those dispersions containing PVA. b.) Magnified Raman spectra showing the shifts in the G'-peak and characteristic CH<sub>2</sub> stretch associated with the polymer backbone stretching of PVA.

514 nm Laser								
Sample	D-Peak		G-Peak		G'Peak		D/G	G/G'
	Shift	Intensity	Shift	Intensity	Shift	Intensity		
SWNT	1338	4339	1589	34316	2636	18070	0.126	1.90
LSZ-TTAB-SWNT Supernatant in PVA	1338	2289	1589	18928	2650	12278	0.121	1.54
LSZ-TTAB-SWNT Mixture in PVA	1332	5668	1586	38497	2646	25287	0.147	1.52

**Table 7.** Raman spectroscopy data for 514 nm excitation laser. The changes in G'-peak position coupled with the decrease in G:G' indicate charge transfer between SWNT and LSZ-TTAB complex present in each fiber.

The electrical conductivity of the fibers was tested as shown in Table 8. As would be expected, the fibers which contain no natural or synthetic polymer have significantly higher conductivities than those which contain PVA or were spun into PVA. This is due to the fact that PVA is an insulator. It should also be noted that although some biopolymers have been shown to help electrical conductivity, LSZ has been shown to have insulating properties which will naturally inhibit the electrical conductivity of the fibers.<sup>211</sup> For reference, pure SWNT fibers have been shown to have electrical resistivity as low as  $0.1 \mu\Omega\text{-cm}$ .<sup>2, 33</sup> Therefore, by comparison, all the fibers created in this research can be classified as insulators although they are capable of carrying small amounts of electrical current. It could be possible to increase the conductivity of these fibers through introduction of additional electrically conductive materials, such as polypyrrole.<sup>109, 212</sup> However, consideration should be taken into how the introduction of other materials is going to affect the mechanical, antibacterial, or optical properties of the dispersion.

Sample	Electrical Resistivity ( $\Omega \cdot \text{cm}$ )	Electrical Conductivity ( $\text{S} \cdot \text{m}^{-1}$ )
LSZ-TTAB-SWNT Mixture 0.24 vol.% - 0.34 vol.% - 0.28 vol.% Wet Spun into 4.10 vol.% PVA	1.17E+07	8.74
LSZ-TTAB-SWNT Mixture 3.17 vol.% - 4.63 vol.% - 3.71 vol.% Dry Spun	4.65E+05	230.32
LSZ-SWNT Mixture in PVA 0.71 vol.% - 0.16 vol.% in 10.21 vol.% Dry Spun	3.38E+09	0.04
LSZ-SWNT Supernatant in PVA 0.36 vol.% - 0.03 vol.% in 9.99 vol.% Dry Spun	2.23E+09	0.05
LSZ-TTAB-SWNT Mixture in PVA 1.00 vol.% - 1.44 vol.% - 1.17 vol.% in 9.68 vol.% Dry Spun	2.94E+08	0.41
LSZ-TTAB-SWNT Supernatant in PVA 0.51 vol.% - 0.73 vol.% - 0.24 vol.% in 10.93 vol.% Dry Spun	2.98E+08	0.41

**Table 8.** Electrical resistivity and conductivity of various fibers from both wet spun and dry spun assembly methods, illustrating the effect of dispersion state and processing methods on the electrical conductivity of macroscopically assembled fibers.

Optical microscopy of fibers of LSZ-TTAB-SWNT mixtures and supernatants in PVA reveal the reduced aggregation state of the dispersion compared to the LSZ-SWNT dispersion microscopy, as well as the anisotropic effects of drawing. Microscopy was done on both the mixture and supernatant fibers. Figure 76 shows the non-polarized and cross-polarized optical micrographs of 0.51 vol.% LSZ - 0.73 vol.% TTAB - 0.24 vol.% SWNT supernatant in 10.93 vol.% PVA fiber extruded from a 0.26 mm diameter needle. As can be seen, both images show homogenous fibers with no visible aggregation. The lines seen in each image are not SWNT aggregates but rather drying defects associated with the PVA present in each fiber.<sup>129</sup> These

defects, which can be folds, tears, wrinkles, etc., can cause increased absorption, reflection, or refraction of transmitted light leading to the lines seen in Figures 76 and 77.<sup>130</sup> In addition to not showing any visible aggregation, the images also do not show optical anisotropy under cross polarized light. This is due to the lack of alignment of either SWNT or PVA. Figure 77 shows optical micrographs of 0.51 vol.% LSZ - 0.73 vol.% TTAB - 0.24 vol.% SWNT supernatant in 10.93 vol.% PVA fiber extruded from a 0.26 mm diameter needle which has been drawn after drying. The non-polarized, partially polarized, and cross-polarized micrographs show the change in color associated with alignment anisotropy. This anisotropy is likely the alignment of the PVA polymer backbone. The differences in Figures 76 and 77 are important as it shows the tailorability of the dispersions, and how different methods in processing can create macroscopic assemblies with unique properties for a wide range of applications.

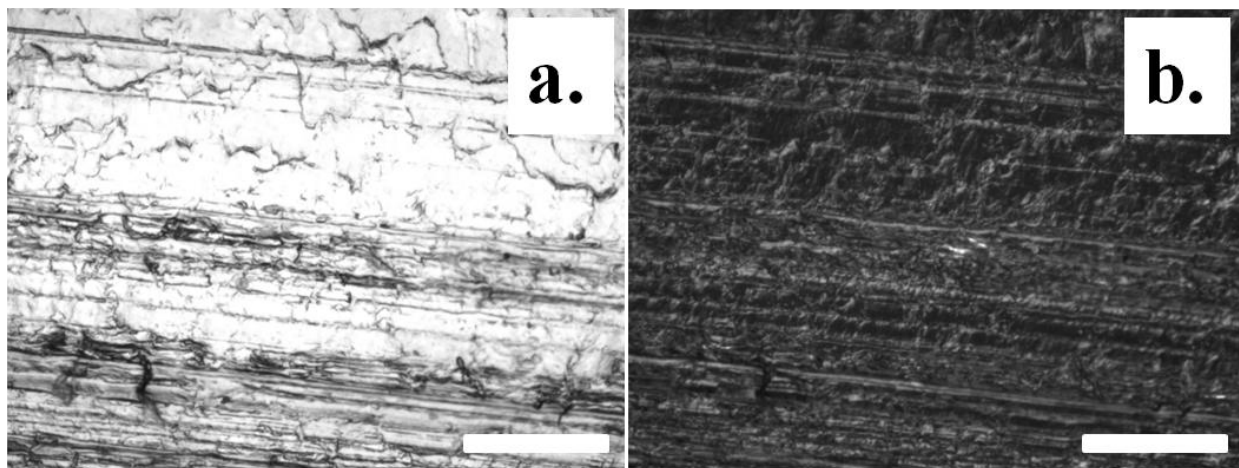


**Figure 76.** a.) Non-polarized ( $0^\circ$ ) and b.) cross-polarized ( $89^\circ$ ) optical micrographs of 0.51 vol.% LSZ - 0.73 vol.% TTAB - 0.24 vol.% SWNT supernatant in 10.93 vol.% PVA fiber extruded from a 0.26 mm diameter needle. The scale bar shown in each image is 100  $\mu\text{m}$ .

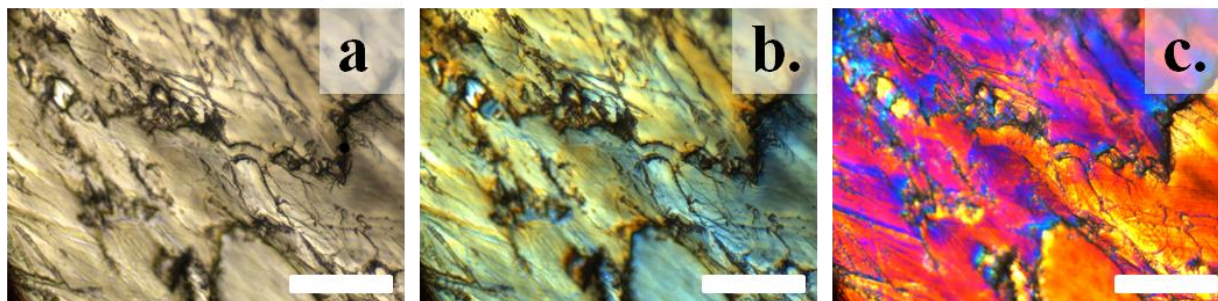


**Figure 77.** a.) Non-polarized ( $0^\circ$ ), b.) partially cross-polarized ( $79^\circ$ ), and c.) cross-polarized ( $138^\circ$ ) optical micrographs of 0.51 vol.% LSZ - 0.73 vol.% TTAB - 0.24 vol.% SWNT supernatant in 10.93 vol.% PVA fiber extruded from a 0.26 mm diameter needle which has been drawn showing alignment anisotropy. The scale bar shown in each image is 100  $\mu\text{m}$ .

To further elucidate the alignment of SWNT and the PVA polymer backbone, polarized Raman spectroscopy was done as shown in Figure 78. Because of the anisotropic polarization of SWNT, the ratio of SWNT Raman G-band intensity, parallel versus perpendicular, provides a useful probe of the relative degree of alignment. The alignment of SWNT fibers has been well documented, and various SWNT materials have been shown to have different alignment ratios: pristine, extruded SWNT fibers – 20:1,<sup>5, 69</sup> magnetically aligned SWNT fibers – 4:1,<sup>213</sup> gel-spun polymer-SWNT composites – 106:1.<sup>214</sup> For the 514 nm and 785 nm excitation laser the alignment is 3.3:1 and 9.1:1, respectively, indicating that post-process drawing of the fibers aligns the SWNT and polymer backbone present in the fibers leading to the anisotropy as seen in Figure 77. However, of interesting note in Figure 78 is that the intensity of the PVA specific stretching at  $\sim 2900$  for 514 nm indicates that the alignment of the polymer backbone is not likely the primary cause of optical anisotropy.

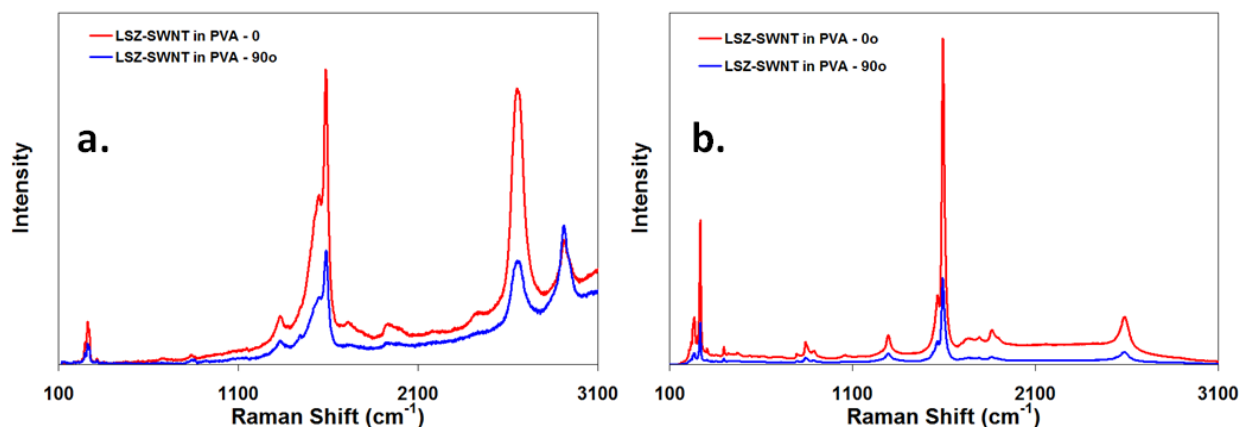


**Figure 78.** Raman analysis of LSZ-SWNT in PVA fibers with excitation laser of a.)514 nm and b.) 785 nm showing alignment through the ratio of  $G_{\parallel}:G_{\perp}$ . Also of note is that the intensity of the PVA specific stretching at  $\sim 2900\text{ cm}^{-1}$  for 514 nm indicates that the alignment of the polymer backbone is not likely the primary cause of optical anisotropy.

<b>514 nm Laser</b>				
Sample	D/G	G/G'	SWNT Alignment	PVA Alignment
LSZ-SWNT in PVA - $0^{\circ}$	0.200	0.840	3.260	1.014
LSZ-SWNT in PVA - $90^{\circ}$	0.372	0.743		
<b>785 nm Laser</b>				
Sample	D/G	G/G'	SWNT Alignment	PVA Alignment
LSZ-SWNT in PVA - $0^{\circ}$	0.153	4.694	9.147	-
LSZ-SWNT in PVA - $90^{\circ}$	0.398	3.492		

**Table 9.** Raman spectroscopy data for 514 and 785 nm excitation laser showing the D/G and G/G' ratio along with the alignment ratio –  $G(0^{\circ}):G(90^{\circ})$  – for LSZ-SWNT in PVA fibers indicating an increase in alignment of polymer backbone and SWNT through post-process drawing.

#### 4.5.2. FILMS

Previous research on the layer-by-layer assembly of aqueous dispersions of 0.30 vol.% LSZ – 0.07 vol.% SWNT with 0.81 vol.% dsDNA – 0.12 vol.% SWNT resulted in a unique coating possessing antibacterial activity and high Young's Modulus.<sup>19</sup> However, depletion attraction limited the robustness of free standing films from higher concentration dispersions. PVA is known for its flexibility and tensile strength, and has been incorporated into LSZ-SWNT dispersions to add elasticity and fill voids between SWNT resulting from microstructural defects.<sup>15</sup> The PVA forms a structural matrix surrounding the LSZ-SWNT bundles to achieve greater durability and elasticity. Film casting was carried out by extrusion of concentrated LSZ-SWNT in PVA dispersions into either a 6 in diameter glass Petrie dish or onto a 4 in diameter circular Teflon mold. The dispersions were manually leveled through rotation of the substrate to allow for homogeneity of the film thickness. After the dispersion was leveled it was allowed to dry in a fume hood. Regardless of LSZ, SWNT, or PVA content in the final, dry film the average moisture content was approximately 6%.

SEM was used to characterize the surface morphology of the film as well as show the presence and size of SWNT. To prepare the film for SEM, a small section of the film was cut and a scalpel was used to create a tear through the middle to allow for visualization of SWNT as shown in Figure 79. The surface of the film was smooth as evidenced in Figure 79a which is expected due to the presence of the PVA. The smoothness of the surface along with no definitive voids or fractures in the macroscopic structure aids in the mechanical robustness of the film, which will be discussed later. The presence of small bundle SWNT of approximately 10 nm diameter, as shown in Figure 79b, indicates the starting dispersion was well dispersed and stabilized. The presence of small bundle SWNT also increases the mechanical robustness of the

film through increased interfacial interactions, as compared to that of large bundle SWNT. It should be noted that electron microscopy of drawn films was completed but showed no difference in surface morphology.

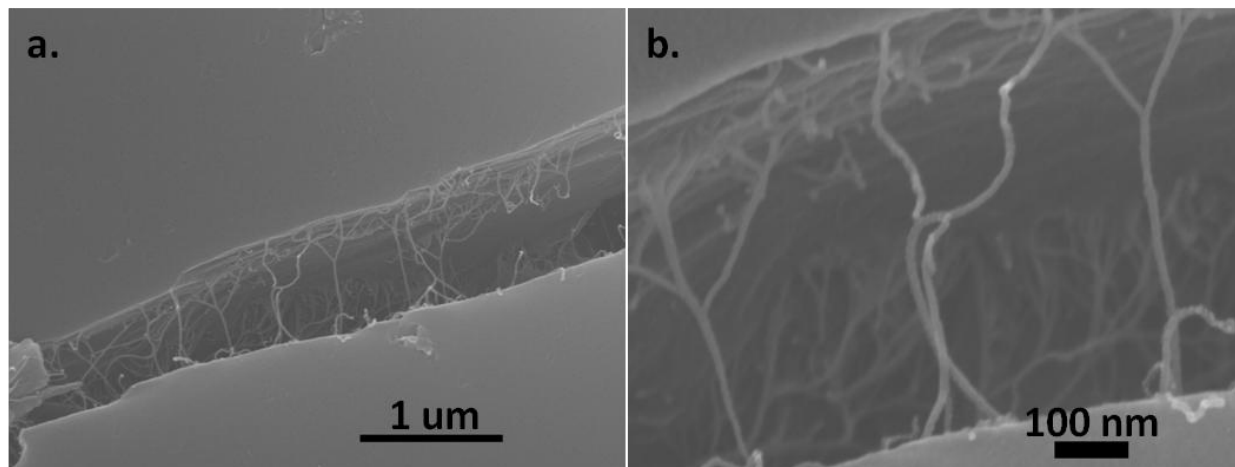


**Figure 79.** SEM images of LSZ-SWNT in PVA film at a) 25,000x and b.) 150,000x showing the smooth surface morphology as well as the presence of SWNT bundles approximately 10 nm in diameter.

Optical microscopy was used to identify anisotropic changes in the film after post-process drawing of the film. As with the fibers, LSZ-SWNT in PVA films show optical anisotropy under cross-polarized light, as shown in Figure 80. The reason for anisotropy is analogous to that seen in the fibers – the alignment of SWNT and PVA polymer backbone. The ability to change the optical properties of both the fibers and films only increases the potential applications and allows for tailorability of the film through processing.

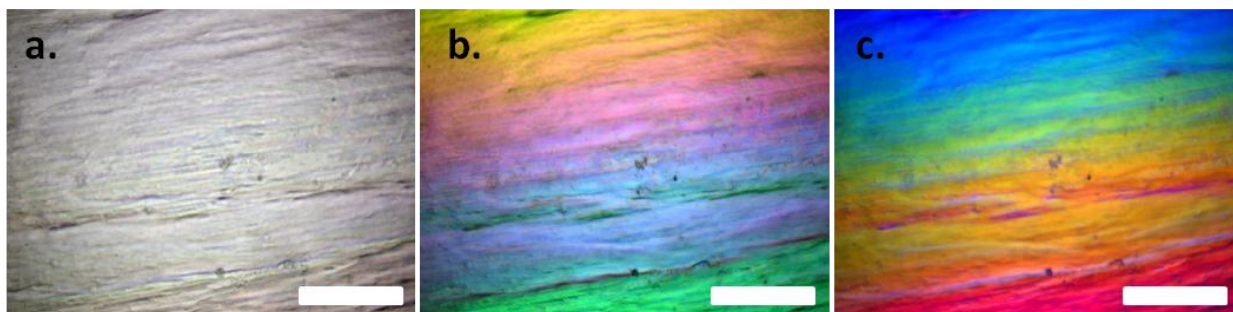


**Figure 80.** Optical micrographs of post-process drawn 40 vol.% LSZ – 5.1 vol.% SWNT in 54 vol.% PVA film at cross polarizations of a.) 4°, b.) 48°, and c.) 93° showing the optical anisotropy induced through alignment of the SWNT and polymer backbone. The scale bar shown in each image is 100  $\mu\text{m}$

FTIR analysis was conducted to ascertain interaction between LSZ, SWNT, and PVA within the solid films. Figure 81 shows the ATR-FTIR spectra of the two LSZ-SWNT in PVA film types: mixture films and a supernatant film. The two film spectra were compared to individual ATR-FTIR spectra of dried SWNT, LSZ, and PVA samples. The characteristic amide I ( $\sim 1650\text{ cm}^{-1}$ ) and amide II ( $\sim 1535\text{ cm}^{-1}$ ) peaks of LSZ were present in the mixture and supernatant films of LSZ-SWNT in PVA. The films also reflected several characteristic peaks of PVA, evident in all three spectra: the C-H stretch in alkyl chains produces a peak at  $\sim 2940\text{ cm}^{-1}$ , the stretching C=O in alcohols present a peak at  $\sim 1740\text{ cm}^{-1}$ , the C-O stretching in alcohols shows a peak at  $\sim 1140\text{ cm}^{-1}$ , and at  $\sim 2950\text{ cm}^{-1}$  a peak is caused by the terminating methyl group in PVA interacting with a terminating amine group in LSZ producing methylamine vibrations.<sup>29</sup> Indications of SWNT can also be ascertained. The LSZ-SWNT mixture and supernatant films show increasing absorbance from  $\sim 1500\text{ cm}^{-1}$  to  $\sim 700\text{ cm}^{-1}$  which is also seen in pristine SWNT. These results clearly indicate that LSZ, SWNT, and PVA interacted and carried over from the liquid dispersion into the film, in agreement with previous work.<sup>8, 51, 134, 146</sup> A primary indication

of the presence of interaction rather than separate individual components is the red or blue shifting of peaks relative to their pure components attributed to the change in molecular orientation due to the effect of being dispersed in aqueous media by the changing polarity of the environment.<sup>9</sup> This ATR-FTIR data thus supports that there is an interaction between LSZ, SWNT, and PVA within the films.

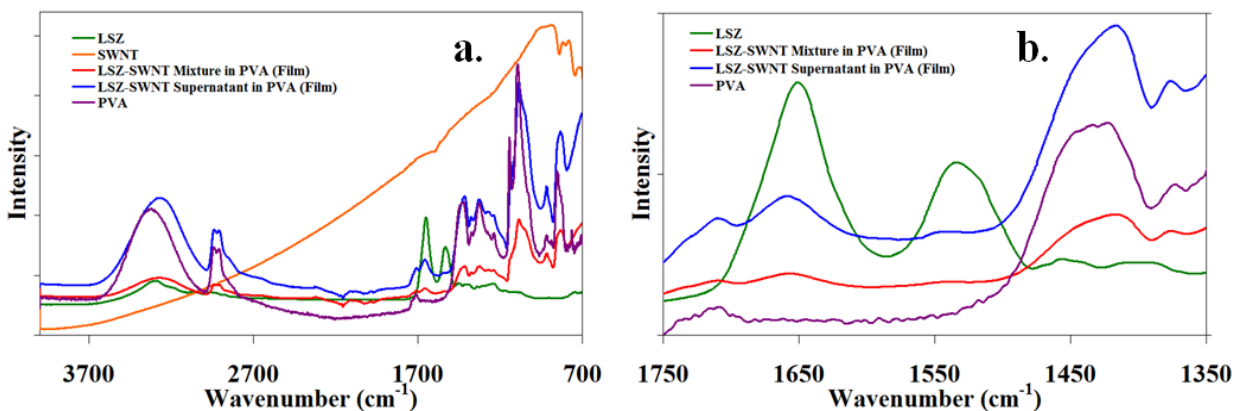


**Figure 81.** ATR-FTIR spectra a.) covering the entire frequency range scanned and b.) an enlarged section showing the amide I (1650  $\text{cm}^{-1}$ ) and II (1535  $\text{cm}^{-1}$ ) peaks of all LSZ containing samples, as well as, the methylamine peak (1430  $\text{cm}^{-1}$ ) present in all LSZ-PVA containing samples.

Mechanical characterization was conducted to determine the tensile properties of each type of film. Significant property differences were seen between the two film types. As shown in Table 10, films cast from the supernatant films were stronger than those from the bulk mixture. The Young's modulus and tensile strengths were 63% and 34% higher respectively. These results can be attributed to the supernatant films being comprised primarily of individual SWNT; individuals have greater specific surface area, and therefore more interfacial interactions with the matrix and greater reinforcement potential.<sup>205, 215</sup> Another way to view the strength results is to

note that the number and size of aggregates present in the mixture is considerably greater and aggregated SWNT do not translate their outstanding mechanical properties to the macroscale. In addition, the aggregates can develop fault lines within the films, where the film will be weaker and more susceptible to stress during tensile testing. Counterintuitively, the film from the bulk mixture had more than twice the elongation at break. At this point it is not clearly understood as to why this phenomena occurred, however, it is likely a function of colloidal interactions in the dispersion state, surface area of accessible SWNT, and/or the concentrations and interactions among the constituents.

Sample	Young's Modulus (MPa)	Tensile Strength (MPa)	Tensile Strain (%)
Control Film: 47 wt.% LSZ - 53 wt.% PVA	490 ± 51	69 ± 4.8	27 ± 0.28
Mixture Film: 45 wt.% LSZ - 9 wt.% SWNT - 45 wt.% PVA	3100 ± 34	86 ± 1.9	6.7 ± 0.77
Supernatant Film: 34 wt.% LSZ - 4.5 wt.% SWNT - 61 wt.% PVA	4100 ± 270	120 ± 4.3	12 ± 0.90

**Table 10.** Mechanical property data collected from the ultimate tensile strain test conducted on both mixture and supernatant LSZ-SWNT in PVA films.

Finally, as expected due to the high PVA concentration, characterization of electrical properties showed no evidence of conductivity for either type of film. The experiments were performed on several film pieces, with varying distances from the edge. Various regions of the film showed negligible differences in results. Only by positioning the electrical leads unrealistically close did any electrical current pass. This suggests that PVA and LSZ are so resistive and in such high loadings that their presence negated the intrinsic conductivity of the SWNT.

#### 4.6. LYSOZYME – CARBON NANOTUBE ANTIBACTERIAL ACTIVITY

LSZ is already commercially used in food packaging and mouthwash,<sup>216</sup> and there is interest in using it for antibacterial surfaces.<sup>8, 217</sup> The combination of the antibacterial activity of LSZ with the mechanical and electrical properties of SWNT has potential for robust multifunctional materials. A key goal of this work was to maintain the antibacterial property of LSZ during processing with SWNT. Although LSZ can be used purely as a dispersant for SWNT, the uniqueness of this system is that LSZ provides enzymatic activity to the dispersion. In order to prove the maintenance of the antibacterial properties of LSZ while dispersed with SWNT, CD was performed to show no significant changes in the secondary structure of LSZ and turbidimetric analysis was done to show the actual antibacterial activity of the LSZ-SWNT dispersions.

CD measurements were taken of 0.30 vol.% LSZ – 0.07 vol.% SWNT dispersions to elucidate that no negative change in secondary structure occurred due to the addition of SWNT as shown in Figure 82. A negative change could have three separate consequences: loss of alpha helical structure, addition of beta sheet structure, or addition of random coil structures. As previously mentioned, alpha helices show characteristic peaks between 200 nm and 230 nm, beta sheets show a characteristic peak centered at 215 nm, and random coils show a characteristic peak centered at approximately 200 nm.<sup>118</sup> As shown in Figure 82, the characteristic alpha helix peaks are present in both the LSZ-SWNT dispersion and processed LSZ solution. The noticeable difference between the LSZ solution and the LSZ-SWNT dispersion is the peak between the wavelengths of 200 nm and 210 nm. This difference in peak magnitude has been described as an alpha helical well, and is possibly caused by the increased ordering of the alpha helices upon binding to SWNT.

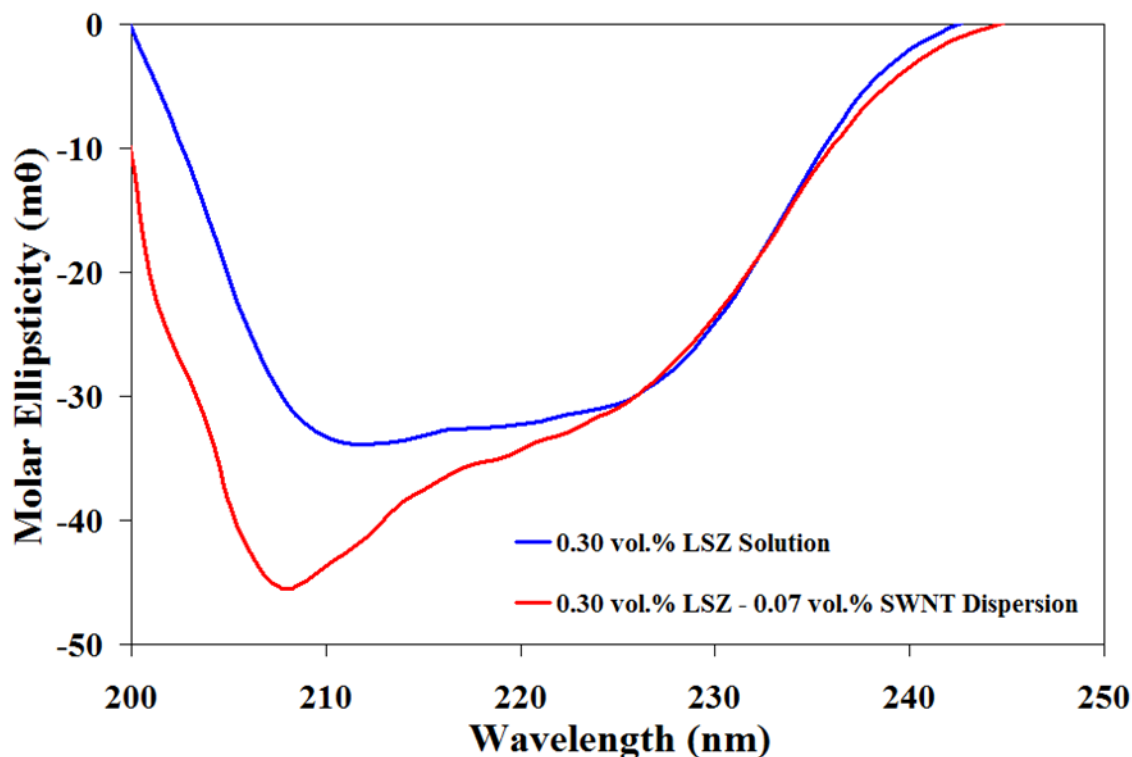


**Figure 82.** Far-UV CD spectrum of 0.30 vol.% LSZ – 0.07 vol.% SWNT and 0.30 vol.% LSZ solution which has been processed showing characteristic alpha helical peaks.

CD measurements are able to determine the secondary structure of proteins and enzymes present in a solution. The material becoming more ordered or more disordered, will lead to changes in the magnitude of a representative peak. The more disordered a molecule becomes, the lower the magnitude of the peak and vice versa. Therefore, the binding of LSZ to SWNT shows increases in the secondary structure ordering of LSZ alpha helices. Although it is not known at this time how the increased ordering affects the LSZ, it is hypothesized that the increased ordering could produce a synergistic enzymatic affect.

Turbidimetric analysis was performed on all dispersions and macroscopic assemblies of LSZ-SWNT to show that the LSZ has maintained its antibacterial properties within the LSZ-

SWNT complex. In order to determine the contribution of each constituent and the contribution of the interactions, all individual constituents were tested for activity. Figure 83 shows the activity analysis for water, LSZ, TTAB, PVA, LSZ-TTAB, and LSZ-PVA solutions. The decrease in absorbance for all solutions containing LSZ shows that they possess lytic activity, whereas the lack of a decrease in all the solutions which do not contain LSZ show no activity. The lack of lytic activity in TTAB and PVA verifies that the only active constituent in all prepared dispersions is LSZ.

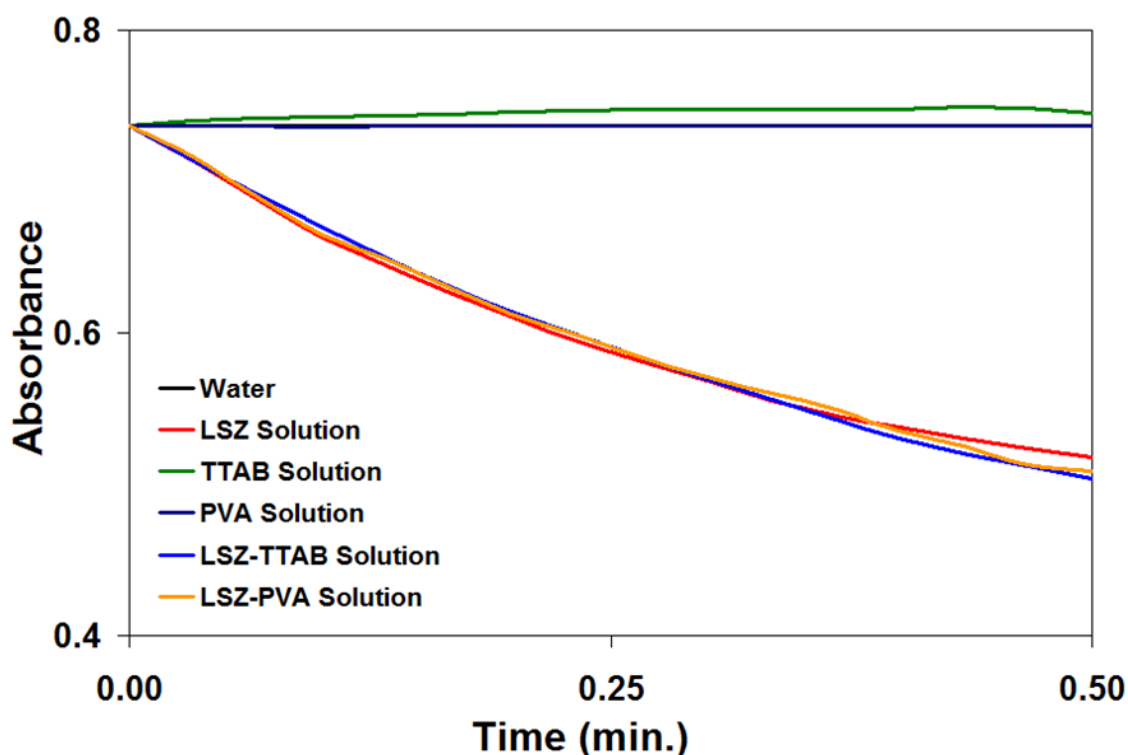


**Figure 83.** Turbidimetric analysis of all individual constituents present within LSZ-SWNT or LSZ-TTAB-SWNT dispersions or macroscopic assemblies showing non-inhibitory effect of TTAB and PVA on native LSZ activity. Activity was tested against *M. lysodeikticus*. It should be noted that the calculated error for each sample was less than that of the UV-vis, therefore, the error shown is that inherent of the UV-vis used in characterization.

Furthermore, the similar rates of cell death during lysis by the LSZ-TTAB and LSZ-PVA confirm the non-inhibitory nature of TTAB and PVA toward the native activity of LSZ. After processing of LSZ-SWNT dispersions, fibers, and films, turbidimetric analysis was done to determine the effect of dispersion state and processing on the LSZ activity in each dispersion and fiber. Figure 84 shows the activity of each dispersion and processed fiber as a percentage of native LSZ activity maintained where each sample has been normalized for the amount of LSZ present in the sample as determined by TGA. The initial LSZ-SWNT dispersions had over 99% of the native LSZ activity. This is greater than that observed by Ding et al. who achieved a maximum of 90% of native LSZ activity in the presence of silica nanotubes.<sup>218</sup> Furthermore, Merli et al. found that covalently bonding LSZ to MWNT via EDC/NHS actually increased activity,<sup>141</sup> however covalent functionalization has the disadvantages of reducing SWNT mechanical and electrical properties.<sup>21</sup> The activity of the supernatants being lower than that of the mixture was most likely due to the removal of excess LSZ during centrifugation thereby leaving only bound LSZ which could be sterically hindered when compared with the unbound LSZ in mixture dispersions. It is hypothesized that if the solid assemblies were normalized to the surface bound LSZ, and not to the total LSZ quantity which is not readily accessible, the activity would be much higher. Therefore the major difference between the dispersions and solid assemblies is likely to be surface to volume ratio and LSZ accessibility dependent. In addition, some studies have shown SWNT have inherent antimicrobial activity, therefore the reduced SWNT concentration may also have contributed to the reduced activity in the supernatant.<sup>219-220</sup> The LSZ-TTAB-SWNT dispersions show a similar trend as the LSZ-SWNT dispersions, however, the supernatant loses less activity. At this time, the reason for this decreased loss in activity is unknown but is likely due to a synergistic interaction between LSZ, SWNT, and TTAB, as there

was no indication of any such relationship between the LSZ and TTAB as seen in Figure 83. The concentrated mixture LSZ-TTAB-SWNT fiber maintains the highest degree of activity when compared with the LSZ-TTAB-SWNT fibers in PVA. The reasoning for this is likely due to the increased steric hindrance caused by incorporation of PVA which prevents the interaction of the LSZ active site with the bacterial cell wall.

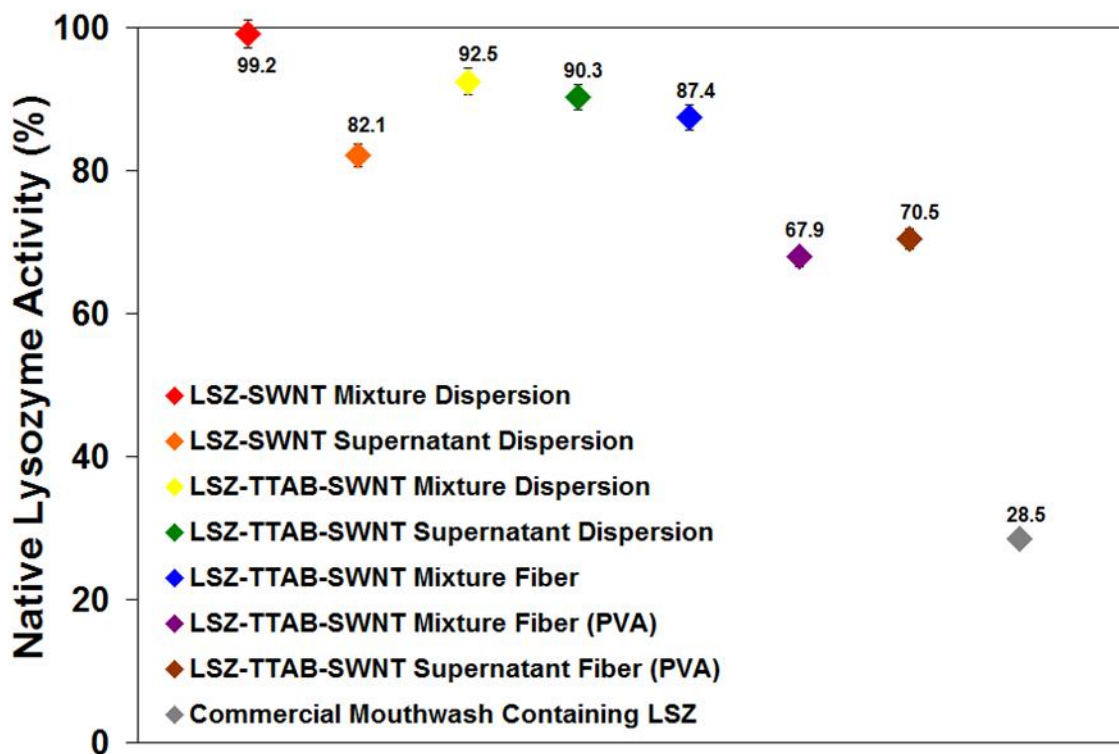


**Figure 84.** Lytic activity analysis of LSZ-SWNT and LSZ-TTAB-SWNT dispersions and macroscopic assemblies. Activity was tested against *M. lysodeikticus* and normalized for the mass of LSZ present in each sample. It should be noted that the calculated error for each sample was less than that of the UV-vis, therefore, the error shown is that inherent of the UV-vis used in characterization.

It should be noted that the loss in activity from LSZ-SWNT mixture dispersion to the resultant fiber (not shown) is approximately 60%, whereas the loss in activity from LSZ-TTAB-SWNT mixture to the least active resultant fiber is approximately 32%. The reasoning for this is unclear, however, likely involves the increased stability of the LSZ-TTAB-SWNT dispersions over the LSZ-SWNT dispersions. Overall, although there is a loss in activity, this data confirms the ability to process LSZ-SWNT dispersions into macroscopic assemblies which maintain antibacterial activity. Furthermore, it should be noted that a commercially available mouthwash containing LSZ maintains only 28.5% of native LSZ activity.<sup>221-222</sup> Therefore, although the loss of activity in LSZ-SWNT fibers seems significant, it is less than that of currently available commercial products.

## 5. CONCLUSIONS

The goal of this research was to expand on the previous research and exploit the properties of both LSZ and SWNT to create dispersions capable of macroscopic assembly for tailorable applications. These results were achieved through processing of LSZ and SWNT from dispersion to fiber or film. In order to fully realize this, the interaction, phase behavior, rheology, stabilization, and macroscopic assembly of LSZ-SWNT dispersions were analyzed and understood. This study led to antibacterial, mechanically robust fibers and films capable of being tailored to specific applications.

The research presented here has shown that LSZ not only disperses SWNT as individuals or small bundles, but molecularly interacts through a  $\pi$ - $\pi$  bond between the sidewall of SWNT and the hydrophobic tryptophan of LSZ, which maintains native antibacterial activity. Sharp van Hove singularities in the UV-vis absorbance of LSZ-SWNT dispersions between 1.6 eV and 2.4 eV qualitatively showed the characteristics of individuals or small bundles of SWNT. SEM images showed 10 nm bundles of SWNT surrounded by LSZ. These images qualitatively verify that LSZ molecularly interacts with SWNT, and quantitatively verifies that LSZ disperses SWNT as individuals or small bundles. In addition to LSZ being able to disperse SWNT through a molecular interaction, the research presented here shows that LSZ maintains its' structure and activity when coupled with SWNT. UV-CD spectra of LSZ and LSZ-SWNT show that each contain characteristic alpha helix peaks at 205 nm and 215 nm wavelengths verifying that the secondary structure of LSZ does not adversely change when coupled with SWNT. Furthermore, turbidimetric analysis in the presence of *M. lysodeikticus* verifies that the antibacterial properties of LSZ are maintained in LSZ-SWNT dispersion mixtures, supernatants, and macroscopic assemblies.

The phase behavior of LSZ-SWNT dispersions has been shown to be complex. Dispersions transition from dilute isotropic liquids to concentrated physical gels. Through optical microscopy the phase transition can qualitatively be seen when the number and size of SWNT aggregates increases due to depletion interactions. Quantitatively the transition is shown through rheological analysis of the frequency sweep tests combined with the deviation of Cox-Merz rule and the viscosity increase. It was then shown that through the addition of a surfactant (TTAB) the LSZ-SWNT dispersion was able to be electrostatically stabilized to a higher degree reducing the amount of SWNT aggregation at a given concentration. Furthermore, the phase behavior was shown to be capable of being altered through the addition of natural or synthetic polymers without the loss of antibacterial activity. Understanding of the phase behavior of LSZ-SWNT dispersions was of extreme importance for determining methods of macroscopic assembly. Until now, no extensive experimental phase behavior or rheological characterization has been done on spherical biomolecule-dispersed SWNT solutions such as LSZ-SWNT.

Fibers and films of LSZ-SWNT dispersions have been shown to be possible through wet and dry fiber spinning and film casting. The mechanical, electrical, and optical properties have been shown to be tailorable depending on dispersion constituents, dispersion state, and processing methods. This was done using a combination of mechanical testing, electrical resistivity testing, UV-vis and Raman spectroscopy, SEM, and optical microscopy. Furthermore, to the author's knowledge, the mechanical toughness has been shown to be greater than any previously made SWNT or SWNT-composite fiber. Finally, in addition to record toughness, the fibers and films were shown to be antibacterial through turbidimetric analysis.

The research presented here has wide ranging potential applications. The antibacterial maintained by all the dispersions would lend for the use of fibers or films in hospitals, airports,

train stations, or any high traffic area as a coating on common surfaces to prevent the spread of communicable illnesses such as the flu and the common cold. The toughness demonstrated by the LSZ-TTAB-SWNT in PVA fibers would make them a useful material for ballistics, aviation, automotive, or any application in which energy absorption is important. These potential applications will only be possible through further research on the foundation that has been presented in this research. Optimization of the fiber spinning or film casting process will only increase the mechanical robustness of the materials. Furthermore, understanding the interactions collectively taking place in LSZ-TTAB-SWNT in PVA dispersions will allow for incremental increases in SWNT concentration prior to aggregation which should result in better mechanical properties. In addition, this research lays the foundation for a route for experimental determination of interactions between biomolecules and SWNT, furthers basic understanding of particle and phase behavior theory of cylinder-sphere systems by helping to extend it to a polydisperse, interacting system, and shows a method for increasing SWNT concentration of kinetically stable dispersions through synergistic effects of compatible dispersants.

## REFERENCES

1. Iijima, S., Helical Microtubules of Graphitic Carbon. *nature* **1991**, 354 (6348), 56-58.
2. Thess, A.; Lee, R.; Nikolaev, P.; Dai, H.; Petit, P.; Robert, J.; Xu, C.; Lee, Y. H.; Kim, S. G.; Rinzler, A. G., Crystalline Ropes of Metallic Carbon Nanotubes. *Science* **1996**, 273 (5274), 483.
3. Ao, G.; Nepal, D.; Aono, M.; Davis, V. A., Cholesteric and Nematic Liquid Crystalline Phase Behavior of Double-Stranded DNA Stabilized Single-Walled Carbon Nanotube Dispersions. *ACS nano* **2011**.
4. Davis, V. A., Liquid Crystalline Assembly of Nanocylinders. *Journal of materials research* **2011**, 26 (02), 140-153.
5. Davis, V. A.; Ericson, L. M.; Parra-Vasquez, A. N. G.; Fan, H.; Wang, Y.; Prieto, V.; Longoria, J. A.; Ramesh, S.; Saini, R. K.; Kittrell, C., Phase Behavior and Rheology of Swnts in Superacids. *Macromolecules* **2004**, 37 (1), 154-160.
6. Kayatin, M. J.; Davis, V. A., Viscoelasticity and Shear Stability of Single-Walled Carbon Nanotube/Unsaturated Polyester Resin Dispersions. *Macromolecules* **2009**, 42 (17), 6624-6632.
7. Mantha, S.; Pedrosa, V. A.; Olsen, E. V.; Davis, V. A.; Simonian, A. L., A Renewable Nanocomposite Layer-by-Layer Assembled Catalytic Interfaces for Biosensing Applications. *Langmuir* **2010**, 26, 19114 – 19119
8. Nepal, D.; Balasubramanian, S.; Simonian, A. L.; Davis, V. A., Strong Antimicrobial Coatings: Single-Walled Carbon Nanotubes Armored with Biopolymers. *Nano letters* **2008**, 8 (7), 1896-1901.
9. Horn, D.; Tracy, K.; Easley, C. J.; Davis, V., Lysozyme Dispersed Single-Walled Carbon Nanotubes: Interaction and Activity. *The Journal of Physical Chemistry C* **2012**.
10. Nepal, D.; Geckeler, K. E., Ph-Sensitive Dispersion and Debundling of Single-Walled Carbon Nanotubes: Lysozyme as a Tool. *Small* **2006**, 2 (3), 406-412.
11. Iijima, S.; Ichihashi, T., Single-Shell Carbon Nanotubes of 1-Nm Diameter. *nature* **1993**.
12. Bethune, D.; Klang, C.; De Vries, M.; Gorman, G.; Savoy, R.; Vazquez, J.; Beyers, R., Cobalt-Catalysed Growth of Carbon Nanotubes with Single-Atomic-Layer Walls. *nature* **1993**.
13. Shin, S. R.; Lee, C. K.; So, I.; Jeon, J. H.; Kang, T. M.; Kee, C.; Kim, S. I.; Spinks, G. M.; Wallace, G. G.; Kim, S. J., DNA-Wrapped Single-Walled Carbon Nanotube Hybrid Fibers for Supercapacitors and Artificial Muscles. *Advanced Materials* **2008**, 20 (3), 466-470.
14. Collins, P. G.; Bradley, K.; Ishigami, M.; Zettl, A., Extreme Oxygen Sensitivity of Electronic Properties of Carbon Nanotubes. *Science* **2000**, 287 (5459), 1801.
15. Li, J.; Ng, H. T.; Cassell, A.; Fan, W.; Chen, H.; Ye, Q.; Koehne, J.; Han, J.; Meyyappan, M., Carbon Nanotube Nanoelectrode Array for Ultrasensitive DNA Detection. *Nano letters* **2003**, 3 (5), 597-602.
16. Dillon, A.; Jones, K.; Bekkedahl, T.; Kiang, C.; Bethune, D.; Heben, M., Storage of Hydrogen in Single-Walled Carbon Nanotubes. *nature* **1997**, 386 (6623), 377-379.
17. Journet, C.; Maser, W.; Bernier, P.; Loiseau, A.; Lamy de La Chapelle, M.; Lefrant, S.; Deniard, P.; Lee, R.; Fischer, J., Large-Scale Production of Single-Walled Carbon Nanotubes by the Electric-Arc Technique. *nature* **1997**, 388 (6644), 756-757.
18. Liu, J.; Rinzler, A. G.; Dai, H.; Hafner, J. H.; Bradley, R. K.; Boul, P. J.; Lu, A.; Iverson, T.; Shelimov, K.; Huffman, C. B., Fullerene Pipes. *Science* **1998**, 280 (5367), 1253.

19. Scott, C. D.; Povitsky, A.; Dateo, C.; Gokcen, T.; Willis, P. A.; Smalley, R. E., Iron Catalyst Chemistry in Modeling a High-Pressure Carbon Monoxide Nanotube Reactor. *Journal of Nanoscience and Nanotechnology*, 3 **2003**, 1 (2), 63-73.
20. Green, M. J.; Behabtu, N.; Pasquali, M.; Adams, W. W., Nanotubes as Polymers. *Polymer* **2009**, 50 (21), 4979-4997.
21. Dyke, C. A.; Tour, J. M., Covalent Functionalization of Single-Walled Carbon Nanotubes for Materials Applications. *The Journal of Physical Chemistry A* **2004**, 108 (51), 11151-11159.
22. Moniruzzaman, M.; Winey, K. I., Polymer Nanocomposites Containing Carbon Nanotubes. *Macromolecules* **2006**, 39 (16), 5194-5205.
23. Dresselhaus, M. S.; Dresselhaus, G.; Eklund, P.; Jones, D. E. H., *Science of Fullerenes and Carbon Nanotubes*. Academic Press New York: 1996; Vol. 965.
24. Haddon, R., Chemistry of the Fullerenes: The Manifestation of Strain in a Class of Continuous Aromatic Molecules. *Science* **1993**, 261 (5128), 1545.
25. Ebbesen, T.; Takada, T., Topological and Sp<sup>3</sup> Defect Structures in Nanotubes. *Carbon* **1995**, 33 (7), 973-978.
26. Yao, N.; Lordi, V.; Ma, S.; Dujardin, E.; Krishnan, A.; Treacy, M.; Ebbesen, T., Structure and Oxidation Patterns of Carbon Nanotubes. *Journal of materials research* **1998**, 13 (09), 2432-2437.
27. Baughman, R. H.; Zakhidov, A. A.; De Heer, W. A., Carbon Nanotubes--the Route toward Applications. *Science* **2002**, 297 (5582), 787.
28. Gao, G.; Çagin, T.; William III, A. G., Energetics, Structure, Mechanical and Vibrational Properties of Single-Walled Carbon Nanotubes. *Nanotechnology* **1998**, 9, 184.
29. Krishnan, A.; Dujardin, E.; Ebbesen, T.; Yianilos, P.; Treacy, M., Young's Modulus of Single-Walled Nanotubes. *Physical Review B* **1998**, 58 (20), 14013.
30. Yu, M. F.; Files, B. S.; Arepalli, S.; Ruoff, R. S., Tensile Loading of Ropes of Single Wall Carbon Nanotubes and Their Mechanical Properties. *Physical Review Letters* **2000**, 84 (24), 5552-5555.
31. Walters, D.; Ericson, L.; Casavant, M.; Liu, J.; Colbert, D.; Smith, K.; Smalley, R., Elastic Strain of Freely Suspended Single-Wall Carbon Nanotube Ropes. *Applied Physics Letters* **1999**, 74, 3803.
32. Frank, S.; Poncharal, P.; Wang, Z.; Heer, W. A., Carbon Nanotube Quantum Resistors. *Science* **1998**, 280 (5370), 1744.
33. Hone, J.; Llaguno, M.; Nemes, N.; Johnson, A.; Fischer, J.; Walters, D.; Casavant, M.; Schmidt, J.; Smalley, R., Electrical and Thermal Transport Properties of Magnetically Aligned Single Wall Carbon Nanotube Films. *Applied Physics Letters* **2000**, 77, 666.
34. Kim, P.; Shi, L.; Majumdar, A.; McEuen, P., Thermal Transport Measurements of Individual Multiwalled Nanotubes. *Physical Review Letters* **2001**, 87 (21), 215502.
35. Hone, J.; Whitney, M.; Piskoti, C.; Zettl, A., Thermal Conductivity of Single-Walled Carbon Nanotubes. *Physical Review B* **1999**, 59 (4), 2514-2516.
36. Kociak, M.; Kasumov, A. Y.; Gueron, S.; Reulet, B.; Khodos, I.; Gorbатов, Y. B.; Volkov, V.; Vaccarini, L.; Bouchiat, H., Superconductivity in Ropes of Single-Walled Carbon Nanotubes. *Physical Review Letters* **2001**, 86 (11), 2416-2419.
37. Tang, Z.; Zhang, L.; Wang, N.; Zhang, X.; Wen, G.; Li, G.; Wang, J.; Chan, C.; Sheng, P., Superconductivity in 4 Angstrom Single-Walled Carbon Nanotubes. *Science* **2001**, 292 (5526), 2462.

38. Collins, P. G.; Avouris, P., Nanotubes for Electronics. *Scientific American* **2000**, 283 (6), 62-69.
39. Palmer, K.; Ballantyne, M.; Galvin, J., The Molecular Weight of Lysozyme Determined by the X-Ray Diffraction Method. *Journal of the American Chemical Society* **1948**, 70 (3), 906-908.
40. da Silva, M. A.; Farhat, I. A.; Arêas, E. P. G.; Mitchell, J. R., Solvent-Induced Lysozyme Gels: Effects of System Composition and Temperature on Structural and Dynamic Characteristics. *Biopolymers* **2006**, 83 (5), 443-454.
41. Szymanska, A.; Hornowski, T.; Kozak, M.; Slosarek, G., The Saxs and Rheological Studies of Hewl Amyloid Formation. *Acta Phys. Pol., A* **2008**, 114, 447-454.
42. Knubovets, T.; Osterhout, J. J.; Connolly, P. J.; Klibanov, A. M., Structure, Thermostability, and Conformational Flexibility of Hen Egg-White Lysozyme Dissolved in Glycerol. *Proceedings of the National Academy of Sciences* **1999**, 96 (4), 1262.
43. White, J. S.; White, D. C., *Sourcebook of Enzymes*. CRC: 1997.
44. Asuri, P.; Bale, S. S.; Pangule, R. C.; Shah, D. A.; Kane, R. S.; Dordick, J. S., Structure, Function, and Stability of Enzymes Covalently Attached to Single-Walled Carbon Nanotubes. *Langmuir* **2007**, 23 (24), 12318-12321.
45. da Silva, M. A.; Areas, E. P. G., Solvent-Induced Lysozyme Gels: Rheology, Fractal Analysis, and Sol-Gel Kinetics. *Journal of colloid and interface science* **2005**, 289 (2), 394-401.
46. Caro, A.; Humblot, V.; Méthivier, C.; Minier, M.; Salmain, M.; Pradier, C. M., Grafting of Lysozyme and/or Poly (Ethylene Glycol) to Prevent Biofilm Growth on Stainless Steel Surfaces. *The Journal of Physical Chemistry B* **2009**, 113 (7), 2101-2109.
47. Corrigan, A. M.; Müller, C.; Krebs, M. R. H., The Formation of Nematic Liquid Crystal Phases by Hen Lysozyme Amyloid Fibrils. *Journal of the American Chemical Society* **2006**, 128 (46), 14740-14741.
48. da Silva, M. A.; Itri, R.; Arêas, E. P. G., Lysozyme Viscoelastic Matrices in Tetramethylurea/Water Media: A Small Angle X-Ray Scattering Study. *Biophysical chemistry* **2002**, 99 (2), 169-179.
49. Hirano, A.; Maeda, Y.; Akasaka, T.; Shiraki, K., Synergistically Enhanced Dispersion of Native Protein-Carbon Nanotube Conjugates by Fluoroalcohols in Aqueous Solution. *Chemistry-A European Journal* **2009**, 15 (38), 9905-9910.
50. Kamiyama, T.; Morita, M.; Kimura, T., Rheological Study of Lysozyme in Dimethyl Sulfoxide+ Water Solution at 298.15 K. *Journal of Chemical & Engineering Data* **2004**, 49 (5), 1350-1353.
51. Matsuura, K.; Saito, T.; Okazaki, T.; Ohshima, S.; Yumura, M.; Iijima, S., Selectivity of Water-Soluble Proteins in Single-Walled Carbon Nanotube Dispersions. *Chemical Physics Letters* **2006**, 429 (4-6), 497-502.
52. Mishraki, T.; Libster, D.; Aserin, A.; Garti, N., Lysozyme Entrapped within Reverse Hexagonal Mesophases: Physical Properties and Structural Behavior. *Colloids and Surfaces B: Biointerfaces* **2010**, 75 (1), 47-56.
53. Mishraki, T.; Libster, D.; Aserin, A.; Garti, N., Temperature-Dependent Behavior of Lysozyme within the Reverse Hexagonal Mesophases (Hii). *Colloids and Surfaces B: Biointerfaces* **2010**, 75 (2), 391-397.
54. O'Connell, M. J.; Boul, P.; Ericson, L. M.; Huffman, C.; Wang, Y.; Haroz, E.; Kuper, C.; Tour, J.; Ausman, K. D.; Smalley, R. E., Reversible Water-Solubilization of Single-Walled Carbon Nanotubes by Polymer Wrapping. *Chemical physics letters* **2001**, 342 (3-4), 265-271.

55. Autumn, K.; Sitti, M.; Liang, Y. A.; Peattie, A. M.; Hansen, W. R.; Sponberg, S.; Kenny, T. W.; Fearing, R.; Israelachvili, J. N., Evidence for Van Der Waals Adhesion in Gecko Setae. *Proceedings of the National Academy of Sciences* **2002**, 99 (19), 12252.
56. Prausnitz, J. M.; Lichtenthaler, R. N.; de Azevedo, E. G., Molecular Thermodynamics of Fluid-Phase Equilibria. **1986**.
57. Parsegian, V. A., *Van Der Waals Forces: A Handbook for Biologists, Chemists, Engineers, and Physicists*. Cambridge Univ Pr: 2006.
58. Hamaker, H., The London--Van Der Waals Attraction between Spherical Particles. *physica* **1937**, 4 (10), 1058-1072.
59. Israelachvili, J. N., *Intermolecular and Surface Forces*. 1991.
60. Derjaguin, B., On the Question About the Repulsive Forces between Surfaces Divided by Liquid Films. *Progress in Surface Science* **1992**, 40, 62-63.
61. Macosko, C. W.; Larson, R. G., *Rheology: Principles, Measurements, and Applications*. VCH New York: 1994.
62. O'connell, M. J.; Bachilo, S. M.; Huffman, C. B.; Moore, V. C.; Strano, M. S.; Haroz, E. H.; Rialon, K. L.; Boul, P. J.; Noon, W. H.; Kittrell, C., Band Gap Fluorescence from Individual Single-Walled Carbon Nanotubes. *Science* **2002**, 297 (5581), 593.
63. Girifalco, L.; Hodak, M.; Lee, R. S., Carbon Nanotubes, Buckyballs, Ropes, and a Universal Graphitic Potential. *Physical Review B* **2000**, 62 (19), 13104.
64. Sun, C. H.; Yin, L. C.; Li, F.; Lu, G. Q.; Cheng, H. M., Van Der Waals Interactions between Two Parallel Infinitely Long Single-Walled Nanotubes. *Chemical physics letters* **2005**, 403 (4-6), 343-346.
65. Coffin, D. W.; Carlsson, L. A.; Pipes, R. B., On the Separation of Carbon Nanotubes. *Composites science and technology* **2006**, 66 (9), 1132-1140.
66. Chen, B.; Gao, M.; Zuo, J.; Qu, S.; Liu, B.; Huang, Y., Binding Energy of Parallel Carbon Nanotubes. *Applied Physics Letters* **2003**, 83, 3570.
67. Sabba, Y.; Thomas, E., High-Concentration Dispersion of Single-Wall Carbon Nanotubes. *Macromolecules* **2004**, 37 (13), 4815-4820.
68. Davis, V. A. Phase Behavior and Rheology of Single-Walled Carbon Nanotubes (Swnts) in Superacids with Application to Fiber Spinning. RICE UNIVERSITY, 2006.
69. Ericson, L. M.; Fan, H.; Peng, H.; Davis, V. A.; Zhou, W.; Sulpizio, J.; Wang, Y.; Booker, R.; Vavro, J.; Guthy, C., Macroscopic, Neat, Single-Walled Carbon Nanotube Fibers. *Science* **2004**, 305 (5689), 1447-1450.
70. Davis, V. A.; Parra-Vasquez, A. N. G.; Green, M. J.; Rai, P. K.; Behabtu, N.; Prieto, V.; Booker, R. D.; Schmidt, J.; Kesselman, E.; Zhou, W., True Solutions of Single-Walled Carbon Nanotubes for Assembly into Macroscopic Materials. *Nature nanotechnology* **2009**, 4 (12), 830-834.
71. Green, M. J.; Parra-Vasquez, A. N. G.; Behabtu, N.; Pasquali, M., Modeling the Phase Behavior of Polydisperse Rigid Rods with Attractive Interactions, with Applications to Swnts in Super Acids. *arXiv preprint arXiv:0903.5112* **2009**.
72. Onsager, L., The Effects of Shape on the Interaction of Colloidal Particles. *Annals of the New York Academy of Sciences* **1949**, 51 (4), 627-659.
73. Isihara, A., Determination of Molecular Shape by Osmotic Measurement. *The Journal of Chemical Physics* **1950**, 18, 1446.
74. Isihara, A., Theory of Anisotropic Colloidal Solutions. *The Journal of Chemical Physics* **1951**, 19, 1142.

75. Flory, P., Statistical Thermodynamics of Semi-Flexible Chain Molecules. *Proceedings of the Royal Society of London. Series A. Mathematical and Physical Sciences* **1956**, 234 (1196), 60.
76. Flory, P., Phase Equilibria in Solutions of Rod-Like Particles. *Proceedings of the Royal Society of London. Series A. Mathematical and Physical Sciences* **1956**, 234 (1196), 73.
77. Ciferri, A., *Liquid Crystallinity in Polymers: Principles and Fundamental Properties*. Wiley-VCH: 1991.
78. Murali, S.; Xu, T.; Marshall, B. D.; Kayatin, M. J.; Pizarro, K.; Radhakrishnan, V. K.; Nepal, D.; Davis, V. A., Lyotropic Liquid Crystalline Self-Assembly in Dispersions of Silver Nanowires and Nanoparticles. *Langmuir* **2010**, 26 (13), 11176-11183.
79. Huggins, M. L., Theory of Solutions of High Polymers<sup>1</sup>. *Journal of the American Chemical Society* **1942**, 64 (7), 1712-1719.
80. Huggins, M. L., Some Properties of Solutions of Long-Chain Compounds. *The Journal of Physical Chemistry* **1942**, 46 (1), 151-158.
81. Beris, A. N.; Edwards, B. J., *Thermodynamics of Flowing Systems: With Internal Microstructure*. Oxford University Press, USA: 1994; Vol. 36.
82. Wang, X.; Zhou, Q. F.; Zhou, Q., *Liquid Crystalline Polymers*. World Scientific: 2004.
83. Fried, J. R., *Polymer Science and Technology*. Prentice Hall Professional Technical Reference Upper Saddle River, NJ: 2003; Vol. 117.
84. Bergin, S. D.; Nicolosi, V.; Streich, P. V.; Giordani, S.; Sun, Z.; Windle, A. H.; Ryan, P.; Niraj, N. P. P.; Wang, Z. T. T.; Carpenter, L., Towards Solutions of Single-Walled Carbon Nanotubes in Common Solvents. *Advanced Materials* **2008**, 20 (10), 1876-1881.
85. Flory, P. J., *Principles of Polymer Chemistry*. Cornell Univ Pr: 1953.
86. Kumar, A.; Gupta, R. K., *Fundamentals of Polymer Engineering*. CRC: 2003; Vol. 66.
87. Dogic, Z.; Fraden, S., Phase Behavior of Rod-Like Viruses and Virus-Sphere Mixtures. *Soft Matter* **2006**, 1-86.
88. Lebowitz, J. L.; Helfand, E.; Praestgaard, E., Scaled Particle Theory of Fluid Mixtures. *The Journal of Chemical Physics* **1965**, 43 (3), 774-779.
89. Dogic, Z.; Frenkel, D.; Fraden, S., Enhanced Stability of Layered Phases in Parallel Hard Spherocylinders Due to Addition of Hard Spheres. *Physical Review E* **2000**, 62 (3), 3925.
90. Adams, M.; Dogic, Z.; Keller, S. L.; Fraden, S., Entropically Driven Microphase Transitions in Mixtures of Colloidal Rods and Spheres. *nature* **1998**, 393 (6683), 349-352.
91. Piech, M.; Walz, J. Y., Depletion Interactions Produced by Nonadsorbing Charged and Uncharged Spheroids. *Journal of colloid and interface science* **2000**, 232 (1), 86-101.
92. Cuetos, A.; Martínez-Haya, B.; Lago, S.; Rull, L. F., Use of Parsons-Lee and Onsager Theories to Predict Nematic and Demixing Behavior in Binary Mixtures of Hard Rods and Hard Spheres. *Physical Review E* **2007**, 75 (6), 061701.
93. Poon, W., Crystallization of Globular Proteins. *Physical Review E* **1997**, 55, 3762-3764.
94. Asakura, S.; Oosawa, F., Interaction between Particles Suspended in Solutions of Macromolecules. *Journal of Polymer Science* **1958**, 33 (126), 183-192.
95. Schilling, T.; Jungblut, S.; Miller, M. A., Depletion-Induced Percolation in Networks of Nanorods. *Physical Review Letters* **2007**, 98 (10), 108303.
96. Urakami, N.; Imai, M., Dependence on Sphere Size of the Phase Behavior of Mixtures of Rods and Spheres. *The Journal of Chemical Physics* **2003**, 119, 2463.
97. Gupta, R. K., *Polymer and Composite Rheology*. CRC: 2000; Vol. 58.
98. Larson, R. G., *The Structure and Rheology of Complex Fluids*. New York: Oxford **2001**.

99. Bird, R. B.; Stewart, W. E.; Lightfoot, E. N., *Transport Phenomena*. Madison, USA **1960**.
100. Mezger, T.; Zorll, U., *The Rheology Handbook*. Vincentz Network Hannover, Germany: 2006.
101. Ferry, J. D., *Viscoelastic Properties of Polymers*. John Wiley & Sons Inc: 1980.
102. Baghdadi, H. A.; Parrella, J.; Bhatia, S. R., Long-Term Aging Effects on the Rheology of Neat Laponite and Laponite–Peo Dispersions. *Rheologica Acta* **2008**, *47* (3), 349-357.
103. Lemons, D. S.; Langevin, P., *An Introduction to Stochastic Processes in Physics*. Johns Hopkins University Press: 2002.
104. Doi, M.; Edwards, S. F., *The Theory of Polymer Dynamics*. Oxford University Press, USA: 1988; Vol. 73.
105. Kirkwood, J. G.; Auer, P. L., The Visco-Elastic Properties of Solutions of Rod-Like Macromolecules. *The Journal of Chemical Physics* **1951**, *19*, 281.
106. Yamane, Y.; Kaneda, Y.; Dio, M., Numerical Simulation of Semi-Dilute Suspensions of Rodlike Particles in Shear Flow. *Journal of non-newtonian fluid mechanics* **1994**, *54*, 405-421.
107. Bibbo, M.; Armstrong, R., Rheology of Semi-Concentrated Fiber Suspensions in Newtonian and Non-Newtonian Fluids. *The Manufacturing Science of Composites, ed. TG Gutowski (American Society of Mechanical Engineers, New York, 1988) pp* **1987**, 105-118.
108. Hu, G.; Zhao, C.; Zhang, S.; Yang, M.; Wang, Z., Low Percolation Thresholds of Electrical Conductivity and Rheology in Poly (Ethylene Terephthalate) through the Networks of Multi-Walled Carbon Nanotubes. *Polymer* **2006**, *47* (1), 480-488.
109. Du, F.; Scogna, R. C.; Zhou, W.; Brand, S.; Fischer, J. E.; Winey, K. I., Nanotube Networks in Polymer Nanocomposites: Rheology and Electrical Conductivity. *Macromolecules* **2004**, *37* (24), 9048-9055.
110. Celzard, A.; McRae, E.; Deleuze, C.; Dufort, M.; Furdin, G.; Mareche, J., Critical Concentration in Percolating Systems Containing a High-Aspect-Ratio Filler. *Physical Review B* **1996**, *53*, 6209-6214.
111. Giessibl, F. J., Advances in Atomic Force Microscopy. *Reviews of modern physics* **2003**, *75* (3), 949.
112. Butt, H. J.; Cappella, B.; Kappl, M., Force Measurements with the Atomic Force Microscope: Technique, Interpretation and Applications. *Surface Science Reports* **2005**, *59* (1-6), 1-152.
113. Schatten, H.; Pawley, J. B.; NetLibrary, I., *Biological Low-Voltage Scanning Electron Microscopy*. Springer New York, NY: 2008.
114. Goldstein, J., *Scanning Electron Microscopy and X-Ray Microanalysis*. Springer Us: 2003; Vol. 1.
115. Fultz, B.; Howe, J. M., *Transmission Electron Microscopy and Diffractometry of Materials*. Springer Verlag: 2007.
116. Egerton, R. F., *Physical Principles of Electron Microscopy: An Introduction to Tem, Sem, and Aem*. Springer: 2005.
117. Misra, P.; Dubinskii, M. A., *Ultraviolet Spectroscopy and Uv Lasers*. CRC Press: 2002; Vol. 30.
118. Greenfield, N. J., Using Circular Dichroism Spectra to Estimate Protein Secondary Structure. *Nature protocols* **2007**, *1* (6), 2876-2890.
119. Griffiths, P. R.; De Haseth, J. A., *Fourier Transform Infrared Spectrometry*. Wiley-Interscience: 2007; Vol. 171.

120. Banwell, C. N.; McCash, E. M., *Fundamentals of Molecular Spectroscopy*. McGraw-Hill New York: 1994.
121. Gardiner, D. J.; Graves, P. R.; Bowley, H. J., *Practical Raman Spectroscopy*. Springer-Verlag Berlin: 1989; Vol. 21.
122. Chou, K., Identification of Low-Frequency Modes in Protein Molecules. *Biochemical Journal* **1983**, 215 (3), 465.
123. Lakowicz, J. R.; Masters, B. R., Principles of Fluorescence Spectroscopy. *Journal of Biomedical Optics* **2008**, 13, 029901.
124. Valeur, B., *Molecular Fluorescence: Principles and Applications*. **2001**.
125. Mims, C. A.; Playfair, J. H. L.; Roitt, I. M.; Wakelin, D.; Williams, R., *Medical Microbiology*. Mosby Europe Limited: 1993.
126. Davis, J. R., *Tensile Testing*. Asm Intl: 2004.
127. McLachlan, D. S.; Blaszkiewicz, M.; Newnham, R. E., Electrical Resistivity of Composites. *Journal of the American Ceramic Society* **1990**, 73 (8), 2187-2203.
128. Montgomery, H., Method for Measuring Electrical Resistivity of Anisotropic Materials. *Journal of applied physics* **1971**, 42 (7), 2971-2975.
129. Pottick, L. A., The Influence of Drying on the Structure and Mechanics of Poly(P-Phenylene Benzobisthiazole) Fibers: High Modulus/Strength, Dry-Jet Wet Spinning, Performance, Processing. **1986**.
130. White, J. L.; Hancock, T. A., Fundamental Analysis of the Dynamics, Mass Transfer, and Coagulation in Wet Spinning of Fibers. *Journal of Applied Polymer Science* **1981**, 26 (9), 3157-3170.
131. Alsoy, S.; Duda, J. L., Modeling of Multicomponent Drying of Polymer Films. *AIChE journal* **1999**, 45 (4), 896-905.
132. Lamberti, G.; Titomanlio, G., Analysis of Film Casting Process: The Heat Transfer Phenomena. *Chemical engineering and processing* **2005**, 44 (10), 1117-1122.
133. Nepal, D.; Minus, M. L.; Kumar, S., Lysozyme Coated DNA and DNA/Swnt Fibers by Solution Spinning. *Macromolecular Bioscience* **2011**.
134. Xie, L.; Chou, S. G.; Pande, A.; Pande, J.; Zhang, J.; Dresselhaus, M. S.; Kong, J.; Liu, Z., Single-Walled Carbon Nanotubes Probing the Denaturation of Lysozyme. *The Journal of Physical Chemistry C* **2010**, 114 (17), 7717-7720.
135. Ahmad, F.; Contaxis, C.; Bigelow, C. C., Free Energy Changes in Lysozyme Denaturation. *Journal of Biological Chemistry* **1983**, 258 (13), 7960.
136. Russel, W., Review of the Role of Colloidal Forces in the Rheology of Suspensions. *Journal of Rheology* **1980**, 24 (3), 287-317.
137. Hiemenz, P. C.; Rajagopalan, R., *Principles of Colloid and Surface Chemistry, Revised and Expanded*. CRC: 1997; Vol. 14.
138. Brady, J. F.; Bossis, G., Rheology of Concentrated Suspensions of Spheres in Simple Shear Flow by Numerical Simulation. *Journal of Fluid Mechanics* **1985**, 155, 105-29.
139. Karrila, S.; Fuentes, Y.; Kim, S., Parallel Computational Strategies for Hydrodynamic Interactions between Rigid Particles of Arbitrary Shape in a Viscous Fluid. *Journal of Rheology* **1989**, 33 (6), 913-947.
140. Mellema, J.; de Kruif, C.; Blom, C.; Vrij, A., Hard Sphere Colloidal Dispersions: Mechanical Relaxation Pertaining to Thermodynamic Forces. *Rheologica Acta* **1987**, 26 (1), 40-44.

141. Merli, D.; Ugonino, M.; Profumo, A.; Fagnoni, M.; Quartarone, E.; Mustarelli, P.; Visai, L.; Grandi, M. S.; Galinetto, P.; Canton, P., Increasing the Antibacterial Effect of Lysozyme by Immobilization on Multi-Walled Carbon Nanotubes. *Journal of Nanoscience and Nanotechnology* **2011**, *11* (4), 3100-3106.
142. Borzooeian, Z.; Safavi, A.; Sheikhi, M. H.; Aminlari, M.; Doroodmand, M. M., Preparation and Investigation on Properties of Lysozyme Chemically Bonded to Single-Walled Carbon Nanotubes. *Journal of Experimental Nanoscience* **2010**, *5* (6), 536-547.
143. Nepal, D.; Geckeler, K. E., Ph-Sensitive Dispersion and Debundling of Single-Walled Carbon Nanotubes: Lysozyme as a Tool. *Small* **2006**, *2* (3), 406-412.
144. Xie, L. M.; Chou, S. G.; Pande, A.; Pande, J.; Zhang, J.; Dresselhaus, M. S.; Kong, J.; Liu, Z. F., Single-Walled Carbon Nanotubes Probing the Denaturation of Lysozyme. *Journal of Physical Chemistry C* **2010**, *114* (17), 7717-7720.
145. Dougherty, D. A., Cation- $\pi$  Interactions in Chemistry and Biology: A New View of Benzene, Phe, Tyr, and Trp. *Science* **1996**, *271* (5246), 163.
146. Nepal, D.; Geckeler, K. E., Proteins and Carbon Nanotubes: Close Encounter in Water. *Small* **2007**, *3* (7), 1259-1265.
147. Nie, H. Y.; Wang, H. F.; Cao, A. N.; Shi, Z. J.; Yang, S. T.; Yuan, Y. A.; Liu, Y. F., Diameter-Selective Dispersion of Double-Walled Carbon Nanotubes by Lysozyme. *Nanoscale* **2011**, *3* (3), 970-973.
148. Han, J. T.; Kim, S. Y.; Jeong, H. J.; Jeong, S. Y.; Lee, G. W., Molecular Engineering to Minimize the Sheet Resistance Increase of Single-Walled Carbon Nanotube/Binder Hybrid Conductive Thin Films. *The Journal of Physical Chemistry C* **2009**, *113* (39), 16915-16920.
149. Parra-Vasquez, A. N. G.; Stepanek, I.; Davis, V. A.; Moore, V. C.; Haroz, E. H.; Shaver, J.; Hauge, R. H.; Smalley, R. E.; Pasquali, M., Simple Length Determination of Single-Walled Carbon Nanotubes by Viscosity Measurements in Dilute Suspensions. *Macromolecules* **2007**, *40* (11), 4043-4047.
150. Lin, Y.; Zhou, B.; Fernando, K. A. S.; Liu, P.; Allard, L. F.; Sun, Y. P., Polymeric Carbon Nanocomposites from Carbon Nanotubes Functionalized with Matrix Polymer. *Macromolecules* **2003**, *36* (19), 7199-7204.
151. Sun, Y. P.; Zhou, B.; Henbest, K.; Fu, K.; Huang, W.; Lin, Y.; Taylor, S.; Carroll, D. L., Luminescence Anisotropy of Functionalized Carbon Nanotubes in Solution. *Chemical physics letters* **2002**, *351* (5), 349-353.
152. Moonosawmy, K. R.; Kruse, P., To Dope or Not to Dope: The Effect of Sonicating Single-Wall Carbon Nanotubes in Common Laboratory Solvents on Their Electronic Structure. *Journal of the American Chemical Society* **2008**, *130* (40), 13417-13424.
153. Poenitzsch, V. Z.; Winters, D. C.; Xie, H.; Dieckmann, G. R.; Dalton, A. B.; Musselman, I. H., Effect of Electron-Donating and Electron-Withdrawing Groups on Peptide/Single-Walled Carbon Nanotube Interactions. *Journal of the American Chemical Society* **2007**, *129* (47), 14724-14732.
154. Rao, A.; Eklund, P.; Bandow, S.; Thess, A.; Smalley, R. E., Evidence for Charge Transfer in Doped Carbon Nanotube Bundles from Raman Scattering. *nature* **1997**, *388* (6639), 257-259.
155. Wang, Y.; Wu, J.; Wei, F., A Treatment Method to Give Separated Multi-Walled Carbon Nanotubes with High Purity, High Crystallization and a Large Aspect Ratio. *Carbon* **2003**, *41* (15), 2939-2948.

156. Datsyuk, V.; Kalyva, M.; Papagelis, K.; Parthenios, J.; Tasis, D.; Siokou, A.; Kallitsis, I.; Galiotis, C., Chemical Oxidation of Multiwalled Carbon Nanotubes. *Carbon* **2008**, *46* (6), 833-840.
157. Zhang, J.; Zou, H.; Qing, Q.; Yang, Y.; Li, Q.; Liu, Z.; Guo, X.; Du, Z., Effect of Chemical Oxidation on the Structure of Single-Walled Carbon Nanotubes. *The Journal of Physical Chemistry B* **2003**, *107* (16), 3712-3718.
158. Nepal, D.; Balasubramanian, S.; Simonian, A. L.; Davis, V. A., Strong Antimicrobial Coatings: Single-Walled Carbon Nanotubes Armored with Biopolymers. *Nano Lett.* **2008**, *8* (7), 1896-1901.
159. Edelhoch, H., Spectroscopic Determination of Tryptophan and Tyrosine in Proteins\*. *Biochemistry* **1967**, *6* (7), 1948-1954.
160. Karachevtsev, V.; Plokhotnichenko, A.; Karachevtsev, M.; Leontiev, V., Decrease of Carbon Nanotube Uv Light Absorption Induced by [Pi]-[Pi]-Stacking Interaction with Nucleotide Bases. *Carbon* **2010**, *48* (13), 3682-3691.
161. Tanaka, F.; Forster, L. S.; Pal, P. K.; Rupley, J. A., The Circular Dichroism of Lysozyme. *Journal of Biological Chemistry* **1975**, *250* (17), 6977.
162. Holzwarth, G.; Doty, P., The Ultraviolet Circular Dichroism of Polypeptides<sup>1</sup>. *Journal of the American Chemical Society* **1965**, *87* (2), 218-228.
163. Lehrer, S.; Fasman, G. D., Fluorescence of Lysozyme and Lysozyme Substrate Complexes. *Journal of Biological Chemistry* **1967**, *242* (20), 4644.
164. Horsley, D.; Herron, J.; Hlady, V.; Andrade, J., Fluorescence Quenching of Adsorbed Hen and Human Lysozymes. *Langmuir* **1991**, *7* (2), 218-222.
165. Blancafort, L.; González, D.; Olivucci, M.; Robb, M. A., Quenching of Tryptophan 1 (II, II\*) Fluorescence Induced by Intramolecular Hydrogen Abstraction Via an Aborted Decarboxylation Mechanism. *Journal of the American Chemical Society* **2002**, *124* (22), 6398-6406.
166. Nishimura, S. Y.; Magana, G. M.; Ketelson, H. A.; Fuller, G. G., Effect of Lysozyme Adsorption on the Interfacial Rheology of Dppc and Cholesteryl Myristate Films. *Langmuir* **2008**, *24* (20), 11728-11733.
167. Freer, E. M.; Yim, K. S.; Fuller, G. G.; Radke, C. J., Interfacial Rheology of Globular and Flexible Proteins at the Hexadecane/Water Interface: Comparison of Shear and Dilatation Deformation. *The Journal of Physical Chemistry B* **2004**, *108* (12), 3835-3844.
168. Roberts, S. A.; Kellaway, I. W.; Taylor, K. M. G.; Warburton, B.; Peters, K., Combined Surface Pressure-Interfacial Shear Rheology Studies of the Interaction of Proteins with Spread Phospholipid Monolayers at the Air-Water Interface. *International journal of pharmaceutics* **2005**, *300* (1), 48-55.
169. Cardinaux, F.; Zaccarelli, E.; Stradner, A.; Bucciarelli, S.; Farago, B.; Egelhaaf, S. U.; Sciortino, F.; Schurtenberger, P., Cluster-Driven Dynamical Arrest in Concentrated Lysozyme Solutions. *The Journal of Physical Chemistry B* **2011**.
170. Zhou, W.; Vavro, J.; Guthy, C.; Winey, K. I.; Fischer, J. E.; Ericson, L. M.; Ramesh, S.; Saini, R.; Davis, V. A.; Kittrell, C., Single Wall Carbon Nanotube Fibers Extruded from Super-Acid Suspensions: Preferred Orientation, Electrical, and Thermal Transport. *Journal of applied physics* **2004**, *95*, 649.
171. Davis, E.; Radhakrishnan, V.; Davis, V., Scalable Route to Well-Dispersed Polyolefin/Carbon Nanotube Composites.

172. Huang, Y.; Ahir, S.; Terentjev, E., Dispersion Rheology of Carbon Nanotubes in a Polymer Matrix. *Physical Review B* **2006**, *73* (12), 125422.
173. Kayatin, M. J., Chemical Functionalization of Single-Walled Carbon Nanotubes for Compatibilization with Unsaturated Polyester Resin. **2012**.
174. Moulton, S. E.; Maugey, M.; Poulin, P.; Wallace, G. G., Liquid Crystal Behavior of Single-Walled Carbon Nanotubes Dispersed in Biological Hyaluronic Acid Solutions. *Journal of the American Chemical Society* **2007**, *129* (30), 9452-9457.
175. Cheng, E.; Li, Y.; Yang, Z.; Deng, Z.; Liu, D., DNA-Swnt Hybrid Hydrogel. *Chemical Communications* **2011**.
176. Adams, M.; Fraden, S., Phase Behavior of Mixtures of Rods (Tobacco Mosaic Virus) and Spheres (Polyethylene Oxide, Bovine Serum Albumin). *Biophysical journal* **1998**, *74* (1), 669-677.
177. Vliegthart, G.; Lekkerkerker, H., Phase Behavior of Colloidal Rod-Sphere Mixtures. *The Journal of Chemical Physics* **1999**, *111*, 4153.
178. Green, M. J., Isotropic–Nematic Phase Separation and Demixing in Mixtures of Spherical Nanoparticles with Length-Polydisperse Nanorods. *Journal of Polymer Science Part B: Polymer Physics* **2012**.
179. Clark, A.; Saunderson, D.; Suggett, A., Infrared and Laser-Raman Spectroscopic Studies of Thermally-Induced Globular Protein Gels. *International journal of peptide and protein research* **1981**, *17* (3), 353-364.
180. Marshall, B. D.; Davis, V. A.; Lee, D. C.; Korgel, B. A., Rotational and Translational Diffusivities of Germanium Nanowires. *Rheologica Acta* **2009**, *48* (5), 589-596.
181. Bomboi, F.; Bonincontro, A.; La Mesa, C.; Tardani, F., Interactions between Single-Walled Carbon Nanotubes and Lysozyme. *Journal of colloid and interface science* **2010**.
182. Rodriguez, F., *Principles of Polymer Systems*. 1982.
183. Vigolo, B.; Pénicaud, A.; Coulon, C.; Sauder, C.; Pailler, R.; Journet, C.; Bernier, P.; Poulin, P., Macroscopic Fibers and Ribbons of Oriented Carbon Nanotubes. *Science* **2000**, *290* (5495), 1331.
184. Poulin, P.; Vigolo, B.; Launois, P., Films and Fibers of Oriented Single Wall Nanotubes. *Carbon* **2002**, *40* (10), 1741-1749.
185. Hartschuh, A.; Pedrosa, H. N.; Novotny, L.; Krauss, T. D., Simultaneous Fluorescence and Raman Scattering from Single Carbon Nanotubes. *Science* **2003**, *301* (5638), 1354.
186. Coleman, J. N., Liquid-Phase Exfoliation of Nanotubes and Graphene. *Advanced Functional Materials* **2009**, *19* (23), 3680-3695.
187. Sun, Z.; Nicolosi, V.; Rickard, D.; Bergin, S. D.; Aherne, D.; Coleman, J. N., Quantitative Evaluation of Surfactant-Stabilized Single-Walled Carbon Nanotubes: Dispersion Quality and Its Correlation with Zeta Potential. *The Journal of Physical Chemistry C* **2008**, *112* (29), 10692-10699.
188. White, B.; Banerjee, S.; O'Brien, S.; Turro, N. J.; Herman, I. P., Zeta-Potential Measurements of Surfactant-Wrapped Individual Single-Walled Carbon Nanotubes. *The Journal of Physical Chemistry C* **2007**, *111* (37), 13684-13690.
189. Bordbar, A.; Hosseinzadeh, R.; Norozi, M., Interaction of a Homologous Series of N-Alkyl Trimethyl Ammonium Bromides with Eggwhite Lysozyme. *Journal of thermal analysis and calorimetry* **2007**, *87* (2), 453-456.

190. Hayashi, K.; Kugimiya, M.; Imoto, T.; Funatsu, M.; Bigelow, C. C., Inhibitory Interaction of Cationic Detergents with the Active Center of Lysozyme. II. Ph Dependence of the Interaction. *Biochemistry* **1968**, *7* (4), 1467-1472.
191. Hayashi, K.; Kugimiya, M.; Imoto, T.; Funatsu, M.; Bigelow, C. C., Inhibitory Interaction of Cationic Detergents with the Active Center of Lysozyme. I. Site of Interaction. *Biochemistry* **1968**, *7* (4), 1461-1466.
192. Subramanian, M.; Sheshadri, B.; Venkatappa, M., Interaction of Proteins with Detergents: Binding of Cationic Detergents with Lysozyme. *Journal of Biosciences* **1986**, *10* (3), 359-371.
193. White, H. E., *Modern College Physics*. Van Nostrand: 1962.
194. Barisci, J. N.; Tahhan, M.; Wallace, G. G.; Badaire, S.; Vaugien, T.; Maugey, M.; Poulin, P., Properties of Carbon Nanotube Fibers Spun from DNA-Stabilized Dispersions. *Advanced Functional Materials* **2004**, *14* (2), 133-138.
195. Wang, Q.; Dai, J.; Li, W.; Wei, Z.; Jiang, J., The Effects of Cnt Alignment on Electrical Conductivity and Mechanical Properties of Swnt/Epoxy Nanocomposites. *Composites science and technology* **2008**, *68* (7-8), 1644-1648.
196. Liu, T.; Kumar, S., Effect of Orientation on the Modulus of Swnt Films and Fibers. *Nano letters* **2003**, *3* (5), 647-650.
197. Duboeuf, F.; Liebgott, H.; Basarab, A.; Brusseau, E.; Delachartre, P.; Vray, D. In *Static Mechanical Assessment of Elastic Young's Modulus of Tissue Mimicking Materials Used for Medical Imaging*, IEEE: 2007; pp 3450-3453.
198. Möller, H.; Grelier, S.; Pardon, P.; Coma, V., Antimicrobial and Physicochemical Properties of Chitosan-Hpmc-Based Films. *Journal of agricultural and food chemistry* **2004**, *52* (21), 6585-6591.
199. Shim, B. S.; Zhu, J.; Jan, E.; Critchley, K.; Ho, S.; Podsiadlo, P.; Sun, K.; Kotov, N. A., Multiparameter Structural Optimization of Single-Walled Carbon Nanotube Composites: Toward Record Strength, Stiffness, and Toughness. *ACS nano* **2009**, *3* (7), 1711-1722.
200. Dalton, A. B.; Collins, S.; Munoz, E.; Razal, J. M.; Ebron, V. H.; Ferraris, J. P.; Coleman, J. N.; Kim, B. G.; Baughman, R. H., Super-Tough Carbon-Nanotube Fibres. *nature* **2003**, *423* (6941), 703-703.
201. Dalton, A. B.; Collins, S.; Razal, J.; Munoz, E.; Kim, B. G.; Coleman, J. N.; Ferraris, J. P.; Baughman, R. H., Continuous Carbon Nanotube Composite Fibers: Properties, Potential Applications, and Problems. *J. Mater. Chem.* **2004**, *14* (1), 1-3.
202. Zhang, M.; Atkinson, K. R.; Baughman, R. H., Multifunctional Carbon Nanotube Yarns by Downsizing an Ancient Technology. *Science* **2004**, *306* (5700), 1358-1361.
203. Zhang, M.; Fang, S.; Zakhidov, A. A.; Lee, S. B.; Aliev, A. E.; Williams, C. D.; Atkinson, K. R.; Baughman, R. H., Strong, Transparent, Multifunctional, Carbon Nanotube Sheets. *Science* **2005**, *309* (5738), 1215-1219.
204. Ajayan, P. M.; Schadler, L. S.; Giannaris, C.; Rubio, A., Single-Walled Carbon Nanotube-Polymer Composites: Strength and Weakness. *Advanced Materials* **2000**, *12* (10), 750-753.
205. Chatterjee, T.; Yurekli, K.; Hadjiev, V. G.; Krishnamoorti, R., Single-Walled Carbon Nanotube Dispersions in Poly (Ethylene Oxide). *Advanced Functional Materials* **2005**, *15* (11), 1832-1838.

206. Bachilo, S. M.; Strano, M. S.; Kittrell, C.; Hauge, R. H.; Smalley, R. E.; Weisman, R. B., Structure-Assigned Optical Spectra of Single-Walled Carbon Nanotubes. *Science* **2002**, *298* (5602), 2361-2366.
207. O'Connell, M. J.; Sivaram, S.; Doorn, S. K., Near-Infrared Resonance Raman Excitation Profile Studies of Single-Walled Carbon Nanotube Intertube Interactions: A Direct Comparison of Bundled and Individually Dispersed Hipco Nanotubes. *Physical Review B* **2004**, *69* (23), 235415.
208. Corio, P.; Jorio, A.; Demir, N.; Dresselhaus, M., Spectro-Electrochemical Studies of Single Wall Carbon Nanotubes Films. *Chemical physics letters* **2004**, *392* (4), 396-402.
209. Cooney, T.; Wang, L.; Sharma, S.; Gaudie, R.; Montana, A., Raman Spectral Study of Solid and Dissolved Poly (Vinyl Alcohol) and Ethylene-Vinyl Alcohol Copolymer. *Journal of Polymer Science Part B: Polymer Physics* **1994**, *32* (7), 1163-1174.
210. Islam, M. T.; x00ED, R.; guez-Hornedo, N. E. D.; Ciotti, S.; Ackermann, C., The Potential of Raman Spectroscopy as a Process Analytical Technique During Formulations of Topical Gels and Emulsions. *Pharmaceutical research* **2004**, *21* (10), 1844-1851.
211. Pedrosa, V. A.; Gnanaprakasa, T.; Balasubramanian, S.; Olsen, E. V.; Davis, V. A.; Simonian, A. L., Electrochemical Properties of Interface Formed by Interlaced Layers of DNA- and Lysozyme-Coated Single-Walled Carbon Nanotubes. *Electrochemistry Communications* **2009**, *11* (7), 1401-1404.
212. Bhat, N.; Gadre, A.; Bambole, V., Structural, Mechanical, and Electrical Properties of Electropolymerized Polypyrrole Composite Films. *Journal of Applied Polymer Science* **2001**, *80* (13), 2511-2517.
213. Fischer, J. E.; Zhou, W.; Vavro, J.; Llaguno, M. C.; Guthy, C.; Haggemueller, R.; Casavant, M.; Walters, D.; Smalley, R. E., Magnetically Aligned Single Wall Carbon Nanotube Films: Preferred Orientation and Anisotropic Transport Properties. *Journal of applied physics* **2003**, *93* (4), 2157-2163.
214. Minus, M. L.; Chae, H. G.; Kumar, S., Interfacial Crystallization in Gel-Spun Poly (Vinyl Alcohol)/Single-Wall Carbon Nanotube Composite Fibers. *Macromolecular Chemistry and Physics* **2009**, *210* (21), 1799-1808.
215. Zhang, X.; Liu, T.; Sreekumar, T.; Kumar, S.; Moore, V. C.; Hauge, R. H.; Smalley, R. E., Poly (Vinyl Alcohol)/Swnt Composite Film. *Nano letters* **2003**, *3* (9), 1285-1288.
216. Carini, S.; Mucchetti, G.; Neviani, E., Lysozyme: Activity against Clostridia and Use in Cheese Production-a Review. *Microbiologie-Aliments-Nutrition* **1985**, *3* (4), 299-320.
217. Eby, D. M.; Luckarift, H. R.; Johnson, G. R., Hybrid Antimicrobial Enzyme and Silver Nanoparticle Coatings for Medical Instruments. *ACS Applied Materials & Interfaces* **2009**, *1* (7), 1553-1560.
218. Ding, H. M.; Shao, L.; Liu, R. J.; Xiao, Q. G.; Chen, J. F., Silica Nanotubes for Lysozyme Immobilization. *Journal of Colloid and Interface Science* **2005**, *290* (1), 102-106.
219. Kang, S.; Pinault, M.; Pfefferle, L. D.; Elimelech, M., Single-Walled Carbon Nanotubes Exhibit Strong Antimicrobial Activity. *Langmuir* **2007**, *23* (17), 8670-8673.
220. Vecitis, C. D.; Zodrow, K. R.; Kang, S.; Elimelech, M., Electronic-Structure-Dependent Bacterial Cytotoxicity of Single-Walled Carbon Nanotubes. *ACS nano* **2010**, *4* (9), 5471-5479.
221. Collins, L.; Dawes, C., The Surface Area of the Adult Human Mouth and Thickness of the Salivary Film Covering the Teeth and Oral Mucosa. *Journal of dental research* **1987**, *66* (8), 1300-1302.

222. Hannig, C.; Hoch, J.; Becker, K.; Hannig, M.; Attin, T., Lysozyme Activity in the Initially Formed in Situ Pellicle. *Archives of oral biology* **2005**, *50* (9), 821-828.